University of Southampton

Faculty of Engineering and the Environment

Astronautics Research Department

A Study of Hybrid Inflatable Space Booms for Small Satellite Applications

by

Andrew James Cook

Thesis for the degree of Doctor of Philosophy

November 2015

University of Southampton

ABSTRACT

FACTULTY OF ENGINNERING AND THE ENVIRONMENT

Astronautics

Doctor of Philosophy

A STUDY OF HYBRID INFLATABLE SPACE BOOMS FOR SMALL SATELLITE APPLICATIONS

by Andrew James Cook

Inflatables have considerable packing efficiencies and allow simple deployment. This is due to their lack of stiffness when deflated, offering low cost solutions for space applications. After inflation, these typically soft systems could be improved using tape springs as structural stiffeners along the length of the boom, creating hybrid structures. These simple low cost single element components are easily stowed gaining strain energy in their collapsed state without permanent deformation providing additional potential to drive boom deployment. Combining both inflatable and tape spring components could create a superior hybrid boom with significant structural performance, whilst maintaining the advantages of gossamer structures.

This research focuses on the structural performance improvement of adding tape springs to cantilever inflatable booms in over 40 experimental permutations. Applied tip loads identify the deflection response of these inflatable and hybrid booms, allowing a comparison between the two technologies. A computational hybrid boom model is developed alongside the experimental analysis using detailed material testing data of the inflatable fabric boom allowing an increased range of permutations and greater detail. The structural analysis has demonstrated the performance flexibility of hybrid booms where specific peak moment and rigidity requirements can be tailored through two key configurations; 2 opposed tape springs vertically aligned to the applied load and 4 tape springs in a cross formation square to the applied load respectively. A performance evaluation between the inflatable and hybrid booms shows significant potential whilst reducing the operational importance of maintaining pressurised systems. The greatest structural performance improvement is at 2.5 PSI with an increase of over 8 and 10 times for peak moment and boom rigidity respectively. This is achieved when adding 4 tapes in a cross formation to the inflatable boom with an added mass of 105%. This research has also highlighted the importance of the attachment method between the tape springs and inflatable boom with respect to packing efficiency, parasitic mass and structural performance tradeoffs.

Contents

List of Figures

List of Tables

List of Equations

Declaration of Authorship

I, Andrew J. Cook

declare that this thesis and the work presented in it are my own and has been generated by me as the result of my own original research.

A Study of Hybrid Inflatable Space Structures for Small Satellite Applications

I confirm that:

1. This work was done wholly or mainly while in candidature for a research degree at this University;
2. Where any part of this thesis has previously been submitted for a degree or any other qualification at this University or any other institution, this has been clearly stated;
3. Where I have consulted the published work of others, this is always clearly attributed;
4. Where I have quoted from the work of others, the source is always given. With the exception of such quotations, this thesis is entirely my own work;
5. I have acknowledged all main sources of help;
6. Where the thesis is based on work done by myself jointly with others, I have made clear exactly what was done by others and what I have contributed myself;
7. Parts of this work have been published as:

   Cook, A.J., Walker, S.J.I., and Dobbs, H., "Experimental Research on the use of Tape Springs on Inflatable Structures," *28th International Symposium on Space Technology and Science*, 2011-c-37, 5-12th Jun, Okinawa, Japan, 2011.

   Cook, A.J., Walker, S.J.I., "Experimental research on tape spring supported space inflatable structures," *Acta Astronautica,* Accepted 21 Oct, Available online 31 Oct, 2015, Pending publication.

Signed: .....

Date:.....

Acknowledgements

I would like to foremost thank my supervisor Dr Scott Walker for guiding me through this Doctorate. Your support and advice throughout my PhD has meant I have been able to reach this position of which I am proud to be able to put together the following research.

Thanks go to all the EDMC staff, Dave, Terry and Simon and to everyone who has helped and contributed to this research. Warin, for all your support, amazing cooking and taking me to the other side of the world, Tony and everyone else in the Astronautics research department. You are an amazing friendly bunch and made my days very enjoyable.

To my family for all their support throughout, Thank you. I would like to make a special thanks to my Mum, Lulu and Bella who made the write up a painless and often enjoyable process.

Thanks go to all my friends I have lived with over the 5 years and all those I have made along the way. To all the members of Sammy C's Jazz Disorder you were and continue to be fantastic and a joy to play with. To Gary who helped me immeasurably both in the technical aspects and morale. Your humour made the countless lab hours spent together as well as away from work great fun.

Special thanks go to Bella for your support. Your love and cajolement has kept me on track especially towards the final stages of my PhD and life post University.

List of Acronyms

BS	Boom Supported
BUS	Boom Unsupported
CFRP	Carbon Fibre Reinforced Plastic
COTS	Commercial Off The Shelf
CTM	Collapsible Tube Mast
DIC	Digital Image Correlation
DOF	Degrees Of Freedom
FEA	Finite Element Analysis
FSA	Flat Surface Array
IAE	Inflatable Antenna Experiment
IDEAS	Innovative De-orbiting Aerobrake System
JWST	James Webb Space Telescope
LEO	Low Earth Orbit
ODISSEE	Orbital Demonstration of an Innovative Solar Sail driven Expandable structure Experiment
PSI	Pounds per Square Inch
RP	Reference Point
SAR	Synthetic Aperture Radar
SRP	Solar Radiation Pressure
STEM	Storable Tubular Extendible Member
TACEDS	Tetragonal Accordion Deployment Control System
TRAC	Triangular Retractable And Collapsible
TSR	Tape Spring Rolling
UPR	Ultimate Packing Ratio
UTS	Ultimate Tensile Strength
UV	Ultra Violet

Nomenclature

a	Width of un-deformed tape spring, m (section 2.3)
D	Flexural rigidity, Nm^4 (section 2.3)
E	Young's modulus, Nm^{-2}
E_B, E_U	Biaxial and uniaxial elastic modulus respectively, Nm^{-2}
E_{Bf}, E_{Bw}	Biaxial elastic modulus in the fill and warp orientations respectively, Nm^{-2}
E_f, E_w	Fill and warp Young's modulus respectively, Nm^{-2}
E_L, E_H	Young's modulus in the longitudinal and hoop directions respectively, Nm^{-2}
E_{45}	Biased elastic modulus, Nm^{-2}
E^*	Estimated Boom Young's Modulus, Nm^{-2}
F_c, F_p	Axial compression and inflation pressure forces respectively, N
F_δ	Boom tip force, N
G	Shear modulus, Nm^{-2}
G_{HL}, G_{wf}	Hoop direction and warp orientation shear modulus respectively, Nm^{-2}
I_x	Boom 2nd moment of area in the tip loading direction, mm^4
L	Boom length, m
M, $\overline{M}$	Moment and non-dimensional moment respectively, Nm
M_{fail}, M^0_{fail}	Failure moment and failure moment under no axial compression respectively, Nm
M_w, M^0_w	Incipient wrinkling moment and incipient wrinkling moment with no axial compression respectively, Nm
M_{max}, M^0_{max}	Maximum moment and maximum moment under no axial compression respectively, Nm
$M^0_{max,BS}$	Maximum boom supported bending moment with no axial compression, Nm
$M^{Fc}_{max,BS}$	Maximum boom supported bending moment with axial compression, Nm
M_{200}	Moment at 200 mm tip deflection, Nm
M^*_+, M^*_-	Steady state moments for opposite and equal sense bends respectively, Nmm
M^{max}_+, M^{max}_-	Peak buckling moments for opposite and equal sense bends respectively, Nmm
n	Normal out of plane fabric direction
P, P'	Reference and deformed subset centre coordinates respectively (section 3.2)
p	Gauge pressure. Calculations throughout thesis use standard metric units of Nm^{-2}. PSI is used to label inflation pressure data for simplicity with the following common conversions.

PSI		Nm^{-2}/ Pa
2.5	–	17238
5	–	34475
10	–	68950
15	–	103400

Q, Q'	Reference and deformed tracked point coordinates respectively (section 3.2)

R	Tape spring radius of curvature, m
r, r_0	Boom radius and initial radius respectively, mm
$\bar{S}$	Non dimensional boom rigidity
T	Torque, Nm (section 2.2)
t	Thickness, mm
t_{Tape}	Tape spring thickness, m
$V_{inflated}$	Inflated boom volume, cm^3
$V_{material}$	Total material boom volume, cm^3
V_{stowed}	Stowed boom volume, cm^3
α	Angle of embrace, rad
δ, $\bar{\delta}$	Tip deflection and non-dimensional tip deflection respectively, mm
ε_{Bf}, ε_{Bw}	Biaxial strain in the fill and warps orientations respectively
ε_{BL}, ε_{BH}	Biaxial strain in the longitudinal and hoop directions respectively
ε_f, ε_w	Fill and warp strains respectively
ε_{fy}, ε_{wy}, ε_{45y}	Fill, warp and biased strains in the longitudinal direction respectively
ε_L,, ε_H	Longitudinal and hoop strains
ε_x, ε_y	Uniaxial transverse and longitudinal strains respectively (chapter 3)
θ, θ_0	Angle and angle encompassing the wrinkled region around the boom circumference respectively, rad (section 2.2)
κ_x, κ_y, κ_{xy}	Longitudinal, transverse, twisting tape spring curvatures respectively (section 2.3)
$\kappa_{x,0}$, $\kappa_{y,0}$, $\kappa_{xy,0}$	Initial longitudinal, transverse, twisting tape spring curvatures respectively (section 2.3)
$\bar{\kappa}_x$, $\bar{\kappa}_y$, $\bar{\kappa}_{xy}$	Non dimensional longitudinal, transverse, twisting tape spring curvatures respectively (section 2.3)
$\bar{\kappa}_{x,0}$, $\bar{\kappa}_{y,0}$, $\bar{\kappa}_{xy,0}$	Initial non dimensional longitudinal, transverse, twisting tape spring curvatures respectively (section 2.3)
λ, η, Ψ_1, Ψ_2	Non dimensional tape spring moment - curvature functions (section 2.3)
v_{fw}, v_{wf}	Fill and warp Poisson's ratios respectively
v_{LH}, v_{HL}	Longitudinal and hoop Poisson's ratios respectively
v_{yx}	Uniaxial longitudinal Poisson's ratio (chapter 3)
ρ	Density, kgm^{-3}
σ_{Bf}, σ_{Bw}	Biaxial stress in the fill and warp orientations respectively, Nm^{-2}
σ_{BL}, σ_{BH}	Biaxial stress in the longitudinal and hoop directions respectively, Nm^{-2}
σ_f, σ_w	Fill and warp stresses respectively, Nm^{-2}
σ_L, σ_H	Longitudinal and hoop stresses respectively, Nm^{-2}
σ_m	Cumulative stress due to inflation and tensile bending, Nm^{-2} (section 2.2)
σ_o	Cumulative stress due to inflation and compressive bending, Nm^{-2} (section 2.2)
σ_x, σ_y	Uniaxial transverse and longitudinal stresses respectively, Nm^{-2} (chapter 3)

Chapter 1

Introduction

1.1 Motivation for Hybrid Boom Development

Gossamer structures are defined as ultra-low mass low volume expandable structures that have high packing efficiencies capable of being stowed from large sizes into a launch shroud volume. They have enabled our first access into the skies and our initial steps towards space. These now iconic lighter than air structures were quickly utilised for diverse means including exploration, travel, scientific endeavour, leisure and military purposes providing a new platform in the sky and fulfilling humans ambition to soar with the birds. Heavier than air aerospace technology quickly surpassed the limited capabilities of airships and balloons; however they continue to find niches, for example with weather balloons. With the advent of space exploration in the 1950s gossamer technology was reborn where inflatable and membrane structures offer significant savings in mass and stowage volume and thus reducing the cost of launch[1]. Other gossamer structures have come to the fore, most notably tape springs. They are generally defined as straight, thin-walled strips with an initially curved cross-section[2,3] and have been developed as deployment devices and simple hinges with significant structural properties when in their deployed state. With the addition of tape springs as structural stiffeners to an inflatable boom creating a hybrid structure could significantly increase the structural performance of a boom. This research investigates the potential of hybrid structures, using inflatable booms and tape springs, and focuses on increasing the structural performance while maintaining the mass and volume advantages of gossamer structures.

It is intuitive that inflatables can create large space structures that would otherwise be difficult to send into orbit from a single launch. TransHab[4], Genesis I and II[5], and Bigelow's space station alpha[6] are examples of simpler and more cost effective methods for creating large structures for human habitation in space. Other examples include the use of inflatable booms instead of traditional support elements to mount equipment such as solar arrays[7], all of which must be stowed during the launch phase.

In recent years, focus has developed towards smaller low mass satellites where traditional deployment systems become inefficient due to an increase in complexity of scaled down mechanisms. Inflatables can reduce the complexity of a structure and offer significant stowage performance lowering both the cost of manufacture overall mass and volume of the structure. Tape springs are an ideal component to be used in conjunction with an inflatable boom due to their light weight simple design with non-permanent deformation when buckled. The stored strain energy in their buckled state has provided self-deployable structures in previous studies[8-13] and could be utilised for inflatable systems reducing complexity and costs further. The significant structural properties of tape springs may also provide substantial structural performance benefits which will provide the main focus of this research.

Interest in large gossamer structures continues and includes the development of the James Webb Space Telescope (JWST) sunshield[14]. These systems have tended to be focused upon larger cost budgets allowing for more expensive, exotic well tested materials. This research is aimed at the increasing demand for 'off the shelf' systems. Low cost payload missions can take advantage of this as the research uses easily sourced materials: Nylon fabric and steel tape springs for the initial investigations.

Other uses of this hybrid technology include the creation of larger inflatable satellites as well as providing booms for various applications such as solar arrays, solar sails and antennas. An array system could be adapted to provide a cheap add-on system to deorbit small satellites in Low Earth Orbit (LEO) utilising aerodynamic drag. It has potential to generate a cheap technology that could reduce costs and system complexities currently incurred.

1.2 Research Aims and Objectives

Combining tape springs with an inflatable boom has had very limited experimental investigation with previous studies considering only the axial loading and buckling of a hybrid boom[15,16] where development tends to consider larger structures for space applications. This research considers smaller structures with the principle objective of quantifying the tip deflection structural performance gains by utilising tape springs on an inflatable boom.

The research aims to determine the feasibility of attaching tape springs to an inflatable boom utilising low cost Commercial Off The Shelf (COTS) components, and establish the key performance characteristics of these novel hybrid structures. The key performance characteristics are: structural (boom rigidity and failure bending moment), mass, packing ratio, deployment, and boom durability (long term rigidisation, and survivability). Experimental tip deflection testing of cantilever inflatable and hybrid booms that may be typically used for small satellite applications. The research aims to determine the comparative structural performances focusing on small scale structures of around 1 m long and providing sub 1 mm deflection accuracy.

A further key objective of this research is to develop an initial hybrid boom numerical model using finite element methods validated by experimental results that will progress the limited knowledge of these types of structures. From experimental testing and numerical models structural performance conclusions can be attained from which future hybrid boom development can progress.

1.3 Report Outline

This thesis presents a detailed account of this research which is split into a further nine chapters. The following chapter provides the reader with a background of gossamer space structures including developments and theoretical understanding of both inflatable and tape spring based booms and concluding with details of inflatable boom construction using a fabric material.

Chapter 3 is a material properties study of the inflatable boom using both uniaxial and biaxial tensile testing to provide a detailed mechanical understanding of the selected construction fabric.

Experimental structural analysis of the inflatable boom is then performed in chapter 4 to establish a baseline performance. This is achieved using tip deflection tests of cantilever inflatable booms across 8 inflation pressures.

Concurrently two Finite Element Analysis (FEA) models described in chapters 5 and 6 are created for an inflatable boom and tape spring respectively. The FEA models are developed and validated against experimental results to achieve a full understanding of the hybrid boom component parts.

The tape springs and inflatable boom are brought together to construct a hybrid boom with experimental structural testing in chapter 7 and the developed FEA model in chapter 8 where further permutations are investigated.

The document evaluates the performance of the hybrid booms created focusing on the structural performance benefit of the addition of tape springs to an inflatable boom in chapter 9. The thesis closes with a summary and conclusions of the project in chapter 10 where key research results and future research areas are highlighted.

Chapter 2

Background and Development

Gossamer structures are typically constructed from thin highly flexible elements where often membranes are utilised. Membrane flexibility is a result of their very low bending stiffness and inability to sustain compressive loads, ideal for stowage capabilities and the low packing ratios required in the space industry. While other tensioning devices exist, deployment and maintained structural supported is frequently provided from inflation and leads to the continued interest and development of inflatable structures for space applications.

2.1 Current Gossamer Structures and Applications

Research of gossamer space structures began with Goodyear among others investigating membrane materials for low mass spacecraft in the 1950s. Research was conducted and continues to focus on large inflatable structures such as the NASA Echo Balloons I & II[17] and the Goodyear radar antennas of the 1950s and 1960s, L'Garde's large inflatable deployable space antenna flown in 1996[18] and the future JWSP inflatable sunshield due for launch in the late 2010s[19]. The range of gossamer space applications is considerable and envelops large structures such as human habitation[4-6], solar sails[20-28], sunshades[29-31] and solar arrays[32-35] where long term precision tolerances are lower. Development of the latter two applications among others range in scales of magnitude from the larger sunshield of the JWSP deploying a 263 m^2 membrane, and the 14 m long ST4 large solar array by NASA and ILC Dover respectively, to the considerably smaller structures of the Mars Rover Solar Array, the 600 g Power Sphere shown in Figure 2.1 and the thermal shield for the ESA far-infrared space telescope[30,31,32,35,36]. Other inflatable space applications ranging in size are the reflector and antenna arrays ranging from the 1 and 3 m microstrip reflect arrays developed by ILC Dover[37] to the 7 m lenticular antenna and the successfully flown 28 m Inflatable Antenna Experiment (IAE) by L'Garde[38].

a) Half – scale JWST sunshield

b) 10 x 3 m Inflatable solar array

c) Mars rover solar array

d) Power sphere

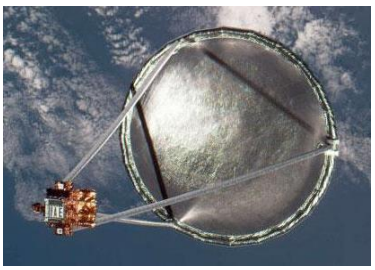

e) Inflatable antenna experiment

Figure 2.1: Example gossamer applications and sizes[30,32,35,36,38].

Other gossamer space applications include inflatable Synthetic Aperture Radars (SARs)[39-43], solar concentrators[45], tethers[46-49], drag augmenters for de-orbiting devices[50-53], aerodynamic deceleration and inflatable re-entry vehicles[54] including the very successful Mars pathfinder impact attenuation system which used a series of airbags to land the pathfinder rovers softly on the planet surface in 1997[55]. Inflatable rovers and wings are also in continued development for both terrestrial and interplanetary missions[56-60]. Gossamer structures are well suited to large structural applications where studies have shown significant mass and cost savings over traditional mechanical structures[61]. However their low complexity also makes them suitable to a wide range of smaller devices that require structural support including used simply as a spacecraft boom. An example is the L'Garde truss[62] demonstrating their significant adaptability to a wide range of configurations. Key areas of concern for gossamer structures that must be taken into consideration during design are manufacture, deployment, performance, and longevity[36]. This stems from the typical materials used in such structures where the low bending stiffness and thinness of the materials cause difficulties in constructing joints and some sort of passive or controlled deployment control being required. Performance issues are a result of these inherently soft flexible structures having a reliance on inflation. In addition being prone to leaks and puncture from material degradation, space debris and micrometeor impacts significantly affect durability and longevity where continued research investigates a variety of methods for long term rigidisation[63-68].

The materials used in the structures outlined above are generally thin film membranes including; organic polymeric materials such as Kapton, Mylar, and polyester with the latter being used on the IAE[38]. Metal foils and laminates such as the Echo balloons are rigidised through inflation strain work hardening. This was also demonstrated by Lou et al. (2002) for an inflatable boom whilst also considering Nylon and Kevlar fabrics. These have been previously used by the IAE[38], the inflatable SAR developed by Lou and Feria (1998), and Transhab[4]. Lou et al. (2002) extended this research with the addition of steel carpenter tape springs to reinforce the inflatable booms creating a hybrid structure. Tape springs commercially constructed from rolled spring steel have also found particular used in a variety of gossamer structural designs including solar sails NanoSail-D[69] and Lightsail[70] using the Triangular Retractable And Collapsible (TRAC) boom as shown in Figure 2.2 created by laser welding two stainless steel strips together. The TRAC booms are easily stowed with a good packing ratio, self-deployable from the strain energy stored in their stowed state and deploy into a rigid strip without permanent deformation. The performance of these booms can be scaled up or down depending on the application resulting in thickness and tape width alterations. The TRAC used in NanoSail-D and Lightsail are stowed within a 430 cm^3 volume for a deployed boom length of 2.3 m[71]. Another tape spring boom configuration that has been considered is the Storable Tubular Extendible Member (STEM)[72]. The boom is constructed into a circular tube which can be collapsed and rolled onto a mandrel similar to TRAC, and is also self-deployable.

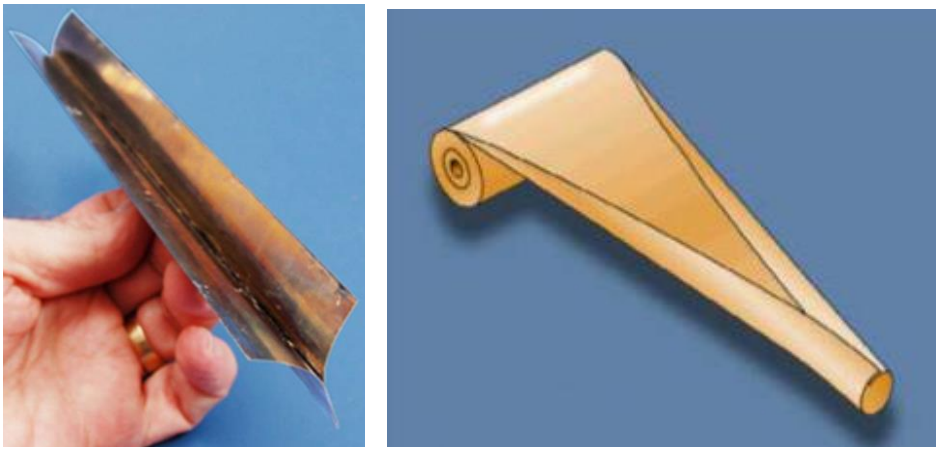

a) TRAC boom b) STEM boom

Figure 2.2: Tape spring based deployable booms[69,71].

A similar style of collapsible structure developed by DLR is the omega shaped carbon fibre reinforced plastic (CFRP) lenticular boom used on the Orbital Demonstration of an Innovative Solar Sail driven by Expandable Structure Experiment (ODISSEE)[73]. The boom is constructed in two identical parts placed opposite to each other and are rolled up for stowage as shown in

Figure 2.3. The boom can be made to any size for specific design requirements, although in the given development stage the boom weighs 62 g/m. The boom diameter is 150 mm which becomes 209 mm wide when stowed without permanent deformation. The thickness of the boom is 0.1 mm. It is designed to support a solar sail of 400 m^2 with studies considering surface arrays as large as 100 x 100 m[44]. Research by Sickinger et al.[74-76] have conducted FEA with ANSYS on these booms showing an average buckling moment of M_x = 57.0 Nm. The analysis took into account manufacture and loading discrepancies such as shell thickness and geometry inaccuracies shown to cause significant changes in results[77]. The buckling moment is M_y = 95.0 Nm, with boom stiffness's of EI = 5073 and 5318 Nm^2 with respect to the x and y bending directions respectively. The load required to buckle this boom in compression is 2000 N. Deployment can be controlled at low cost and complexity with an internal inflatable boom and Velcro along the boom length increasing the boom mass by 50% to 93 g/m.

a) b)

Figure 2.3: Omega shaped carbon fibre boom, a) being wound up with labelled boom axes at boom tip, and b) possible low cost deployment device[77].

Another type of gossamer structure uses wires and battens placed into tension to create a boom. The ATK solar sail uses this style of boom illustrated in Figure 2.4 and is capable of being stowed to less than 1% of its deployed length while being self-deployable using stored strain energy in the stowed longerons. Other similar concepts include research by Brown (2011) and the ST8 Sailmast by McEachen et al. (2005). The 40 m ST8 Sailmast of 34 g/m is capable of compressive loads of up to 115 N[78]. A boom constructed by Tibert (2002) has a comparable design using bi-stable tubes as hinges between rods that are held in tension by wires. The 60 m structure of 1.1 m diameter has a mass of 290 kg and is capable of a maximum bending moment of 8140 Nm. The stiffness of the structure is 13 MNm^2 and has a length packing ratio of 2.7%[79].

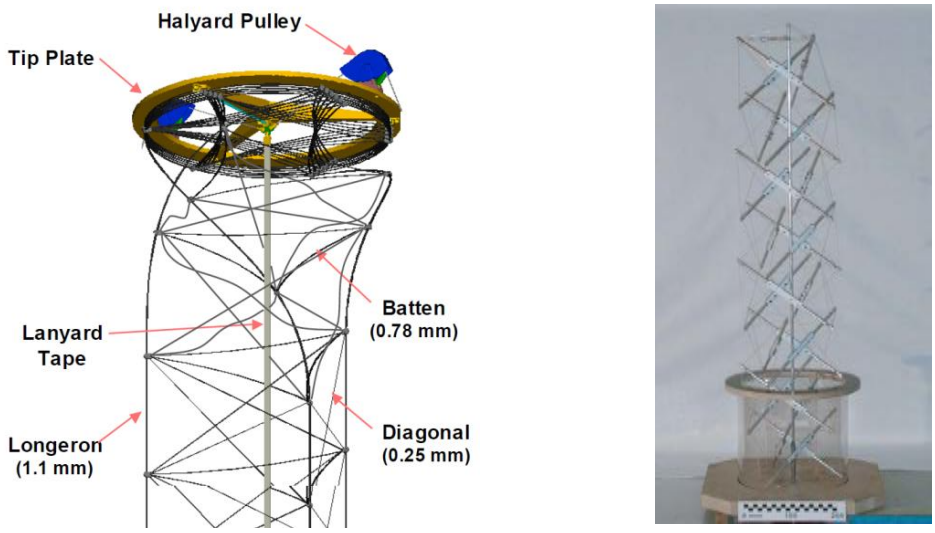

a) b)

Figure 2.4: Deployable booms to a) support ATKs solar sail[80] and b) a developed eight stage mast using bi-stable tubes[79].

A different collapsible structure without permanent deformation is the ILC Dover shape memory space frame constructed from carbon fibre composite as shown in Figure 2.5. The memory structure requires heating and inflation to drive deployment. A similar boom using a carbon reinforced isogrid[64,66] is cured with Ultra Violet (UV) radiation once deployed using inflation. Both types of boom have been subjected to compression testing with the UV curable iosgrid and the shape memory composite isogrid booms able to withstand over 170 N[66], and 1600 N[65] respectively for a boom length of 0.4 m. The shape memory composite is significantly stronger as it uses more interlinking trusses and adds mass to the structure. It is therefore possible to create a boom optimised to a particular specification. The carbon composite used has a density of 1.8 g/cm^3 but the total mass of the structure is currently unknown. The UV cured isogrid has a mass of 109 g/m length of boom with the Mylar bladder adding a further 56.5 g/m.

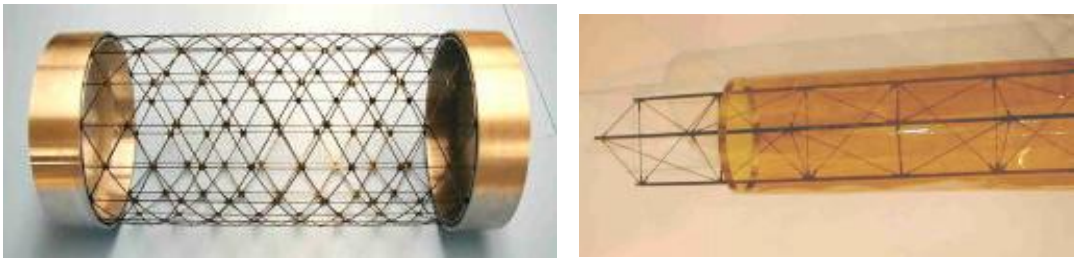

a) Shape memory space frame b) Isogrid beam

Figure 2.5: ILC DOVERs rigidisable space inflatable booms[65].

The CubeSail[22] mission also uses UV curable booms that are deployed using inflation. The mass of the booms, sail and deployment mechanism is 0.2 kg, which provides a flat surface area of 25 m^2. This comprises of 4 supporting 3.5 m long booms with a mass of 35 g each. The booms and sail both use a polyimide less than 1 µm thick resulting in a sail mass of 60 g. The booms are slightly thicker with a UV rigidisable layer and have a diameter of 4 cm which can maintain a pressure of 206.8 kPa[22]. This results in a predicted maximum bending moment of 41.5 Nm. Other solar sail projects use and propose various types of booms. The GeoSail has a total solar sail system mass of 59 kg of which 28 kg is the sail and the supporting booms aiming to create a 150 m^2 sail. The supporting booms are 40 g/m and over 100 m long[23]. L'Garde uses an inflatable monocoque boom that rigidises using a cold cure resin impregnated into the boom. The boom is supported by a series of Kevlar wires that are placed in tension when the sail is subjected to Solar Radiation Pressure (SRP) and have shown successful vacuum deployment tests[21].

Other inflatable booms include the Innovative De-orbiting Aerobrake System (IDEAS)[81] and the structural support for the JWST sunshield. The inflatable 7 and 16 m long booms for the JWST have a diameter of 130 mm and are inflated to 22.06 kPa able to maintain 29 Nm before failure[29]. The booms are constructed using a heat curable carbon fibre prepreg fabric that increases the maximum bending moment to 69.77 Nm once rigidised. The booms mass is 290.5 g/m with the addition of root and tip end caps of 171.3 g and 159.9 g respectively. IDEAS uses a 3.2 m polyimide inflatable boom with a diameter of 160 mm capable of supporting a 112 N compression force before buckling. The boom also has a deflection stiffness of 660 N/m[7] and a packing ratio of 45. The deorbiting application is of specific interest as it could be scalable for a range of CubeSats in LEO utilising aerodynamic drag by means of a Flat Surface Array (FSA). This could provide a simple low cost solution to help mitigate space debris. Table 2.1 provides a summary of performance of other drag de-orbiting concepts. The literature shows inflatable and tape spring like structures are common solutions strategies to create FSAs. The literature suggests these technologies can be scalable for specific de-orbiting requirements.

Table 2.1: **Performance overview of FSA drag de-orbit concepts.**

Device Name	Structural component to create FSA	Device Mass	De-orbit performance		
			Time to decay	Satellite Mass	Initial orbit altitude
iDod[50]	Inflatable boom	0.12 kg	25 years	1 kg	900 km
Cubesail[141]	2 seperated cubesats	3 kg	285 days	500 kg	800 km
Cubesat de-orbit device[142]	Inflatable pillow	0.14 kg	11 years	1 kg	800 km
IDEAS[81]	Inflatable boom	11 kg	25 years	200 kg	790 km
Drag Sail[51]	Omega CFRP boom	3 kg	25 years	200 kg	650 km
NanoSail-D[69]	TRAC tape springs	3 kg	4 days	3 kg	330 km

The structural performance of the supporting booms for these FSAs are specific to the mission specification. Aerodynamic drag and hence bending moment applied to the structure is a function of the starting altitude (a), satellite mass (m) and surface area (S) and the required time to deorbit with the change in orbit height per orbit (δa) shown in Equation 2.1[143]. Equations 2.2 and 2.3 give the orbit period (τ) and the drag force (D) where C_D is the drag coefficient constant at 2.2[143,144], ρ is the atmospheric density empirically determined by the solor activity[144], μ is the Earth's gravitational constant and v is the spacecraft velocity determined by Kepler's third law of Equation 2.2.

$$\delta a = -2\pi\rho\frac{SC_D}{m}a^2 \quad \textbf{(Equation 2.1)}$$

$$\tau = 2\pi\sqrt{\frac{a^3}{\mu}} \quad \textbf{(Equation 2.2)}$$

$$D = \frac{1}{2}\rho v^2\frac{S}{4}C_D \quad \textbf{(Equation 2.3)}$$

Focusing on 1U CubeSats (1 kg, 0.1 x 0.1 x 0.1 m) in LEO (200-2000 km) for small satellite applications, the aerodynamic drag can generate over 30 Nm acting on the supporting booms of a simply supported FSA that will deorbit the CubeSat within 25 years. Boom rigidity is also important to account for foreshortening of these FSAs. A softer structure will require a larger FSA to achieve the same deorbiting performance resulting in increased mass and stowage volume. This creates a tradeoff between the booms rigidity against mass and packing efficiency. Table 2.2 below gives an example highlighting the impact of a structure that

becomes twice a stiff and twice as soft. Data is taken from structural performance of the NGST inflatable sun shield booms[14] with the referenced values shown in *italics.* The remaining data is calculated based on tip deflections at 30 Nm applied tip load extrapolated from Sandy (2000) cantilever tip deflection tests[14] from which the foreshortening effect is calculated.

Table 2.2: Effect of altering the boom rigidity on required length for a FSA (Referenced data in *italics*).

Boom length	**Bending Stiffness, EI**	**Tip deflection @ 30 Nm**	**Effective length for a FSA**	**Boom mass**
2.24 m[14]	*1144 Nm^2[14]*	0.8 m	2.09 m	*448 g[14]*
2.12 m	2288 Nm^2	0.39 m	2.09 m	425 g
2.99 m	572 Nm^2	2.14 m	2.09 m	599 g

Doubling the stiffness of the NGST inflatable boom would achieve a required length reduction of 5% which would see equivalent savings in boom mass and packing volume. The effect of this is more prominent with large deflections that approach the boom length. Halving the stiffness of the NGST inflatable boom would require a 34% longer and hence requiring 34% more stowage volume and boom mass.

Research by Darooka and Jensen (2001) compared the structural performance of various boom technologies and is displayed in Figure 2.6. The information shown takes data from the typical properties of other structures[61] using mass per length as the efficiency function and plotted against the axial load a boom can withstand. Figure 2.6 clearly shows that isogrid and inflatable trusses have the greatest structural efficiency with a significant increase from traditional mechanical deployable structures. Coilable longerons such as the TRAC also suggest a possible use for small low loading applications. However the low complexity easily sourced materials of inflatables and tape springs will make them an attractive option for low cost applications. The following sections give greater detail of the properties to these types of structures.

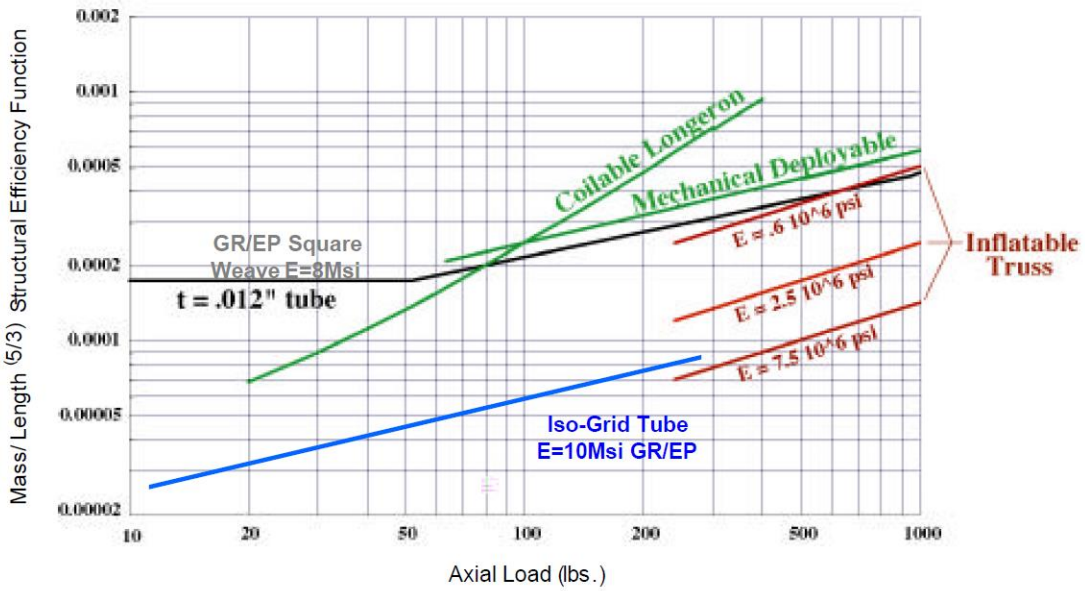

Figure 2.6: Comparison of structural efficiency of various space deployable structures[61].

2.2 Inflatable Booms – General Properties

Many experimental, analytical and computational studies of inflatable booms have been and continue to be undertaken to develop and further the understanding of inflatable structures for both space and terrestrial applications. It is well known for thin walled cylindrical pressure vessels the hoop and longitudinal stresses as defined in Figure 2.7 are

$$\boldsymbol{\sigma_H = \frac{pr}{t}} \text{ and } \boldsymbol{\sigma_L = \frac{pr}{2t}} \text{ [82]}, \qquad \textbf{(Equations 2.4 and 2.5)}$$

respectively, where; *r* is the tube radius, *p* is the internal gauge pressure and *t* is the skin thickness.

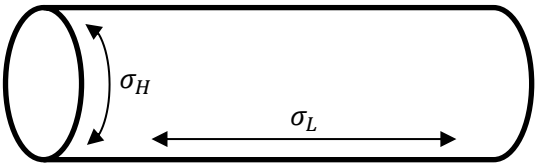

Figure 2.7: Longitudinal and hoop stress directions of an inflatable boom.

Many studies have been completed that consider the behaviour of inflatable tubes under various loading profiles. Comer and Levy (1963) developed an analytical relationship describing the moment – deflection response of an inflatable cantilever beam under tip and uniform loading with the analysis assuming a thin isotropic membrane with no bending or compressive

stiffness. Figure 2.8 describes the cross-sectional stress profile in a cantilever beam with an applied load. It highlights the wrinkling of the membrane once the compressive stresses of the bending moment profile from the applied loading become larger than the tensile inflation pressure stress. As the load is increased further the wrinkles propagate around the circumference of the boom and along boom length.

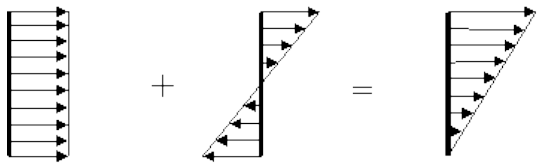

Longitudinal tensile stress due to inflation pressure, *p*

Stress profile from applied bending moment, *M*

Leading to incipient wrinkling on compression surface

a)

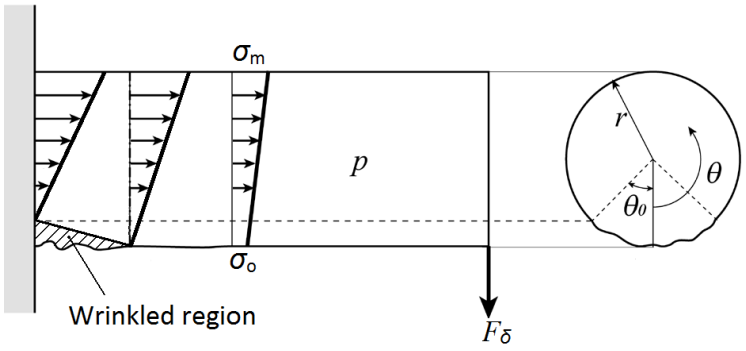

b)

Figure 2.8: Cross sectional stress profiles of an inflatable cantilever boom under bending in a) constituent parts, and b) along boom length and around boom radius with an applied tip load[83].

The stress profile when there is no wrinkling is assumed to change linearly and is defined as

$$\boldsymbol{\sigma = \sigma_0 \left(\frac{1-\cos\theta}{2}\right) + \sigma_m \left(\frac{1-\cos\theta}{2}\right)},$$ **(Equation 2.6)**

where θ is measured from $\sigma = \sigma_0$. Once tensile inflation forces are overcome wrinkling occurs and stress is zero in this region. The stress distribution around the boom circumference is then defined as

$\sigma = \left(\frac{\cos\theta_0 - \cos\theta}{1+\cos\theta_0}\right)\sigma_m$ for $\pi > \theta > \theta_0$ Non-wrinkled region,

$\sigma = 0$ for $\theta_0 > \theta > 0$ Wrinkled region [84-87]. **(Equation 2.7)**

Balancing moments about the transverse axis through the centre of the beam and axial forces from inflation respectively are described by

$$\boldsymbol{M = -2\int_0^{\pi} t\sigma r^2 \cos\theta \, d\theta,} \qquad \textbf{(Equation 2.8)}$$

$$\boldsymbol{p\pi r^2 = 2\int_0^{\pi} t\sigma r \, d\theta.} \qquad \textbf{(Equation 2.9)}$$

Substituting the resultant stress profile from Equation 2.7 into Equations 2.8 and 2.9 and equating σ_m gives

$$\frac{\boldsymbol{M}}{\boldsymbol{pr^3}} = \frac{\boldsymbol{\pi(2\pi - 2\theta_0 + \sin\theta)}}{\boldsymbol{4[(\pi - \theta_0)\cos\theta_0 + \sin\theta_0]}} \quad \text{for} \quad \boldsymbol{\pi > \theta > \theta_0.} \qquad \textbf{(Equation 2.10)}$$

By assuming $\theta_0 = 0$ at the point of wrinkling Equation 2.10 becomes

$$\boldsymbol{M_w = \frac{\pi r^3 p}{2}.} \qquad \textbf{(Equation 2.11)}$$

Comer and Levy (1963) define the collapsed load of the boom as $\theta_0 \rightarrow \pi$ leading to the relationship

$$\boldsymbol{M_{max} = \pi r^3 p.} \qquad \textbf{(Equation 2.12)}$$

Main et al. (1994) comments on this beam collapse assumption where a strip of fabric on the top surface must remain unwrinkled to be able to carry the applied load causing beam collapse. They demonstrate analytically that Equation 2.9 occurs at $\theta_0 = 0.99\pi$. An analogous relationship is also presented by Webber (1982) confirming beam collapse is twice the incipient wrinkling load verified through experimental testing. Webber (1982) also performs a static analysis on an inclined plane considering both bending and torsion of slender inflatable beams resulting in Equation 2.13 for incipient wrinkling. Taking bending moments alone results in the same relationship of Equation 2.11.

$$\boldsymbol{T^2 + 4\pi p r^3 M = 2\pi^2 p^2 r^6} \quad \text{for} \quad \boldsymbol{\theta_0 = 0.} \qquad \textbf{(Equation 2.13)}$$

Boom deflections are typically determined by Euler-Bernoulli beam theory[83-85,87,88] or more recently using Timoshenko beam theory[89-94]; however many including the Comer and Levy (1963) model assume an isotropic material. Further studies have extended this to include orthotropic materials including Main et al. (1995) who considered the varying planar material properties of fabrics resulting in Equation 2.9 altering to

$$\boldsymbol{M_w = \frac{\pi p r^3}{2}(1 - 2\nu_{LH})}, \qquad \textbf{(Equation 2.14)}$$

where ν_{LH} is the Poisson's ratio of the orthotropic material in the longitudinal boom direction. This is supported by experimental findings from Webber (1982) observing a much lower than predicted incipient wrinkling and collapse loads of his 1.5 m long cantilever beams. Webber (1982) used 50 µm thick polyester booms with a Poisson's ratio 0.24. The boom diameters of 0.2, 0.3, and 0.4 m were inflated to 4 pressures between 6.8 to 16.9 kPa. The 0.3 m diameter boom collapses at approximately 125 Nm for a 16.9 kNm^{-2} inflation pressure[86]. This is 54 Nm lower than the predicted value from Equation 2.12. However model evaluation using experimental testing by Main et al. (1995) encountered difficulties defining incipient wrinkling as their appearance occurred significantly after the fabric was not carrying longitudinal loads. Main et al. (1995) used Nylon fabric beams of smaller diameters and higher pressures. These changes in setup along with the much thinner isotropic transparent material used by Webber (1982) may have contributed to these wrinkle detection problems.

Experimental research by Thomas and Wielgosz (2004) has shown highly inflated booms create pressure stiffening effects affecting the load-deflection response and increasing the load capacity of booms. Davids (2007) formalised this by incorporating work done by pressure from deformation induced volume changes to a Timoshenko finite beam element model. The adjusted model assumes the pressurised beams are a closed system with no leaks once inflated. The geometric nonlinearities from shear, bending, axial strain and wrinkling of the beam causes an increase in the inflation pressure as the volume reduces.

With the advent of finite element analysis (FEA), inflatable computational models have been developed and are used alongside experimental results to verify analytical developments including the previous Timoshenko beam adaptation by Davids (2007). Apedo et al. (2010) have developed these typically 2D analyses[89-93] to a 3D Timoshenko beam with an orthotropic woven fabric. The developed nonlinear model is particularly useful for applications where

wrinkling will not occur under high loading conditions and with materials of low mechanical properties. The research also concludes that inflatable beams with high mechanical properties are influenced less from nonlinear effects and a linearized model is sufficient to analysis these systems. This area of work continues to be developed for increasingly involved permutations including non-constant boom radius, arches and toroidals under various loading conditions, and further understanding of wrinkling behaviour[96-102].

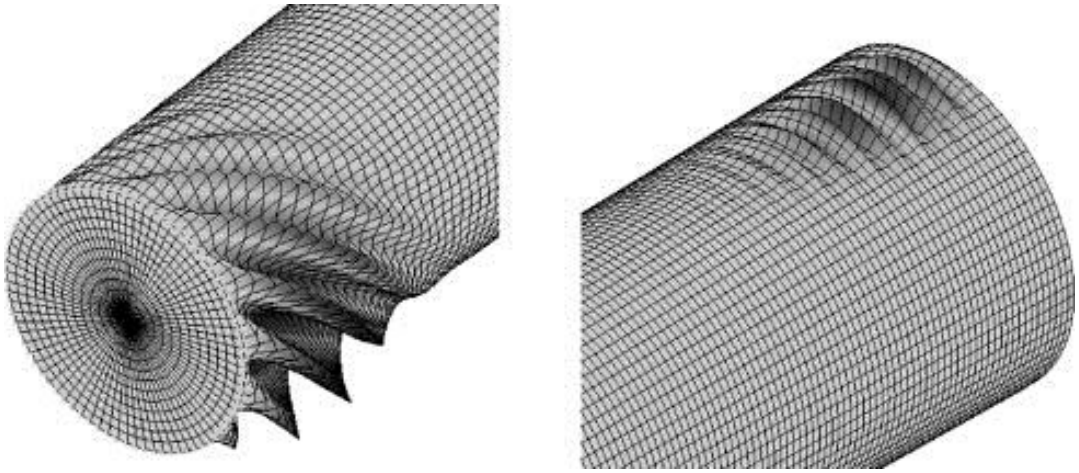

a) b)

Figure 2.9: FEA of an inflatable boom under a) torsion, and b) bending using shell elements[103].

Although more computationally expensive, shell and membrane finite element analyses are more accurate than beam elements[90,95] automatically capturing the geometric nonlinearities that results in pressure stiffening. Veldman (2006) used ABAQUS, a robust nonlinear FEA solver, to create a shell inflatable boom shown in Figure 2.9 to investigate boom bending and torsion similarly to Webber (1982). By treating the boom as a shell rather than a membrane resulted in an altered analytical relationship that includes the Young's modulus, *E*.

$$M_w = \frac{\pi^2}{8} pr^3 + \frac{2\sqrt{2}}{9} Ert^2 \sqrt{\frac{1}{1-\nu^2} + 4\frac{p}{E}\left(\frac{r}{t}\right)^2} \text{ [104]}. \qquad \textbf{(Equation 2.15)}$$

The three wrinkling moment relationships of Equations 2.8, 2.11 and 2.12 using the material properties of the 0.3 m diameter boom inflated to 16.9 kPa presented by Webber (1982) are given in Table 2.1. The Young's modulus, Poisson's ratio and film thickness are 4 GPa, 0.24, and 0.05 mm respectively. The various relationships show significant variance in incipient wrinkling moments. Although the experimental M_w is not explicitly stated by Webber (1982), considering the material properties of the inflatable boom improves the initial relationship of Equation 2.8.

Table 2.3: Theoretical and experimental incipient wrinkling moments of the 0.3 m diameter inflatable boom by Webber (1982) (*Based upon half the observed collapsed load).

Wrinkling relationship	Equation	M_w
Experimental result (Webber (1982))	-	*63** Nm
Membrane theory (Comer and Levy (1963))	2.8	91 Nm
Membrane with material property consideration (Main et al. (1994))	2.11	48 Nm
Shell theory (Veldman (2006))	2.12	76 Nm

Veldman et al. (2006) demonstrates Equation 2.12 underestimates the wrinkling moment with respect to their own FEA and experimental[104] data that also diverges with increased inflation pressure. Although the FEA model result is dependent on the mesh size and inherently over predicts boom stiffness the data shows stiffening terms from inflation are crucial to analytically model the moment – deflection response of inflatable structures.

Experimental verification of these models typically consists of tip deflection tests of a cantilever boom from which the structural performance of the peak moment and boom stiffness can be determined. Tip deflection tests were also undertaken by Lou et al. (2000) with a 0.1 m diameter, 1.1 m long Nylon boom. The tests were not taken to boom collapse but achieved a maximum of 7.6 Nm for a tip deflection of 81.2 mm at an inflation pressure of 66.9 kPa. A second test program determined the force required to axially buckle a 5 m long inflatable boom constructed out of an aluminium laminate is 391 N, where the boom is pre-strained by 0.5%. By using 4 COTS tape springs as structural stiffeners along the length of the booms, it was possible to increase this buckling force to an average of 641 N over the final five tests. Modelled using FEA predicts a failure value of 743 N. The difference in values can be accounted for by the manufacturing defects in the experimental booms as it was reported test booms where not perfectly circular or straight and had possible imperfections. The five experimental buckling results vary by up to 10% further confirming this. Further testing also showed a reduction in the buckling force after stowage by an average of 32%. Experimental work with shorter hybrid booms by Walker et al. (2011) has shown that tape springs can increase the maximum tip deflection bending moment from 21 to 25 Nm. The hybrid boom was inflated to 103.4 kPa, had a 0.1 m diameter and was 0.6 m long. The increase in mass from the added tape springs was 21.5 g/m length of the boom for a 350 g/m initial inflatable boom.

The research presented in this document will consider shorter hybrid booms that can be developed for smaller spacecraft applications. The following section provides further detailed background to tape springs and their development as gossamer structures.

2.3 Tape Springs Background

Tape springs are commonly used as tape measures manufactured out of steel as displayed in Figure 2.10. However they have several properties that are desirable for use in gossamer structures including a simple light weight design with a high buckling moment. They are an inexpensive, easy to manufacture COTS component that are ideal to be used as a structural element when combined with an inflatable boom to create a hybrid structure.

Figure 2.10: A typical tape spring.

A tape spring section can be defined by three geometric parameters; radius of tape spring curvature, R, thickness, t, and angle of embrace, α, as shown by Figure 2.11[5].

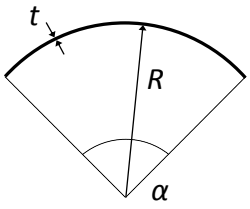

Figure 2.11: Cross sectional tape spring parameters.

Tape springs use their curvature to enable them to resist buckling when being subjected to a moment normal to the soft plane of the tape spring. Depending on the direction of the applied moment, the tape spring will buckle producing a longitudinal radius of curvature either on the same or the opposite side to the initial transverse radius of curvature as illustrated in Figure 2.12.

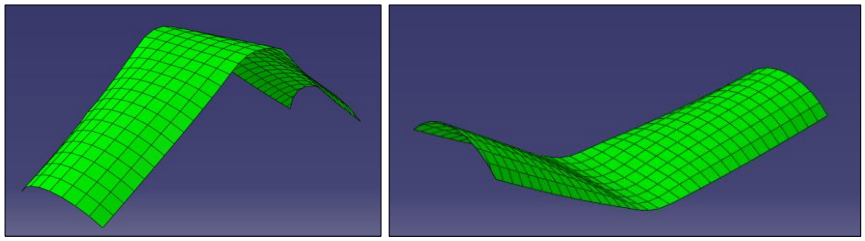

a) b)

Figure 2.12: Tape spring in a) equal sense bend b) opposite sense bend.

These folds are known as two-dimensional equal and opposite sense bends respectively. Depending on the tape spring orientation the maximum bending moment the tape spring can achieve will vary. It is known from previous research that a tape spring buckles through a snap-through mode in the opposite sense bend, and a torsional mode for an equal sense bend[2]. This results in a higher buckling moment magnitude for an opposite sense bend (M_{+}^{max}) compared to an equal sense bend (M_{-}^{max}). This is displayed in Figure 2.13, which also shows that after buckling there is a steady state bending moment (M_{-}^{*}, M_{+}^{*}) irrespective of further rotation. Changes to any of the defining geometric parameters shown in Figure 2.11 will also alter a tape spring's structural performance with all parameters being directly proportional to tape spring stiffness and maximum bending moments.

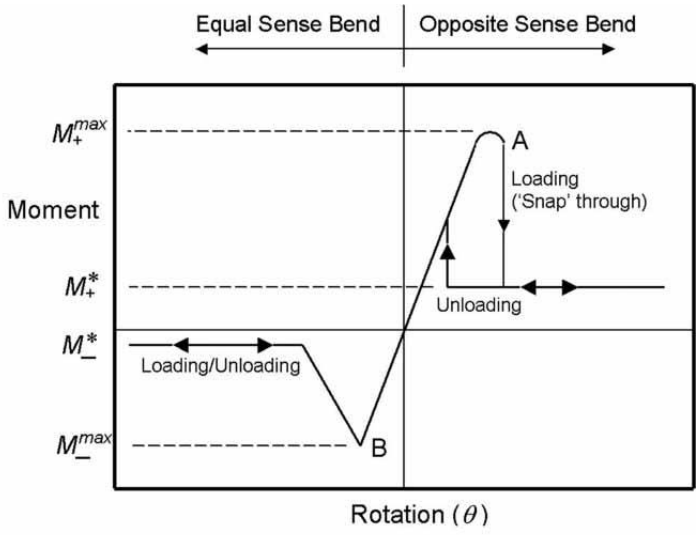

Figure 2.13: Moment characteristics when bending a tape spring in the soft plane[3].

Theoretical steady state bending moment relationships have been developed from previous mathematical studies[106,107] by Seffen and Pellegrino (1999) which assume the transverse curvature flattens and the buckled longitudinal radius is equal to the initial transverse radius for the tape spring in the buckled steady state leading to Equations 2.13 and 2.14.

$$\boldsymbol{M_{+}^{*} = (1+\nu)D\alpha,} \quad \textbf{(Equation 2.16)}$$

$$\boldsymbol{M_{-}^{*} = -(1-\nu)D\alpha,} \quad \textbf{(Equation 2.17)}$$

for opposite and equal sense bends respectively where D is the flexural rigidity defined as

$$\boldsymbol{D = \frac{Et^3}{12(1-\nu^2)}}. \quad \textbf{(Equation 2.18)}$$

Mansfield (1973)[106] developed his mathematical relationship to describe the moment-curvature response of a tape spring displayed in its non-dimensional form in Equation 2.16,

$$\boldsymbol{\bar{M} = \bar{\kappa}_x - \bar{\kappa}_{x,0} + \left\{\frac{\lambda}{(1-\nu^2)}\right\}\{\eta\Psi_1 - \lambda\bar{\kappa}_x\Psi_2\},} \quad \textbf{(Equation 2.19)}$$

where ν is the tape spring Poisson's ratio and η, λ and Ψ are functions of longitudinal (κ_x) and transverse (κ_y) tape curvatures given in appendix I. Initial tape curvatures are denoted by $\kappa_{x,0}$, $\kappa_{y,0}$ and $\kappa_{xy,0}$. The moment and curvature normalisation procedure is also given in appendix I and are inverse functions of the flexural rigidity. The moment-curvature relationship has been compared successfully to experimental results but remains limited by the low manufacture tolerances for the conventional COTS tape springs produced. Thickness variations are typically 10%[108] resulting in large changes in peak and steady state moments easily seen in Equation 2.15. Defects and imperfections in the material also cause difficulties in peak moments prediction. However their non-permanent deformation and stored strain energy in the buckled state lead to an easily sourced component for a variety of applications.

Previous tape spring development for space applications have predominantly been as hinges or deployable devices for their inherent advantages of being a simple, single element, low cost components, with no complex moving parts requiring lubrication, that are able to lock out in a deployed state. Other developed concepts include deployable masts and beams such as the STEM and the Collapsible Tube Mast (CTM)[72].

Tapes springs used as hinges have been developed as far back as 1968. Vyvyan (1968) patented a hinge that utilises three tapes as shown in Figure 2.14. Placing the tapes in both bend orientations increases the bucking load in either bend direction when deployed.

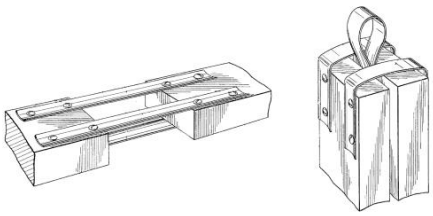

Figure 2.14: Tape spring hinge by Vyvyan (1968).

More recent research includes the Tape Spring Rolling (TSR) and the METRAVIB hinges[110,8] displayed in Figures 2.15 and 2.16. The TSR hinge by Pellegrino et al. (2000) have developed a design to create a low mass hinge with predictable deployment by forcing the two opposed tape springs to buckle at a set radius while also increasing the deployed buckling moment.

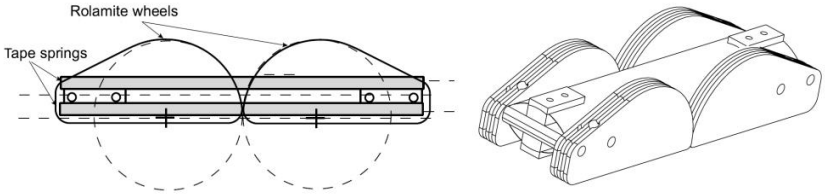

Figure 2.15: Tape Spring Rolling Hinge[110].

Work by Givois et al. (2001) resulted in the creation of the METRAVIB hinge which presents a light weight alternative for deployable structures. The tapes are offset to increase resistance to twist and has been successfully used on missions to deploy solar arrays[8].

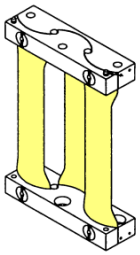

Figure 2.16: METRAVIB Hinge[8].

Larger deployable structures have also been considered. Research by Astrium and the University of Southampton have used a large number of tape springs to model and to experimentally deploy a three hinged three dimensional structure as shown in Figure 2.17. The large number of tape springs exacerbates the 'snap through' problem which exists in self-deployable tape spring hinge devices. The deployment of the three hinged structure produced substantial shocks for a deployment that lasts less than one second[11,13]. Damping has been

shown to reduce this problem on the TSR hinge[112] and must be considered if large shocks are expected. Walker and Aglietti (2002) outline the possible use of utilising tape springs for hinges of a deployable array blanket using tapes in a 3D folding pattern to deploy an 8 panel array, where detailed analysis of 3D bending has been studied by Walker and Aglietti (2007). Another quality of tape springs is their structural performance when deployed requiring considerable bending moments to buckle in specific orientations which could be exploited for this application as shown by references[71,72,12].

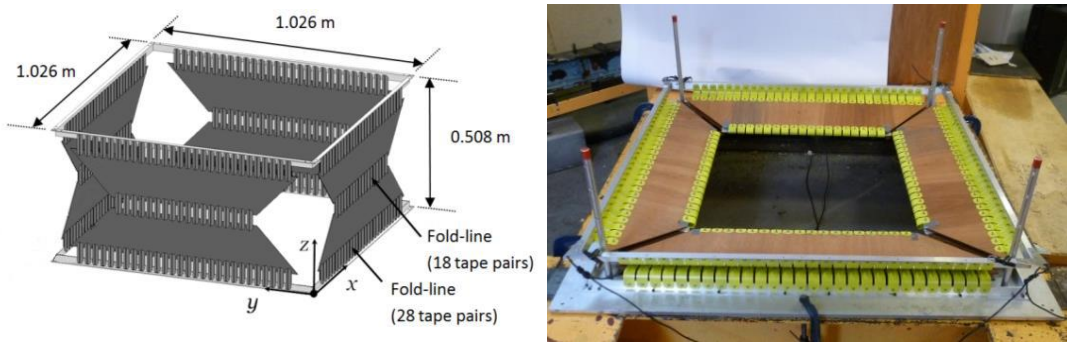

a) Schematic b) Collapsed state

Figure 2.17: Three dimensional, three hinged self-deployable structure using 296 tape spring pairs[13].

Tape springs are a widely used structure, which are easily sourced. In conjunction with their significant structural properties, light weight, low complexity and high packing efficiency, they are ideal for use with gossamer structures to enhance inflatable boom performance, creating a hybrid structure. This will continue to drive the current research of inflatable and hybrid booms using COTS components. Prior to assessing the structural benefits of using tape springs in hybrid booms it is important to establish a baseline in current inflatable boom technology from which a comparison can be made.

2.4 Inflatable Boom Background Construction

To assess the structural performance of inflatable and hybrid booms computational analysis of the systems are conducted. This is validated by experimental testing of the inflatable and hybrid booms with various permutations, including; size, pressures, and tape spring configurations. The structural performance of the booms is determined through tip deflection tests to measure rigidity and maximum bending moments.

Leading on from previous work at the University of Southampton[3], the inflatable boom construction is in a cantilever configuration from which tip deflection testing can be conducted. The material selection for the inflatable booms is based upon cost, supply, and material properties. Inflatable space applications commonly use advanced materials such as Kevlar[15] for their superior performance. However for an initial investigation to establish inflatable fabric boom trends, Nylon fabric was chosen because it is one of the strongest 'off the shelf' fabrics at a low cost. Nylon is a cheap alternative that has previously been used in space applications[15,17] and has sufficient structural properties for an inflatable boom. A selection of materials were tested in a previous test program and found the ripstop Nylon and rubber latex the most suitable considering a number of parameters, including density and strength[3]. The materials used to manufacture the booms are Fibremax 94, a 0.2 mm thick ripstop Nylon, and a 0.5 mm rubber latex to provide an airtight bladder. The Nylon creates the outer shell which provides the rigidity of the boom while the bladder inflates taking the shape constrained by the Nylon. The Nylon outer shell is manufactured in two pieces; the boom length and the circular boom tip as shown in Figure 2.18. These are stitched together by Nylon thread in a simple single stitch at the end of the boom length, and closed to form a tube by a seam running the length of the boom. A dummy seam is also stitched into the boom length on the opposite side to give a symmetric profile and to match previous experiments by Lou et al. (2000). The bladder was similarly constructed in two pieces and bonded with a water based adhesive called Copydex. An aluminium disc of 52 g with several small holes in its centre was placed between the bladder and Nylon inside the tube. This was to stop the boom tip ballooning as seen with other studies[15], giving a fixed flat end to the boom from which length and deflections can be accurately measured. It also provided a loading point to apply the bending moment, where a 3 mm nylon cord was threaded through the disc and attached to the suspended weights. This allowed the load to be applied in the neutral axis at the boom tip, ensuring neither top nor bottom surface is preferentially loaded. The booms are manufactured to 0.4 m long and have a radius of 0.05 m. This was set due to the ergonomics of handling the boom during setup.

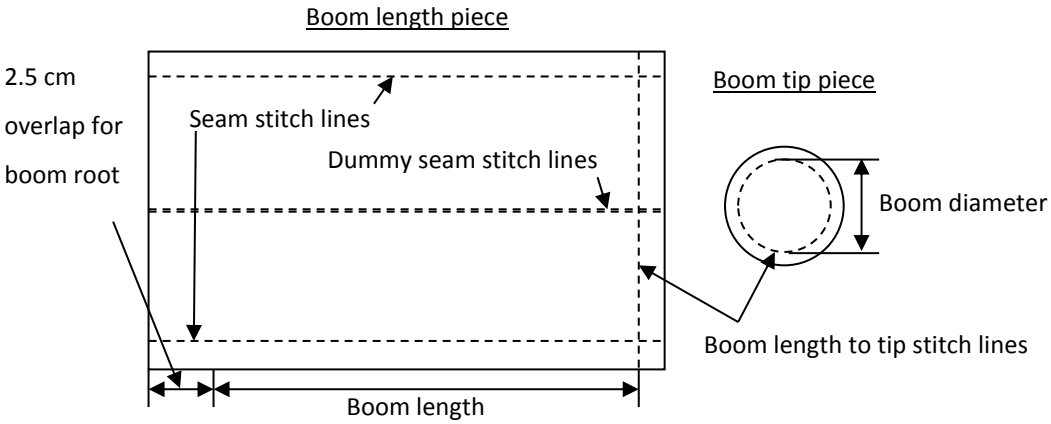

Figure 2.18: Diagram of the manufactured inflatable boom pieces with stitch lines.

The cantilever inflatable boom is attached at its root to a base plate by wrapping the nylon shell and rubber bladder around an inner plate as shown by the schematic diagram of the boom root attachment in Figure 2.19. An O-ring creates an airtight seal between the Nylon fabric and outer plate. Figure 2.20 shows the completed setup of the boom, including the Nylon cord attached to the end plate providing a flat boom tip and attachment for the suspended weights.

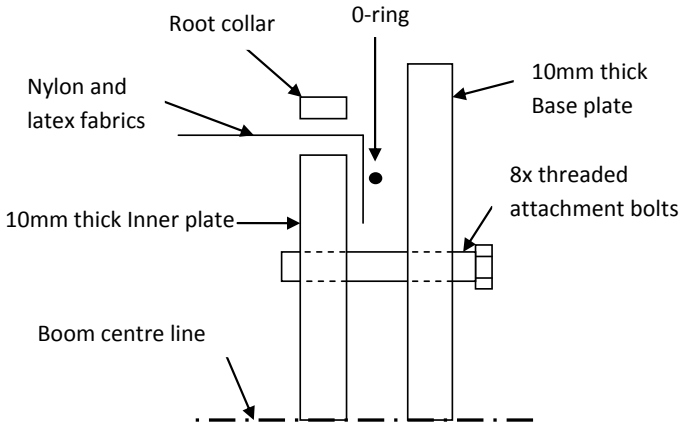

Figure 2.19: Schematic of the boom root attachment.

Figure 2.20: Setup of inflatable boom attached at base plate.

Table 2.2 shows the mass of the inflatable boom in its component parts. The test mass of a 0.4 m inflatable boom (Nylon shell, bladder, tip end plate and cord) is 135 g. The remaining root attachment masses (inner plate, bolts, O – ring, and root collar) total 216 g and are ignored when calculating mass changes to the boom.

Table 2.4: Mass breakdown of the inflatable boom components.

Boom component	Mass
Nylon shell	40.5 g/m
Bladder	166 g/m
Tip plate	52.3 g
Weight attachment cord	0.5 g
Inner plate	150.1 g
Root collar	31.9 g
O – ring	2.3 g
Attachment bolts	32.0 g

When using woven materials, it is important to consider their anisotropic behaviour. Fabrics are manufactured using longitudinal yarns (known as the warp direction) that are interwoven by transverse yarns (known as the fill direction) as illustrated in Figure 2.21. As a result, fabrics tend to be stronger in the warp direction and weakest in the bias direction (45^0 between warp and fill). This is an important consideration as the hoop stress will determine the maximum operating pressure of the boom and is calculated from tensile testing of the material. A detailed understanding of the material properties is also required for inputs to analytical models.

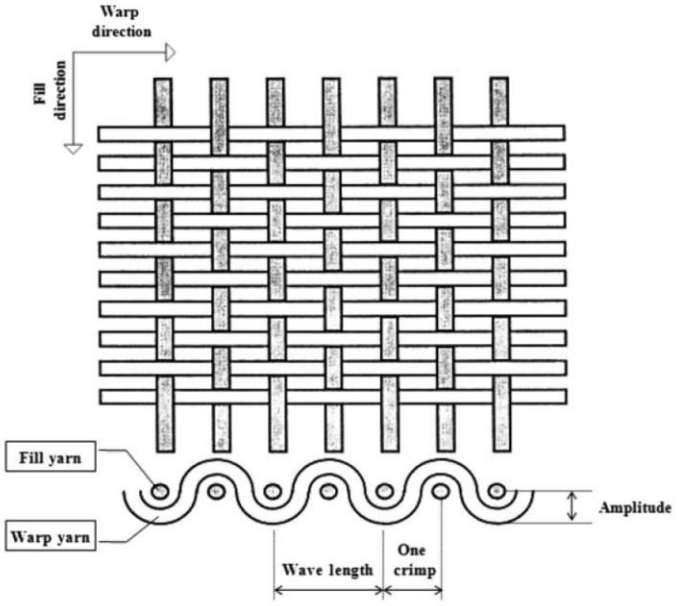

Figure 2.21: Fabric structure depicting warp and fill yarns creating a plain weave cloth[112].

2.5 Summary

Tape springs and inflatable booms have independently demonstrated their significant performance capabilities for use in space applications along with detailed theoretical, computational and experimental analysis of these systems. However combining these two components creates a hybrid structure that has only had limited investigation across a narrow range of configurations and permutations. The focus of these hybrid booms has been towards large applications, experimentally demonstrating the potential structural performance benefit of the booms under axial compression alongside a possible deployment strategy[15,16]. There has also been no in depth assessment of the tape spring arrangement and the multitude of hybrid boom permutations possible when combining these two components or a structural performance evaluation with respect to tip loading. This also includes the structural performance changes of various inflation pressures and tape spring thicknesses. In addition an accurate FEA model is also required to develop this technology further. This project aims to address these areas of investigation with experimental and computational structural analysis of smaller hybrid booms suitable for small satellite applications. This research will progress the structural performance knowledge of these hybrid systems and reveal key areas where this technology requires future investigation.

A developed hybrid boom FEA model validated against component FEA models and verified against experimental results will allow a designer to understand and accurately predict the structural response of a hybrid boom across a wide variety of permutations and evaluate the performance against an inflatable boom or other structures. This is presented in the remaining chapters where a detailed assessment of the material properties is initially required and given in the following chapter.

Chapter 3

Fabric Material Properties Study

It is important to know the material properties of the fabric boom with suitable accuracy. This includes the density (ρ), thickness (t), Young's Modulus (E), shear modulus (G) and Poisson's ratio (v) that are required as inputs for analytical models. To achieve this, tensile testing of the fabric is conducted which also allows the Ultimate Tensile Strength (UTS) to be assessed giving the maximum operating pressure of an inflatable boom. The stress – strain response will provide a detailed understanding of the fabric which behaves nonlinearly.

3.1 Background

The material used in the boom is the fabric Fibremax 94[113] which uses a ripstop nylon weave that is lightly impregnated with a resin to hold the weave together securely and gives added stiffness to the material. The resin acts like a matrix in composite materials and significantly increases the shear rigidity of the fabric. Fabrics without the impregnated resin (loose weave fabrics) have negligible initial shear rigidity where the yarns are free to slip past one another due to the relative free space once frictional forces holding the weave in place are overcome. Figure 3.1 illustrates the relative yarn movement of a loose plain weave fabric with increasing shear deformation. If shear deformation is continued a third region occurs where the yarns bunch together. This is known as shear locking and results in significant stiffness increases and usually causes the fabric to buckle into wrinkles[112]. These regions are dependent on the geometry and structure of the fabric including the density of yarns defined as the packing ratio.

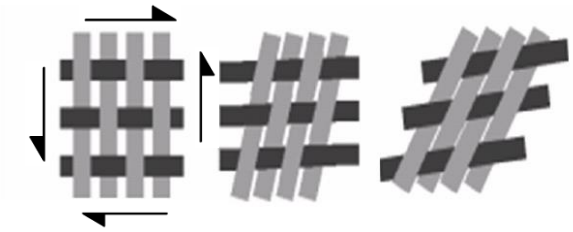

a) b) c)

Figure 3.1: A plain weave fabric with applied shear causing yarn slip at b) and the onset of shear locking at c)[114].

There are numerous other factors that affect fabric properties and primarily concern fabric and yarn geometry, and yarn and filament material properties[114-118]. Research of fabrics falls into three distinct areas centred on three scales; continuum, yarn, and fibre based as shown in Figure 3.2. Lin (2010) uses a geometrical approach to model the fabric in the yarn scale to predict the elastic response of a plain woven fabric using the two yarn geometries and elastic moduli. Yarns are constructed out of individual fibres of varying lengths and spun helically along the yarn length. Various fibre based models have been developed to predict the yarn response[115] and includes research by Xia and Nadler (2011) which combine the three scales to predict the fabric behaviour from fabric geometry and material properties of a fibre.

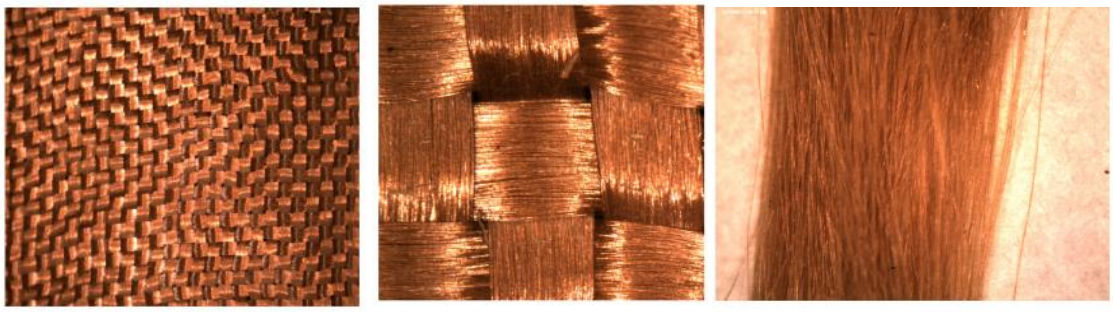

a) b) c)

Figure 3.2: The three scales applied to woven material modelling; a) continuum, b) individual yarns, c) filaments[116].

The majority of fabric properties research is at the continuum scale[119-121] with an understanding of the yarn interactions to explain the overall material behaviour. This approach is common for FEA of fabric applications as it allows less complicated models to describe the fabric response for a significant reduction in computational expense[112].

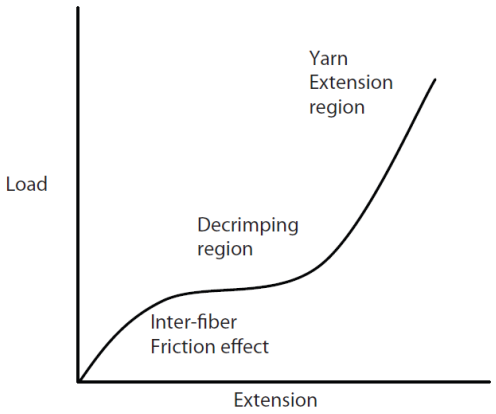

Figure 3.3: Outline of fabric extension response under uniaxial load[115].

To calculate the properties of a material a specimen is typically placed in uniaxial tension where stress and strain are recorded. The accurate measurement of the material properties is complicated due to the orthotropic nature of fabrics and their nonlinear behaviour. The orthogonal behaviour is caused by the constructed geometry of the two yarn types while the nonlinearity is a result of several distinct stages during deformation. Figure 3.3 outlines the general load-extension response of woven fabrics in uniaxial tension identifying the three stages; inter-fibre frictional effect, decrimping, and the yarn extension region[115]. The initial high stiffness of the fabric under tension is caused by the impregnated resin and the friction between fibres within yarns to prevent yarn bending and decrimping[115,122]. The following region decrimps the yarns in tension as shown in Figure 3.4 and results in increasing the orthogonal yarns crimp amplitude. This is limited by the yarn length which is subjected to pure extension once the yarn is fully decrimped. Yarn extension continues until the ultimate tensile strength of the material is reached where sufficient numbers of fibres within the yarns have separated causing failure. The magnitude of each region is specific to individual fabrics where each region is dependent on geometrical and material properties of the yarns to varying degrees.

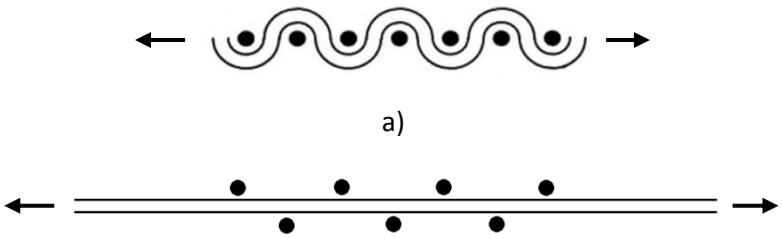

Figure 3.4: Cross sectional schematic of a plain weave fabric under uniaxial load, a) before decrimping, b) after decrimping.

When fabrics are placed under biaxial tension, as is the case for a pressurised boom, the behaviour of the fabric changes. The decrimping region is limited as the orthogonal yarns are also under tension. This affect is dependent on both yarns elastic modulus and the ratio of the applied loads. The decrimping and yarn extension regions both occur simultaneously during biaxial extension and lead to a linear response[123,124] that can be determined by the averaged elastic moduli of the decrimping and yarn extension regions from a uniaxial tensile test[124].

A number of methods are available to experimentally determine the shear modulus of fabrics. These include the picture frame test, torsional tests of an inflatable boom and uniaxial tensile biased tests and are depicted in Figure 3.5.

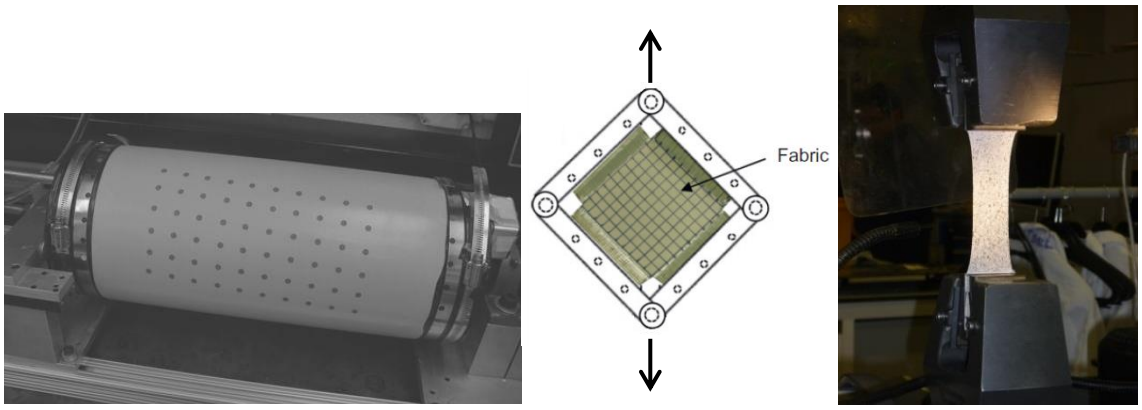

a) b) c)

Figure 3.5: Experimental fabric shear measurement techniques, a) torsional inflatable boom, b) picture frame, c) biased uniaxial extension[124,125].

The biased tests are the easiest to implement as they require no additional test apparatus to the standard uniaxial tests while only requiring careful selection of the measured strain area. Figure 3.6 shows three areas that occur during tensile testing of a biased fabric specimen where pure shear only occurs in region A. The biased elastic modulus of the specimen, denoted as E_{45}, is determined and used alongside the other orthogonal material properties to calculate the shear modulus using Equation 3.1[126] where the subscripts *w* and *f* are the warp and fill material orientations respectively.

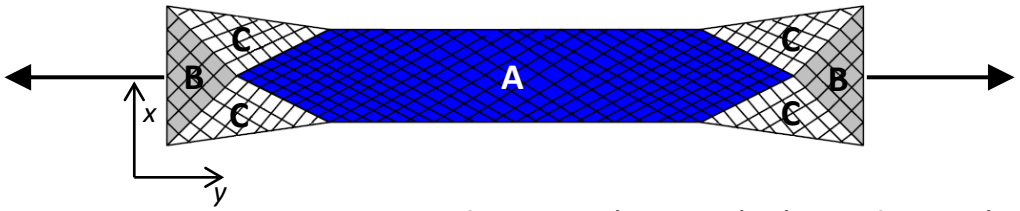

Figure 3.6: Biased extension schematic identifying areas A (pure shear), B (little deformation), and C (partial shear and extension deformation)[122].

$$G_{wf} = \frac{1}{\frac{4}{E_{45}} - \frac{1}{E_w} - \frac{1}{E_f} + \left(\frac{\nu_{fw}}{E_w} + \frac{\nu_{wf}}{E_f}\right)} \quad \textbf{(Equation 3.1)}$$

This section has shown that fabrics behave differently under various loading conditions caused by the structural interactions of the yarns. An averaged uniaxial Young's modulus is usually taken for material properties when placed in biaxial tension and leads to constant material properties for 1:1 biaxial tension[123,124]. For an inflatable boom the biaxial tension of the fabric in the boom length is 2:1. Measuring the stress-strain response during inflation will give a greater understanding of the material in this state and will show if the linear material properties assumption is justified. This is possible by using Digital Image Correlation (DIC) which removes the need for specific biaxial test rigs and measures the material properties of the fabric in its application.

3.2 Measurement Technique

DIC is used to accurately measure strains in both plane directions and can therefore calculate the Poisson's ratio and Young's modulus of a material easily. Other techniques find difficulties being applied to fabrics when designed for typical isotropic or composite materials. Extensometers are found to slip on fabric specimens whilst the compliance in the load cell and actuator of a uniaxial test rig give inaccurate strain data. DIC offers an accurate strain measurement solution whilst also being a nonintrusive technique. A review of DIC is described in Pan et al. (2009) providing extensive details on the algorithms to calculate strain. In brief, the method captures a series of pictures of the specimen during a tensile test from one or more cameras. They are then compared to each other and correlated by tracking specific points on the specimen surface as shown in Figure 3.7. The specimen is broken down into a grid where the average translation and rotation of the speckles is taken. The grid size creates a resolution against accuracy tradeoff that is also dependent on the quality of the unique speckle pattern and the solving algorithm used. Further DIC detail and solving techniques can be found in Pan et al. (2009) and the Lavision handbook[128]. For these tests a default solver and grid size provided sufficient accuracy using the least squares solver. This allows a strain map to be built over the whole test area that can show accurate strain fluctuations across the specimen and not just an averaged value as measured by an extensometer. This is particularly valuable across discontinuities such as a stitch or seam line. The points on the specimen are measured in both translation and rotation and allow strains to be measured longitudinally, transversely, that can be coupled to calculate the Poisson's ratio, and in shear to determine the elastic and shear moduli if synchronised with the stress data.

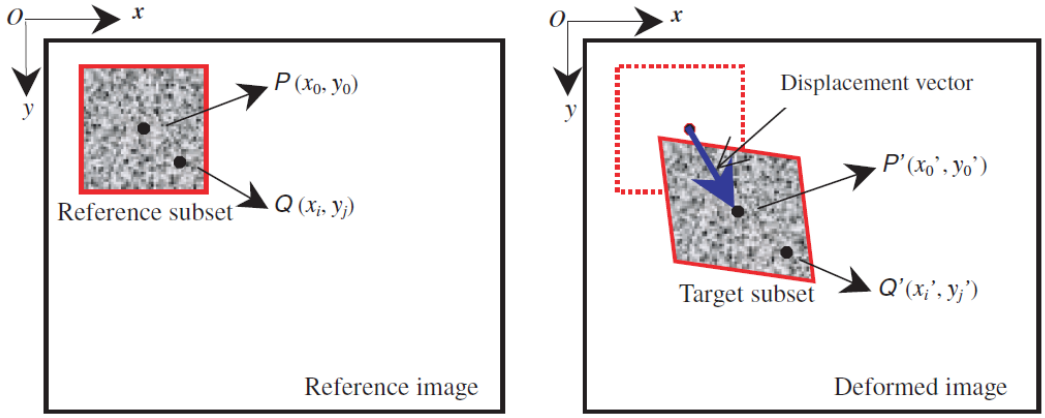

Figure 3.7: Image correlation process schematic[127].

These points are usually applied to the test piece as a speckle pattern from a spray paint. This is because it is important to get a unique pattern with a variety of speckle sizes so the spots are easily distinguishable for the software algorithm and a complete strain map is achieved. Other methods are available such as a dot matrix displayed in Figure 3.8, but a sprayed speckle is by far the most effective, easy to apply, and applicable to the majority of materials[127]. An exception is fabrics that are not or only lightly impregnated with a stiffening resin. In these cases the applied paint could act as a matrix, especially for lose weave fabrics, and significantly affect the material properties. Some fabrics including the Fibremax 94 are impregnated with a resin for various reasons (weather proofing, oil resistance) and it should be possible to apply a speckle pattern without affecting the fabric significantly. However the weave may provide a sufficient unique pattern for the image processing to achieve a fully non-intrusive measuring technique. This is investigated in the uniaxial tests to confirm the approach and to determine if sprayed paint affects the Fibremax 94 fabric.

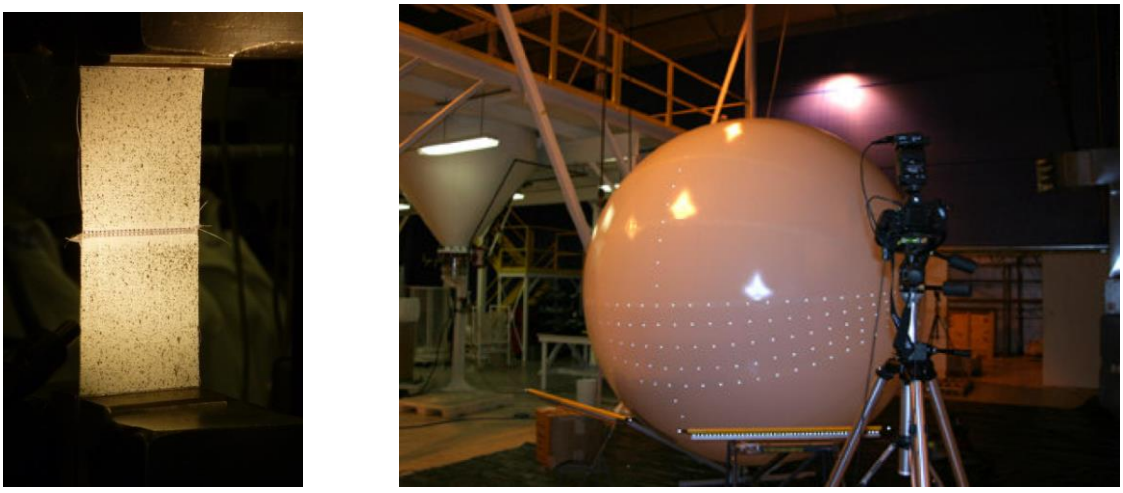

a) b)

Figure 3.8: Imaging techniques a) Speckle pattern on fabric b) Dot matrix approach[129].

By using two or more cameras directed at the same target area it is possible to build a stereo composite image of the test specimen. This allows strain maps to be created for objects with a curved surface including an inflatable boom. It also increases the accuracy of the image correlation and removes the necessity to accurately position one camera directly in-plane for flat specimen tests.

3.3 Material Test Setup and Procedure

The DIC was setup using two E-lite 2M cameras pointed approximately 1 m from the test specimen at 15^0 to the normal as shown in Figure 3.9. Sufficient lighting was applied to illuminate the specimens that were speckled with a black spray paint. The images captured were then processed using the DaVis LaVision software to generate the stress-strain data.

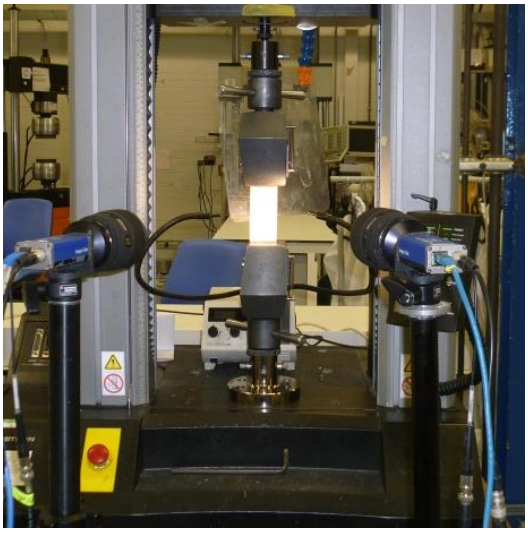

Figure 3.9: The DIC camera and specimen setup in the uniaxial tensile test.

The two test regimes were the uniaxial and biaxial tensile tests. The uniaxial test used a servo-hydraulic Instron machine which evenly gripped a 200 x 50 mm specimen leaving a free length of 100 x 50 mm. The machine used a 5 kN load cell that gave an accuracy of 0.01 N and placed the specimens under tension at 5 mm/min extension rate until failure. The strain data was collected at 5 s intervals.

The biaxial tensile tests used an inflatable boom to achieve a tensile ratio of 2:1 acting on the fabric. The boom was hung from a frame under its own weight as shown in Figure 3.10. This was so data could be taken at the lower pressures as fabrics have no compressive or bending

resistance. The strain data was measured using DIC of a speckle pattern on part of the boom. The cameras took an image at 1 PSI intervals up to 16 PSI. The pressure increase was not constant but in discrete steps where strain data was collected once the pressure level had reached equilibrium. Preliminary tests showed that at 1 PSI or lower the fabric was not under complete tension and wrinkles were present around the circumference of the boom. In all tests a zeroed image is taken from which strain and stress are then measured. The wrinkles in the fabric at low pressures would lead to propagated inaccurate strains as the fabric filled out the full boom shape rather than stretch during initial pressure rises. To accommodate this, the analysis was taken in reverse where the 16 PSI image is the zeroed referenced image used to correlate the strain data. The data is then translated to a new zeroed point knowing at 0 PSI the stress-strain values are 0,0. The wrinkles still cause inaccuracies from pressures lower than 1 PSI however they are not propagated forward in the analysis and allow the gradient for the elastic modulus to be measured with accuracy.

Figure 3.10: The DIC camera and lighting of the inflatable boom biaxial tensile test rig.

The coordinate systems used to refer to the measured material properties for the uniaxial strip and biaxial inflatable boom tensile tests are given in Figure 3.11. The uniaxial tests have transverse and longitudinal directions denoted as *x* and *y* respectively. The biaxial tests have boom length and hoop directions denoted as *L* and *H* respectively. The 3 fabric orientations are also shown in Figure 3.11 where the biased tests are indicated with the suffix ‘45’.

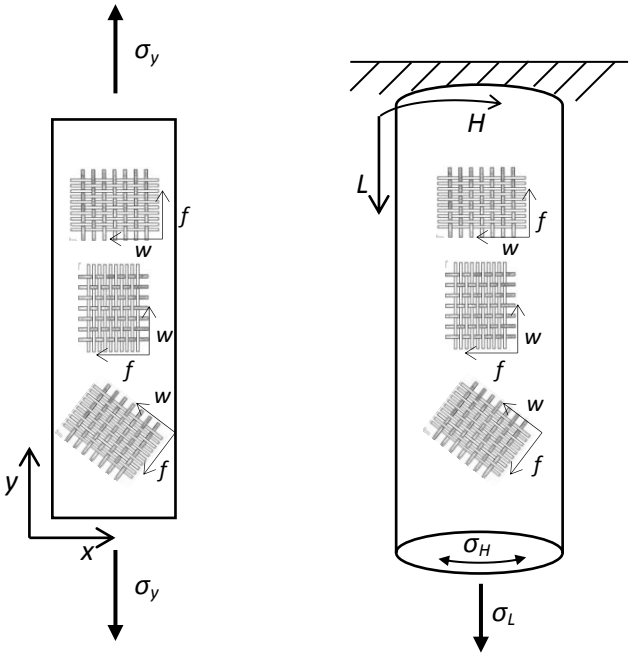

a) Uniaxial strip b) Biaxial boom

Figure 3.11: Coordinate systems showing the three material orientations.

3.4 Material Test Program

The test program is split into two sections; uniaxial and biaxial tensile tests. In each case the warp, fill and bias directions of the fabric are placed in tension. To create an inflatable boom a seam is required to join the fabric together along its length. It is therefore important to know the properties of the stitch and how it will behave under pressure. For the uniaxial warp and fill fabric orientations a stitched specimen was also tested. Preliminary testing using the Instron machine for uniaxial tensile tests of the fabric showed the performance of the seam is significantly improved by using a double stitch. Figure 3.12 displays the stress strain response of several stitch types each with 3 repeat tests. The preliminary results show the double and triple stitch can achieve a maximum stress of 72.0 and 69.4 MPa respectively. This results in a 14% increase in the maximum operating pressure of an inflatable boom for a negligible increase of 0.16 g/m boom length. As the double stitch specimens showed the greatest performance gain all subsequent tests and booms used double stitched seams. The mass of the boom contributes a negligible 0.04 MPa in the boom length direction induced by gravity and as such can be ignored for this analysis.

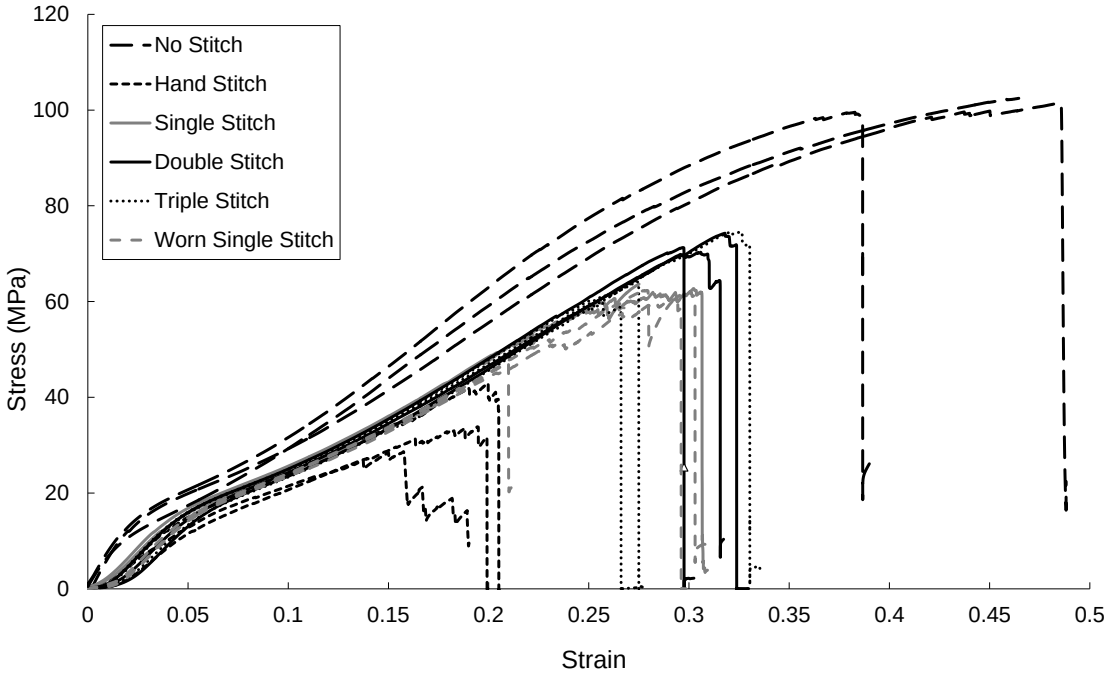

Figure 3.12: Preliminary uniaxial tensile tests using Fibremax 94 in the warp direction and various stitch types with 3 repeat tests each.

The specimens in all uniaxial tests were taken to failure to measure the UTS. A single pressure failure test was also conducted on an inflatable boom to conclude if the uniaxial tensile tests could determine the maximum operating pressure and observe if the stress – strain trends remain constant. For each type of test, except the single boom failure test, there were three repeats. To calculate the stress of the Fibremax 94 fabric the material thickness also needed to be measured.

3.5 Fabric Thickness and Density

The thickness of the material is important to calculate the material properties accurately. Although the material properties of the fabric will be applied as a continuum the material is constructed from interlacing yarns and creates a varying thickness. An average thickness of 0.195 ±0.001 mm was measured using a measuring table, slips and clock accurate to 0.5 μm. The density of the fabric is simply measured using digital scales accurate to 0.01 g and the dimensions of 12 fabric samples at 50 x 200 mm ±1 mm giving an average density of 588 ±11 kgm^{-3}. The mass of the samples varied at 1.14 ±0.02 g.

3.6 Uniaxial Testing Results

The uniaxial tensile tests consist of warp, fill and bias specimens. The warp and fill tests also included a non-speckled and a stitched tests resulting in seven types of test, each with three repeats with the setup shown in Figure 3.9.

Figure 3.13 shows a longitudinal strain map of the warp orientated specimens with a double stitch at 65.5 MPa tension at the onset of stitch failure. The stitched specimens all showed significant increases in localised strain at the stitch. This is caused by the stitching holes being lengthened as the two fabric pieces are pulled apart with the transverse yarns immediately below the stitch line being highly distorted in the fabric plane. This stitch pull-out caused an effective peak strain of 1.0 before failure. The strain map in Figure 3.13 shows the length of localised strain increase is 13 mm before the constant fabric properties are observed with the stitch pull-out occurring over 2.5 mm of this length.

The whole strain map or a selected section can be averaged and then plotted against stress as shown in Figure 3.14. The stitched specimens selected an area of 15 mm square located as shown in Figure 3.13 and was used to take an appropriate average of the fabric strain. This area is increased to 25 mm square and centred for the remaining specimens as the lack of a stitch allows a greater area to be measured whilst ensuring edge effects do not skew the results. This is plotted alongside the non-stitched specimens in Figures 3.14 and 3.15 showing the material remains constant for stitched and non-stitched tests for both warp and fill orientated specimens. This was not the case for the preliminary tests as displayed in Figure 3.12 where the strain data includes the effect of the stitch pull-out and compliance in the loading test frame.

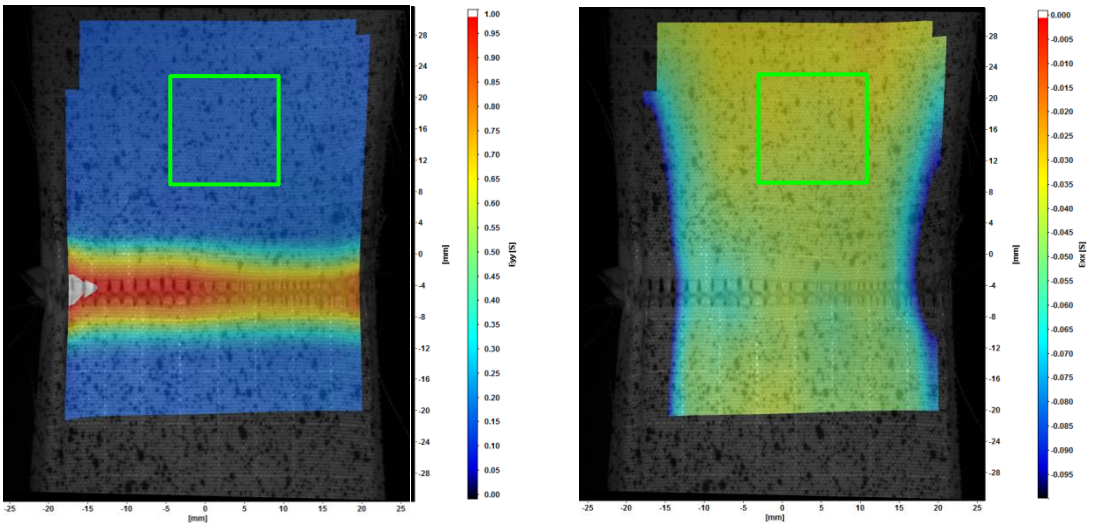

a) Longitudinal (ε_y) b) transverse (ε_x)

Figure 3.13: Uniaxial strain maps of the warp with a stitch specimen test 3 and selected averaging area under 65.5 MPa tension.

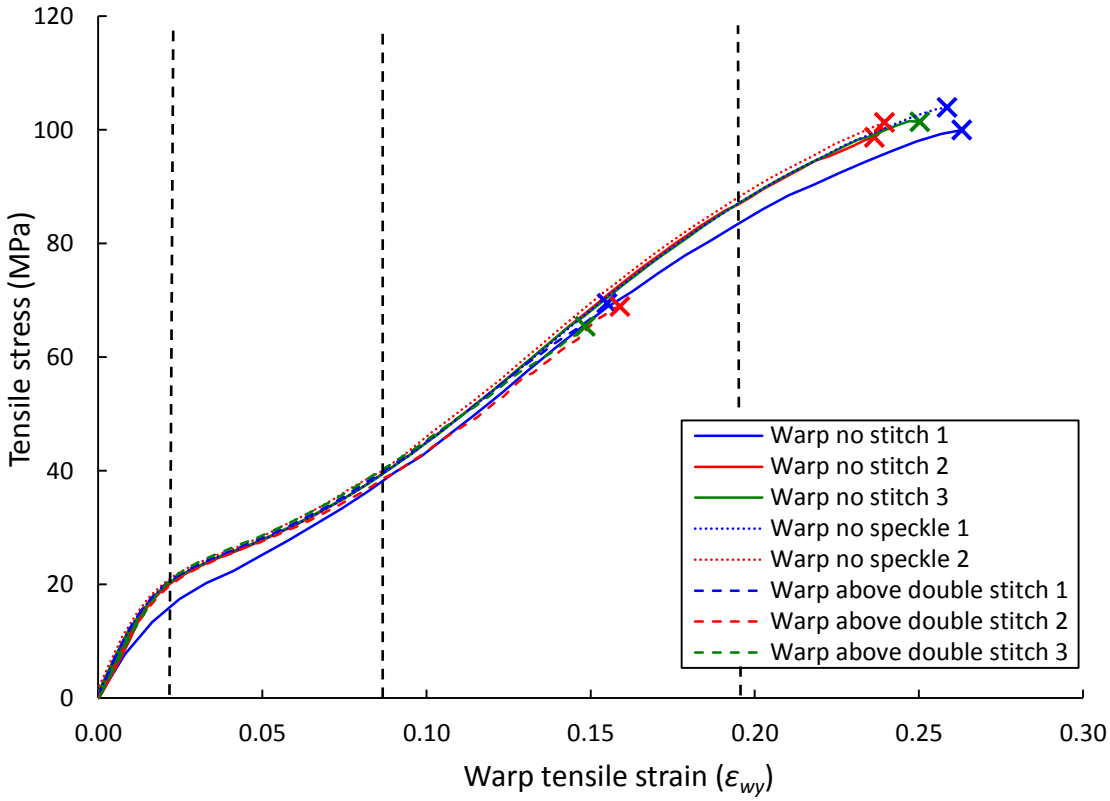

Figure 3.14: Uniaxial tensile stress – strain data for warp orientated specimens of Fibremax 94.

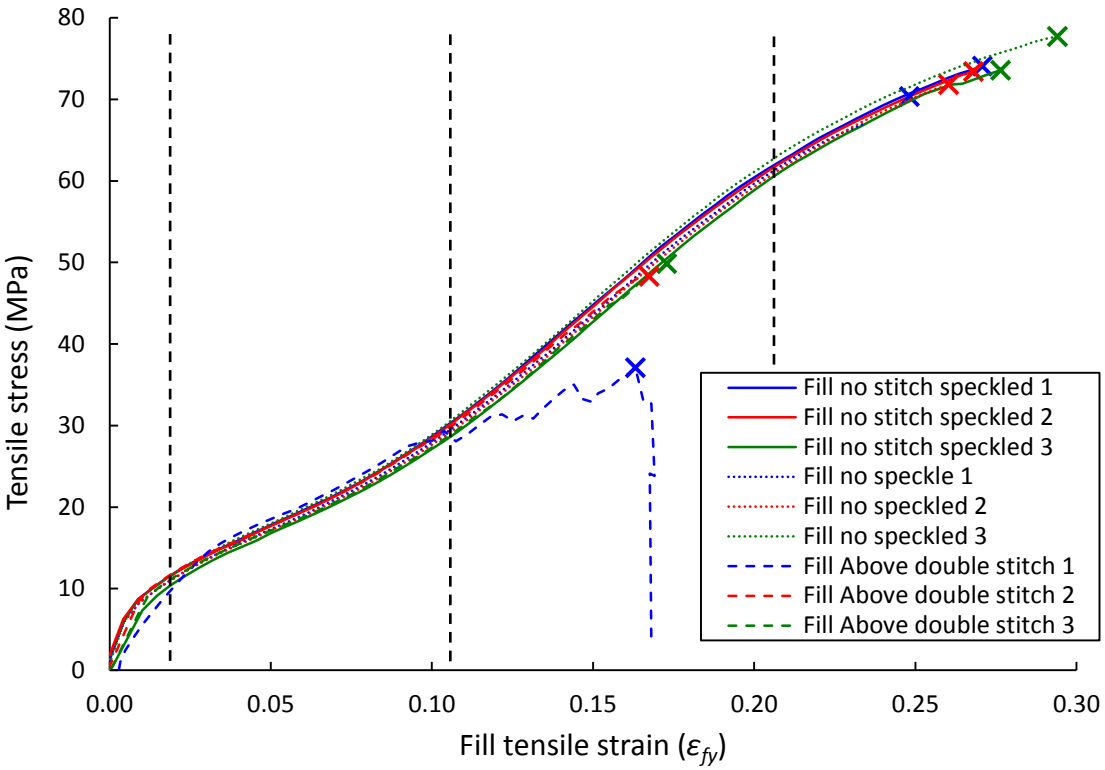

Figure 3.15: Uniaxial tensile stress – strain data for fill orientated specimens of Fibremax 94.

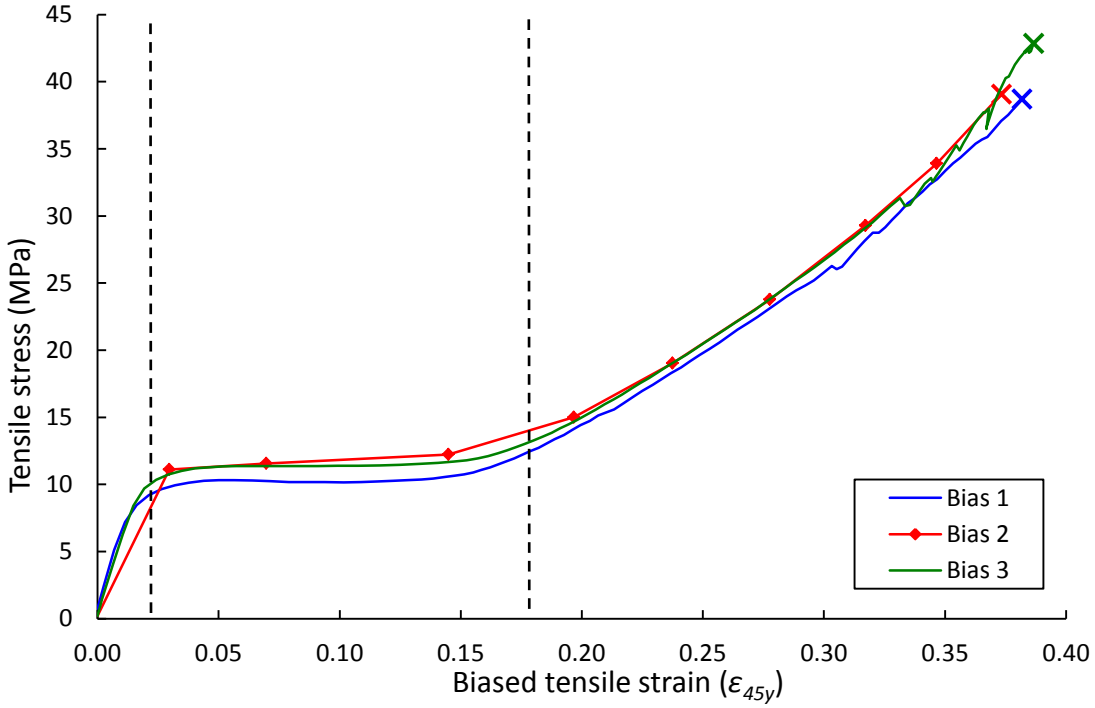

Figure 3.16: Uniaxial tensile stress –strain data for bias orientated specimens of Fibremax 94.

Figures 3.14, 3.15 and 3.16 display the stress – strain data for the warp, fill and bias orientated specimens respectively where an 'X' marks the failure point. The UTS of the Fibremax 94 is collated in Table 3.1 and is shown to change between all three fabric orientations and for

stitched and non-stitched specimens. The response of 'Warp no stitch 1' and 'Fill above double stitch 1' are anomalies with the remaining trends. The latter is caused by a gradual unzipping of the stitch at one edge from 30 MPa which limits its UTS to 37 MPa. This cannot happen in the boom as the seam ends are wrapped around the inner plate and overlapped by the tip end stitching forcing the stitch to fail similarly to the remaining specimens. The variation in stress-strain gradient of the 'Warp no stitch 1' specimen could be caused by hysteresis effects where cyclic tests have shown a similar change in response to other Nylon fabrics[112,120]. Glaser and Caccese (2013) suggest disentanglements, slips and reorientation of the fibres cause this effect. This could be brought about by excessive wear on this specimen prior to testing. The data for both these anomalies is ignored for calculating the material properties of the Nylon.

Table 3.1: UTS of Fibremax 94.

Orientation	Type	UTS (MPa)	Ultimate tensile strain
Warp	Non-stitched	101 ±2	0.25 ±0.01
	Stitch	68 ±2	0.15 ±0.01
Fill	Non-stitched	73 ±4	0.27 ±0.02
	Stitch	50 ±3	0.17 ±0.01
Bias	Non-stitched	40 ±2	0.38 ±0.01

The warp results show the UTS are reduced by 32% to 68 MPa when joining the fabric together with a stitch. The weaker fill direction has an average value of 50 MPa for the stitched specimens while the bias direction is significantly lower with an UTS of 40 MPa. The data shows along with Equations 2.1 and 2.2, that an inflatable boom will fail under pressure at the seam running along its length. It suggests a maximum operating pressure of 33 and 25 PSI for a 0.05 m radius boom with the warp and fill yarns orientated around the hoop respectively.

The fabric in both warp and fill show the sequential regions of fabric extension; inter-fibre frictional effects, decrimping and yarn extension. A similar change of nonlinearity is observed in the biased tests that correspond to inter-yarn frictional effects, yarn slippage and shear locking successively. Each region is highlighted in Figures 3.14, 3.15 and 3.16 to the average of the repeat test data. For the warp and fill orientated specimens a forth stages is present where the fabric begins to yield from approximately 0.15 strain. This is likely due to the fibres in the yarns separating causing a weakening of the fabric before catastrophic failure.

The UTS of the stitched specimens is exceeded prior to any fabric yielding. Therefore the Young's modulus can be calculated by taking the average gradients of the crimp pull-out and

the yarn extension regions similarly to Hutchings and Braun (2009)[124] for biaxial tensile applications. This gives Young's moduli of E_w = 384 ±5 MPa, E_f = 273 ±6 MPa and E_{45} = 71.5 ±5 MPa where E_w, E_f and E_{45} are warp, fill and bias weave orientations respectively.

To determine the shear modulus of the fabric using Equation 3.1 the Poisson's ratio needs to be calculated. This can be done using several methods including analytically by using an equation created by Sun et al. (2005) where the fabric structure is modelled using the yarn radius, crimp angle and extensible yarns. The study concludes that the Poisson's ratio is determined by the woven structure and the interaction between the yarns but can be modelled as a continuum[118].

The DIC technique can measure the transverse strains in the same manner as the longitudinal strains and determine the Poisson's ratio directly. Figure 3.13 shows the longitudinal and transverse strain maps for test 3 of the 'warp with a stitch' specimen. The selected area to take an average value is highlighted in green to avoid any effects from the stitch or the fabric necking. The Poisson's ratio is then determined using Equation 3.2 and plotted against the tensile stress in Figure 3.17 and 3.18. The distinct regions of extension are also indicated.

$$\nu_{yx} = -\frac{\varepsilon_x}{\varepsilon_y} \qquad \textbf{(Equation 3.2)}$$

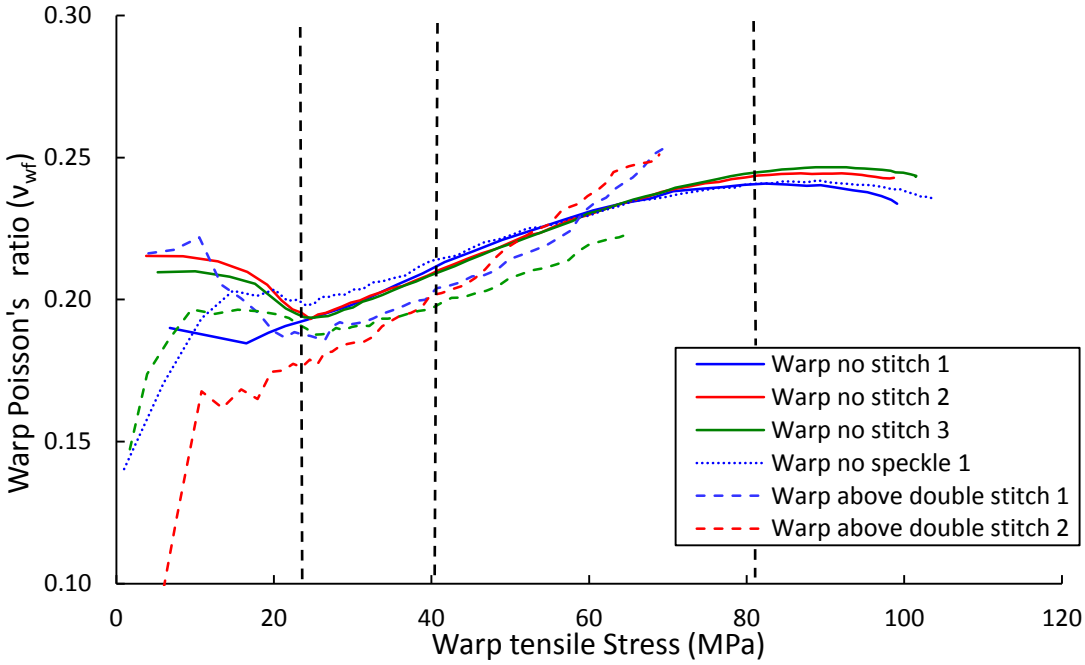

Figure 3.17: Warp Poisson's ratio (v_{wf}) against tensile stress.

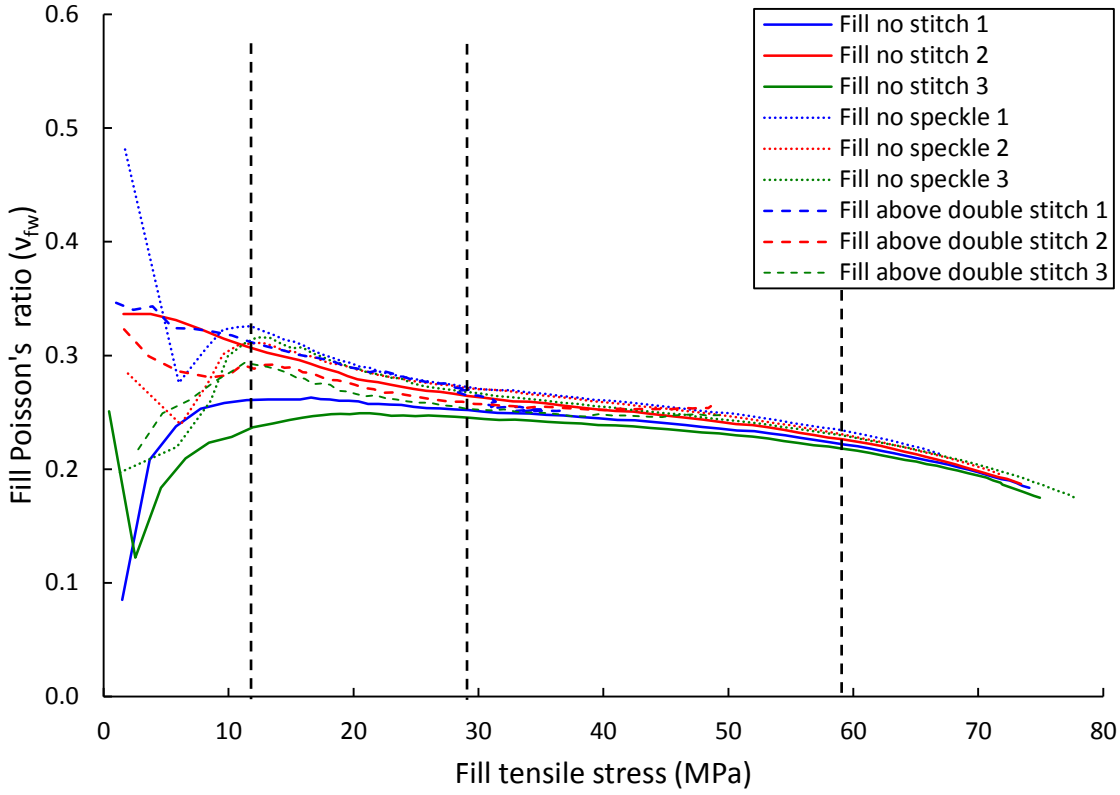

Figure 3.18: Fill Poisson's ratio (v_{fw}) against tensile stress.

Figures 3.17 and 3.18 shows that unlike typical orthotropic materials the Fibremax 94 does not have a constant Poisson's ratio. A similar response is found in other fabrics which vary with an increase in tension and between samples due to imperfections in the weave structure and the changing structural mechanisms[112]. The values obtained vary between 0.05 and 0.48 but the majority of the calculated values range between 0.2 and 0.25. After the inter-fibre friction region of high stiffness, the Poisson's ratio for specific tests tend to converge with one another. The Poisson's ratios tend to change linearly in the decrimping and yarn extension regions. These values range between 0.19 – 0.23, and 0.27 – 0.24 in the warp (v_{wf}) and fill (v_{fw}) directions respectively. The tensile yarns in the decrimping section become flat lengthening the fabric at relatively low stiffness. This results in the transverse yarns becoming increasingly crimped giving an appearance of Poisson's effect occurring when no structural change is occurring to the yarns themselves. In the following yarn extension region the tensile yarns are extending and a local different Poisson's effect is occurring specifically to the yarns as they thin with increased tension. The transverse yarns are under no load at this point and remain unchanged. This gives the perceived effect when taken as a whole of the Poisson's ratio varying as the fabric moves through these two regions. In reality the regions are blurred as the yarns change between the preferential mechanisms. This leads to a gradual gradient changes between regions shown in both the σ-ε and Poisson's ratio plots.

As decrimping and yarn extension occur simultaneously under biaxial tension[124] the Poisson's ratio can be averaged similarly to the Young's modulus and remain a constant. This gives Poisson's ratios of v_{wf} = 0.210 ±0.003 and v_{fw} = 0.250 ±0.020. Given the calculated elastic moduli and Poisson's ratios it is possible to implement Equation 3.1 to determine the shear modulus of the fabric. For the measured material properties given in Table 3.2 the shear modulus is 20 ±2 MPa.

Table 3.2: Material properties of Fibremax 94 tested in uniaxial tension averaged for biaxial applications.

Material property	Value	Error range (±)
E_w	384 MPa	5 MPa
E_f	273 MPa	6 MPa
E_{45}	72 MPa	5 MPa
v_{wf}	0.21	0.003
v_{fw}	0.25	0.020
G	20 MPa	2 MPa
ρ	588 kgm^{-3}	11 kgm^{-3}
t	0.195 mm	0.001 mm

The uniaxial tensile testing has provided the material properties of the Fibremax 94 ripstop nylon fabric. It has shown that the fabric is highly nonlinear having three distinct regions; frictional effects, decrimping, and yarn extension. An additional region of fabric yielding also occurs when the warp or fill yarns are placed in tension. The material properties of the fabric change depending on the applied stress. However for evenly stressed biaxial applications it is known that the decrimping and yarn extension occurs evenly giving rise to constant material properties[120,123,124]. For an inflatable boom, where the biaxial tension ratio is 2:1 between the axial and longitudinal directions respectively, the fabric may behave differently. It is therefore important to know the material behaviour in this application by conducting DIC on inflatable booms under various pressures.

It is noteworthy that the DIC technique remains non-intrusive for the Fibremax 94. It is possible to correlate images with no sprayed speckle pattern by using only the pattern described by the weave. This was possible with all but one specimen, 'warp no speckle 3', suggesting the weave on other fabrics could also be suitable as a reference pattern for DIC. Future research may have particular interest in investigating DIC on lose weave fabrics as spray paint would act as a stiffening matrix and affect the material properties. For the Fibremax 94 however, Figure 3.14 and 3.15 show the material properties remain unchanged by the addition of spray paint.

3.7 Biaxial Testing Results

Biaxial tensile testing was conducted on an inflatable boom constructed as shown in Figure 2.18. Three boom types were constructed; warp, fill and biased yarns orientated around the hoop of the boom. There were three repeat tests for each boom type including two where the DIC cameras contain the boom seam to allow measurements of stitch pull-out to be determined. Figure 3.19 displays the strain maps of the inflatable boom including the seam for both longitudinal and hoop strains at 16 PSI inflation. The boom has the warp yarns in the hoop direction and is shown to have a seam pull-out of 6 mm at this pressure.

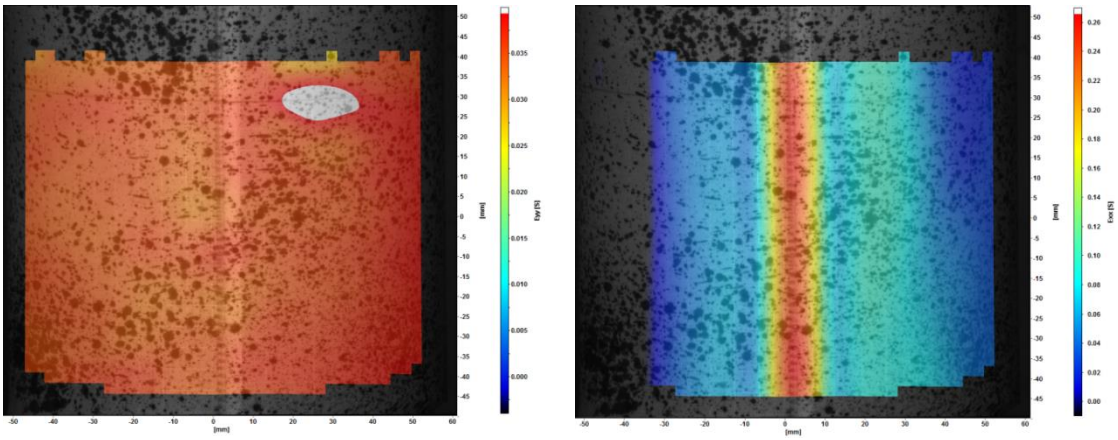

a) Longitudinal (ε_L) b) Hoop (ε_H)

Figure 3.19: Biaxial strain maps of an inflatable boom at 16 PSI inflation pressure with the warp yarns in the hoop direction.

The stress is calculated using Equation 3.3 and 3.4 which takes into account the radius change from the fabric strain where σ_H and σ_L are hoop and longitudinal boom stresses respectively and ε_H is boom hoop strain.

$$\boldsymbol{\sigma_H = \frac{pr(\varepsilon_H + 1)}{t}} \quad \textbf{(Equation 3.3)}$$

$$\boldsymbol{\sigma_L = \frac{pr(\varepsilon_H + 1)}{2t}} \quad \textbf{(Equation 3.4)}$$

The stress – strain data is given in Figures 3.20 and 3.21 displaying the material response for the warp and fill yarns aligned to a boom coordinate direction respectively. Figure 3.22 shows the biased boom response where the yarns are not aligned to the coordinate system. The figures show the material behaves linearly around the circumference of the boom for each fabric orientation. However along the length of the boom the initial inflation pressures cause a

nonlinear strain response for either warp or fill orientations. The greatest effect is seen when the warp yarns are placed in the boom length where initial inflation pressures show some booms to reduce in length in Figure 3.20. After approximately 14 and 7 MPa hoop and length tensile stresses respectively (8 PSI inflation pressure) both warp and fill yarns tend to respond linearly. The gradient is also the same as when the same yarn is placed in the hoop direction. This nonlinear material response is caused by the crimp pull-out for the yarns in the hoop direction. This is because the hoop direction is under twice the longitudinal stress resulting in an increase crimp of the longitudinal yarns effectively shortening the boom. As the system is under biaxial tension yarn extension occurs at the same time creating a linear response around the hoop of the boom. After approximately 8 PSI the crimping effect is balanced between the two yarn directions and the longitudinal yarns then exhibit a linear response. The nonlinearity differences between the two yarn types are likely to be a result of weave as warp yarns tend to have a higher crimp angle so have more de-crimping capability. Further detailed analysis of the fabric weave is required to establish this and is outside of the scope of this research. For inflation pressures greater than 8 PSI constant material properties can be applied where the nonlinearity can be assumed to effectively shorten the boom by up to 1.5% depending on the yarn orientation with respect to the boom. The biaxial elastic moduli for the warp (E_{Bw}) and fill (E_{Bf}) fabric orientations are 489 ±32 MPa, 359 ±9 MPa respectively.

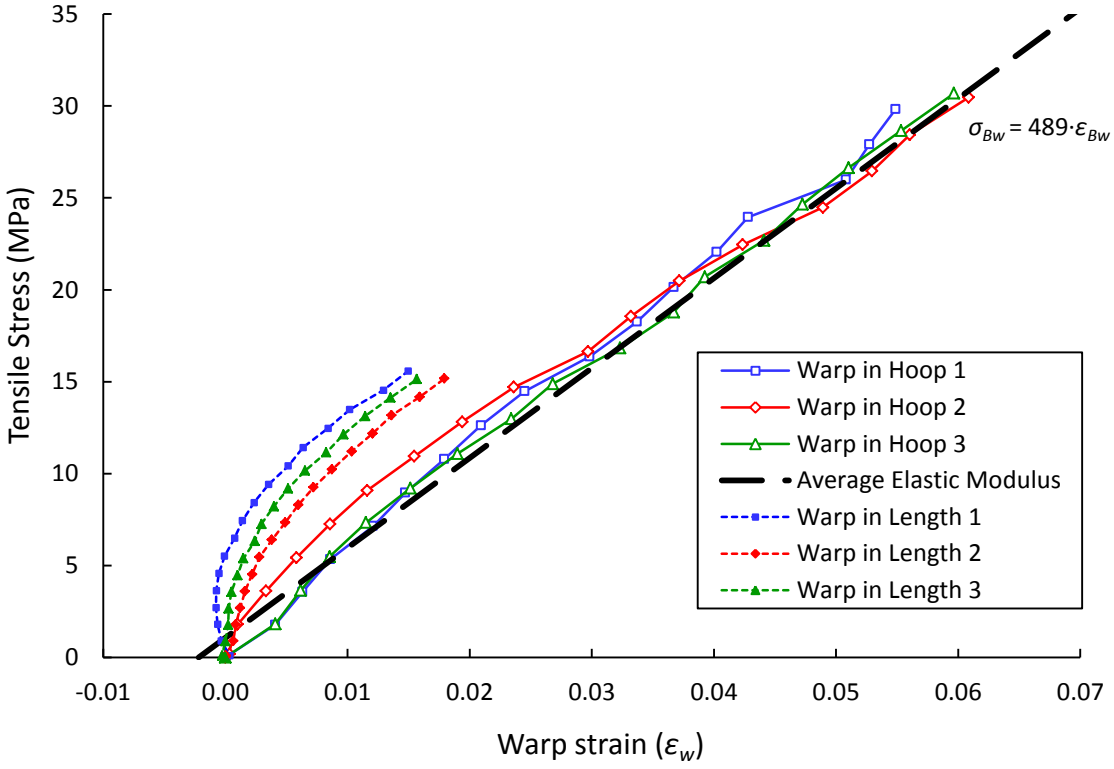

Figure 3.20: Warp yarn stress – strain response in an inflatable boom.

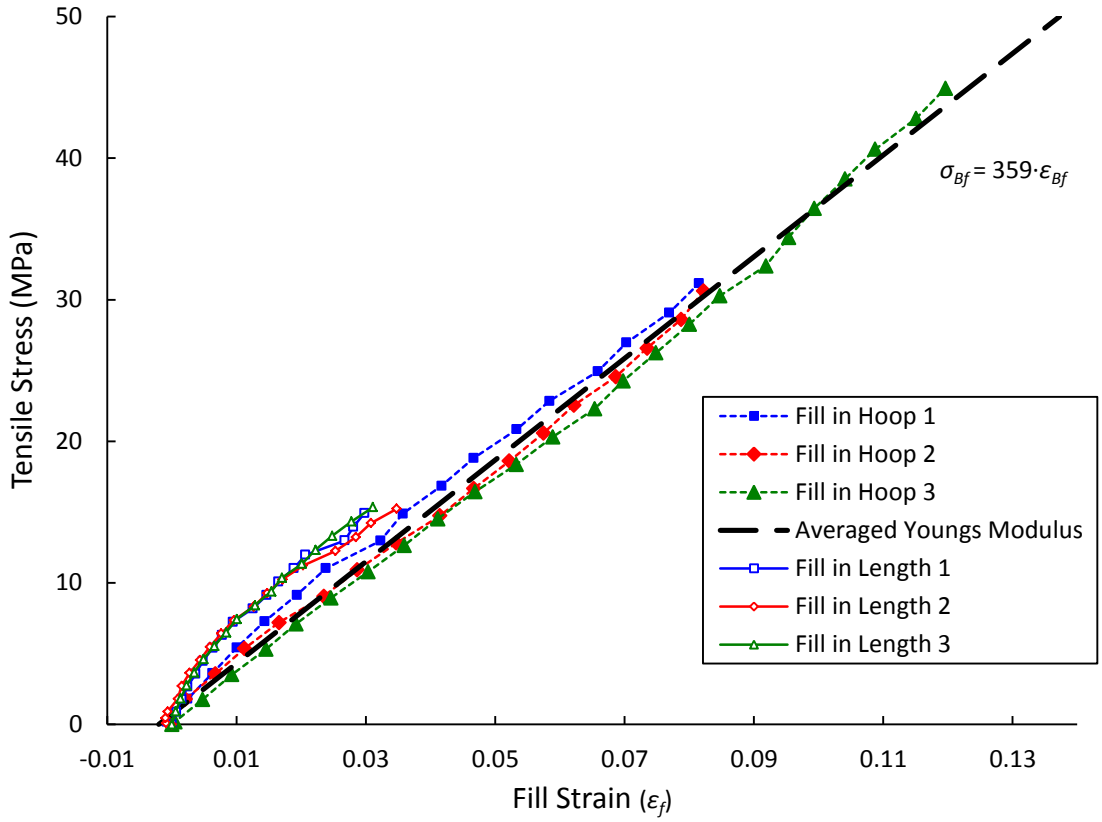

Figure 3.21: Fill yarn stress – strain response in an inflatable boom.

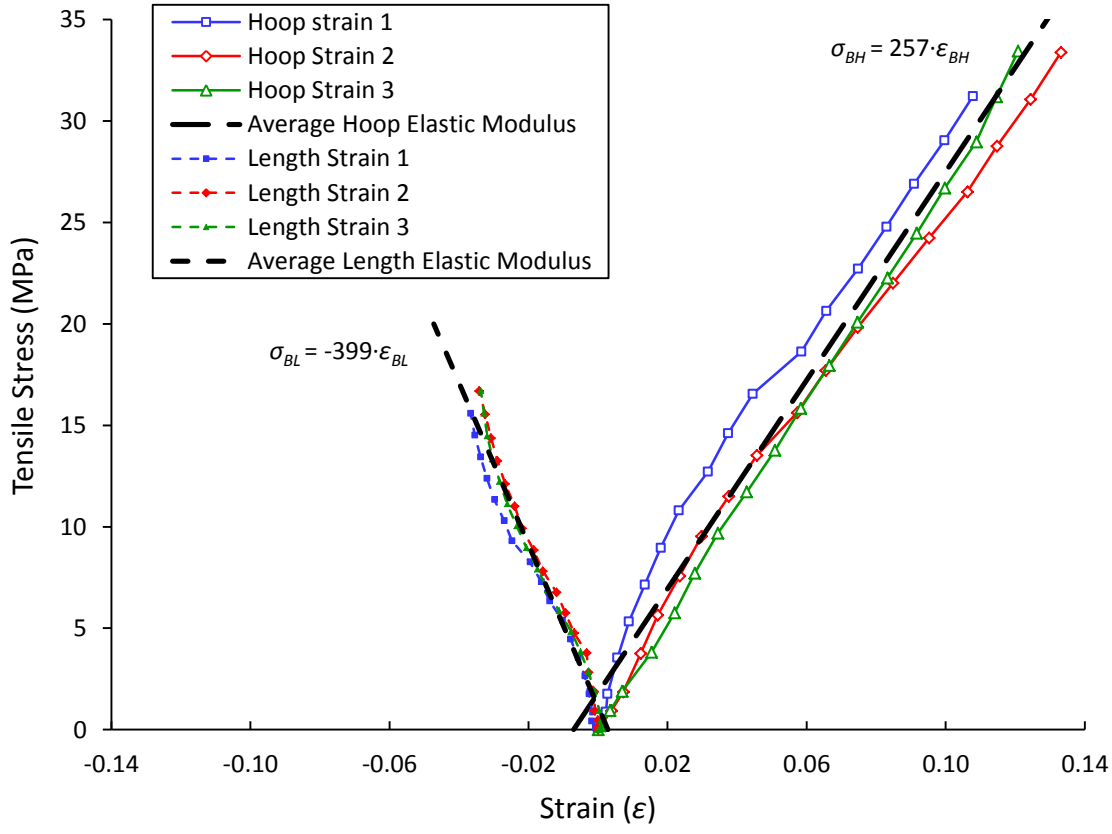

Figure 3.22: Biased stress – strain response in length and hoop directions of an inflatable boom.

The biased boom shows a different linear response where the low shear stiffness of the fabric results in the boom becoming significantly shorter as the larger hoop stress causes shearing and the yarns tending to align towards the hoop direction. The biased booms increase in radius and decrease in length to 55.4 ±0.4 mm and 361 ±1 mm at 15 PSI respectively.

3.8 Discussion

The biaxial tests have determined the warp and fill biaxial elastic moduli, E_{Bw} and E_{Bf} respectively, showing the material behaves differently to uniaxial tests. Equations 3.5, 3.6 and 3.7 are the fundamental equations of a planar orthotropic material from the stiffness matrix where Equation 3.7 is a relationship between the in plane orthogonal Poisson's ratios. In certain conditions it is possible to simplify Equation 3.5 and 3.6 to determine the fabric material properties. Namely when $\sigma_x = 0$ (uniaxial tension) or $\varepsilon_y = 0$ (biaxial tension where one edge is held stationary)[130]. However in this circumstance where both $\sigma_{x,y}$ and $\varepsilon_{x,y} \neq 0$ it is not possible to attain the material properties from purely biaxial boom tests[92]. This is because there are only 3 equations where E_w, E_f, ν_{wf} and ν_{fw} are all unknown.

$$\boldsymbol{E_w = \frac{\sigma_w}{\varepsilon_w} - \nu_{wf}\frac{\sigma_f}{\varepsilon_w}} \qquad \textbf{(Equation 3.5)}$$

$$\boldsymbol{E_f = \frac{\sigma_f}{\varepsilon_f} - \nu_{fw}\frac{\sigma_w}{\varepsilon_f}} \qquad \textbf{(Equation 3.6)}$$

$$\boldsymbol{\frac{\nu_{wf}}{E_w} = \frac{\nu_{fw}}{E_f}} \qquad \textbf{(Equation 3.7)}$$

An alternative approach to determine the complete stiffness matrix must assume a material constant between uniaxial and biaxial tests. As $2\sigma_L = \sigma_H$, Equation 3.5 can be rewritten as

$$\boldsymbol{E_w = E_{Bw}\left(1 - \frac{\nu_{wf}}{2}\right)} \qquad \textbf{(Equation 3.8)}$$

where $E_{Bw} = \frac{\sigma_w}{\varepsilon_w}$ in the biaxial test case. A similar equation for an isotropic material is derived by Solderman and Giroud (1995). Equation 3.8 is used to calculate the Young's modulus of the warp fabric orientation using the measured biaxial elastic moduli and the averaged uniaxial Poisson's ratio which assumes constant material properties for these biaxial tests. The fill

orientation is similarly calculated by symmetry of the stiffness matrix. This gives values of 438 ±29 MPa and 314 ±8 MPa for warp and fill fabric orientations respectively. This error range is increased if the Poisson's ratio assumption is incorrect. Taking the range of the possible Poisson's ratios stated in the uniaxial test section of 0.19 – 0.23, and 0.27 – 0.24 in the warp (v_{wf}) and fill (v_{fw}) directions respectively changes the Young's modulus values to E_w = 438 ±34 MPa, and E_f = 314 ±10 MPa. These values are similar to the predicted values from the uniaxial test data but take into account any unrealistic assumptions that the uniaxial method may have made and are specific to an inflatable boom application. This includes the linear decrimping and yarn extension mechanisms biaxial systems are assumed to have[124] as well as the initial frictional effects that were only seen in the uniaxial tests.

As it is difficult to conclusively state the material properties for the fabric in 2:1 biaxial tension, computational modelling will consider the range of material property values in an iterative process to fine tune the model that best represents the experimental response. This is a common practice for woven materials which display high levels of nonlinearity when modelling them as a continuum material[123]. Using the updated Young's moduli the shear modulus from Equation 3.1 changes from 20 to 19 MPa.

A failure test was conducted on a boom with the collected data shown in Figure 3.21. The boom could maintain an inflation pressure of 23 PSI corresponding to a 45 MPa stress in the fill yarns orientated in boom hoop direction. At 24 PSI, or 48 MPa in the fill yarns, the seam failed as shown in Figure 3.23. This matches the UTS of the stitched fill orientated specimens from the uniaxial testing given in Table 3.1. Previous preliminary tests also failed at 22 and 25 PSI but would require further testing to confirm that uniaxial UTS tests can predict the maximum operating pressure of an inflatable boom. As boom failures occurred from 22 PSI, a conservative maximum operating pressure of 15 PSI was selected. The failure test also showed that the material continues to have a linear response for pressures greater than 16 PSI.

Figure 3.23: Boom failure at 24 PSI with fill yarns orientated in the hoop direction.

3.9 Summary

Uniaxial and biaxial material testing has determined the material properties of the Fibremax 94 ripstop nylon given in Table 3.3. Uniaxial data displayed a highly nonlinear material with up to four distinct sequential mechanisms; inter-fibre frictional effects, decrimping, yarn extension and yarn yielding. The uniaxial biased specimens show; inter-yarn friction effects, yarns slippage and shear locking. However biaxial testing, through an inflatable boom, confirmed a predicted linear response where properties can be assumed constant for pressures greater than 8 PSI. The linear response is brought about as the distinct uniaxial mechanisms occur at the same time when in biaxial tension[124]. This is confirmed by the elastic modulus ratio between the two fabric orientations remaining at 1:0.72 for both biaxial, E_B, and uniaxial tests, E_U.

With the previous assumption the Poisson's ratio is calculated using the averaged uniaxial test data and used with the biaxial stress – strain data to calculate the Young's modulus of the fabric in both yarn directions specific for an inflatable boom.

The nonlinearity observed in the boom length and stitch pull-out of the seam is taken into consideration by an effective length and radius change in the boom for specific pressures which then can take constant material properties for inflation pressures of 8 PSI or greater.

Table 3.3: Material properties of Fibremax 94 used in an inflatable boom.

Material property	Value	Error range (±)
E_w	438 MPa	34 MPa
E_f	314 MPa	10 MPa
E_{45}	72 MPa	5 MPa
v_{wf}	0.21	0.02
v_{fw}	0.25	0.02
G	19 MPa	2 MPa
ρ	588 kgm^{-3}	11 kgm^{-3}
t	0.195 mm	0.001 mm

The shear modulus is calculated by Equation 3.1[126] which uses E_{45} measured in the biased uniaxial tensile test. The uniaxial tests also took the specimens to failure to establish the UTS of the material in warp, fill and bias orientations. It can be concluded that the Fibremax material used for an inflatable boom will fail along the boom seam and would maintain a higher operating pressure with the warp yarns orientated in the hoop direction of the boom. A failure test of the inflatable boom with the fill yarns in the hoop direction showed correlation between the uniaxial UTS and the maximum achievable pressure of 23 PSI. Further repeat tests are required to validate this result but show the booms will survive at a conservative maximum operating pressure of 15 PSI.

The DIC was shown to be a successful method to accurately and reliably measure strain in the fabric. The non-invasive technique allowed strains to be measured directly on the material application instead of specialist biaxial test rigs being developed. The required unique speckle pattern applied with spray paint was also shown to have no effect on the Fibermax 94 material properties. This was achieved by comparison between speckled and non-speckled specimens with the result probably due to the fabric already having a stiffening matrix from an impregnated resin. It also meant the pattern of the nylon weave, although repetitive, could be used to sufficiently capture the strains in the material. This leads to the possibility of this method being successfully implemented for other non-impregnated loose weave fabrics where an applied spray paint would act as a stiffening matrix and affect the material properties.

From the material tests of the Fibremax 94 a clear understanding of the material is known when used for an inflatable boom. Maximum operating pressures are determined and it is known how the boom will strain under various pressures including across the seam. The material properties are calculated as an orthotropic planar continuum material and will be used for inputs to analytical models.

Chapter 4

Experimental Structural Analysis of an Inflatable Boom

To determine the structural performance of the manufactured inflatable booms, experimental tip deflection testing was undertaken to establish the change in stiffness and maximum bending moments for various boom configurations. This data can then be used for inflatable boom optimisation, validation of computation analysis and comparison against the structural performance of hybrid booms. The booms were manufactured using the Fibremax 94 sailcloth as described in section 2.4. Table 4.1 gives an outline of the inflatable boom test configurations conducted. This allows the structural performance of the boom to be determined for various scenarios including fabric orientation, boom length, and fabric thickness. The multitude of boom permutations also gives increasing validity to a developed numerical model that can then be used with confidence over a wide range of designs. Prior to these tests preliminary studies were conducted to confirm the procedural method to attain accurate and reliable results.

Table 4.1: Experimental inflatable boom tests.

Test Name	Boom lengths (m)	Fabric orientations	Pressures (PSI)	Number of skins
Fabric orientation	0.2, 0.4, 0.6	Hoop, Longitudinal	10, 15	Single
Boom length	0.4, 0.6, 0.8, 1.0	Hoop	2.5, 5, 10, 15	Single
0.4 m Multiple skins	0.4	Hoop	2.5, 5, 10, 15, 20, 25, 30, 45	1, 2, 3, 4
1.0 m Multiple skins	1.0	Hoop	2.5, 5, 10, 15, 20, 25, 30	1, 2
Partially layered boom	0.2, 0.4, 0.6	Hoop	10	1.5 top and side

4.1 Experimental Procedural Method and Preliminary Studies

The boom deflections were created by fixing the boom at the root, creating a cantilever structure and hanging weights at the boom tip. The weights have an error of 0.1% and were added at 1 kg intervals unless otherwise stated. The boom length, radius and deflections were measured using DIC where a speckle pattern applied to the boom allowed the cameras to track their position. The cameras have 2 megapixels giving a deflection accuracy greater than 0.4 mm. The inflation pressure of the booms was measured using a manometer accurate to 1 Nm^{-2} and each boom configuration had 5 repeat tests. Figure 4.1 displays the correlated images with an overlaid strain field along the boom length highlighting the increasing tensile and compressive strains on the top and bottom surfaces as the applied tip loading is increased. The tensile and compressive strains peak at 18 and 10% respectively from the zeroed 0 kg inflated boom. The difference can be attributed to the fabric not sustaining compressive loads as illustrated previously in Figure 2.8.

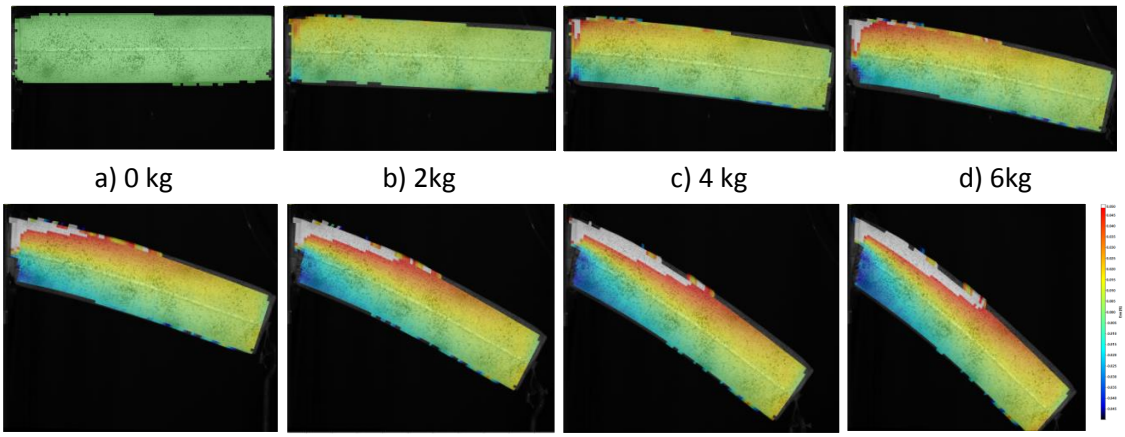

Figure 4.1: DIC of a 0.4 m inflatable boom at 15 PSI under tip loading with the calculated strain map along the boom length.

It was observed during preliminary testing that deflections did not reach equilibrium. This is because the inflatable boom is a soft system and will flex under loading. This causes the boom to behave in a quasi-static nature during tip deflection testing. The boom equilibrium during applied loads was observed to have a settling period of several minutes. A short test program showed the effect of measuring the deflections at various time intervals. Figure 4.2 shows the tip deflections of a 0.05 m radius, 0.4 m inflatable boom at 10 PSI and confirms that the booms takes several minutes to reach equilibrium. Tests 1 and 2 increase the applied load by 1 kg every 5 minutes and show that the boom took longer to reach equilibrium as it approached

the buckling point at 7 kg. The maximum change between the 1st and the 5th minute was 7 mm and highlighted that measurements should be taken at equal time intervals. Taking a measurement after 2 minutes reduces this change to a maximum of 4 mm. Test 3 focuses on the buckling region of the applied bending moment where the change in deflection was greatest. This is between 6 and 8 kg applied to the boom tip and increases the applied load every 20 minutes. It shows that equilibrium is still not completely reached after this time and the boom continues to increase in deflection by up to 0.2 mm per minute. However to allow testing to be achieved on a suitable timescale deflection measurements were taken at 60 s intervals which are within 5% the final deflections achieved.

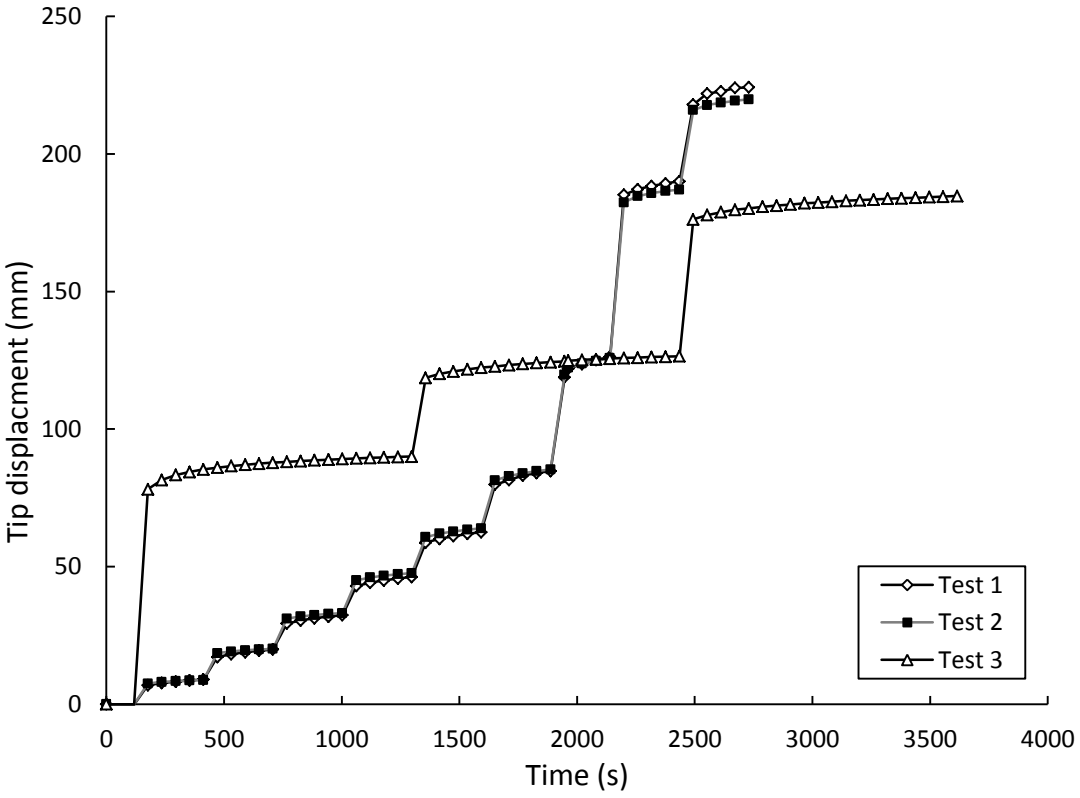

Figure 4.2: Equilibrium study of a 0.4 m long 0.05 m radius inflatable boom at 10 PSI.

The subsequent data generated is displayed on applied moment – tip deflection graphs to demonstrate the response and determine rigidity and achieved peak moments of each of the inflatable boom permutations tested. Figure 4.3 displays a typical tip deflection response confirming the 5 experimental repeat tests are representative of the averaged result which is within 5% of the repeat variability. For clarity subsequent experimental data is represented by the averaged results where a repeat variability is stated and full repeat test data is given in appendix II to confirm the results are representative. It is also important to consider the effect of gravity acting on the boom in this setup. The 0.4 m long boom mass is 135 g. This is

distributed as a 53 g tip mass and an 82 g uniformly distributed mass along the boom length. The boom mass accounts for an additional 0.37 Nm acting on the boom prior to any loading. This is less than 1% of the maximum applied bending moment in Figure 4.3. However lower test pressures and longer booms can expect the effect of gravity to have a more significant impact on results and as such will be considered in the analysis. The effect of gravity on tip deflections cannot be measured in this setup. For a tip deflection approximation the first two data points in Figure 4.3 show a linear relationship that is within the repeat variability. Extrapolating this suggests the effect of gravity provides an additional 1.6 mm tip deflection. This is a negligible increase that will not significantly alter the measured stiffness.

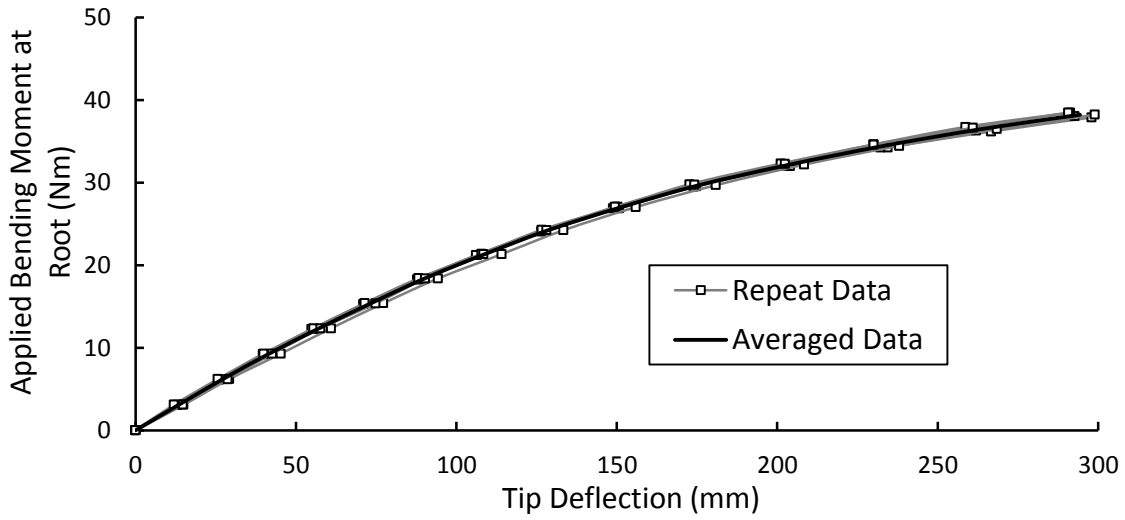

Figure 4.3: Typical applied moment – tip deflection response of an inflatable boom with 5 repeat tests.

4.2 Fabric Orientation Tests

UTS testing of the Fibremax 94 shows the operating pressure is maximised when placing the stronger warp yarns in the hoop direction of the boom. As the maximum bending moment an inflatable can sustain is proportional to inflation pressure, the structural performance is predicted to be maximised when placing the warp yarns in the hoop direction. However the stiffer warp yarns placed longitudinally may affect the boom rigidity under bending. This section of research investigates any performance trends when altering the warp and fill directions in the boom.

Two fabric orientations were considered by placing the warp yarns in the boom's hoop and longitudinal directions. Each fabric orientation was tested on 0.2, 0.4 and 0.6 m long booms

and at two pressures of 10 and 15 PSI giving a total of 12 test configurations with 5 repeat tests each. Figure 4.4 and 4.5 display the averaged tip deflections against the applied bending moment data for each test configuration. The full data set is given in appendix II and shows all repeats have tip deflections within 5%. They show the trend that under increasing pressure and boom length, the warp yarns in the longitudinal direction increasingly contribute to a stiffer boom where at 0.6 m and 15 PSI the initial boom rigidity prior to wrinkling is increased by 11%.

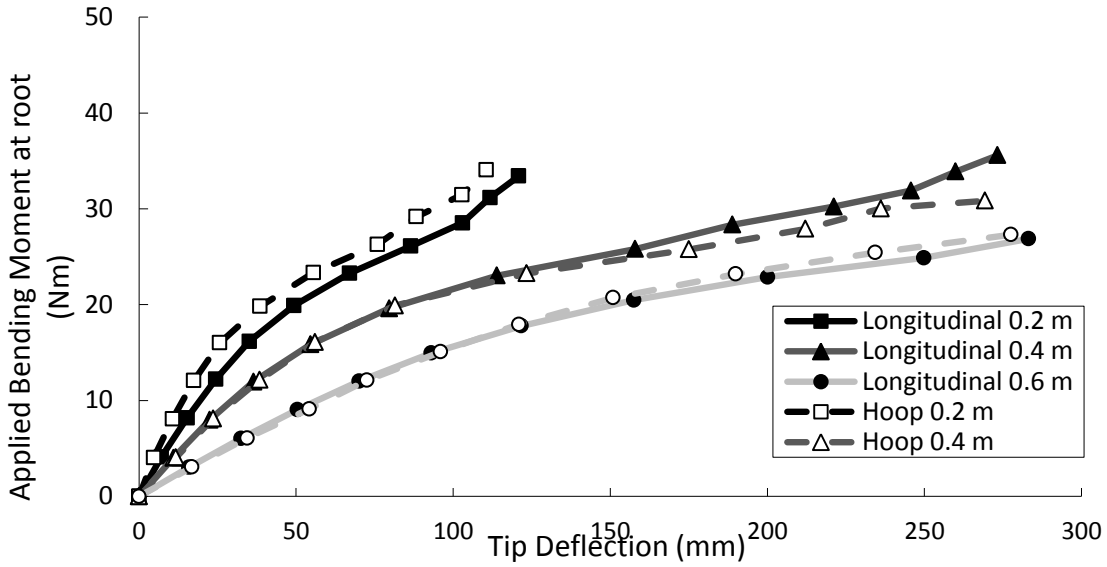

Figure 4.4: Averaged tip deflections of two fabric orientations at 10 PSI.

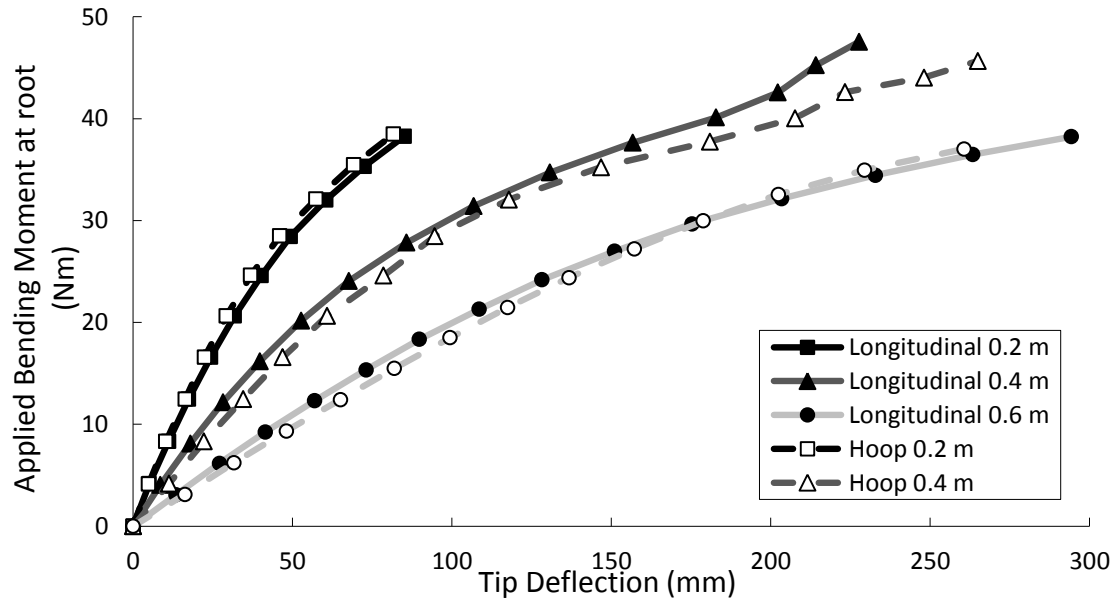

Figure 4.5: Averaged tip deflections of two fabric orientations at 15 PSI.

Maximum bending moments (M_{max}) could not be achieved as the boom impinged on the base plate at large tip deflections. This resulted in an apparent rigidity increase that can be seen on some of the 0.2 and 0.4 m boom deflection curves. At this point any further deflection is not representative of the performance of the boom. However through observation of the initial wrinkling point it is possible to predict the M_{max} by equating Equations 2.8 and 2.9 as derived by Webber (1982) and Comer and Levy (1963). Table 4.2 displays the applied bending moment at initial wrinkling (M_w) of the booms showing that the predicted M_{max} is up to 4 Nm greater for booms with the warp yarns in the hoop direction. However the error range is up to 5 Nm due to the discrete loading profile at the boom tip. Although there is a general trend for wrinkling to occur earlier with the warp yarns orientated along the boom length, the majority of the booms start to wrinkle within this error range. This is reflected in the predicted M_{max} which also shows a close correlation to the calculated peak moment from the Comer and Levy model (1963). Using their Equation 2.9 shows a range of 0.8 and 1.4 Nm for 10 and 15 PSI respectively due to the change in average radius of each of the booms at different pressures and lengths. The booms radii expand from 50 mm to a maximum of 53 and 54.5 mm at 10 and 15 PSI respectively with the latter shown in Figure 4.6 including the constraining 50 mm boom root radius. Ignoring the radius change leads to the Comer – Levy model underestimating peak moment by 14 and 17% for these two inflation pressures respectively showing boom radius change from inflation must be considered.

Table 4.2: Initial wrinkling moment and predicted maximum bending moment for the fabric orientation study.

Pressure (PSI)	Length (m)	Warp direction	M_w (Nm)	Predicted M_{max} (Nm)
10	0.2	Longitudinal	12	24
		Hoop	16	32
	0.4	Longitudinal	12	24
		Hoop	16	32
	0.6	Longitudinal	15	30
		Hoop	18	36
10		Comer – Levy Model	15.8	31.5 ±0.8
15	0.2	Longitudinal	25	49
		Hoop	25	49
	0.4	Longitudinal	26	53
		Hoop	26	53
	0.6	Longitudinal	24	48
		Hoop	27	54
15		Comer – Levy Model	24.6	49.2 ±1.4

For all subsequent tests the inner plate and root collar were increased in depth from 10 to 50 mm. This is shown in Figure 4.6 with an increasing offset between the boom and baseplate and thereby delaying the interaction between the baseplate and boom to a larger tip deflection.

Calculations from the UTS and strain data using Equation 2.1 and 2.2 show a performance loss of 24% due to maximum operating pressure reduction when placing the warp yarns longitudinally over the hoop direction. Together with the greater increase in M_w and small loss in rigidity shows that the warp yarns should be placed in the boom's hoop direction to maximise inflatable boom structural performance. This was done for all subsequent tests.

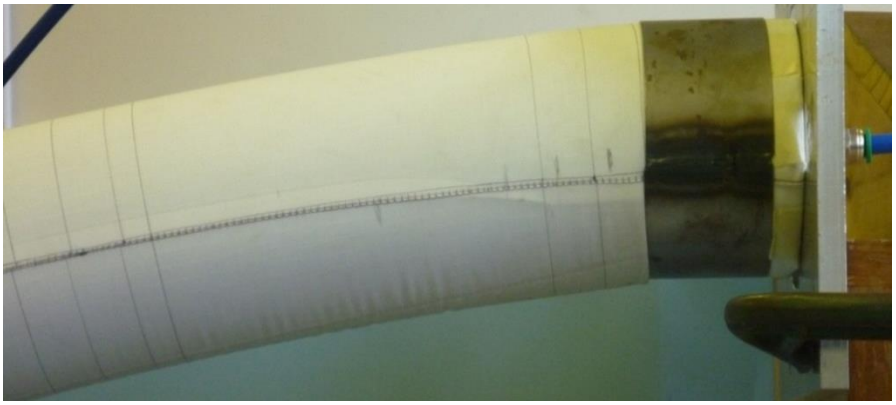

Figure 4.6: Updated 0.05 m inner plate and root collar setup with an inflatable boom at 15 PSI under 34 Nm showing wrinkling of the fabric.

4.3 Boom Length Tests

A length study was conducted to confirm that the trends from a 0.4 m inflatable boom are consistent for a range of boom lengths and can therefore be applied to a wider selection of boom designs. The study looked at 4 boom lengths between 0.4 and 1.0 m at four inflation pressures; 2.5, 5, 10 and 15 PSI, giving a total of 16 test configurations. Mass increments at constant intervals were varied between of 0.1 and 1 kg depending on the inflation pressure and the boom length. For example; at 2.5 PSI inflation pressure the 0.4 and 1 m booms had mass increments of 0.25 and 0.1 kg per minute respectively. This was to ensure sufficient data points with a minimum of 10 were captured. The tip deflection (δ) data is non-dimensionalised ($\bar{\delta}$) with respect to the boom length (L) where

$$\bar{\delta} = \frac{\delta}{L}. \qquad \textbf{(Equation 4.1)}$$

This allows the data to be clearly presented for varying boom lengths where the averaged repeat test data is given in Figure 4.7. The data shows the initial non dimensional rigidity is increased as the boom length is reduced.

However as the booms approach M_{max} this trend discontinues where the 1.0 m boom appears to become stiffer. This occurred at 59 ±9% of the expected M_{max} as predicted by the wrinkling data. This can be attributed to the repeat test variability in the tip deflections of up to 5% and inconsistencies in boom dimensions from the manufacturing process. This takes place for all pressures except 2.5 PSI where M_{max} reduces with boom length almost linearly between 7.9 and 6.7 Nm.

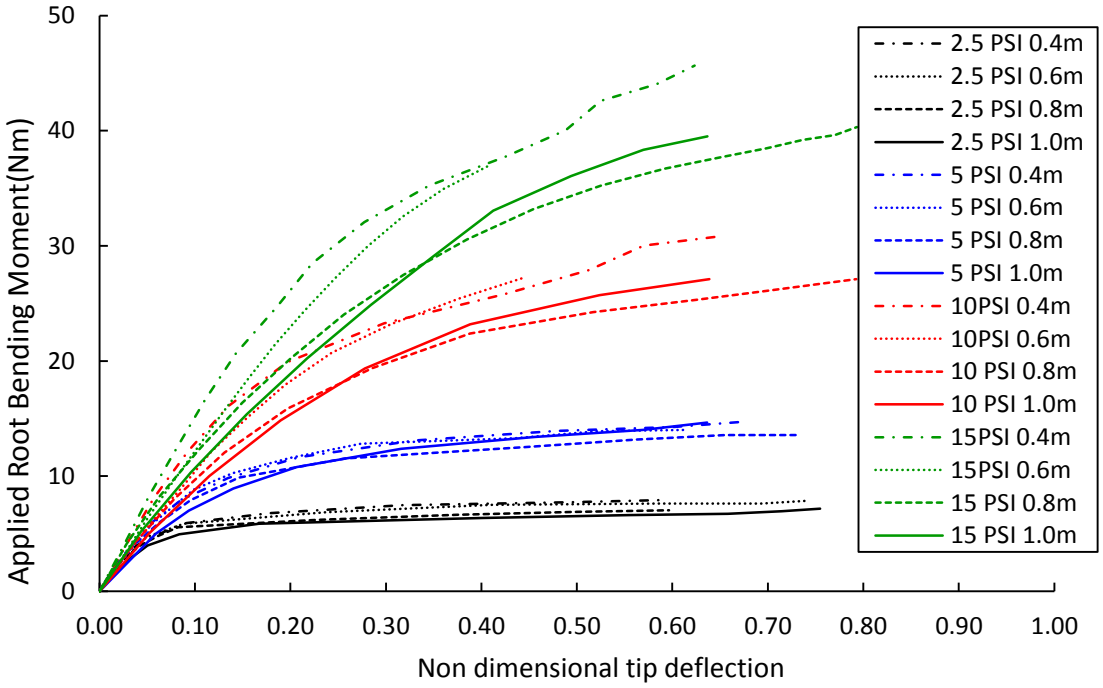

Figure 4.7: Varying boom length non dimensional tip deflection data averaged from the repeat tests.

As found in the fabric orientation study, the higher pressures of 10 and 15 PSI did not allow the boom to converge to a constant M_{max} as can be seen at the lower inflation pressures. This was also observed by Thomas and Weilgosz (2004) who investigated the deflections of inflatable booms under high pressures. This occurs because tip deflection induced volume changes lead to an increase in inflation pressure causing boom stiffening by the additional work done. This was developed by Davids (2007) that considered volume changes from boom bending, shear and axial strain showing a significant increase in the structural performance through the load-deflection response of inflatable booms and aches[91] when under high inflation pressures. This effect is increased with inflation pressure and boom length reduction as the volume changes become proportionally larger.

A prediction using the initial wrinkling point and Equations 2.8 and 2.9 show the booms reached 80 ±7% and 77 ±4% of M_{max} at 10 and 15 PSI respectively. At the lower pressures of 2.5 and 5 PSI the booms are able to achieve higher values of 92 ±8% and 85 ±6% respectively. This shows even though there is a difference between the predicted and achieved M_W and peak moments at the lower pressures, the higher pressures of 10 and 15 PSI were still not able to reach M_{max} with the updated inner plate within the tip deflections considered. Table 4.3 shows the predicted M_{max} from the wrinkling moment along with the average inflated radius of each boom. The data shows little change in wrinkling moments between boom lengths for all inflation pressures where the variance in the predicted peak moment is within the error range of up to 4 Nm caused by experimental inaccuracies. Using the average inflation radius, the peak moment predictions from the incipient wrinkling observation show a close correlation to the Comer – Levy model with the wrinkling moment error causing the range in results. However the predicted M_{max} change between boom lengths are relatively small and therefore cannot be accurately determined from the wrinkling observation. It is also clear in Figure 4.7 that M_{max} is inversely proportional to the boom length unlike the predicted increase due to the small average radius increase. At 2.5 PSI the moment-deflection data can be empirically approximated to $M_{max} = pr^3\pi - 2.5L + 1.6$, where L is the boom length. This relationship can be adjusted for the 5 PSI inflation pressure, although it assumes the booms have reached M_{max} with the data taken at 0.60 non dimensional tip deflection.

Table 4.3: Initial wrinkling moment and predicted buckling bending moment for varying boom lengths.

Pressure (PSI)	Boom Length (m)	M_w (Nm)	Average inflated radius (mm)	Predicted M_{max} (Nm)	% of Comer – Levy equation prediction
2.5	0.4	3.9	51.3	8	107%
	0.6	3.9	51.4	8	106%
	0.8	4.0	51.4	8	109%
	1.0	4.3	51.9	9	114%
5	0.4	7.9	52.0	16	104%
	0.6	8.8	52.2	18	114%
	0.8	7.9	51.9	16	104%
	1.0	8.9	52.3	18	115%
10	0.2	15.9	51.9	32	105%
	0.4	16.0	52.7	32	101%
	0.6	17.9	52.9	36	112%
	0.8	15.9	53.3	32	97%
	1.0	19.4	52.9	39	121%
15	0.2	24.7	52.7	49	104%
	0.4	26.3	53.5	53	106%
	0.6	27.2	53.7	54	108%
	0.8	24.3	54.2	49	94%
	1.0	24.9	54.7	50	93%

The data has shown the varying boom lengths do not significantly affect the peak moments but do increase the relative stiffness as length is reduced. The boom rigidity is averaged up to the wrinkling moment where further loading quickly causes the booms to become too soft and unsuitable for practical applications. Although the wrinkling moment is inaccurate due to the experimental incremental applied tip load it has been shown to be consistent between boom lengths and inflation pressures where there was no change between repeat tests. The rigidity error as a result of the discrete loads is a maximum of 6%. The boom rigidity remains relatively constant with pressure increases and the averaged results given in Table 4.4 including the non-dimensional tip deflection rigidities. The variability of the results over the 2.5 – 15 PSI inflation pressure range is a maximum of 12% occurring for the 1 m boom. The non-dimensional tip deflection stiffness ($\bar{S}$) is calculated as shown in Equation 4.2 (where F_δ is the applied tip load) and confirms the softening structure with increasing boom length that can be clearly seen in Figure 4.7.

$$\bar{S} = \frac{F_\delta}{\bar{\delta}} = \frac{M}{\delta}. \qquad \textbf{(Equation 4.2)}$$

This is caused by the deformation induced volume changes being proportionally smaller as boom length increases. It should be expected as boom length increases the boom rigidity should tend towards a constant that can be seen in the longer 0.8 and 1.0 m booms. However the 0.4 m booms have shown consistent trends with respect to inflation pressure against the longer booms up to 0.50 non-dimensional tip deflections and along with ergonomic suitability are therefore used for subsequent experimental tests.

Table 4.4: Inflatable boom rigidity with varying lengths over the 2.5 to 15 PSI pressure range.

Boom Length (m)	Average Stiffness (N/m)	Non dimensional tip deflection average stiffness (N)
0.2	3567 ±1	746 ±17
0.4	764 ±58	312 ±28
0.6	293 ±18	179 ±9
0.8	159 ±12	131 ±9
1.0	83 ±10	86 ±10

4.4 Multiple Skinned Tests

Multiple skinned booms were primarily conducted on the 0.4 m boom where additional tests were conducted on a 1 m double skinned boom to validate trends. The multiple skinned booms were achieved by fitting up to four boom outer skins over each other before being attached to the inner and base plate as normal. The tip plate remained between the bladder and the innermost skin leaving the skins unconstrained from each other between the root and tip. The research looks at the effect of increasing the thickness of the booms and if layering the nylon skins performs similarly to numerical models when adjusting the thickness of a single skin. Layering the nylon in this way aims to only increase the thickness of the boom and not affect the other material properties. In contrast, using a single skin would require a range of fabrics that will likely vary the yarn thickness's and change the fundamental characteristics of the material properties while still using the same nylon material. This was identified by Walker et al. (2011) where similar nylon fabrics with varying thickness's had different Young's moduli. However it must be noted that the unconstrained skins may allow movement along the boom with respect to each other.

The investigation was conducted using four different thicknesses; 1, 2, 3 and 4 nylon skins with a thickness of 0.195 mm/skin. The results of this research are twofold; increased maximum operating pressure, and increased boom rigidity at the original operating pressures. Each are investigated in the following two sections and can be assessed against the mass gain from the added skins and compared against the performance advantage of a hybrid boom. The range of pressures tested was between 2.5 and 45 PSI and dependant on the skin thickness. Table 4.5 gives the detailed test programme where 15 PSI per skin was limited as the maximum operating pressure for safety and boom durability resulted in 34 test configurations. A further 12 configurations were also investigated in a final study investigating partially layered booms. This was to determine the trends of non-uniform fabric thickness and considered two profiles shown in Figure 4.8. Each profile had half a second skin attached by additional stitching along the boom length. For each test configuration the inflatable booms were subjected to tip deflection testing to assess their structural performance.

Table 4.5: Multiple skinned test programme.

Length (m)	Skins	Inflation pressures (PSI)	Number of test configurations
0.4	1	2.5, 5, 10, 15	4
0.4	2	2.5, 5, 10, 15, 20, 25, 30	7
0.4	3	2.5, 5, 10, 15, 30, 45	6
0.4	4	2.5, 5, 10, 15, 30, 45	6
1.0	1	2.5, 5, 10, 15	4
1.0	2	2.5, 5, 10, 15, 20, 25, 30	7
0.2	1.5 (vertically and	10, 15	4
0.4	horizontally aligned	10, 15	4
0.6	to the applied load)	10, 15	4

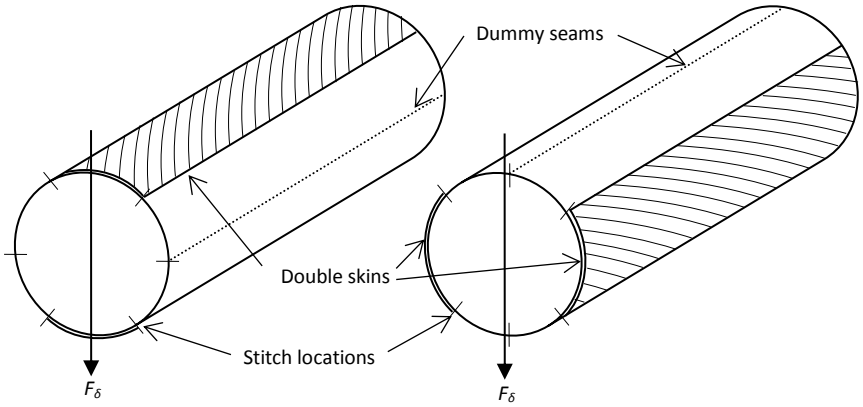

Figure 4.8: Cross section layout of a partially double skinned tube, in a) the vertical load orientation, b) the horizontal load orientation, where half the circumference has a double skin split into two equal areas on opposite sides with the applied load, F_δ.

4.4.1 Boom Rigidity Investigation

The boom rigidity investigation looks at the structural performance gains from increasing boom thickness with additional skins while maintaining constant inflation pressures. This is considered for pressures up to 15 PSI as this is the single skinned maximum operating pressure. Figure 4.9 displays the averaged tip deflection results of the 0.4 m boom with varying skin thickness's showing a significant increase in boom rigidity for double and triple skinned booms. This is quantified in Table 4.6 where skin thickness is almost directly proportional to rigidity for all inflation pressures as expected. The boom mass increases by 16 g per additional skin with the variance in stiffness results remaining relatively constant at less than 10%. The results vary by 5% between repeat tests and a further 2.6% between inflation pressures for the single skin.

This is increased a further 1.8 and 2.5% for double and triple skinned booms respectively which can be attributed to frictional effects between the skins with the ability to move relative to one another and will vary with inflation pressure. This is highlighted with the 4 skinned inflatable booms which show a rigidity range of 20% over the 4 inflation pressures. There is also a limited rigidity advantage between the 4 and 3 skinned booms showing an average reduction of 12%. This could be caused by variations in boom dimensions and corresponding transfer of stresses between each layer not being uniform. This leads to skins not being evenly load bearing depending on radius strain rates across the 2.5 – 15 PSI inflation pressure range and hence a perceived performance drop for the fourth skin.

Table 4.6: Rigidity performance of a 0.4 m inflatable boom with variable thickness.

Skins	Total Nylon thickness (mm)	Average Rigidity (N/m)	Boom Mass (g)
1	0.195	764 ±58	135
2	0.390	1303 ±123	151
3	0.585	2438 ±245	167
4	0.780	2134 ±426	184

The achieved peak moments also vary with skin thickness. This is up to 15% for 2.5 and 5 PSI inflation pressures but rises significantly up to 29% for 10 and 15 PSI when taking moments from 200 mm tip deflections. All boom radii are increased due to pressurisation. However, as thickness is inversely proportional to strain, this data contradicts Equation 2.9 which has previously shown small reductions in boom radius will significantly reduce M_{max}. This is likely caused by both the differences between boom dimensions and the interaction between boom layers. The boom manufacture radius tolerance is 1 mm and results in negligible differences of up to 0.5 mm between inflated boom radiuses for booms with more than one skin. The significant increase of peak moments for higher pressures is attributed to the boom not reaching M_{max}.

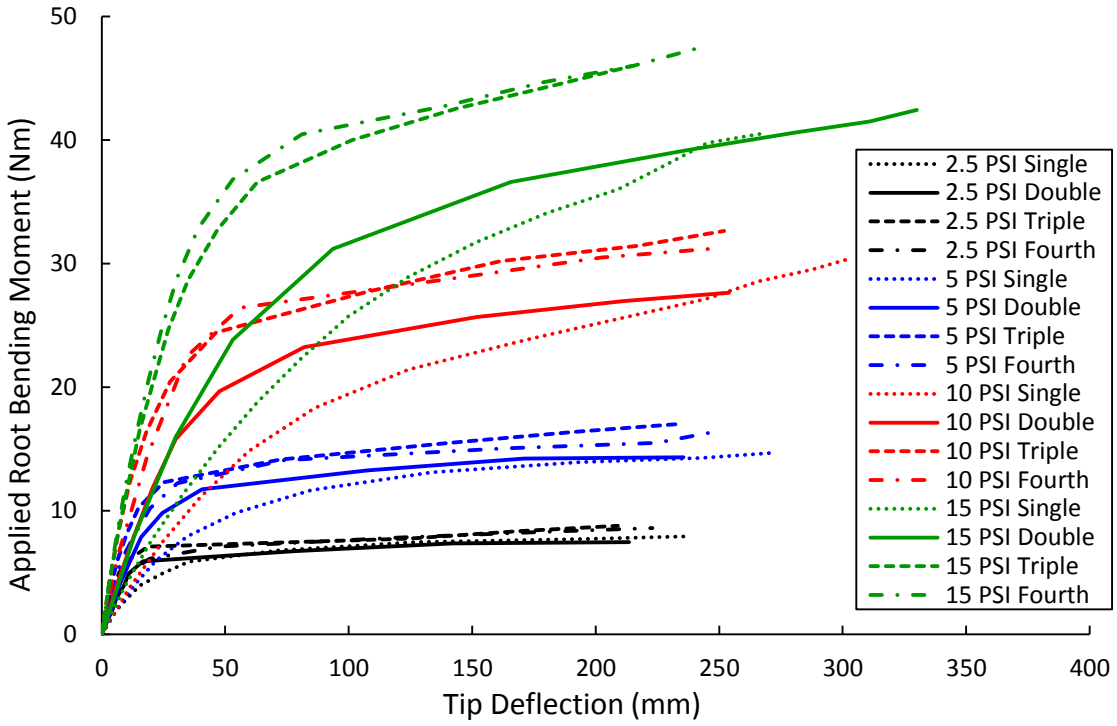

Figure 4.9: Low operating pressure tip deflection tests of a 0.4 m inflatable boom with multiple skins.

A comparison between 0.4 and 1.0 m booms was conducted to validate the structural performance trends found in the 0.4 m booms with varying skin thickness's. Figure 4.10 displays the averaged non dimensional tip deflections against the applied root bending moment for the double skinned 0.4 and 1.0 m booms. It also gives the tip deflection data for the higher pressures achieved of 20, 25 and 30 PSI.

The data shows the non-dimensional tip deflection rigidity is again reduced between the two boom lengths by 3.5 times and is consistent with the single skinned boom performance loss. Correspondingly both boom lengths increase the rigidity by 1.7 times when doubling the thickness. As with all booms tested, the initial rigidity prior to wrinkling also remains relatively constant with inflation pressure for both boom lengths. The double skinned 1.0 and 0.4 m booms have rigidities of 155 ±12 and 1303 ±123 N/m respectively. The moment – deflection response of the double skinned booms converge after boom wrinkling at all inflation pressures except 5 and 10 PSI which are within 5% of the experimental variability.

The double skinned booms were able to successfully operate at increased inflation pressures up to 30 PSI with the same trends in performance. The following section considers the performance change from the available increased maximum operating pressures of the multi-skinned booms.

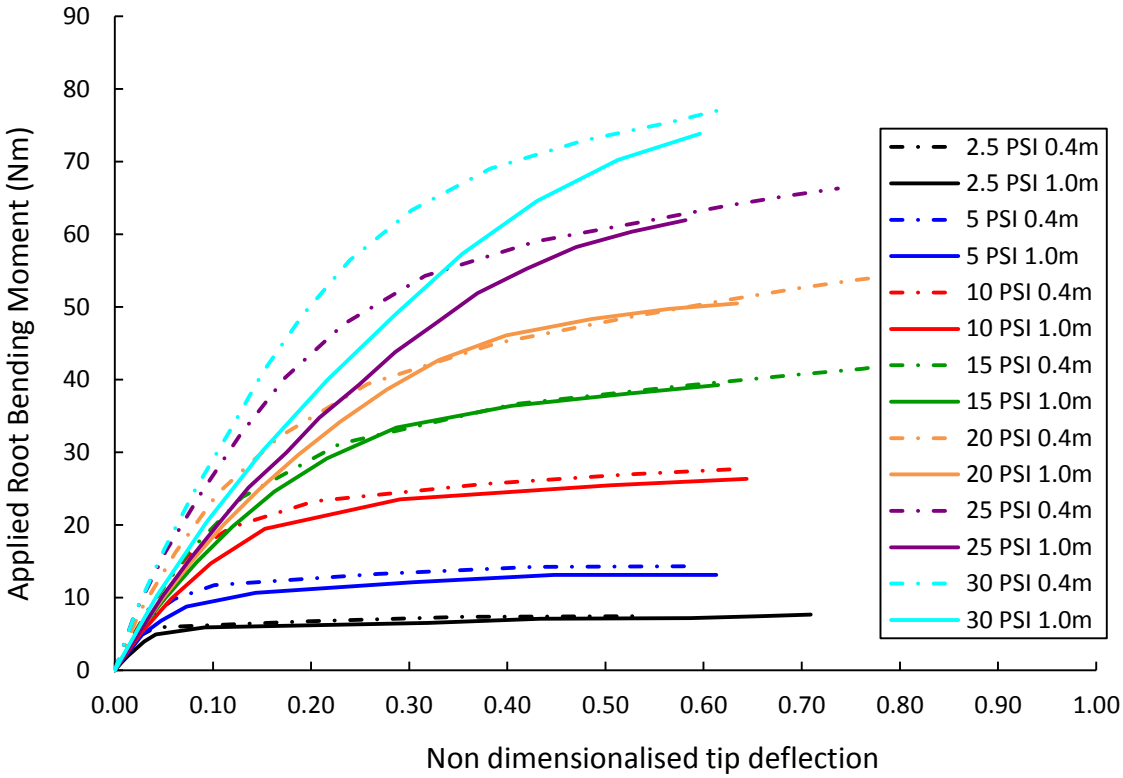

Figure 4.10: Average non dimensional tip deflections for double skinned booms.

4.4.2 Maximum Operating Pressure Investigation

The maximum operating pressure of an inflatable boom is directly proportional to the skin thickness shown in Equations 2.1, which in turn has a direct impact on the structural performance of a boom. Figure 4.11 shows the tip deflection data of the maximum operating pressures of 15, 30, and 45 PSI for single, double and triple skinned booms respectively. For completeness, the tip deflection data for all boom thicknesses is given at these pressures with the quantified data given in Table 4.7. The fourth skinned boom would have a maximum operating pressure of 60 PSI. Tests at this pressure and failure pressure tests of multi-skinned booms were not conducted for safety reasons but would be required to comprehensively confirm the maximum operating pressure is directly proportional to skin thickness. As no failures occurred at the higher pressures it can be concluded that no ultimate performance is lost for double and triple skinned booms and can safely operate at 30 and 45 PSI respectively.

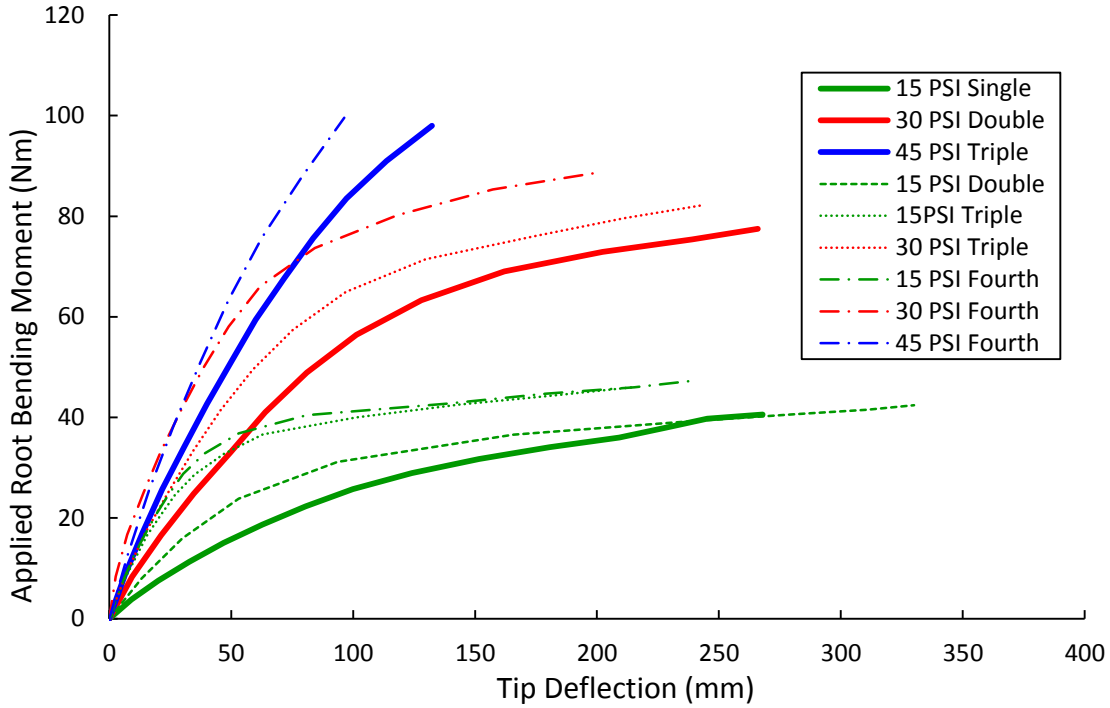

Figure 4.11: High operating pressure tip deflection tests of a 0.4 m inflatable boom with multiple skins.

The higher inflation pressures of 30 and 45 PSI continue to show the relatively constant rigidities proportional to skin thickness for both double and triple skinned booms. The boom rigidity using four skins remains variable but shows an increase in performance over the triple skinned booms at these higher pressures. This is caused by the increase in boom radius from higher inflation pressures. The difference in inflated radii between 3 and 4 skins of the 0.4 m booms are 0.1, 0.5 and 1.0 mm at 15, 30 and 45 PSI respectively showing the dimension differences between skins becoming negated as all skins become load bearing under the higher pressures. The boom wrinkling moment also continues to increase proportionally to the inflation pressure and remains constant irrespective of boom skin thickness.

Table 4.7: Structural performance of a 0.4 m inflatable boom with variable thickness at high pressure.

Pressure (PSI)	Skins	M_w (Nm)	Average Rigidity (N/m)	Average radius (mm)
15	**1**	**25**	**833**	**53.5**
	2	28	1293	52.2
	3	29	2555	51.8
	4	29	2757	51.7
30	**2**	**49**	**1690**	**54.4**
	3	50	2445	53.0
	4	50	4486	52.5
45	**3**	**76**	**2502**	**54.4**
	4	76	3283	53.4

4.4.3 Non Uniform Thickness Investigation

Experimental testing of partially double skinned tubes allows trends from non-uniform boom thickness to be studied. The varying thickness booms were constructed as shown in Figure 4.8 with two equal layers on opposing sides covering half the boom surface area. The warp yarn was orientated in the hoop direction, to maximise the structural performance of the boom. The stitching between single and double skinned layers act as additional seams which may become present in future research. The partially double skinned booms investigate the nonlinearity that added seams in a boom will present and begins to explore structural performance gains by specifying the location of additional boom mass through varying the skin thickness around the boom circumference.

The results of the partially double skinned booms are tabulated in appendix II with the resulting moment-deflection graphs in Figure 4.12 and 4.13. The data shows the additional double skin in the vertical sense (illustrated in Figure 4.8) creates a more rigid boom over the horizontal sense for all boom lengths and tested pressures. The five repeat tests are within 5% of the average tip deflection values, making the change in these values between the two orientations significant. The maximum difference in bending moments is up to 5 Nm at 100 mm tip deflection with 15 PSI inflation pressure. This accounts for a 15% increase from the horizontal to vertical orientation. The effect of the horizontal orientation is greatly reduced as the double skin is closer to the neutral axis. In the vertical orientation, the bottom surface double skin would have little or no impact on the M_{fail} as it is under compression which fabrics cannot withstand. This would suggest placing additional skin mass on the top surface only, however this would increasingly affect the boom shape under pressure causing it to arch. Increasing the second moment of area by placing the second layer furthest from the neutral axis in tension maximises the added mass effectiveness and requires an equally stiff layer on the bottom surface to maintain the straight pressurised shape of the boom.

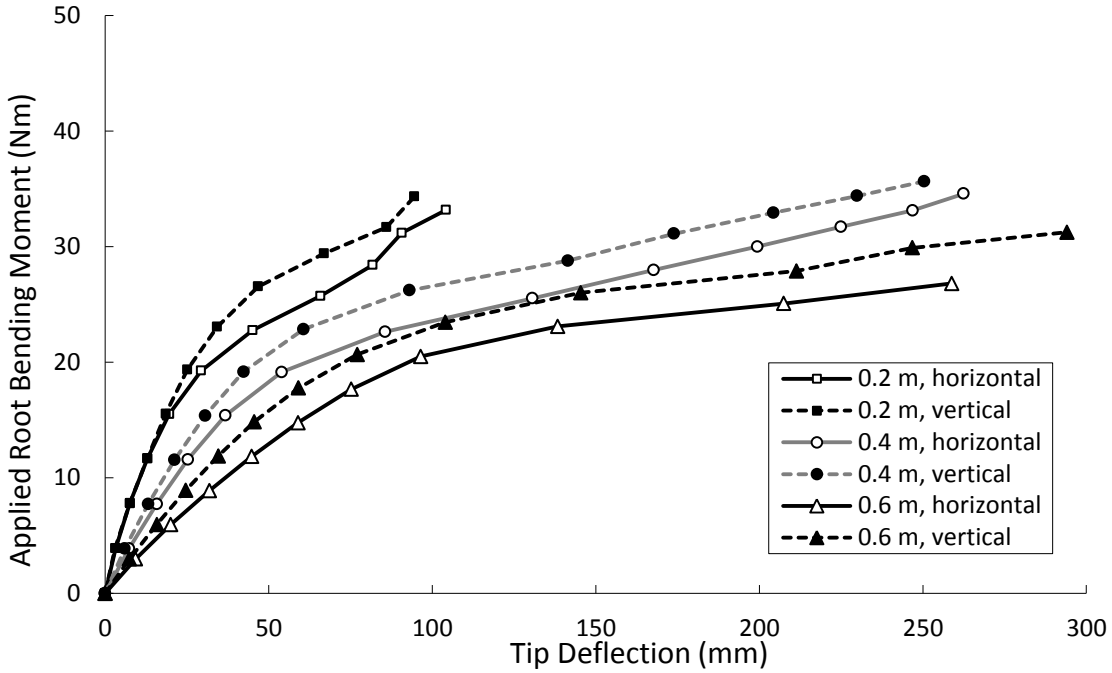

Figure 4.12: Averaged results of the non-uniform 1.5 skinned tubes at 10 PSI.

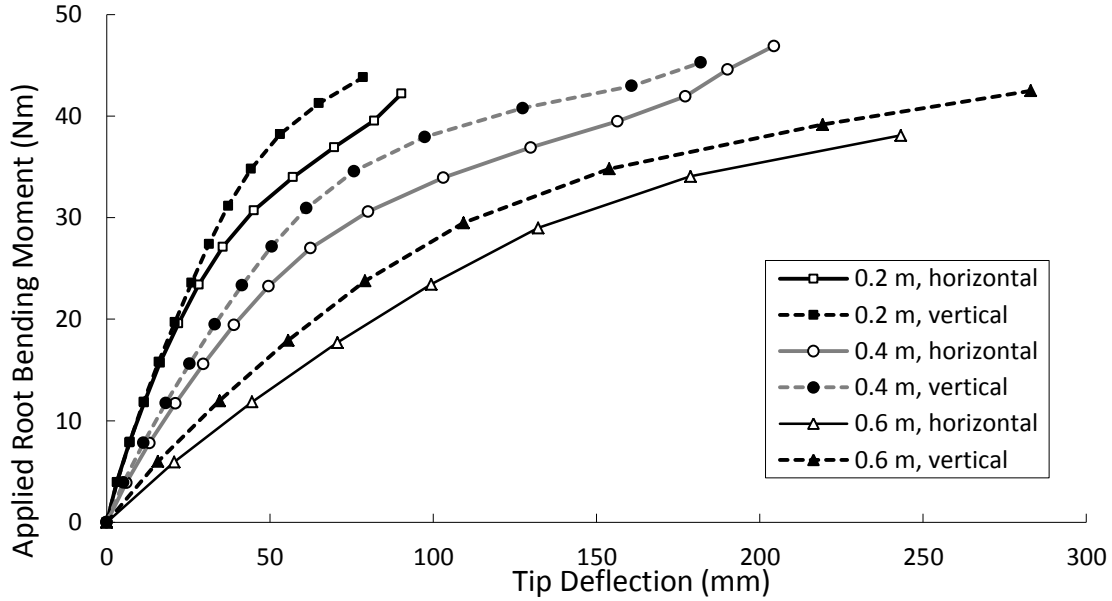

Figure 4.13: Averaged results of the non-uniform 1.5 skinned tubes at 15 PSI.

Similarly to previous multi thickness tests, the partially double layered boom rigidities remain constant over the two pressures tested with the range of results caused by the repeat tests. The 0.4 m long boom rigidity is compared to single and double skinned booms displayed in Table 4.8. Boom rigidity is proportional to skin thickness as shown in the previous section. It can therefore be expected that a uniform thickness of 1.5 skins (0.293 mm) would create a boom rigidity of 1146 ±87 N/m based upon the average single skin rigidity data. This is within

the variability range of the horizontal orientated 1.5 skinned boom showing no gain by placing additional skin mass in this location. However the data shows the partially double layered boom in the vertical orientation has the same performance as the double skinned boom and thereby saving 6% in additional mass for a small cost of the two additional manufacture procedures. As boom rigidity and peak moment are dependent on skin thickness and inflation pressure respectively the primary uniform skin would be sized for the required operating pressure (to achieve the specified M_{max}), with additional skin thickness placed in specific locations for the required boom rigidity whilst minimising added mass.

Table 4.8: Rigidity performance of a 0.4 m boom with nonlinear skin thickness.

Skins	Orientation	Average Rigidity (N/m)	Mass (g) (% increase of *)
1	-	764 ±58	135*
1.5	Horizontal	1231 ±100	143 (6%)
	Vertical	1456 ±120	143 (6%)
2	-	1380 ±87	151 (12%)

4.5 Summary

The experimental research on inflatable booms has shown the applied moment – tip deflection response of cantilever inflatable booms of various permutations including 8 pressurisation intervals up to 45 PSI, 5 boom lengths up to 1 m, and 4 skin thicknesses up to 0.780 mm totalling 234 individual tests. Preliminary studies identified key setup and procedural methods to account for boom deflection equilibrium and the increased rigidity from baseplate impingement. The fabric orientation study revealed that the warp yarns should be placed in the hoop direction of a boom to maximise performance through the operating pressure. The higher pressure tests were not able to achieve a constant M_{max} seen in the lower pressures of 2.5 and 5 PSI. The M_w data allowed an estimate of M_{max} to be calculated through Equations 2.8 and 2.9 and was verified through the lower pressures experimental results. Although this was limited in accuracy due to the discrete tip loading of the booms, M_w was shown to remain constant for all boom lengths and thicknesses. Boom rigidity is affected by skin thickness and boom length where the latter shows a non-dimensional tip deflection rigidity reduction as boom length is increased. Each boom shows a constant initial rigidity between inflation pressures.

The 0.4 m long inflatable booms were able to achieve an initial wrinkling moment of 25 Nm with a peak moment of 47 Nm before ending the test run at 15 PSI. The initial average rigidity before wrinkling was 833 N/m. Both these performance parameters are increased proportionally with inflation pressure and skin thickness respectively as shown in Table 4.7. The maximum bending moment applied was 100 Nm at 45 PSI using 3 and 4 nylon skins where testing was halted for safety reasons. The non-uniform skin thickness tests investigate partially double skin booms and show a 6% saving in mass is possible while maintaining the boom rigidity. These experimental inflatable boom results can be used for comparison against hybrid boom performance and also allow numerical models to be validated. An initial comparison to the Comer – Levy model showed that the peak moment is significantly affected by the radius change from inflation and must be considered in the analysis. The radius changed by a maximum of 10% at 15 PSI and results in an increase of 31% for the predicted M_{max} using Equation 2.9and confirmed with M_w observations.

Researchers within the field of inflatable structures are continually developing the accuracy of the numerical models[84-104]. The Comer – Levy model advanced by Main et al. (1994) focused on the nonlinear bending response from incipient wrinkling by considering the boom material response when in tension only. These models are typically applied to isotropic materials[85,86,96,99,101,103] and as such, when applied to fabric booms the significantly lower shear stiffness of the fabric needs to be considered. Braided and woven fabrics have been considered by Davids (2008) and Apedo (2010) respectively where their developed FEA models use modified Timoshenko beam elements to take into account nonlinear deformations after wrinkling. Davids (2007) also introduced additional work done by the inflation pressure caused by the change in volume of an inflatable boom under deformation from shear, bending and axial strain. This showed improved accuracy for booms under higher pressures exhibiting non-constant peak moments after wrinkling that has been observed in this study and also by Thomas and Weilgosz (2004). FEA offers an approach that can be usefully applied to highly nonlinear systems and easily adjusted for various permutations[103] making it ideal for comparison to the experimental results for both inflatable and hybrid structures. The ABAQUS FEA software is a robust nonlinear solver[95] and has been shown to successfully model both inflatable[103] and tape spring[108] systems individually and is therefore used in this research to create computational models of inflatable and hybrid booms.

Chapter 5

Finite Element Analysis of an Inflatable Boom

A FEA study of an inflatable boom was conducted to establish a base line computational model from which a hybrid boom model could be developed from and compared against. The inflatable boom FEA model was validated against the experimental structural performance tests in the previous chapter and was built and run using the COTS ABAQUS 6.9-3 software.

5.1 Background and Setup

When modelling the inflatable boom, several choices are required regarding assumptions and simplifications of the model. The major complexity is modelling the fabric accurately. This can be achieved at various levels of detail where the material can be modelled as a continuum[120,121], individual yarns[117,118,122] or to include yarn fibres[115,116]. For the latter two approaches the fabric is modelled as it is constructed which takes into account the weave type and includes the crimp length and angle as shown in Figure 5.1. The yarns are either assumed a continuum in themselves or detailed further where the fibres are studied to determine their material properties. The advantage of modelling the yarns is they can accurately account for the varying mechanisms that commonly occur in fabrics such as decrimping and yarn extension.

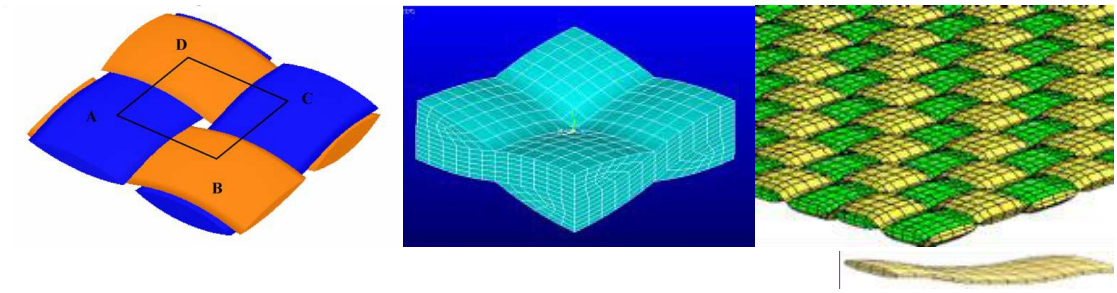

a) Repeat pattern of yarns b) Meshed geometric unit block c) Meshed yarns in a fabric

Figure 5.1: FEA modelling of a simply woven fabric using continuum yarns[122,124].

Research by Lin (2010) has developed the detailed modelling of fabrics by determining the differing yarn characteristics and their geometric properties including spacing between yarns within a unit block that can then be tessellated to create a woven cloth. Other factors such as nonlinear frictional effects and shear locking between the yarns significantly affect these fabric models and as such are under continued development. Another factor is the considerable computational cost to this approach where each yarn is modelled. A common and computationally efficient approach to model fabrics is to assume the material behaves as a continuum. This allows the physics of a fabric to be assumed constant throughout the material without concern for the specific behaviour of the yarns themselves. This is also done when measuring the fabric material properties as whole samples rather than as individual yarns. Fabrics are typically modelled as planar orthotropic materials due to their thickness and changing material properties between yarn orientations[91,95,103,120,123].

The current development of FEA models for inflatable booms tend to concentrate on the computationally efficient beam elements[90-95] adding complexity to account for nonlinear deflection response from initial wrinkling. Shell and membrane elements are significantly more accurate than beam elements[92] automatically capturing the geometric nonlinearities resulting in pressure stiffening. These elements are often used to validate updated complex models[90-92,95] providing a method which is ideal for an initial hybrid boom model when combining tape springs to the booms. For this research the FEA booms were constructed out of M3D4R membrane elements which describe the physics of a thin material which cannot support bending or compressive loads and have been previously used to model fabrics[132-134]. The Fibremax 94 material properties measured in chapter 3 were used for an orthotropic laminar material. This reduced the stiffness matrix by assuming normal stresses are zero leading to four in-plane constants; E_H, E_V, ν_{HL} and G_{HL}. The boom was constructed with the warp yarns placed in the hoop direction with the values given in Table 5.1 and the material orientation shown in Figure 5.2.

The shear modulus is calculated using Equation 3.1 from the tensile testing of the fabric in chapter 3. The literature also indicates other methods to estimate the shear modulus in FEA models including using the isotropic relationship $G = \frac{E}{2(1+\nu)}$ [115] and $G = 0.001E$ [123] where the value is iterated to match the experimental results[123]. The latter assumes fabrics are loosely woven together and therefore have negligible shear rigidity as the yarns slip past each other relatively freely except for small frictional effects. However as the Fibremax 94 fabric is

lightly impregnated with a stiffening resin matrix these two approaches significantly over and under estimate the shear modulus with respect to the value calculated using Equation 3.1. From the preliminary studies the tensile testing approach provides an appropriate starting value to fine tune the material properties for specific inflation pressures.

Table 5.1: Material properties for the FEA inflatable boom.

Abaqus boom and yarn direction material properties	Value
$E_H = E_w$	438 MPa
$E_L = E_f$	314 MPa
$v_{HL} = v_{wf}$	0.21
$G_{HL} = G_{wf}$	19 MPa
t	0.195 mm
ρ	588 kg/m^3

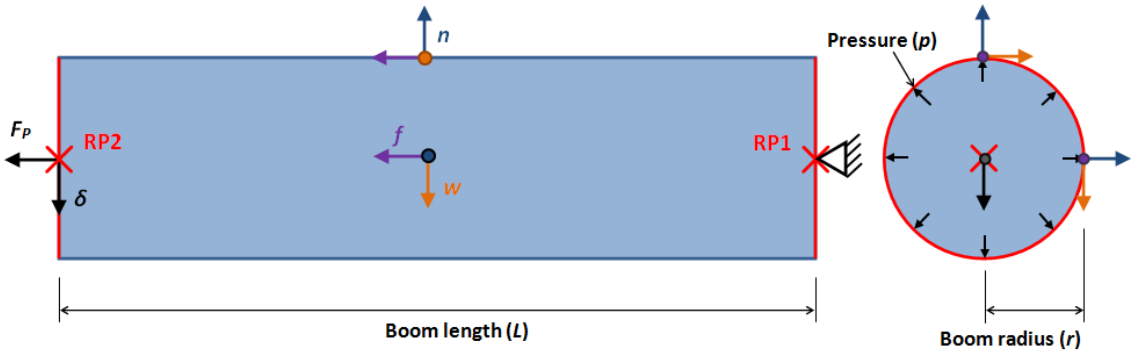

Figure 5.2: FEA inflatable boom model with material orientation.

The boom was modelled explicitly in three steps; initial boundary conditions, inflation and tip deflection. The dynamic explicit approach was chosen to give good convergence in modelling inflatable and hybrid booms particularly through buckling regions and large deflections where other methodologies become unstable and fail. Figure 5.2 displays the initial boundary conditions where the root and tip edges of the boom are rigidly tied to reference point (RP) 1 and RP2 respectively. This simulated the constraints from the inner and tip plates used in the experimental tests. RP1 was placed in ENCASTRE to keep the root fixed. During the inflation step the axial boom inflation was applied and acts on the internal surface off the boom shell elements. A longitudinal point load (F_p) is applied to RP2 to simulate the inflation pressure acting in the boom length. This is calculated using Equation 5.1 where this approach has been used in previous research[89,94,95]. The inflation step was applied as a linear pressure increase over the time step.

$$F_p = pr^2\pi. \quad \textbf{(Equation 5.1)}$$

The tip deflection step applies a displacement boundary condition to RP2 after the model has inflated the boom. The displacement was also applied linearly over the tip deflection time step resulting in a constant angular velocity at the boom tip with a total final displacement of 75% of the boom length. This was chosen instead of the applied tip load as it generates good convergence for explicit analysis with buckling models. Mesh convergence and time step studies were conducted to confirm the appropriate FEA model in preliminary studies while all simulations were run using double precision and full nodal setup.

5.2 Preliminary Studies

The preliminary studies consisted of mesh, time step and material property investigations where each parameter was adjusted in an iterative process to finalise the FEA inflatable boom model. All preliminary simulations were conducted on the standard experimental boom size of 50 mm radius and 0.4 m length. From the DIC tests on the inflatable booms in chapter 3 the nonlinear longitudinal and seam pull-out responses shown in Figures 3.19 and 3.21 resulted in an effective length shortening of 1% and radius increase of 4.5 x 10^{-3} mm/kPa. The initial model shown in Figure 5.3 had 63 regular square elements around the circumference of a 50.47 mm radius boom totalling 5040 for an initial 0.396 m long boom. The material properties of the nylon skin are given in Table 5.1, and the inflation and tip deflection time steps ran linearly across 1 s each.

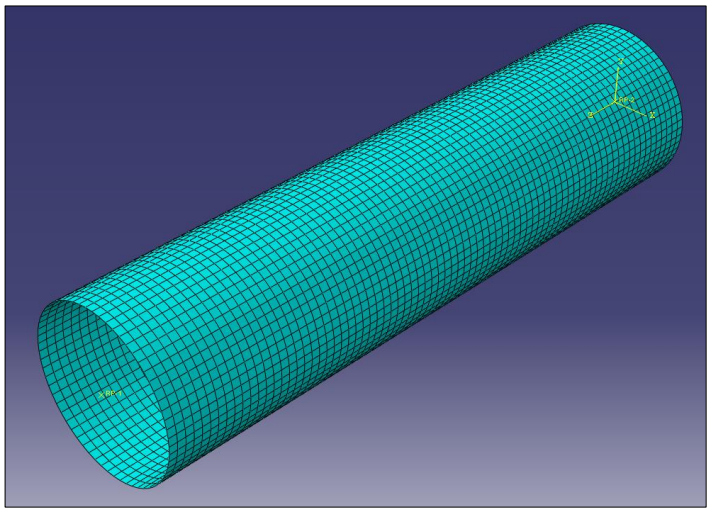

Figure 5.3: Initial FEA inflatable boom mesh totalling 5040 elements.

5.2.1 Time Step Study

The time step study confirmed the simulation stability over both the inflation and deflection of the inflatable boom. The moment-tip displacement response at the boom root for various tip deflection step times is displayed in Figure 5.4 for a standard boom at 15 PSI inflation. It clearly shows the model becomes increasingly unstable when taking the tip deflection time step greater than 1 s or less than 0.25 s. A similar assessment on the inflation time step analysing the boom radius revealed no change in the model between 0.05 and 20 s. Therefore the selected time steps were 0.5 s for both inflation and tip deflection. Tests were also conducted on finer and coarser meshes to ensure computation stability and showed negligible effect on the time step stability.

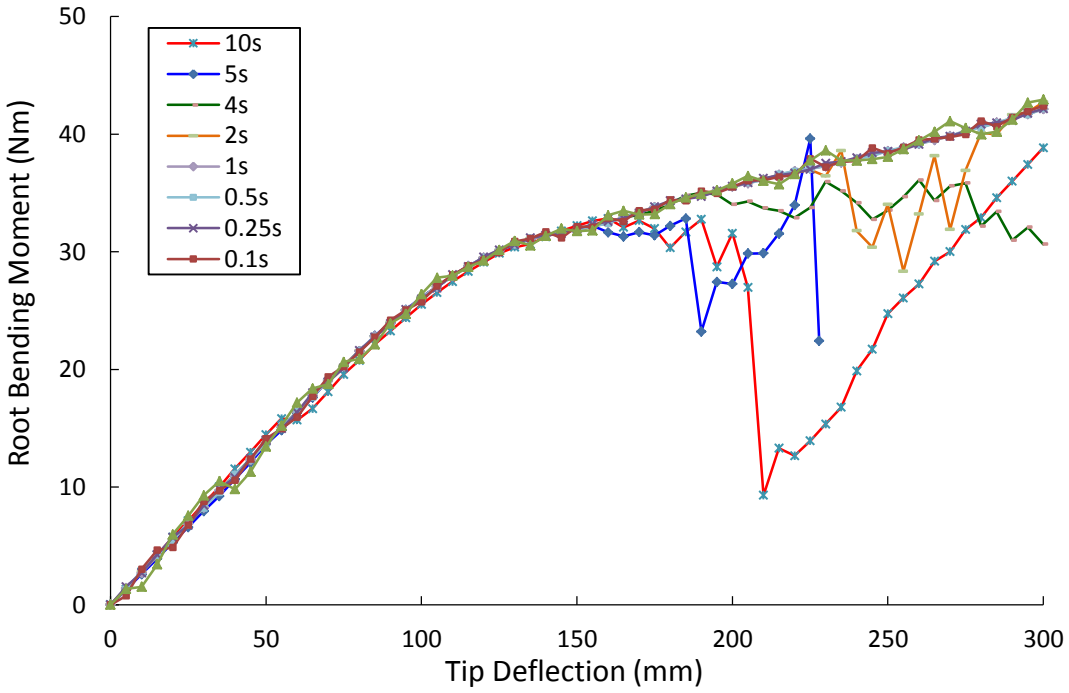

Figure 5.4: Inflatable boom tip deflection time step study.

5.2.2 Mesh Convergence Study

The mesh convergence study was completed on a 0.396 m long, 50.31 mm radius inflatable boom at 10 PSI to determine a suitable mesh density. Six meshes were selected as shown in Figure 5.5 which totalled 143, 320, 1280, 5040, 19782 and 80960 elements. This corresponds to 11, 16, 32, 63, 126, 253 elements around the circumference of the boom respectively.

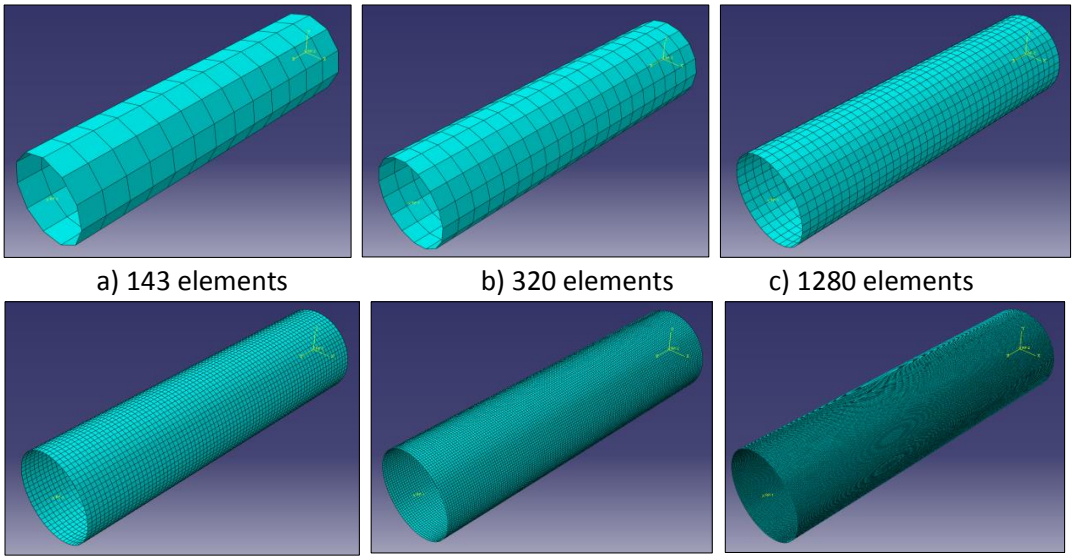

a) 143 elements b) 320 elements c) 1280 elements

d) 5040 elements e) 19782 element f) 80960 elements

Figure 5.5: 0.396 m inflatable boom with 6 mesh densities.

The tip deflection data from the six meshes is displayed in Figure 5.6 and shows three distinct regions that are affected by the mesh density; initial deflection, boom wrinkling, and loading to M_{max}. These occur between 0 – 60, 60 – 165, and 165 – 300 mm tip deflections respectively. Generally the boom stiffness decreases as the number of elements increases to progressively match the experimental average. However this stiffness divergence occurs from 15 Nm at the initial wrinkling point on the bottom surface of the boom. Prior to compression effects buckling elements the solution remains relatively constant for all mesh densities. When the boom wrinkles, due to bending, the courser elements present a greater change in area when buckling. The larger changes in areas therefore require a greater local force to act against the internal inflation pressure to cause the same tip deflection. This is illustrated in Figure 5.7 between 3 meshes with relative element sizes of 400, 100 and 25 mm^2 respectively. Figure 5.6 shows the boom wrinkling region increasingly matches the experimental average by increasing in mesh density with a significant improvement between meshes b) and c). The finest mesh using 80960 elements shows a negligible change in moment-deflection response of a maximum 0.6 Nm in comparison to mesh e) for a doubling in mesh density showing solution convergence.

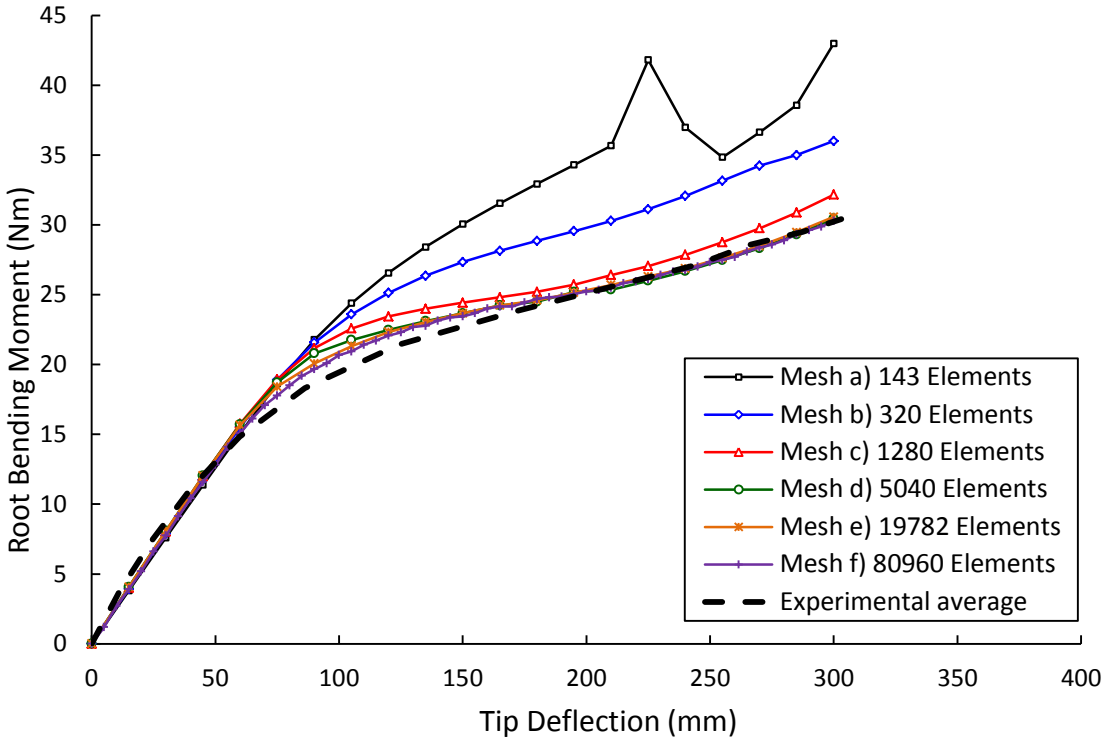

Figure 5.6: Mesh convergence study on a 0.396 m long, 50.31 mm radius, 10 PSI inflatable boom.

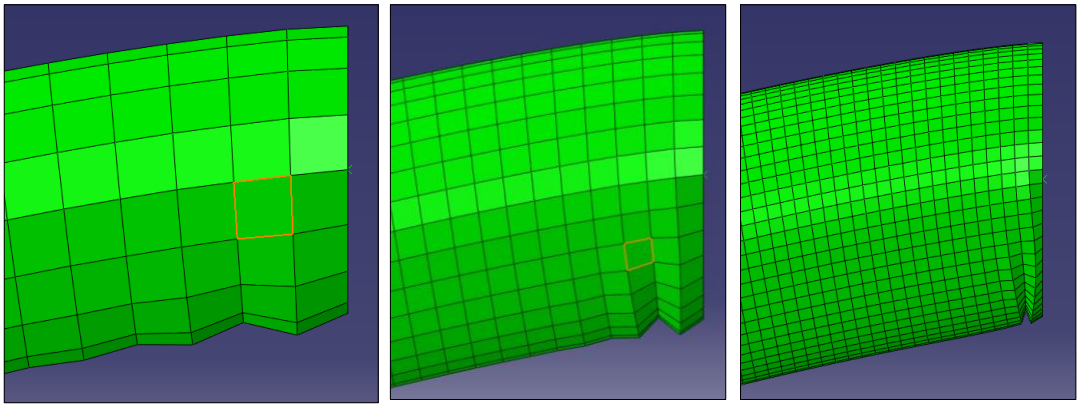

Mesh b) 23.6 Nm, Mesh c) 22.6 Nm, Mesh d) 21.8 Nm.

Figure 5.7: Root buckling at 105 mm tip deflection for 3 meshes.

The maximum bending moment is also reduced when using more elements as the finer meshes increasingly describe the volume changes with greater accuracy. For highly pressurised systems Davids (2009) has shown the deformation induced volume changes are significant and lead to an increasing loading capacity of the inflatable boom once wrinkling has occurred unlike the constant M_{max} at lower pressures. This is seen in Figure 5.6 for both experimental and FEA results. The mesh convergence study shows using 5040 elements with a size of 25 mm^2 is sufficient to accurately capture the moment-deflection response at these larger deflections from 135 mm. The finest mesh using 80960 elements shows a moment reduction of 0.3% at 300 mm tip deflection from mesh e). The experimental averaged data shows the

FEA model is in close approximation for the finest three meshes resulting in less than 1% difference from 180 mm tip deflection. This is increased to 6 and 18% for the 1280 and 320 element meshes respectively.

The greatest divergence between FEA and experimental is in the boom wrinkling section between 60 – 165 mm. This highlights the need for a sufficient number of elements in the mesh to accurately model the wrinkling behaviour of the boom. As the number of elements increases the boom wrinkling accuracy continues to improve. However, this has diminishing returns as larger element numbers correspond to increased computational expense. Figure 5.8 gives the mesh convergence with respect to the average boom rigidity across the wrinkling region and at 98 mm tip deflection where the rate of change in the boom stiffness is greatest. Figure 5.8 also plots the computation solution time for comparison. The rigidity data shows the solution converges from 63 elements around the circumference corresponding mesh d) and is within 6% of the finest mesh rigidity. The bending moment is within 1.1 Nm occurring at the wrinkling region midpoint of 98 mm tip deflection. Halving the element size to mesh e) shows limited improvement where the rigidity and maximum moment difference is within 5% and 0.6 Nm respectively for almost a fourfold increase in the number of elements and over 14 times the computational expense. Mesh d) using 5040 elements was selected for subsequent tests to minimise computational expense whilst reliably capturing the moment-deflection response with an accuracy within 6% of the finest mesh considered.

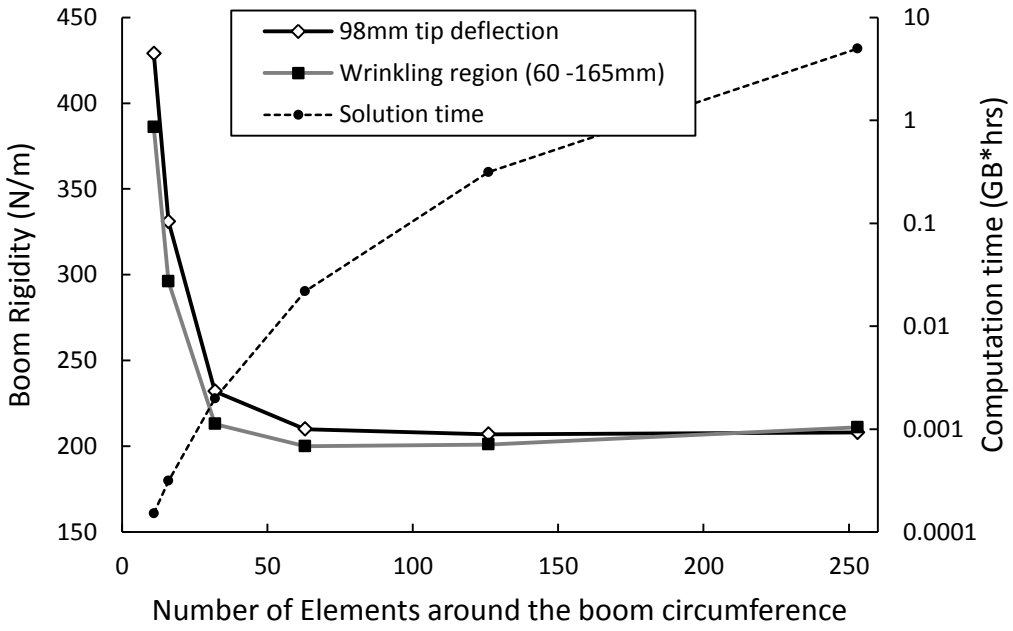

Figure 5.8: Boom rigidity convergence within the wrinkling region with computational time comparison.

The initial material properties selected from chapter 3 have shown a good correlation between experimental and the FEA model at 10 PSI. The most significant difference in results is the boom rigidity when the fabric wrinkles and is shown to approach the experimental tip deflection response as element size is reduced. Another difference is in the pre wrinkling deflection stage of up to 15 Nm. At this stage the FEA deflects linearly unlike the experimental result which shows a constant yielding of the booms stiffness and highlights the fabrics nonlinearity. The averaged stiffness of the FEA and experimental booms is 666 and 740 ±17 N/m respectively showing the linear continuum orthotropic model gives a good approximation using the experimentally determined material properties. Detailed consideration of the material properties used in the FEA model is investigated in the following section. Subsequent simulations have a mesh of 5040 elements unless otherwise stated.

5.2.3 Material Property Study

The tensile testing in chapter 3 measured the material properties of the Fibremax 94 fabric that are required as inputs to the FEA model. However it was found that the fabric is nonlinear and behaves differently between uniaxial and biaxial tensile applications. As the values for the material properties using both uniaxial and biaxial methods are not conclusive for an inflatable boom a material property study was conducted to assess the error range in the FEA model. Furthermore it is common practice to fine tune a model that best represents the experimental response for a woven material that shows high levels of nonlinearity when modelled as a continuum[123]. Further details are given in chapter 3 for the measurement and calculation of the Fibremax 94 material properties. The material property study considered the Young's modulus, Poisson's ratio, shear modulus, thickness and density parameters.

The Young's modulus was calculated using Equation 3.8 where E_{Bw} and v_{wf} were measured using biaxial and uniaxial tensile tests respectively. The uncertainty of using v_{wf} in a biaxial application gives a range of up to 8% in the Young's Modulus given in Table 3.3. The first investigation considered a varying Young's modulus while keeping the orthotropic warp to fill ratio constant at 1:0.72. For clarity a condensed set of key results are plotted in Figure 5.9 where all other parameters remain the same.

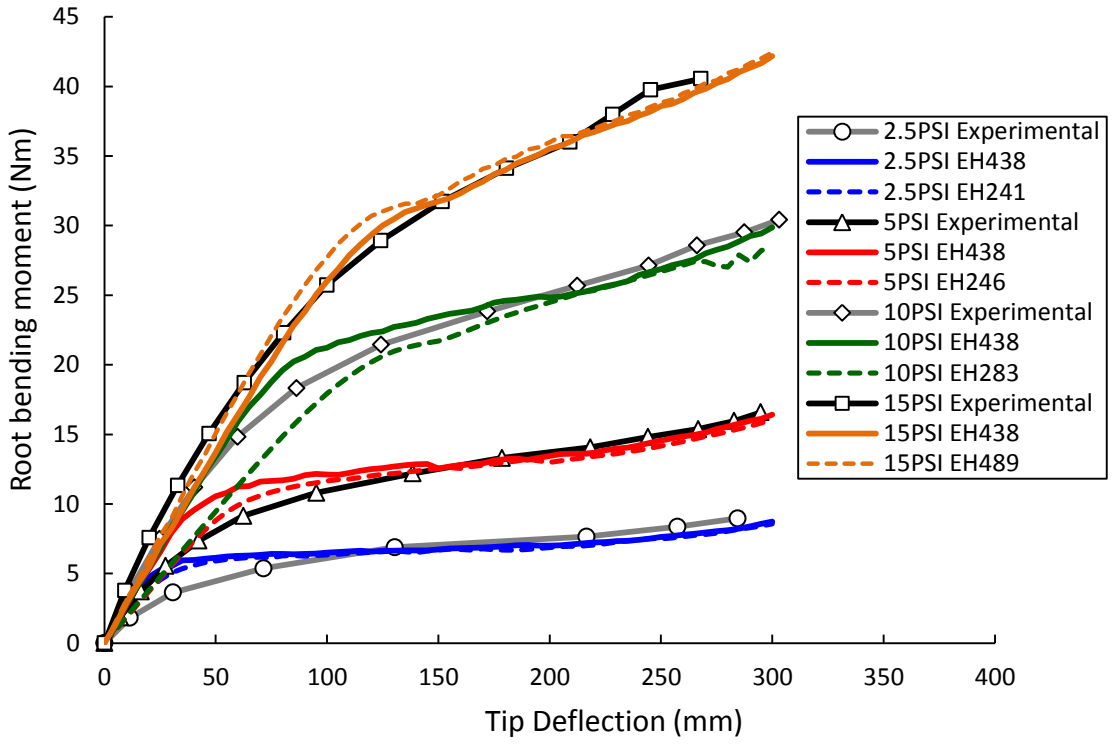

Figure 5.9: Variable Young's modulus study with a constant orthotropic ratio of 1:0.72.

Figure 5.9 shows that inflation pressure determines the accuracy of the initial FEA model with respect to the experimental data based upon the material properties measured in chapter 3. These are given in Table 5.1 and plotted as EH438. The higher pressures of 10 and 15 PSI show relatively good correlation against the experimental results. The FEA gives a constant initial stiffness of 666 N/m whereas the experimental results have a yielding initial stiffness prior to wrinkling confirming the nonlinear material properties of the fabric. Biaxial tensile testing in Figure 3.21 shows that the elastic modulus is not constant for pressures below 8 PSI suggesting a variable Young's modulus dependant on the inflation pressure. This resulted in the FEA model significantly overestimating the boom rigidity for pressures less than 10 PSI. Altering the Young's modulus has shown to be proportional to the initial stiffness displayed in Figure 5.9. However at 2.5 PSI the significant drop in modulus of 55% from E_H = 438 to 241 MPa shows little benefit to improving the moment-deflection response. Therefore other material property parameters are considered to optimise the FEA model for various inflation pressures. The yielding stiffness of the boom for all inflation pressures may be caused by the shear modulus not being constant during boom bending. This is supported by the tensile tests data of uniaxial and biaxial results which show nonlinear responses in Figure 3.14 and 3.20.

The shear modulus was varied for specific pressures with the key results shown in Figure 5.10. The data shows the shear modulus is proportional to both the initial stiffness and 'through the

buckling region' stiffness where a 5 MPa shear modulus for the 2.5 PSI inflation pressure gives a significantly improved correlation to the experimental result. The remaining difference in boom stiffness between the FEA and experimental result at this pressure is between 30 and 70 mm tip deflection and is likely to be a combination between insufficient experimental data points and the FEA mesh density. The altered shear modulus was determined for specific inflation pressures by matching the average initial stiffness of the experimental boom prior to wrinkling. This led to the relationship $G = 280p$ and provides a significant improvement to the FEA model against the experimental data. Furthermore research by Turner et al. (2008) also showed experimentally varying material properties with respect to pressure while remaining approximately constant at each pressure interval. This was demonstrated on a woven polyester fabric inflatable boom using the torsional test displayed in Figure 3.5 a) with the results implemented by Davids (2009). Davids (2009) also confirms neglecting the shear stiffness can lead to significant overestimation of the structural performance of an inflatable structure similarly to the initial material input results seen in Figure 5.9. The updated FEA model is within the experimental data range where tip deflections vary by up to 5% and also show that the boom does not reach a constant M_{max}. This validates the model and shows it accurately captures the deformation induced volume changes that cause the non-constant M_{max}.

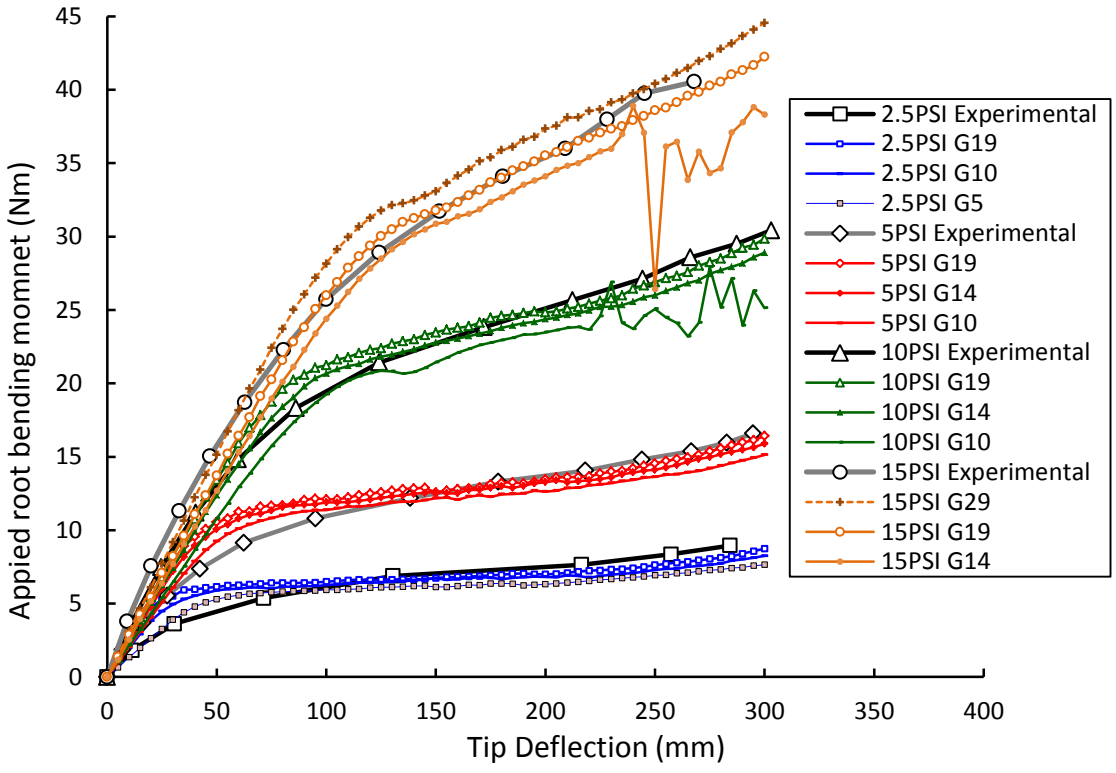

Figure 5.10: Variable shear modulus tip deflection tests.

Another characteristic of reducing shear modulus results in the model stability being reduced. It was found that the current model could not converge on a solution when $G < 140p$ in the pressure range of 2.5 to 15 PSI. This problem is considered in further detail by Diehl et al. (2003) where the low shear stiffness of fabrics presents numerical instability after small strains. Consequently the mesh zig-zags as shown in Figure 5.11 and has a similar appearance to hour glassing. However this also occurs for triangular S3R elements[123] and is a particular problem for low shear modulus materials such as unimpregnated fabrics. Several alternative approaches have been successfully developed to overcome this problem[123] and typically increase the shear modulus to a value which prevents this instability. In this study the lightly impregnated Fibremax 94 fabric inflatable boom remains stable under the considered inflation pressures where the shear modulus is successfully adjusted to optimise the tip deflection with the experimental data. Model stability was also reduced with Young's Modulus reduction and pressure increases that are seen in Figures 5.9 and 5.10 but remain stable within the tested pressure range and material properties selected.

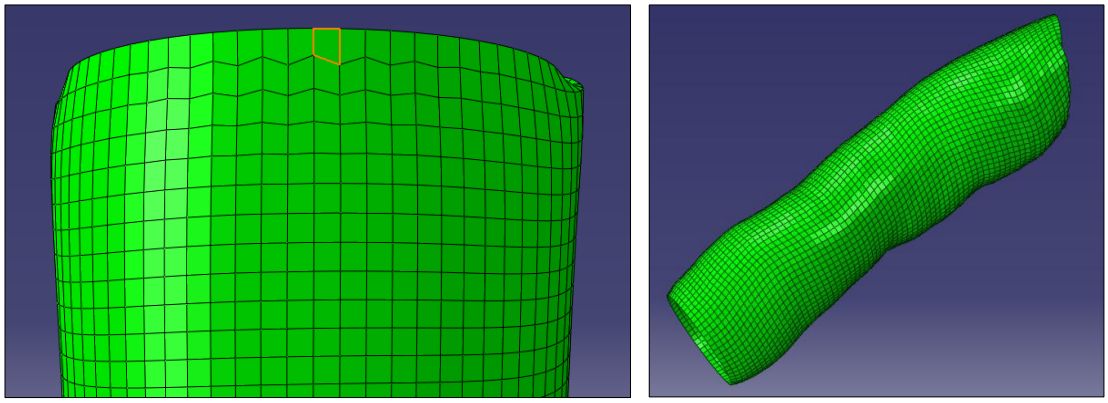

a) 235 mm tip deflection b) 245 mm tip deflection

Figure 5.11: Onset of element distortion at a) the top of the boom root due to low in-plane shear stiffness resulting in b) numerical instabilities along the boom length under increased load (15 PSI using *G*=14 MPa).

The Poisson's ratio, thickness and density error of the material was also considered and presented little effect on structural properties of the boom. The error values were taken from Table 3.3 and calculated in the material properties study. Table 5.2 displays the change in structural performance for the standard 0.4 m long boom which shows a combined maximum error of 1.3%. The material properties study in chapter 3 demonstrated the Poisson's ratio of the fabric could vary significantly. Two additional tests considered 0.0 and 0.5 Poisson's ratio inputs displaying a maximum combined error within 3% if the measured uniaxial Poisson's ratio is incorrect for biaxial inflatable boom systems.

Table 5.2: Inflatable boom structural performance variation from material property error ranges.

Parameter	Input Value	Pressure	Initial stiffness		Bending Moment at 300 mm	
		(PSI)	(N/m)	% change	(Nm)	% change
Thickness	0.195	2.5	668 ±3	0.45	8.67 ±0.04	0.46
	±0.001 mm	5	664 ±3	0.45	16.41 ±0.08	0.49
		10	666 ±4	0.53	29.90 ±0.03	0.10
		15	675 ±4	0.52	42.14 ±0.08	0.19
Density	588	2.5	668 ±4	0.59	8.67 ±0.01	0.12
	±11 kg/m^3	5	664 ±1	0.15	16.41 ±0.02	0.12
		10	666 ±1	0.15	29.90 ±0.07	0.23
		15	675 ±1	0.15	42.14 ±0.04	0.10
Poisson's	0.21	2.5	668 ±1	0.15	8.67 ±0.06	0.69
ratio	±0.02	5	664 ±1	0.15	16.41 ±0.01	0.06
		10	666 ±1	0.15	29.90 ±0.01	0.03
		15	675 ±2	0.30	42.14 ±0.01	0.02
	0.5	2.5	680	1.80	8.61	0.69
	0.0	2.5	665	0.45	8.77	1.15

The FEA material property study has established that the calculated material properties from chapter 3 give a good initial starting point to model an inflatable boom. Altering the Young's modulus gives limited effect on the initial boom rigidity and the material properties determined in chapter 3 suggest the values are constant. Varying the shear modulus gives greater variability in the boom rigidity and alongside the experimental inflatable boom results suggest it is not constant and significantly dependant on the inflation pressure. The yielding stiffness of the boom highlights the nonlinearity of the fabric which is a limitation of the linear FEA model. However with simple adjustment of the shear modulus gives a good approximation of the moment-deflection response using the relationship $G = 280p$. This shear modulus relationship is applied to all subsequent numerical analysis.

The close correlation between experimental data and the FEA model is reduced once wrinkling occurs. The region of inaccuracy is typically between 50 – 75% of the bending moment at 300 mm tip deflection. However the mesh convergence study has shown as mesh density increases the correlation between experimental and a FEA result improves significantly. A mesh using 5040 elements is selected for subsequent tests due to computational cost which is likely to increase significantly when developing this model into a hybrid boom. The simplified model otherwise accurately predicts the structural performance of inflatable booms using the assumed linear material properties approach with results that are within the experimental variability.

From these preliminary studies a suitable inflatable boom model has been developed against the experimental tip deflection data. To further validate the FEA model comparative studies are conducted against other experimental results. The FEA model used for this research is given in Table 5.3 where r_0 is the initial radius prior to inflation.

Table 5.3: Key parameters of a 0.4 m inflatable boom for FEA.

Parameter	Value
Element type	M3D4R
Element number	63 around the circumference
Radius	$r = r_0 + \frac{4.5\times10^{-6}}{p}$
Constraints	ENCASTRE rigid root
	Rigid tip
Loads	Internal pressure, p
	Tip force, $F_p = \pi r^2 p$
Length	99% of Experimental *L*
$E_H = E_w$	438 MPa
$E_L = E_f$	314 MPa
$v_{HL} = v_{wf}$	0.21
$G_{HL} = G_{wf}$	*280p*
t	0.195 mm
ρ	588 kg/m^3

5.3 FEA Inflatable Boom Results

The preliminary studies have developed and validated a FEA model against the 0.4 m long, 0.05 m radius boom under 4 inflation pressures. To confirm the trends found in the experimental inflatable booms in chapter 4 further FEA studies are undertaken. This also further verifies the FEA model over a wider range of designs including boom length, skin thickness and increased maximum operating pressures.

5.3.1 Fabric Orientation

A comparison between the two fabric orientations in the FEA model is given in Figure 5.12 for 0.4 m long booms. It shows that the structural performance is increased when placing the fill yarns in the boom hoop direction. This is the same trend observed in the experimental tests where increasing the pressure shows an increase in the performance advantage also displayed in Figures 4.3 and 4.4. The FEA model reveals the rigidity performance increase is 21 and 27%

for 10 and 15 PSI inflation pressures respectively. The experimental data shows a lower rigidity advantage of 5 and 19% for the same respective inflation pressures. The difference in results can be attributed to both experimental and FEA model inaccuracies previously discussed including the material properties, mesh density, boom manufacture tolerances and model simplifications. The consistent FEA model between yarn orientations shows a maximum increase of 4.5 Nm in the bending moment capacity occurring at M_w with 70 mm tip deflection for a 15 PSI pressurised boom. This is similar to the experimental data where the sustained bending moments at 200 mm showed a 5% and 6% increase for FEA and experimental data respectively. The moment performance gain remains below the significant 24% loss from the restricted operating pressure when placing the fill yarns in the boom hoop direction. This confirms the experimental conclusion where the warp yarns should be placed in the boom hoop direction to maximise operation pressure. However the results do suggest that any additional skin thickness to increase boom rigidity should be applied in the longitudinal direction of the boom.

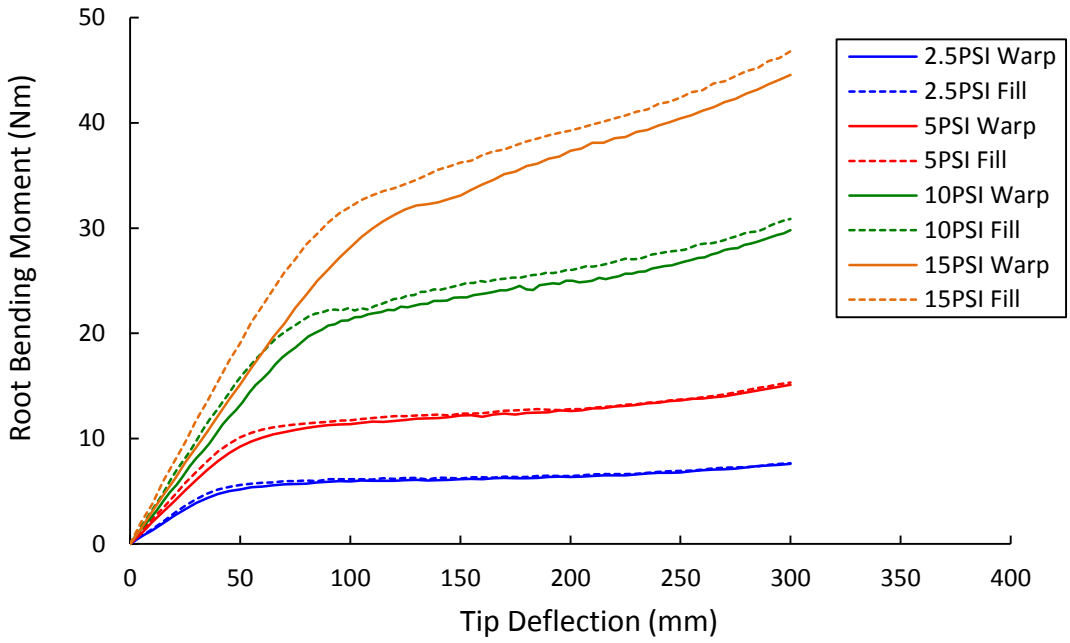

Figure 5.12: FEA of the fabric orientation moment-deflection response with specific yarns placed in the boom hoop direction.

5.3.2 Fabric Thickness

The varying boom thickness studies the same permutations in chapter 4. Four sizes were considered of 0.195, 0.390, 0.585 and 0.780 mm thick fabric booms and inflated between 2.5 and 45 PSI. Each thickness represents an additional boom skin as was conducted in the

experimental campaign, maintaining a constant warp yarn orientation in the boom hoop direction. Unlike the experimental multi skinned booms the FEA model assumed a simple increase of fabric thickness in a single layer which does not take into account the unconstrained layers found in the experimental setup. Table 5.4 gives the structural performance summary of the various thicknesses at the maximum operating pressures where M_{200} is the required bending moment to achieve a 200 mm tip deflection. The remaining boom permutations are presented in appendix III. The FEA data shows regular linear increases in boom performance with an increase in shell thickness. The initial rigidity prior to wrinkling displays a directly proportional increase with thickness with all data within 4% of this trend. The booms bending moment loading capacity also show this trend with respect to inflation pressure as concluded by the experimental results in the previous chapter. The fabric thickness also affects the loading capacity of the booms at large deflections. Taking the achieved bending moment values at 200 mm tip deflections shows an increase of up to 4 Nm when increasing the skin thickness up to 0.780 mm.

Table 5.4: Structural performance of multi-skinned booms at peak operating pressure.

Pressure (PSI)	Thickness (mm)	FEA initial rigidity (N/m)	Percentage of experimental averaged initial rigidity	FEA M_w (Nm)	Percentage of experimental averaged M_w	FEA at M_{200} (Nm)	Percentage of experimental average at M_{200}
15	0.195	739	89%	21	84%	37	93%
	0.390	1508	117%	24	86%	40	105%
	0.585	2263	89%	26	90%	40	89%
	0.780	3012	109%	28	97%	41	91%
30	0.390	1691	101%	45	92%	80	110%
	0.585	2603	106%	47	94%	80	101%
	0.780	3510	78%	49	98%	83	95%
45	0.585	2844	114%	75	99%	118	-
	0.780	3879	118%	76	100%	122	-

The majority of the FEA data is within 10% of the experimental average exhibiting particularly close correlation at M_{200}. The results show the experimental data consistently over predicts the wrinkling moment and is a consequence of the discrete loading intervals producing reliable but inaccurate incipient wrinkling observations. The greatest variance in results between experimental and FEA is the initial rigidity. Figure 5.13 gives further detail showing the moment-deflection response for a 0.390 mm thick FEA boom in comparison to the experimental double skinned boom. It shows the accuracy of the model is within 5% for pressures up to 10 PSI and is consistent for all boom thicknesses considered. The FEA model

increases the boom stiffness with pressure due to the increase in shear modulus previously defined by $G = 280p$. This relationship begins to fail for pressures greater than 15 PSI demonstrated by Figure 5.13 where the FEA model increasingly overestimates boom performance from this pressure. This may be caused by the interaction between skin layers in shear that is dependent on both inflation pressure and the total skin thickness. Running the FEA model with an adjusted empirical relationship of $G = 3.7 \times 10^5 pt$ gives both rigidity and bending moment performances within 15% for pressures greater than 10 PSI. This highlights the need to validate the boom with experimental results and tailoring the FEA material properties with the expected deformation due to the nonlinear properties of the fabric boom. A similar overestimation in model moment-deflection response at higher pressures is seen in previous research[92,93] and also confirms the material properties are significantly affected by inflation pressure[135]. However a universal shear modulus relationship was not developed as the hybrid boom inflation pressures are restricted to 15 PSI where the current FEA model provides sufficient accuracy.

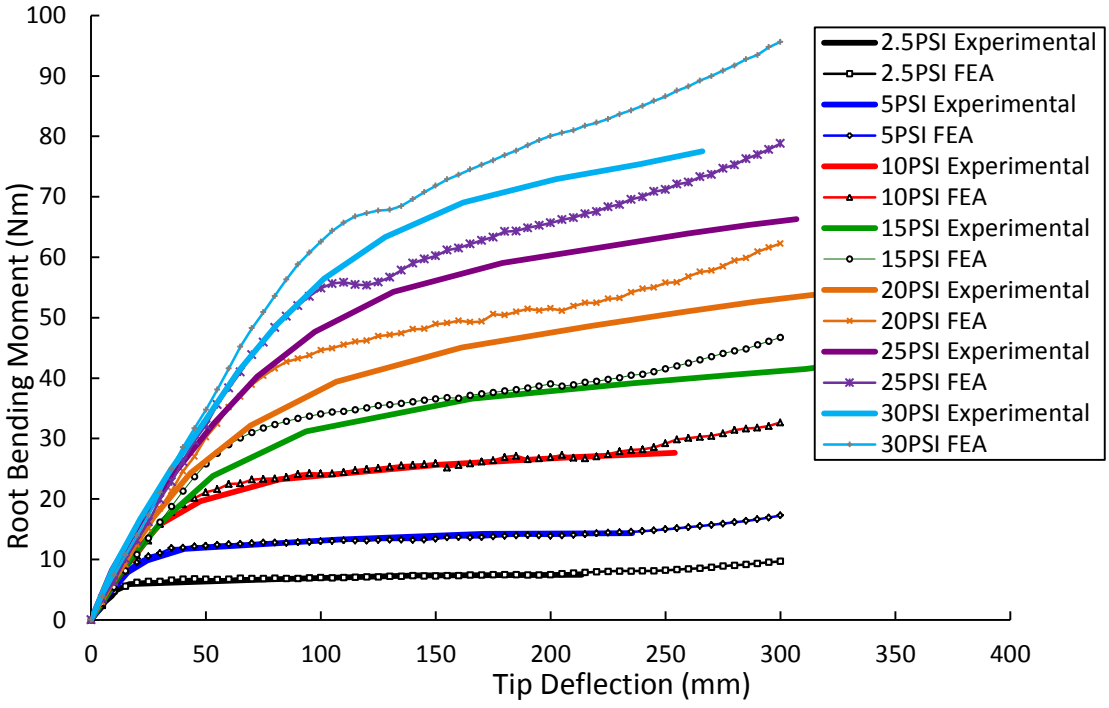

Figure 5.13: Tip deflection data of a 0.396 m double skinned boom.

A final difference between the FEA model and the experimental result is the overestimation of M_{max}. This occurs from 200 mm tip deflections in the FEA model that increases in magnitude with inflation pressure. The stiffening effect observed in the FEA model is caused by the additional work done by the inflation pressure produced by the deformation induced volume changes. Also accountable for the non-constant bending moments after boom wrinkling when

at higher inflation pressures, the volume changes become increasingly large when the wrinkles coalesce and impinge at the boom root. This shows a limitation of the model at large deflections and is caused by a physical inaccuracy around the boom root from 200 mm tip deflection shown in Figure 5.14. Although similar to the large experimental boom deflections shown in Figure 5.15 a refined FEA model should simulate the rigid inner plate to prevent this considerable volume reduction. The experimental booms allowed the fabric to wrap around the inner plate for large deflections whilst remaining inflated and therefore resulting in a less significant volume reduction. The FEA model was not developed further to consider this as the structures are too soft and unsuitable for applications once incipient wrinkling arises, which occurs prior to this stiffening effect in all the tested pressures. Hybrid booms will also have likely failed through tape spring buckling prior to these large deflections.

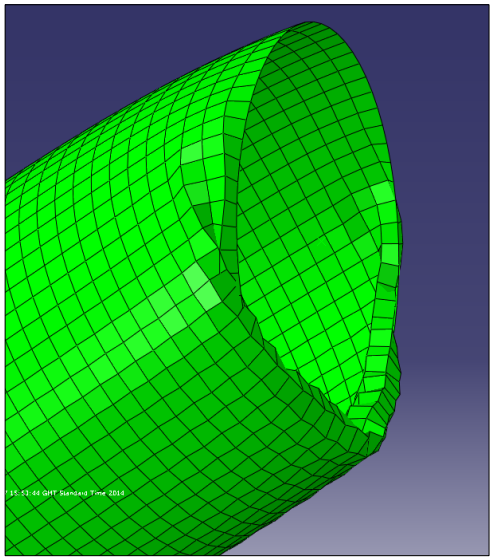

Figure 5.14: 15 PSI FEA boom root at 205 mm tip deflection.

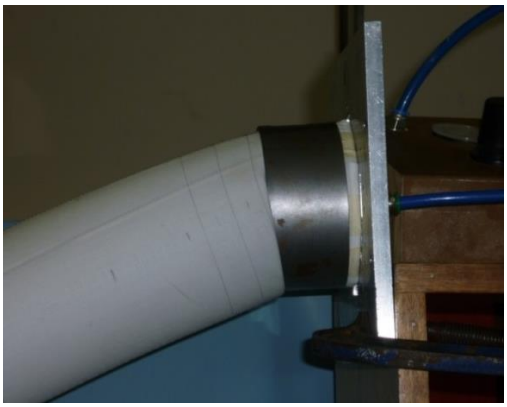

Figure 5.15: 20 PSI Experimental 0.4 m boom at 232 mm tip deflection.

To confirm the single skinned FEA model is applicable to the multi-skinned experimental data a further multi-skinned analysis was conducted to model the experimental setup with greater

accuracy. Multiple layers where added to the model with the root and tip constrained similarly to a single skinned boom and inflation applied to the inner most skin. A simple surface to surface hard contact was applied between skins which were offset by 0.390 mm radius increases. The multi-skinned model is shown in Figure 5.16 where the radiuses are altered to give clarity. These models significantly increase computational expense by up to 6 times and showed no difference in the results as shown in Figure 5.17. This additional model did not include any frictional effects between the layered skins. This would need to be considered in further detailed analysis to confirm the variability attributed to the experimental results but is outside the scope of this research. The experimental and FEA boom thickness studies were conducted to confirm the structural performance gain by increasing a single skin thickness whilst maintaining the remaining material properties at a constant.

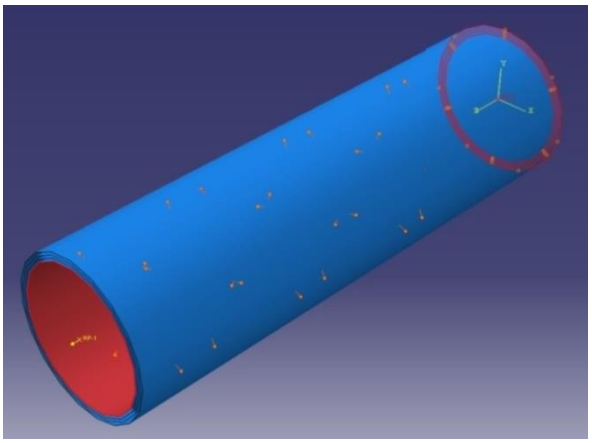

Figure 5.16: Overlapping skin FEA model with oversized radiuses (not to scale).

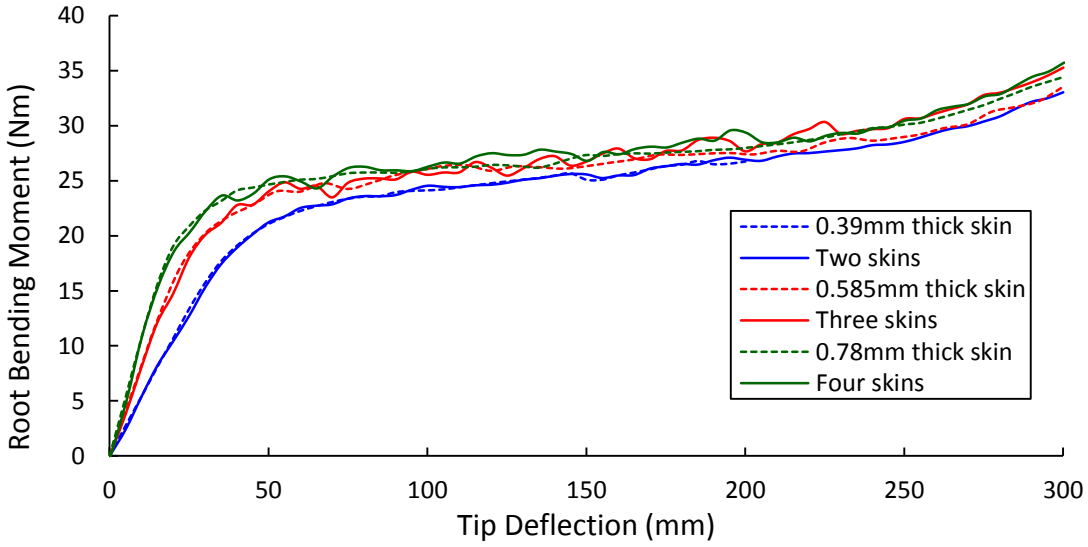

Figure 5.17: Tip deflection comparison between multi-skinned and varying skin thickness FEA models.

5.3.3 Boom Length

To confirm the boom length trends observed in chapter 4 a similar study was conducted with the FEA model. The study also allowed the model to be applicable to a variety of boom lengths for future design analysis and considered 0.2, 0.4, 0.6, 0.8, and 1.0 m booms inflated at 10 PSI. Figure 5.18 displays the tip deflection data for FEA and experimental results and shows a reasonable correlation between data sets. The FEA model predicts a similar initial stiffness when considering the average experimental rigidity prior to wrinkling. However the biggest problem with increasing the boom length for FEA is the significant increase in computational expense required to maintain the same element density. The 0.8 and 1.0 m FEA booms are also limited in accuracy shown by the poor numerical stability in the normally meshed 1.0 m boom model. Model stability is increased with an increase in element size from 25 to 49 mm^2 causing a trade-off against the moment-deflection response accuracy shown with the course meshed models in Figure 5.18. An alternative is to increase the time step which is applied relatively successfully to the normal 25 mm^2 meshed 0.6 m boom with an increase from 0.5 to 10 s. However this significantly increases the computational expense by over 2 times for 0.6 and 1.0 m booms. The 1.0 m boom required a 60 s tip deflection time step to become relatively stable using 49 mm^2 elements resulting in an increased computational expense of over 7 times but an inaccurate solution. To achieve an accurate solution at 1.0 m the FEA model would require a time step estimated at 120 s with an element size of 25 mm^2 for a huge computational expense. In comparison to the refined 0.4 m the 1.0 m boom with the same mesh density and a 10 s time step is over 18 times more computationally expensive.

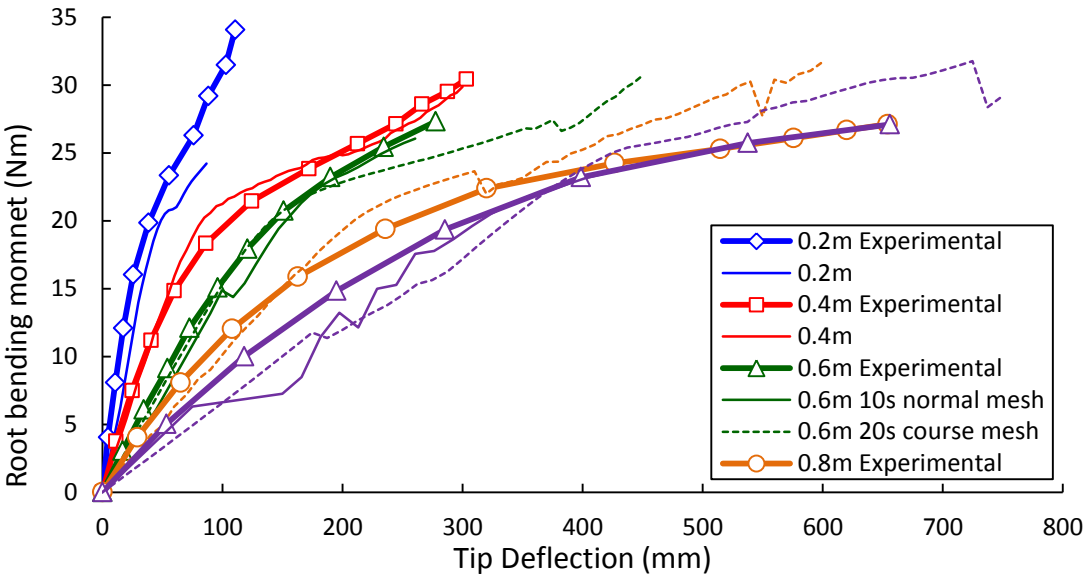

Figure 5.18: Tip deflections for various boom lengths at 10 PSI inflation.

As the 0.6 m FEA model shows it is possible to maintain an accurate correlation to the experimental data and the remaining boom lengths show similar trends to the refined 0.4 m boom it is assumed that the FEA model is suitable for various boom lengths when a suitable mesh density and tip deflection time step are selected. The 0.4 m long boom is selected for comparison between inflatable and hybrid boom permutations due to the significant computational expense for longer booms.

5.3.4 Compression Effects

The compressional effects were considered because a possible application for inflatable and hybrid booms is to create a solar sail or drag augmentation deorbiting device by suspending in tension a membrane as shown in Figure 5.19. It is therefore important to assess the potential impact on the inflatable boom structural performance due to membrane tension acting on the booms which is typically 20 N[7,14]. The FEA model is a convenient tool to investigate this effect and other future permutations at negligible cost in comparison to an experimental study where additional setup rigs would be required.

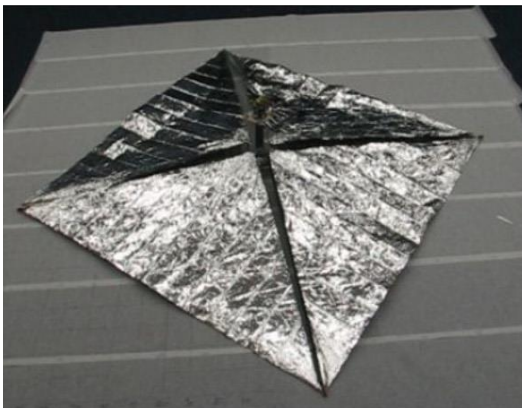

Figure 5.19: Cubesail[27].

The study considered a standard 0.4 m long, 0.05 m radius boom inflated to 2.5, 5, 10 and 15 PSI with the remaining FEA model characterised in Table 5.3. For each inflation pressure an increasing tip compression was applied up to 100 N prior to bending altering Equation 5.1 to

$$\boldsymbol{F_p = pr^2\pi - F_c}\,, \qquad \textbf{(Equation 5.2)}$$

where F_c is positive for a compression force in the longitudinal boom direction. A selection of tip deflection responses are given in Figure 5.20 and shows boom compression reduces M_{max}.

This is an effective pressure reduction that has also been observed by Davids and Zhang (2008) who also presented a proportional pressure increasing effect when additional tensioning was applied to the boom length. Equating $F_c = \frac{F_p}{2}$ for 5 and 10 PSI shows a moment-deflection response almost identical to a pressure reduction of a half. The small differences can be attributed to the different volume changes caused by the axial strain and the change in shear modulus as a material input. Experimental testing is required to establish if the compression force alters the shear modulus of the boom which could have a significant impact on the rigidity of the boom under compression, however this is likely to be minimal for nominal 20 N compressions.

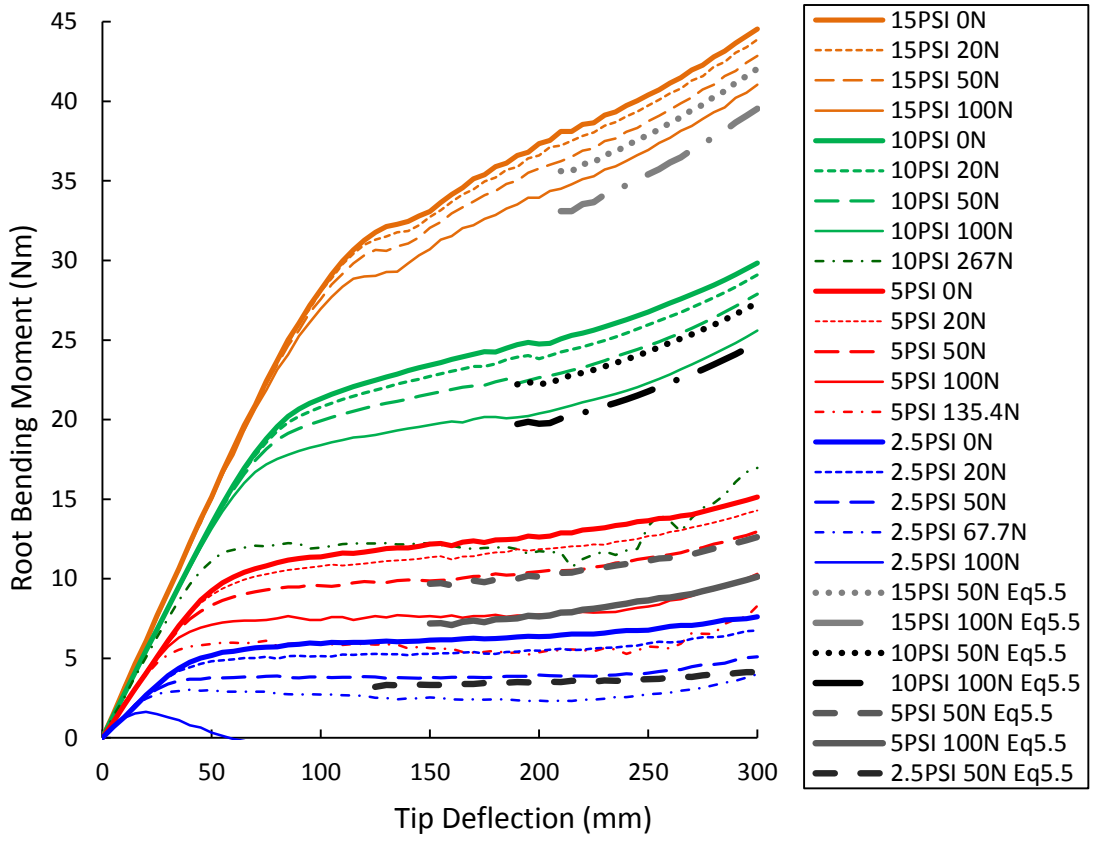

Figure 5.20: Tip deflections for a 0.396 m boom under compression.

Equating the failure moment predicted by Comer and Levy (1963) in Equation 2.9 to the axial pressure force of Equation 5.1,

$$M_{fail} = pr^3\pi,$$

$$M_{fail} = pr^2\pi \cdot r,$$

$$\boldsymbol{M_{fail} = F_p r}. \qquad \textbf{(Equation 5.3)}$$

When taking any compression effects into account alters Equation 5.3 to

$$M_{fail} = (pr^2\pi - F_c)r,$$

or alternatively written

$$\boldsymbol{M_{fail} = M^0_{fail} - F_c r,} \quad \textbf{(Equation 5.4)}$$

where M^0_{fail} is the failure bending moment when there is no compression acting on the boom. Although Equation 2.9 by Comer and Levy under predicts the M_{max} due to deformation induced volume changes[91] it may be possible to use the same philosophy to determine the effect of compression on booms using

$$\boldsymbol{M_{max} = M^0_{max} - F_c r,} \quad \textbf{(Equation 5.5)}$$

where M^0_{max} is the maximum sustained bending moment achieved when under normal inflation conditions. Equation 5.5 is also plotted in Figure 5.20 for 50 and 100 N compression loads to compare against the FEA model. They are plotted for each inflation pressure once the difference between the compressed and non-compressed FEA boom bending moments are constant. Equation 5.5 shows a good relationship for 5 and 10 PSI inflation pressures where M_{max} is within 4%. At increased inflation pressures the equation increasingly over predicts the compression effect on the boom to 5% at 15 PSI. For pressures lower than 5 PSI the equation under predicts the effect of compression by up to 0.9 N or 23% at 2.5 PSI inflation however this is caused only from 200 mm tip deflections where the root stiffening effect occurs.
Equation 5.5 is limited in reliability by the deformation induced volume changes causing non constant peak bending moments seen in both experimental and FEA results. This is a function of inflation pressure and significantly affects booms at higher pressures from 10 PSI.
However it does give a good initial estimate for designers to assess compression effects. Further analysis would be required to develop this theoretical model including incorporating large volume changes affecting M_{max} and experimental validation. This is outside the scope of this research where a performance comparison between hybrid and inflatable booms is considered.

While the initial rigidity remains constant with pressure regardless of compression, the wrinkling moment is reduced proportionally to the peak moment reduction similarly to a pressure drop. Davids and Zhang (2008) propose an updated incipient wrinkling moment equation to incorporate compressive or tensile forces acting on an inflatable boom.

$$\boldsymbol{M_w = \frac{p\pi r^3 - F_c r}{2}}. \qquad \textbf{(Equation 5.6)}$$

Equation 5.6 is compared to the incipient wrinkling moments of the FEA model displayed in Table 5.5 showing good agreement with the FEA results within 10% for inflation pressures up to 10 PSI. To calculate the wrinkling moment an average radius is taken when the boom is inflated providing reasonable accuracy at lower inflation pressures. At higher pressures the considerable change in radius from the constrained 0.05 m root causes wrinkling to occur at increasingly lower than predicted bending moments. Similarly to Equation 5.5, applying the known wrinkling moments from non-compressed booms (M_w^0) Equation 5.6 becomes

$$\boldsymbol{M_w = M_w^0 - \frac{F_c r}{2}}, \qquad \textbf{(Equation 5.7)}$$

with the values given in Table 5.5. Equation 5.7 shows significantly improved M_W prediction at higher pressures that are within 0.4 Nm and 2.3% at 15 PSI. This provides a suitable method in predicting the wrinkling moment of highly inflated compressed booms using only a simple non-compressed tip deflection test.

Table 5.5: FEA and theoretical bending moment performance of an inflatable boom under compression.

Pressure (PSI)	F_c (N)	FEA M_w (Nm)	Eq.5.6 M_w (Nm)	Eq.5.7 M_w (Nm)	FEA M_{200} (Nm)	Eq.5.5 M_{200} (Nm)
2.5	50	2.1	2.3	2.0	4.0	3.5
	100	0.9	1.0	0.8	-	0.9
5	50	5.7	6.0	5.7	10.5	10.1
	100	4.3	4.7	4.4	7.8	7.6
10	50	13.3	14.2	13.3	22.6	22.2
	100	12.0	12.9	12.0	20.4	19.7
15	50	19.4	23.5	19.6	35.8	34.8
	100	17.8	22.2	18.2	33.9	32.3

If sufficient compression is applied to the boom the buckling mode changes as seen by the 2.5 PSI 100 N compressed boom in Figure 5.21. The boom buckles away from the root and then travels towards the root as tip deflections are increased. The FEA model calculates forces based upon set displacements which results in the bending moment data in Figure 5.20 becoming negative until the buckle reaches the boom root. In practical terms where load is increased and deflection is a response, the buckle would immediately move to the root causing instantaneous large deflections. This effect occurs when $F_c > \frac{pr^2\pi}{2}$ but is not studied in detail as M_{max} can be attained at the buckling point and the boom rigidity prior to wrinkling.

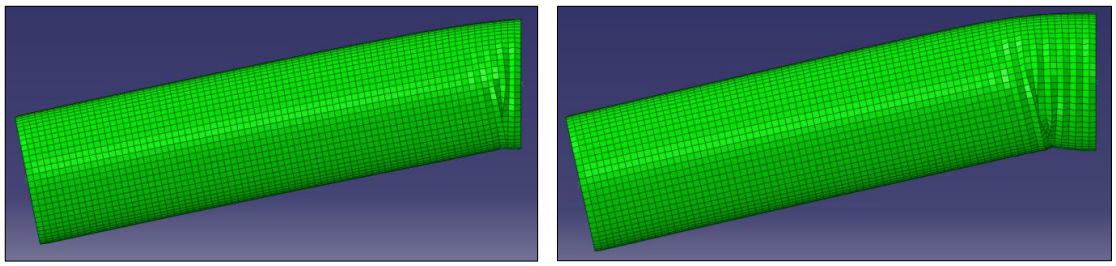

a) 50 N compression b) 100 N compression

Figure 5.21: Buckling modes of the 2.5 PSI inflatable boom under tip compression at 75 mm tip deflection.

5.4 Summary

The aim of this chapter was to provide an inflatable boom model that is thoroughly validated to allow a wide range of boom designs to be implemented and tested computationally including the development of a hybrid boom model with confidence of the component parts. The inflatable boom FEA model can also be used alongside the experimental data to compare against the structural performance of hybrid booms.

The fabric skin of the boom was modelled as a continuum using membrane shell elements that have previous heritage[132-134]. The initial inputs were determined from the previous material properties in chapter 3 and considered the nonlinear strains from inflation seen in the inflatable booms. This reduced the length by 1% for inflation pressures greater than 8 PSI and increased the radius by 4.5 x 10^{-3} mm/kPa to account for the linear stitch pull-out.

Preliminary studies investigated time and mesh convergence demonstrating a 0.5 s tip deflection time step and an element of 25 mm^2 is sufficient to accurately capture the moment-deflection response of a 0.05 m radius inflatable boom. Deformation induced volume changes are known to prevent constant M_{max} after wrinkling for inflatable booms at high pressure[90] and was observed in both experimental and FEA model results that are in close approximation to each other. The material properties study further validated the FEA model against the experimental data considering 4 pressures up to 15 PSI. The study highlighted the material properties are not constant in the experimental setup and vary with both inflation pressure and tip deflections. Turner (2008) has shown material properties of a fabric inflatable boom vary with inflation pressure and is often implemented as constant after inflation[92,93,135]. This simplifies the model and is applied in this study where a shear modulus – pressure relationship of $G = 280p$ was developed against the experimental tip deflection data. This showed a good approximation within the 5% of the repeat variance of the experimental results up to 15 PSI. The error range from the material inputs created a maximum moment – deflection error of 1.3%.

The finalised inflatable boom model looked at fabric orientation, thickness, length, and compression forces. Fabric orientation showed a clear performance advantage by placing the warp yarns longitudinally, but remained less than the performance loss from the maximum operating inflation pressure confirming this conclusion from the experimental chapter.

Boom thickness was shown to be proportional to boom rigidity with reasonable correlation to the experimental results. The additional detail afforded by FEA showed the loading capacity of the inflatable boom will have a small increase with boom thickness. The difference between experimental and FEA results again highlighted the nonlinear fabric properties and the limits of the original shear modulus-pressure relationship to 15 PSI where a further adjustment is required for higher pressures. The comparison also highlighted the FEA modelling inaccuracy at the boom root where large deflections above 0.5L lead to a stiffening term not seen in the experimental results and observations. This is caused by the difference in volume changes, however large deflection model accuracy was not developed as these structures become too soft and unsuitable for applications and hybrid booms will also have likely failed through tape spring buckling. The inflatable boom structural performance will be characterised by M_w and the average rigidity up to this point for comparison against hybrid booms.

Increasing the boom length showed significant problems with model stability and accuracy with a trade-off between the two resulting in substantial increases to computational expense. Adjustments to the mesh and time step demonstrated the model is applicable to longer booms.

Applying a compression force to the boom showed a proportional reduction in peak and wrinkling moments displaying an effective pressure drop. An equation was proposed to determine the adjusted peak moment showing a good approximation for lower inflation pressures where differences between volume changes are minimal. Davids and Zhang (2008) present a similar incipient wrinkling moment relationship showing good agreement with the FEA model at pressures up to 10 PSI. The change in radius from the constrained root at higher inflation pressures limits its accuracy but is improved upon by taking the known wrinkling moments of non-compressed booms. The boom rigidity remains unchanged, however experimental validation is required to determine if the nonlinear material properties are affected by any compression forces.

This chapter has provided a good base model for which FEA hybrid booms can be constructed accurately. Before this model can be developed further into a hybrid system it is important to model the tape springs separately. This will determine the structural performance of the component parts and allow a hybrid boom FEA model to be validated and ensure it is reliable.

Chapter 6

Tape Spring Analysis

To create a hybrid boom, tape springs are placed along the length of an inflatable boom acting as structural stiffeners increasing the structural performance of the boom. They are chosen because of their light weight to high buckling moment ratio, simple design, and are collapsible without permanent deformation storing strain energy in the buckled state. This gives them desirable structural, packing and deployment qualities for gossamer structures. Prior to being implemented into a hybrid boom tape springs need to be modelled and correctly defined through experimental testing and FEA.

The tapes used in this study have the properties given in Table 6.1 where the mass per length was 21.25 g/m. The elastic properties of the steel tape springs were calculated experimentally using tensile testing of five specimens.

Table 6.1: Tape spring properties.

R	14.5 mm
t	0.11 ±0.01 mm
α	1.72 rad
ρ	7860 kg/m^3
E	198 ±8 GPa
ν	0.3

Experimental tip deflection tests of five 0.4 m tape springs showed an average peak bending moment of 93 ±2 Nmm and 813 ±35 Nmm for equal (M_{-}^{max}) and opposite (M_{+}^{max}) sense bending respectively. This was conducted using a root clamp shown in Figure 6.1 to ensure the tape spring curvature was maintained at the root while mass was applied to the tape tip. This was to test the tape spring in the similar setup it will be used in the cantilever hybrid boom loading case. This cantilever setup differs from the majority of research on tape springs[105-111]. This includes the moment-curvature relationship developed by Mansfield (1973) with Equation 2.16 where equal and opposite moments are applied to either end of the tape spring forcing buckling to occur in the centre. The tape springs in this experimental setup caused buckling near the tape root which was offset by the constrained root clamp assembly. The steady state Equations 2.13 and 2.14 derived by Seffen (1999)[2] corresponded to steady state

moments (M_{-}^{*}, M_{+}^{*}) of 29 mm and 55 Nmm, however the cantilever setup may also affect these results.

Figure 6.1: Tape spring root clamp assembly.

To confirm these four bending moment values an FEA study was conducted which can then be used to validate the tape spring components in a hybrid boom FEA model. The model used ABAQUS 6.9-3 explicit that was selected for its robust nonlinear solver. A 0.4 m long tape spring was constructed out of S4R shell elements from the tape spring properties in Table 6.1. It was rigidly tied at the root and tip edges to RPs 1 and 2 respectively as shown in Figure 6.2. The constraint at RP1, at the tape root, was ENCASTRE and an increasing displacement was applied to RP2 at the tape tip in both opposite and equal sense directions. Five mesh densities were considered using square regular elements totalling 4, 6, 8, 10 and 16 across the tape width. Figure 6.2 displays the 8 element across the width mesh which has a total of 1064 elements at a size of 10 mm^2.

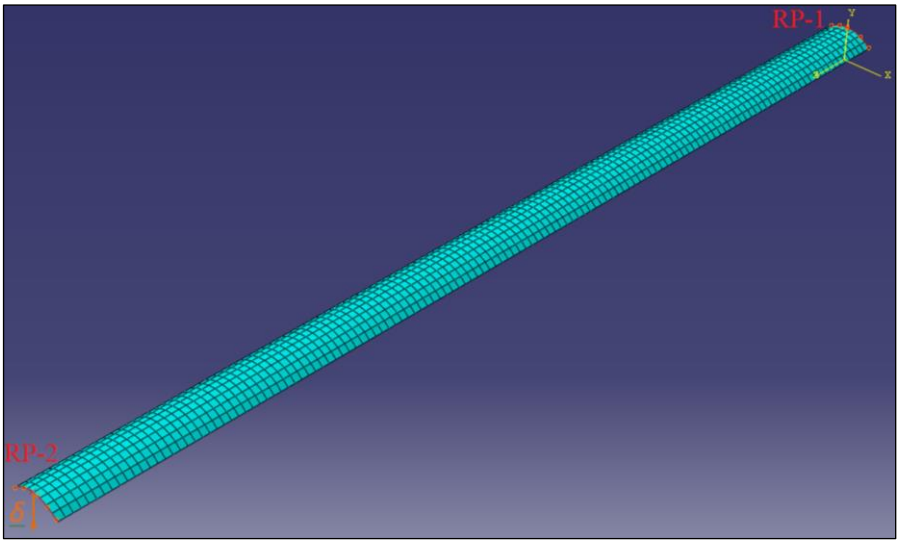

Figure 6.2: FEA tape spring model.

The mesh convergence study in Figure 6.3 shows the bending moment response as the tape is deflected from straight and unbent through equal and opposite sense bends. The figure shows the peak bending moments converge for meshes with 8 or more elements across the width. The peak bending moments from the finest mesh are -176 and 646 Nmm for equal and opposite sense bends respectively where the 8 element mesh has values within 2%. After the peak bending moments the model shows significant oscillation and is seen in the bending moment data. This is due to the buckling point travelling towards the tape root, as shown in Figure 6.4. Increasing the time step was found to reduce the oscillations however a time step of 5 s was suitable by capturing the more important peak moments accurately whilst limiting computational expense. This was used for all FEA tape spring models. The oscillations in the model are most severe in the equal sense bend where the tape correctly buckles through a torsional mode and is displayed in Figure 6.4. The equal sense peak bending moment occurs prior to any tape torsion (Figure 6.4 a)) at -9 mm tip deflection. Further deflection leads the tape spring to buckle in a skewed sense and the resulting hinge not being normal to the tape length as shown in Figure 6.4 c). This is caused by the torsional failure mode of equal sense tape spring bends. Steady state is achieved when the skewed tape spring buckle becomes normal to the tape length at -247 mm tip deflection and shown in Figure 6.4 d).

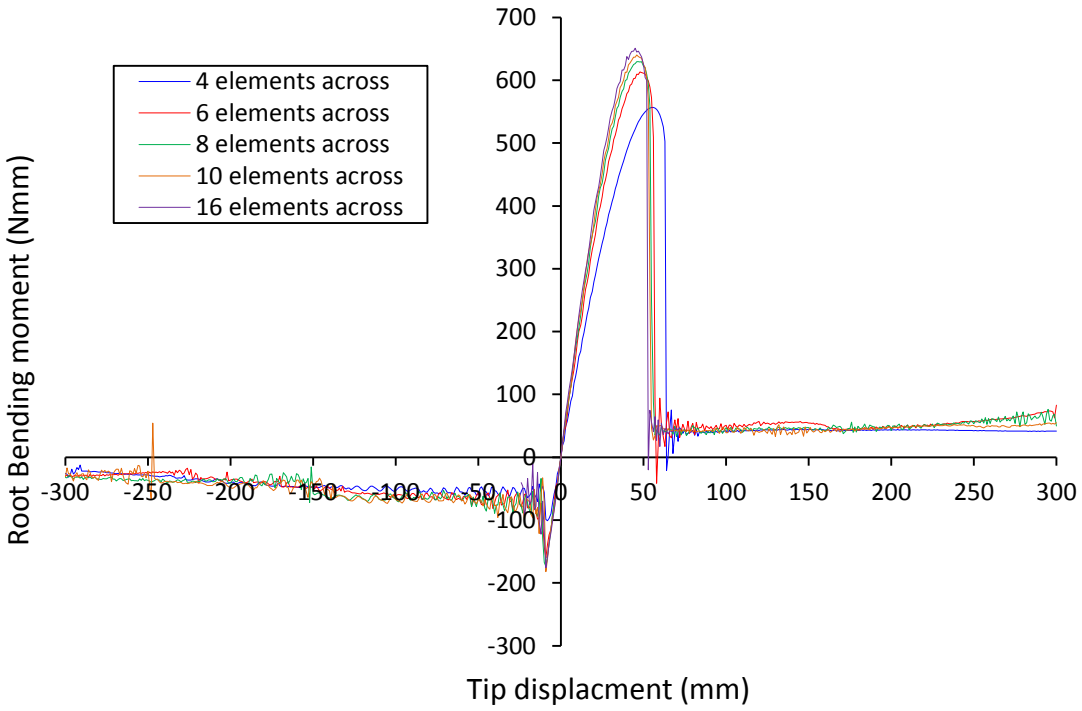

Figure 6.3: Mesh convergence study of a 0.4 m tape spring.

Using 8 elements across the tape width is sufficient to accurately capture tape spring bending behaviour which has also been shown by Walker et al. (2007), maintaining the element

thickness to width ratio greater than 15:1[136], and is used for subsequent investigations. The general tape spring bending profile is similar to Figure 2.13 with a snap through in the opposite sense and a gradual moment reduction to steady state after the peak moment in the equal sense bend.

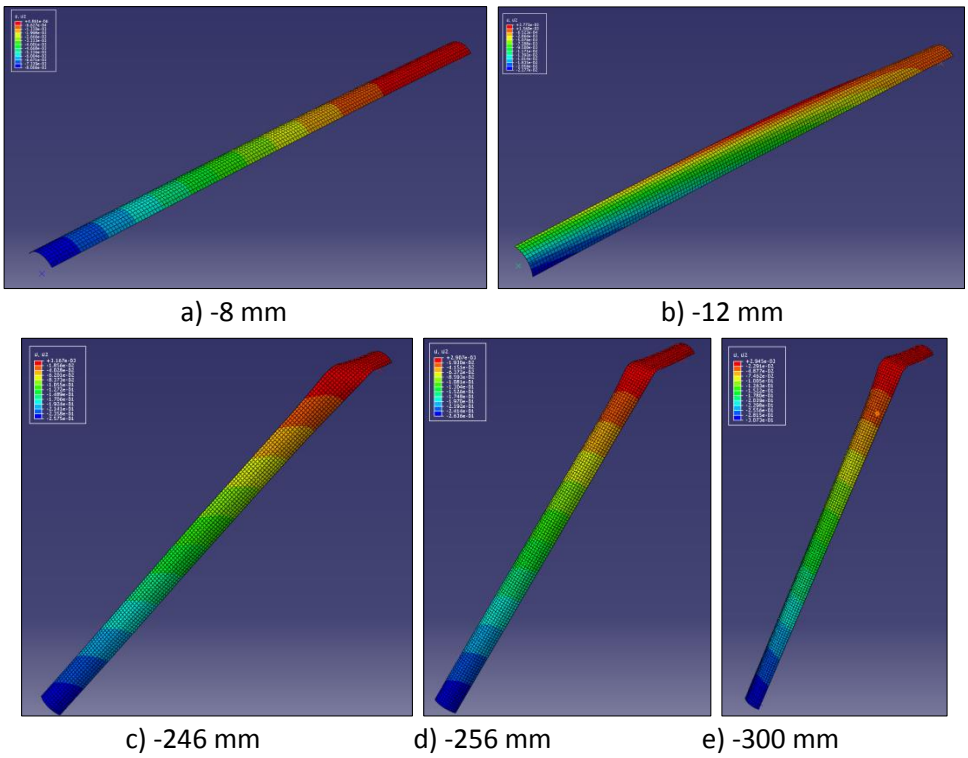

a) -8 mm b) -12 mm

c) -246 mm d) -256 mm e) -300 mm

Figure 6.4: Equal sense tip deflections of the 10 element mesh showing a) pre torsional effect, b) post peak moment, c) pre steady state moment, d) steady state moment, e) tape buckle movement.

The thickness of the tape has shown to have a significant effect on the peak and steady state bending moments[3,108,111]. The measured thickness of the tape springs varied by 0.11 ±0.01 mm which corresponds to a 28% range in the steady state moments calculated by Equations 2.13, 2.14 and 2.15. To account for this variance a thickness study was conducted in the FEA tape spring model and the peak and steady state moments are given in Table 6.2.

Table 6.2: FEA tape thickness sensitivity.

FEA tape thickness (mm)	M_{-}^{max} (Nmm)	M_{+}^{max} (Nmm)	M_{-}^{*} (Nmm)	M_{+}^{*} (Nmm)
0.10	-174	632	-28	43
0.11	-207	756	-39	54
0.12	-244	890	-50	70
Experimental tape	-93 ±2	813 ±35	-	-
Mansfield equation (0.11 ±0.01 mm)	-	-	-29 ±8	54 ±14

Table 6.2 shows the FEA tape spring model has peak bending moments that vary by 17% for both equal and opposite sense bends over the thickness range specified in Table 6.1. The comparison between the experimental and FEA model shows the thickness of the tape spring makes a significant difference to the peak moments where the opposite sense peak moment and both steady state moments are within the measured tape spring thickness range. The differences can be attributed to the experimental tape springs where the manufacturing tolerances are low and have variations along the length of the tape.

The experimental equal sense bend peak moment is significantly smaller than the thinnest FEA model and may be attributed to the key difference between the experimental and FEA model. The experimental tapes have a natural twist that can be seen in Figure 6.5. The twist magnitude is 144^0/m in tape length and Figure 6.4 shows the tape spring in a similar position to the straight FEA tape spring post equal sense peak moment. This is displayed in Figure 6.4 b) and could significantly affect the equal sense peak moment as the tape spring is already in the torsional bend state.

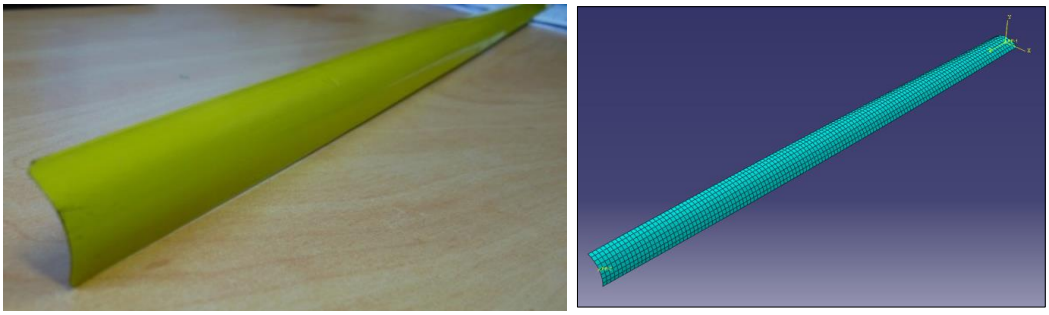

a) Actual b) FEA model

Figure 6.5: Tape springs showing natural twist of 144^0/m.

The tape spring moment-deflection response of the twisted tape spring is significantly altered in the equal sense bend with a peak moment reduced to -91 Nmm. The added twist causes the tape to miss stage a) in Figure 6.4 resulting in a greatly reduced stiffness before following the non-twisted tape spring response from -61 mm. The twist also affects the opposite sense bend where the response is offset by 7 mm as the tape untwists before bending and snapping through in the nominal manner. This increased tip deflection results in the tape spring buckling earlier reducing the opposite sense peak moment by 7%. The steady state moments remain unchanged. This twisted FEA tape spring model corresponds to the experimental peak moment results which are within the error range and 2% of the average equal sense peak bending moment. For most applications including hybrid booms the tape spring twist is unnecessary

and is removed at attachment points. As the rate of twist is low the tape spring is compliant when clamped to a hybrid boom. Previous experimental and FEA studies where each end of a tape spring is held in line to each other, removing any tape twist along its length, have shown good agreement in the equal sense bend producing the more traditional moment-deflection response shown in Figure 6.3[108].

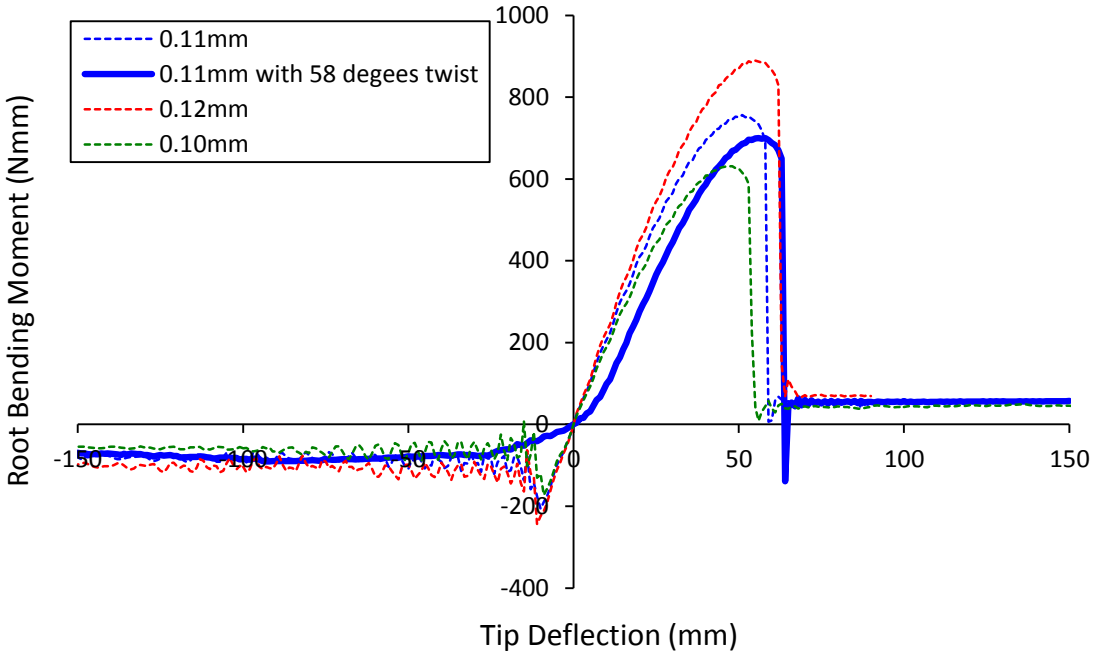

Figure 6.6: Bending moment – deflection response of a 0.4 m tape spring including tape twist.

A material study varied the Young's Modulus by 8 GPa showing the peak and steady state moments are directly proportional to the error range of 4%. Varying the Poisson's ratio and the material density showed negligible effect where a 10% input change resulted in a combined error of less than 1%.

A final consideration to the FEA tape spring model was the cross sectional profile. Tape springs are often not the same as the idealised constant radius definition that is given in Figure 2.11. The manufacturing process takes a metal strip and presses a radius into the mid width to cause the curvature. However this results in tapes with straight edges. Figure 6.7 shows the idealised and actual tape spring cross-sections where the idealised profile is created by measuring the tape width and height when curved and assumes a constant radius.

Although there is little difference between the two profiles a FEA model off the actual tape spring was constructed, similarly to the previous tape spring model shown in Figure 6.2, to

determine any structural effects between the two profiles. The opposite sense bending response is given in Figure 6.8. The moment characteristics displayed negligible difference between the two profiles where the idealised tape spring underestimates the peak and steady state moments by up to 4% and 10% respectively, a similar result to previous research by Walker (2004).

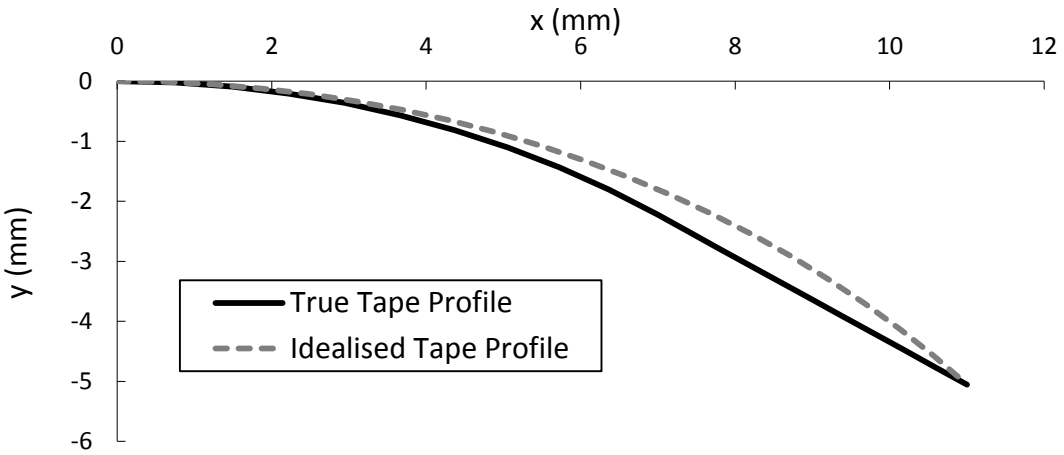

Figure 6.7: Idealised and actual tape spring cross-sectional profile.

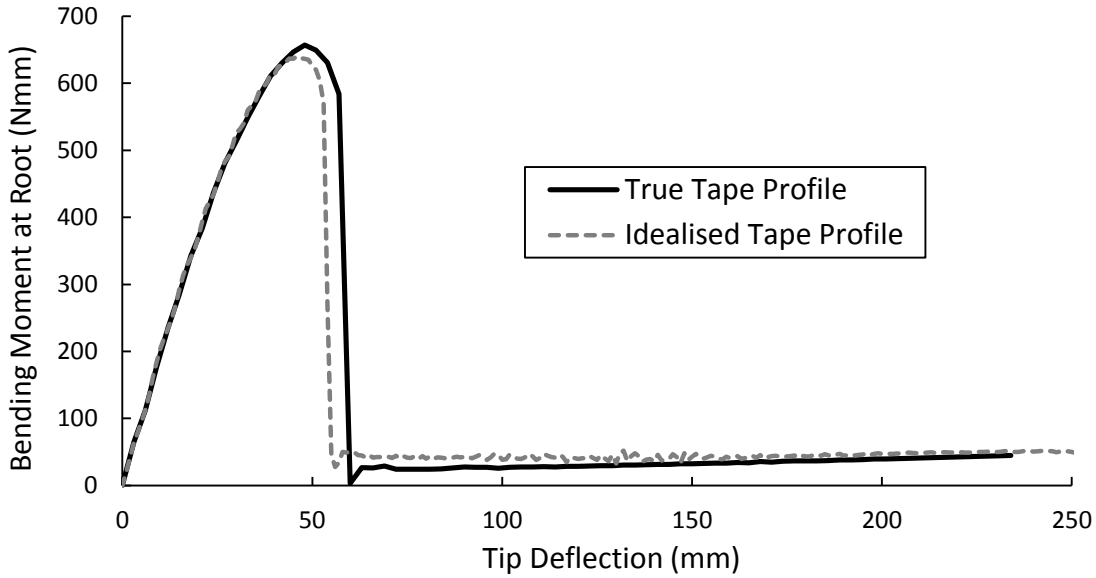

Figure 6.8: The FEA model opposite sense bend moment characteristics of idealised and true 0.4 m long tape spring profiles.

Table 6.3: FEA profile study of a 0.1 mm thick 0.4 m long tape spring.

Tape profile	M_{-}^{max} (Nmm)	M_{+}^{max} (Nmm)	M_{-}^{*} (Nmm)	M_{+}^{*} (Nmm)
Idealised	-174	632	-28	43
True	-181	657	-27	39

As the bending moment was applied to a fixed end of a cantilever tape spring, the buckling of the tape spring occurred near the constrained root as shown in Figure 6.4. End effects have shown to cause changes in the bending moment response of tape springs[108] which will be affected by tape length. Figure 6.9 displays the bending moment characteristics for 0.1, 0.2, 0.4, 0.6 and 1.0 m tape springs with the same profile and mesh density of the initial model shown in Figure 6.2.

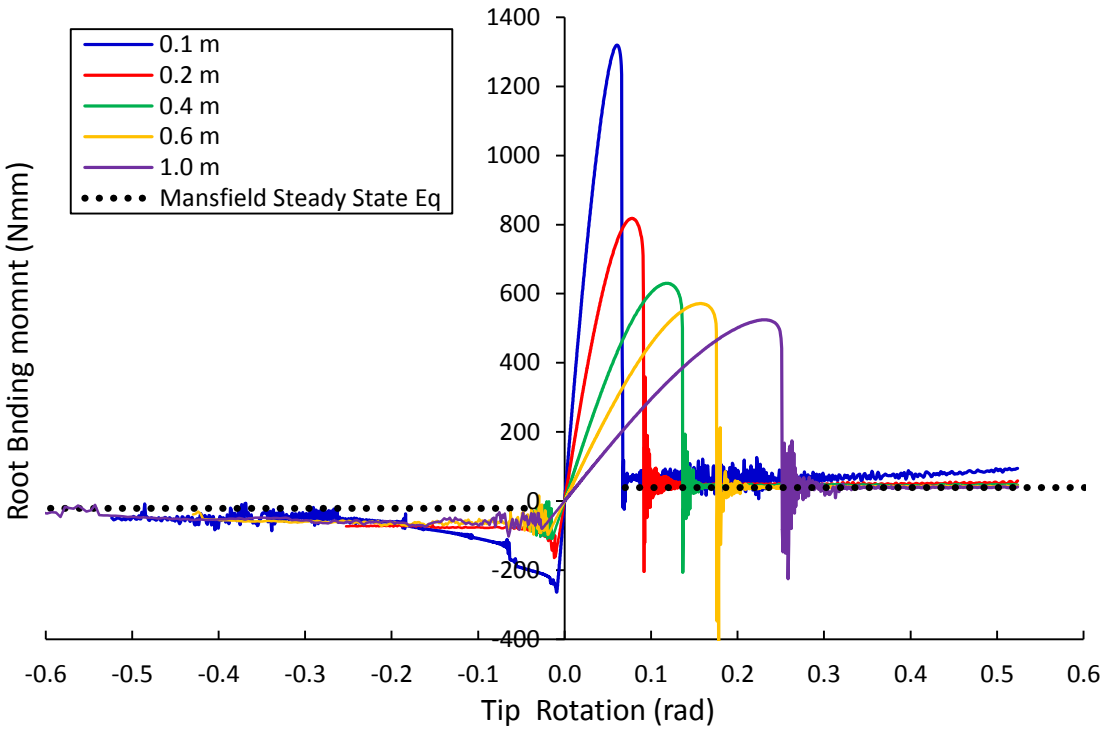

Figure 6.9: FEA tape spring length study.

The FEA length study in Figure 6.9 shows a significant reduction in structural performance as the tape spring length increases. A reduction in tape spring length increased rigidity and peak moments. This is an exponential increase where the difference between 0.6 and 1.0 m tape springs is 9% whereas from 0.2 to 0.1 m results in an increase of 61%. Running the model with a 0.05 m tape spring continued to increase the peak moments further to 2900 and 324 Nmm for opposite and equal sense bends respectively. The tape spring is stiffened around the rigid root which requires increasingly greater loads to force buckling as the point of buckle approaches the constrained root. This is caused by the constraint preventing the tape flattening that is required for the tape to buckle in the normal mode. The opposite sense peak moment occurred at 110 and 38 mm from the tape root for 1.0 and 0.1 m lengths respectively given in Table 6.4. Reducing the tape length forced the buckling location to occur closer to the rigid root resulting in both stiffer and larger peak moments. This peak moment change is not

seen in other studies including Walker (2004) where the tested tape lengths are independent of peak moments. This is because the tape spring is held at either end with an equal bending moment applied causing the tape to buckle in the mid-section where end effects are significantly reduced. The steady state moment is also affected with tape length and is increased when tape length decreases. This corresponds to the change in peak moment response where the end effects become significant for tapes shorter than 0.4 m in this cantilever setup. For tape springs less than 0.1 m a non-constant moment is clearly seen in the opposite sense bend in Figure 6.9. This is observed in other studies[2,108] and has been related to the propagation of bulges seen in the inflation of balloons[107].

Table 6.4: Opposite sense bend data for various tape spring lengths (†initial steady state moment).

Length (m)	Opposite sense bend buckle distance from root	M_{-}^{max} (Nmm)	M_{-}^{*} (Nmm)
0.05	25 mm	2900	105†
0.1	38 mm	1320	67†
0.2	59 mm	818	48
0.4	83 mm	627	44
0.6	103 mm	571	41
1.0	110 mm	522	39

This chapter has created a FEA tape spring model that was applied as a cantilever beam similarly to the intended use as part of a hybrid structure. A mesh convergence study showed 8 elements across the tape width provided sufficient accuracy in capturing the peak moment response. The model was verified with experimental peak moment results and Mansfield's steady state moment Equations 2.13, 2.14 and 2.15 and were within the error range for the opposite sense bend when considering the tape spring thickness variability of 0.11 ±0.01 mm. The experimental equal sense peak moment is significantly lower and was likely to be a result of the natural twist of the tape spring. Incorporating the tape spring twist in the FEA model resulted in a softer tape spring response with an equal sense peak moment within the experimental variability.

The tape spring profile was also considered with results similar to Walker (2004) where the idealised constant radius cross-section under predicts the peak and steady state moments by up to 4 and 10% respectively. A tape length study has also shown the cantilever tape spring is significantly affected by tape length and is likely caused by the constrained rigid root having a significant effect when tapes are shorter than 0.4 m. The tape spring thickness variability has shown to produce the greatest change in results of up to 17 and 28% in peak and steady state

moments respectively. This variability is caused by low manufacture tolerances that as a result can produce in quantity at very low cost a simple off the shelve component.

The research along with the inflatable boom study in chapters 4 and 5 allows a direct comparison between a hybrid boom and its component parts. The FEA tape spring and inflatable boom models are verified with experimental results and can be combined to create a FEA inflatable hybrid boom model to confirm trends found in the experimental hybrid booms.

Chapter 7

Experimental Structural Analysis of a Hybrid Boom

Tape springs require a significant peak force to cause buckling and are collapsible without permanent deformation storing strain energy in the collapsed state. This gives them desirable structural, packing and deployment qualities while still maintaining the light weight, low volume advantages of gossamer structures. Combining tape springs with an inflatable boom offers the possibility of creating a superior hybrid structure. Attached along the length of the boom, the tape springs act as structural stiffeners and affect the structural, deployment, and packing efficiency performances whilst potentially using cheap 'off the shelf' components.

This chapter considers the feasibility of hybrid booms and their experimental structural performance trends for tape springs as part of a hybrid structure. It gives details of the manufacture, setup and test permutations that have taken place. The test permutations are given in Table 7.1 and Figure 7.1 illustrates the cross-sectional tape spring configurations considered where Configuration A is an inflatable boom with no tape springs. The test campaign used the inflatable boom and tape springs previously defined in Tables 5.1 and 6.1.

Table 7.1: Hybrid boom tested configurations.

Configuration	Description	Inflation pressures (PSI)
B	2 opposed tapes vertically aligned to the applied load	0, 2.5, 5, 10, 15
C	2 opposed tapes at 45^0 to the applied load	0, 10, 15
D	2 opposed tapes horizontally aligned to the applied load	0, 10, 15
E	Doubled top tape springs	10
F	Double bottom tape springs	10
G	Single top tape spring	10
H	Single bottom tape spring	10
I	Double thickness tapes in Configuration B	0, 2.5, 5, 10, 15
J	Triple thickness tapes in Configuration B	0, 2.5, 5, 10, 15
K	4 tapes in a square cross formation to the applied load	0, 2.5, 5, 10, 15
L	4 tapes in a cross formation at 22.5^0 to the applied load	0, 2.5, 5, 10, 15
M	4 tapes in a diagonal cross formation to the applied load	0, 2.5, 5, 10, 15

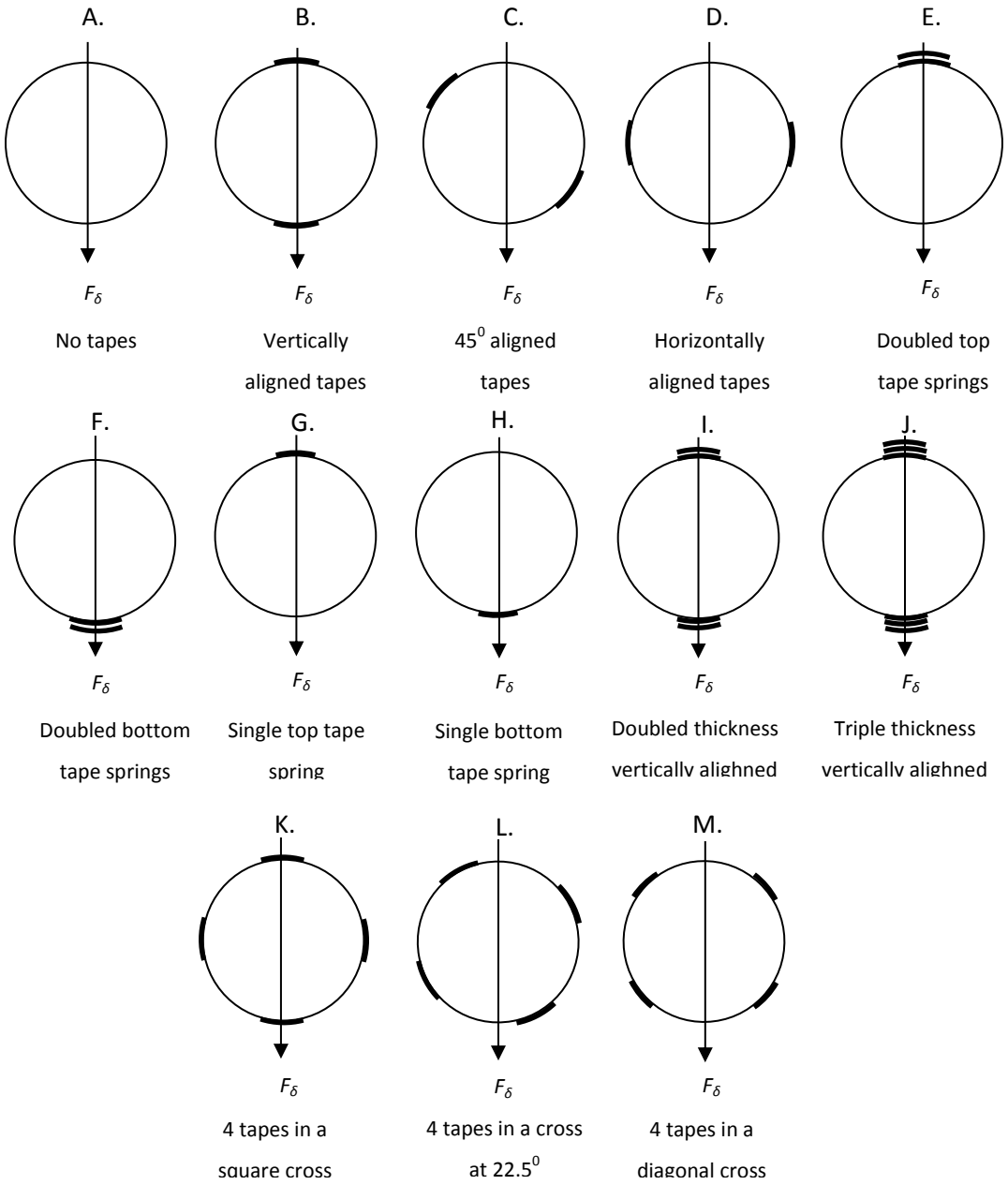

Figure 7.1: Cross-sectional diagram of the tape spring configurations with respect to the applied load, F_δ (Not to scale).

7.1 Setup and Preliminary Testing

The structural testing of the hybrid booms was conducted with the same setup as the inflatable boom tip deflections tests in chapter 4 using DIC to accurately measure the tip deflections of the booms under increasing load.

The hybrid booms were created using the existing inflatable fabric booms as shown in chapter 2, and attaches steel tape springs along the length of the boom. This creates a hybrid

boom constructed from COTS materials although any similar advanced space grade materials including Kevlar or Vectran fabrics and carbon fibre tape springs could be utilised. The attachment method of the tape springs is significant and will affect the inherent stiffness of the inflatable boom, tape springs and the resultant hybrid boom as well as other performance criteria including the stowage capability. There are a multitude of methods to attach the tape springs to the inflatable boom each with benefits and drawbacks to be considered to maximise their effectiveness. Research by Walker et al. (2011) attached the tape springs using pockets sewn into the fabric. This resulted in a 31% increase in M_{max} to 25 Nm for a 0.4 m long inflatable boom with a 0.05 m radius. The attached pockets shown in Figure 7.2 allowed limited tape movement which was restricted by end tabs. This movement in relation to the boom reduced the tapes contribution to the compression or tension bending forces acting on the boom and were therefore not utilising their maximum stiffness.

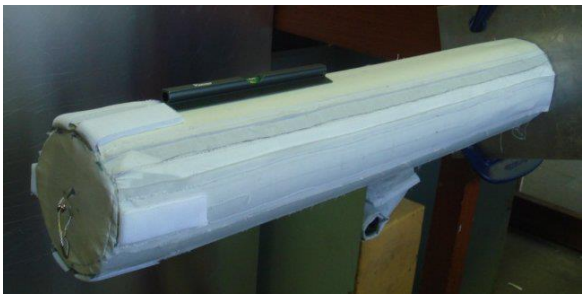

Figure 7.2: Hybrid boom with tape springs held in pockets[105].

Preliminary testing focused on the tape spring attachment to maximise the structural performance potential of the tape springs whilst providing a suitable and easily repeatable hybrid boom. Four attachment setups where considered; attached along the whole tape length, attached at 5 locations, attached at 5 locations using inserts, and attached at 5 locations using collars. Each method attaches two tape springs on to a 0.4 m long inflatable boom, each positioned in the equal and opposite sense bend orientations with respect to the applied load as shown in Figure 7.1 named configuration B. Research by Walker et al. (2011) considered this configuration to maximise the second moment of area and potential structural performance of the hybrid booms. Araldite rapid epoxy adhesive was used to attach the tape springs to the inflatable booms to prevent relative movement between the two components. The first attachment method considered is to simply glue the tape springs directly to the boom along the whole length to stop the tapes 'slipping' along the boom length. Gluing along the entire length of the tape springs is not a practical solution with the current rigid epoxy as the boom cannot be stowed without permanent damage occurring to the structure. Using an

adhesive that allows limited shearing between the tape springs and inflatable boom would allow packing of the hybrid boom by being rolled up, similarly to the CFRP omega boom[77], at the tradeoff of structural performance. An analysis of adhesive shear properties would be required to optimise this stowage-structural performance tradeoff and is outside the scope of this research. It may also be necessary to attach the tape springs at intervals along the boom length to allow relative movement between components during stowage. This also allows the tapes to be bent in a zigzag pattern as an alternative packing solution that can be achieved with the current adhesive. In this preliminary study a second attachment method used 5 connections between each tape spring and the boom at regular 0.1 m intervals over a 10 mm width. This allowed sufficient distance for the tape springs to fold into a stowed configuration.

Figure 7.3: Perspex connecting insert with tape spring outer radius and boom inner radius.

It is also important to consider that the tape springs buckle at lower values when the tape curvature is reduced as shown by Mansfield (1973) with the non-dimensional Equation 2.16. Gluing the tapes directly onto the boom leads to the inflated boom forcing the tapes to take the larger 50 mm radius and reduce the maximum bending moment they can sustain. Due to radius strain from inflation this will differ between inflation pressures. For a final design gluing directly onto the boom means the inflation pressure becomes a design parameter driving the initial boom radius so the inflated radius matches the required tape spring curvature. However for investigative purposes placing an insert between the tape and boom allows the tape spring to maintain its curvature and maximise the tape spring structural performance irrespective of the range of test inflation pressures. Figure 7.3 shows an insert manufactured out of 10 mm thick Perspex with a mass of 2.3 g with internal and external radiuses of 50 and 14.5 mm respectively. Two sets of four inserts were glued at 0.1 m intervals along the boom length with two tape springs glued onto the inserts. The tapes where held at the boom root by the root clamp assembly as shown in Figure 6.1 and bolts directly onto the base plate. The completed structure is shown in Figure 7.4 where masking tape used during the manufacturing process covers each insert attachment location and has a total boom mass of 188 g.

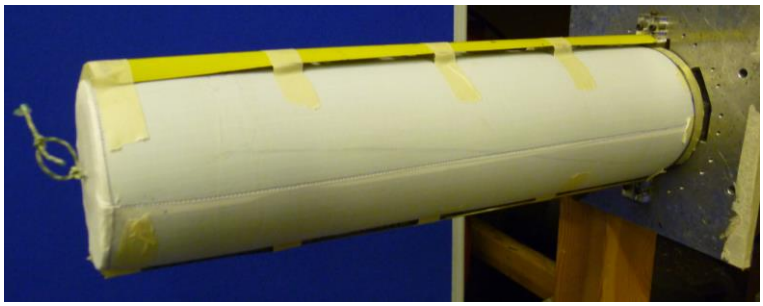

Figure 7.4: Hybrid boom using 4 evenly spaced Perspex inserts per tape spring to maintain tape curvature of two opposed tapes in configuration B.

All previous attachment methods were labour and resource intensive as for all tests a complete new hybrid boom needed to be constructed. An alternative is to clamp the tape springs into position thus allowing tape replacement between tests and not a whole new boom. Using attachment collars at intervals along the boom length provided a tape attachment method that significantly reduced labour and resources. It maintained tape spring curvature and constrained the tape springs position relative to the boom while allowing tapes to be interchangeable for a variety of permutations. The collars were manufactured out of 5 mm thick Perspex with 12 circumferential locations to position the tape spring as shown in Figure 7.5. The mass of each collar and a tape collar clamp are 14 g and 2.2 g respectively. The tapes were again held at the boom root by the tape spring root clamp assembly bolted to the base plate. Each tape spring attached to the inflatable boom required one root attachment assembly and a collar clamp per collar with the mass breakdown of the hybrid boom given in Table 7.2. The assembled hybrid boom shown in Figure 7.6 used 8 attachment collars evenly spaced along the 0.4 m long boom. The tape springs also required a 3 mm clearance hole punched in each clamping location. The preliminary collar attachment investigation used 4 collars spaced at 0.1 m intervals.

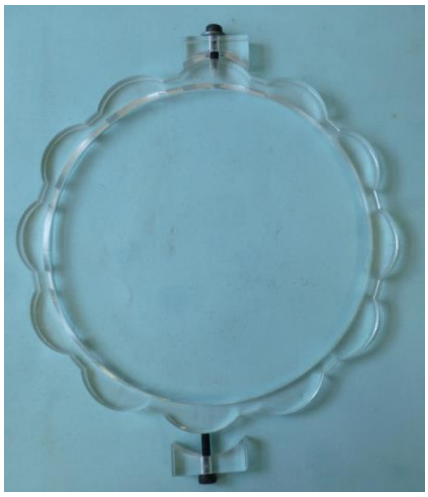

Figure 7.5: Perspex collar and tape collar clamps.

Table 7.2: Mass breakdown per part for the tape spring collar attachment assembly.

Tape spring	21.25 g/m
Root attachment assembly	8.9 g
Collar	14 g
Collar clamp	2.2 g

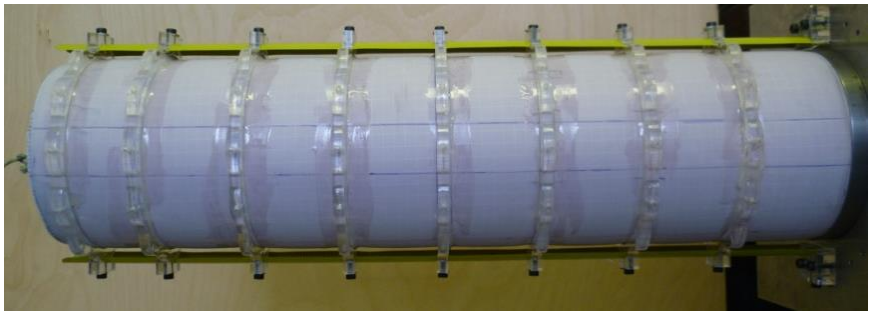

Figure 7.6: Hybrid boom using 8 evenly spaced attachment collars for 2 opposed tape springs in configuration B.

Five repeat tip deflection tests of each attachment method were conducted on the preliminary hybrid booms inflated to 10 PSI with the average performance given in Figure 7.7 and the collected data tabulated in appendix IV.

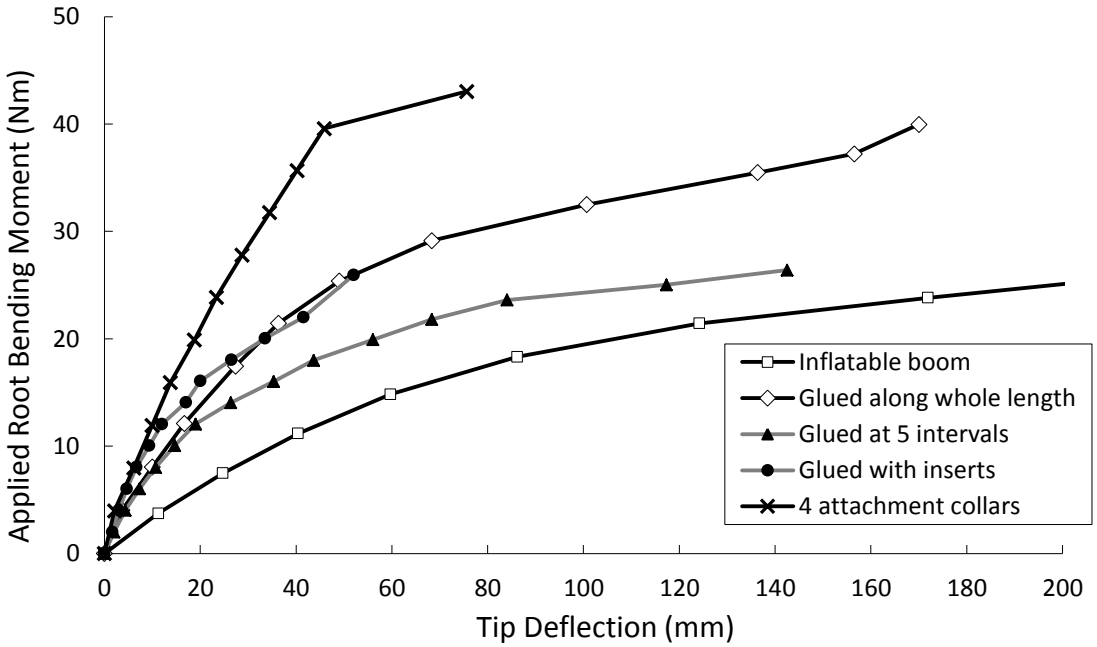

Figure 7.7: Average tip deflection results for various attachment methods of a 0.4 m inflatable boom at 10 PSI with two attached tape springs in configuration B.

The initial attachment method, gluing the tape spring along the whole length, shows a significant increase in boom rigidity over an inflatable boom and achieves a M_{max} greater than 30 Nm. While limiting the attachment to 5 locations shows a similar initial stiffness averaged of

2513 N/m up to 12 Nm. At greater loads the boom rigidity is reduced until the tapes buckle at 24 Nm. Using inserts to maintain the tape spring curvature has shown to increase the boom rigidity in comparison to gluing directly onto the boom where the average initial boom stiffness up to 12 Nm is increased by 61% and is able to achieve a M_{max} of 29 Nm before tape buckling. After 12 Nm the moment-deflection response is irregular and may be caused by the ductile failure of the adhesive between the tape spring and insert joints in addition to the lack of rigid connections between top and bottom tape springs. These affects limit the ultimate stiffness of the boom at higher bending moments before tape buckling. A revised connection between the two surfaces may provide a hybrid boom capable of maximising the tape spring potential.

Figure 7.7 shows the significant structural performance improvement when placing 4 collars and a root clamp attachment evenly along the length of the boom to attach two tape springs. The M_{fail} is increased by 150% over an inflatable boom to 40 Nm before the tape springs buckle. The rigidity of the boom in this attachment configuration is superior to all other attachment techniques where it maintains an averaged stiffness of 2066 N/m before buckling. The collars and tape springs create a framework structure around the inflatable boom which becomes the primary load bearing part of the hybrid boom producing this significant performance advantage. The considerable disadvantages of the collar attachment system are the significant increase in mass and volume to the hybrid boom which limit its viability as a final design. Specifically as the framework structure is only collapsible into a zigzag pattern where voids in the stowed boom will cause significant packing inefficiencies with respect to a rolled up design. A final solution would likely attach the tape springs directly onto the inflatable boom with a suitable adhesive allowing the structure to be rolled onto a mandrel preventing voids and maintaining the significant packing efficiencies of inflatable structures.

Although not suitable as a final design, the collar attachment method is selected for all further structural analysis. It is used in the following studies as it is a simple system that can be modified easily for testing various tape spring configurations whilst minimising time and resources and maximising the number of tested permutations. By maintaining the tape spring curvature and limiting the relative movement between the tapes and boom the collar attachment system maximises the structural potential of a hybrid boom. This will allow an assessment of the effectiveness of tape springs in various configurations and the hybrid boom structural performance trends. From this analysis the results and trends can be correlated to a final design. Figure 7.7 shows the likely tradeoff to structural performance between

attachment methods. Tape springs glued along the whole length show a significant 38% drop in the initial rigidity of the hybrid boom at 64% of the 40 Nm peak moment achieved using the 4 attachment collars. The tape springs glued along the length can sustain greater peak moments at a significant cost to rigidity likely to leave the structure too soft for applications. The significant structural advantage of the attachment collars is caused because the framework structure of the collars provides through thickness strength between tape springs where all other attachment approaches rely on the shear stiffness of the inflatable boom provided by the inflation pressure.

Outlined in Table 7.1 and Figure 7.1, four tip deflection test campaigns were conducted; two opposed tape springs, single and double tape springs, varying thickness of opposed tapes and 4 tapes in a cross formation, to identify key trends in a hybrid boom with three repeat tests for each configuration. Figure 7.8 illustrates a tip deflection test using the collar attachment system to create a hybrid boom. All subsequent tests use the collar attachment approach at evenly spaced intervals along the 0.4 m long inflatable booms with each permutation stating the number of collars used. Similarly to the inflatable boom analysis the effect of gravity acting on the cantilever booms prior to any loading is taken into account. The additional moment acting on these hybrid booms will vary between 0.5 and 0.8 Nm dependant on the configuration used. Approximating the preliminary data of the 4 attachment collar hybrid boom in Figure 7.7 to a linear relationship suggests an additional 0.7 mm tip deflection that will not significantly affect the results.

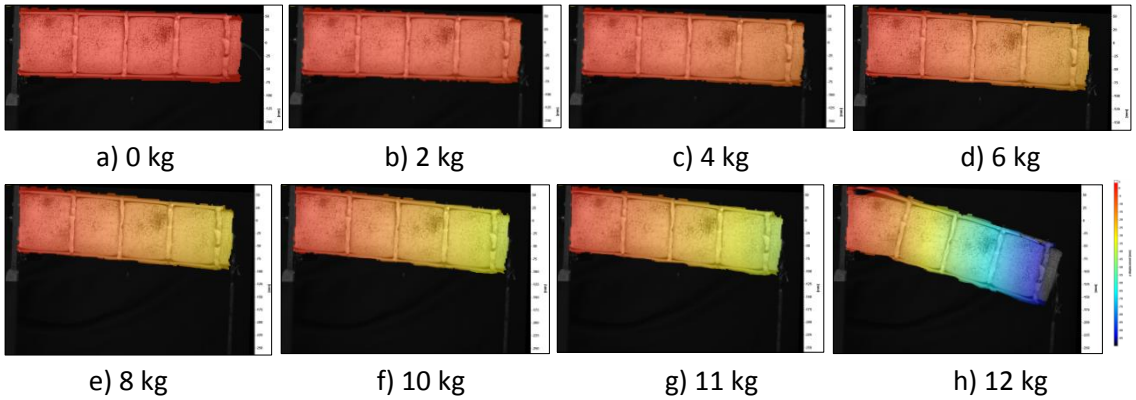

Figure 7.8: Tip deflections using DIC of a hybrid boom using 4 evenly spaced attachment collars in configuration B at 15 PSI with an overlaid vertical displacement field map.

7.2 Opposed Tape Springs

The opposed tape spring hybrid booms are configurations B, C and D which place two opposed tape springs aligned vertically, at 45^0 and horizontally to the applied load respectively and are illustrated in Figure 7.1. Previous research by Walker et al. (2011) identified configuration B to have a significant performance benefit over inflatable booms and provides a suitable starting point to investigate hybrid boom trends with the multitude of tape spring combinations. The opposed tape springs investigate the hybrid boom characteristics when loaded in various orientations. This allows the boom to maximise the structural performance by placing tape springs in their most effective position and identify the performance trends when the applied loading is not in the desired orientation. The tip deflection tests for each configuration was conducted at three inflation pressures; 0, 10 and 15 PSI. Testing at 0 PSI is possible due to the framework structure created from the attachment collars resulting in the hybrid boom being self-supported without inflation pressure. The boom used 8 evenly spaced attachment collars along the 0.4 m long inflatable boom located as shown in Figure 7.6 with a total mass of 317 g.

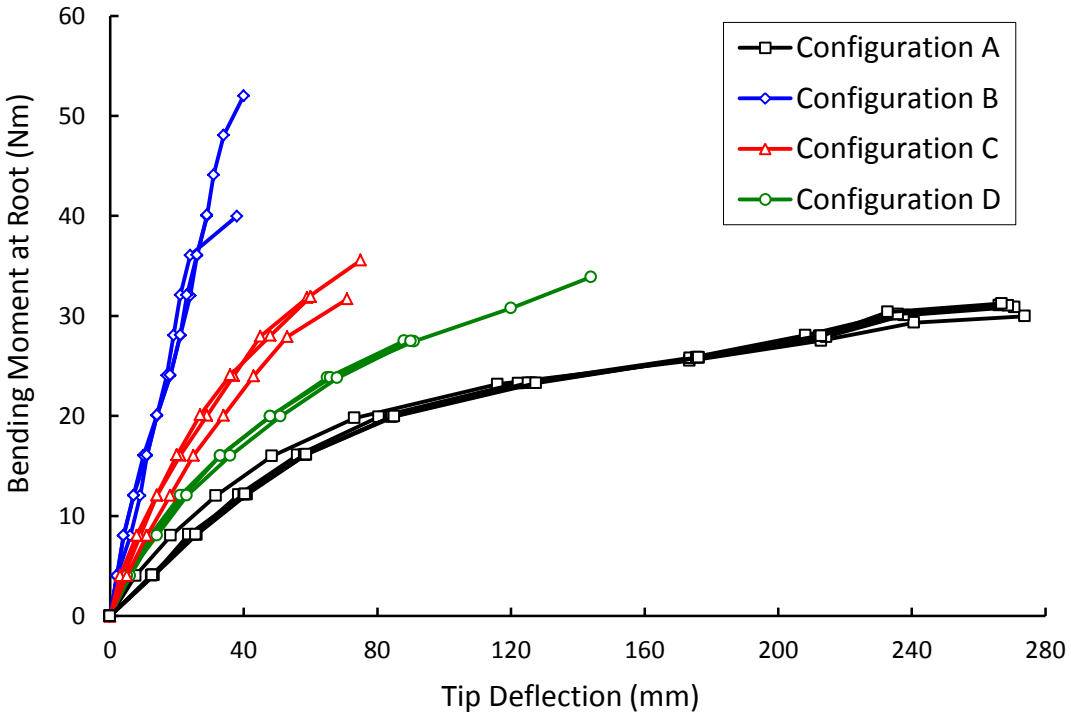

Figure 7.9: Hybrid boom moment – deflection response for two opposed tape springs with 8 attachment collars at 10 PSI.

Figure 7.9 displays the applied bending moment and resultant deflections of the booms at 10 PSI inflation pressure for configurations A-D with the same trends observed for 15 PSI given

in appendix IV. This graph shows the repeatability of these configurations similarly to the experimental inflatable boom tests in Figure 4.3 to confirm the averaged data is representative. Where subsequent data for the remainder of this chapter is given as averaged moment-deflection results, the full repeat tests can be found in appendix IV to confirm the trends are representative.

The increased structural stiffness and buckling moment the hybrid booms can achieve is seen immediately. The hybrid boom is most rigid when the pair of tape springs are placed in configuration B, creating an average stiffness of 3258 and 4058 N/m for booms inflated to 10 and 15 PSI respectively. The booms are deemed to have failed (M_{fail}) when wrinkling occurs on the inflatable boom at M_w. This is because the tapes on the hybrid booms have buckled and are no longer providing structural support and the inflatable boom has deflected to such large values the stiffness would leave the boom too weak for the majority of applications. This also allows a direct comparison between boom rigidities taking the average stiffness of the booms up to this failure point with the average structural performances for each boom given in Table 7.3.

Table 7.3: Average boom performances in various configurations with 8 attachment collars (* peak values).

Boom configuration (with boom mass)	Pressure (PSI)	M_{fail} (Nm)	Average stiffness (N/m)
A [No tapes]	10	16	781
(135 g)	15	25	833
B [Vertically aligned]	0	11	389
(317 g)	10	41*	3258
	15	39	4058*
C [Aligned at 45^0]	0	3	236
(317 g)	10	32	1537
	15	37	1627
D [Horizontally aligned]	0	2	80
(317 g)	10	28	987
	15	32	1013

The opposed tape springs increase the stiffness of an inflatable boom by up to 4.9 times when tapes are added in configuration B using the collar attachment system, from 833 N/m to 4058 N/m, at 15 PSI. This is for a mass increase of 2.3 times to the inflatable structure. It was observed that as the boom is rotated from configuration B towards configuration D the buckling of the tape springs changes from a simple hinge. Figure 7.10 shows that the opposed tapes in configuration D behave similarly to a simple cantilever beam where the resultant

tension and compression stresses across the tape width cause the tape springs to buckle as a simple Euler – Bernoulli beam. Tape spring pivoting with respect to the collar and root clamp assemblies was also observed for configurations C and D. This resulted in the boom tip deflections being greater than if the tapes were rigidly clamped at the boom root and is a significant limitation to this tape spring attachment method. This tape spring buckling and rotation occurs gradually as tip mass is increased, and is mirrored by the deflection curve data. Configuration D provides 22% additional stiffness to an inflatable boom at 15 PSI. This is significantly lower in comparison to the performance of configuration B. Unlike the horizontally aligned tapes in configuration D, the vertically aligned tape springs of configuration B buckle as a hinge previously described in chapter 6. This happens suddenly at the boom root, and can be seen by the abrupt change in boom stiffness in the deflection curves.

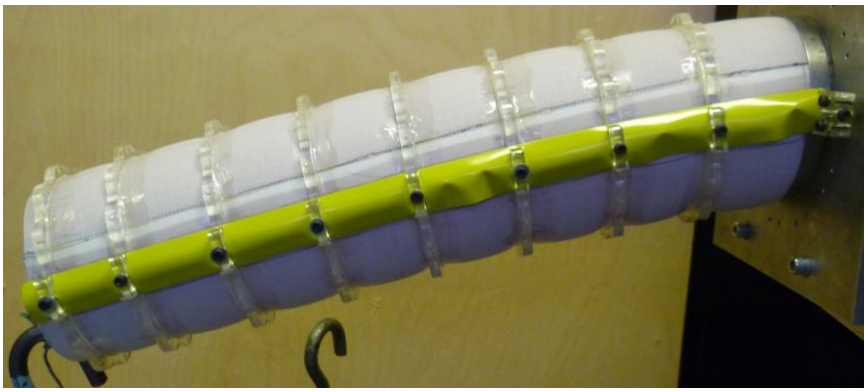

Figure 7.10: Configuration D with 8 evenly spaced attachment collars under 32.8 Nm applied root bending moment at 15 PSI.

This first initial hybrid boom used 8 attachment collars showing a significant increase in structural performance, however mass and stowage volume are the main design drivers for space applications and must be considered. Reducing the number of tape attachments allows the tape springs greater operational flexibility and overall capability for the stowed hybrid boom whilst also removing a sizeable mass. An additional test programme considers the structural performance of a hybrid boom using 4 attachment collars in configuration B. This allows a comparison between the two hybrid booms while also including 5 inflation pressures from 0 – 15 PSI to evaluate the structural performance with respect to inflation pressure. The mass of the hybrid boom is reduced by 23% to 243 g when removing 4 attachment collars and 8 clamps.

The averaged moment-deflection response of configuration B using 4 collars is given in Figure 7.11 with comparisons to the 8 collared hybrid and inflatable booms. Reducing the number of collars shows a rigidity performance loss that might be expected based upon the tape spring length study in Figure 6.9. Increasing the free length between attachment points from 0.05 to 0.1 m shows a rigidity loss of 37 and 34% for 10 and 15 PSI respectively. The average peak moment of the 10 PSI 4 collared boom remains constant however at 15 PSI with the average peak moment shows an increase of 10 Nm when reducing from 8 to 4 collars. This is likely caused by the variable thickness and defects between tape springs leading to sizable peak moment differences in the hybrid boom repeat tests seen clearly in Figure 7.9.

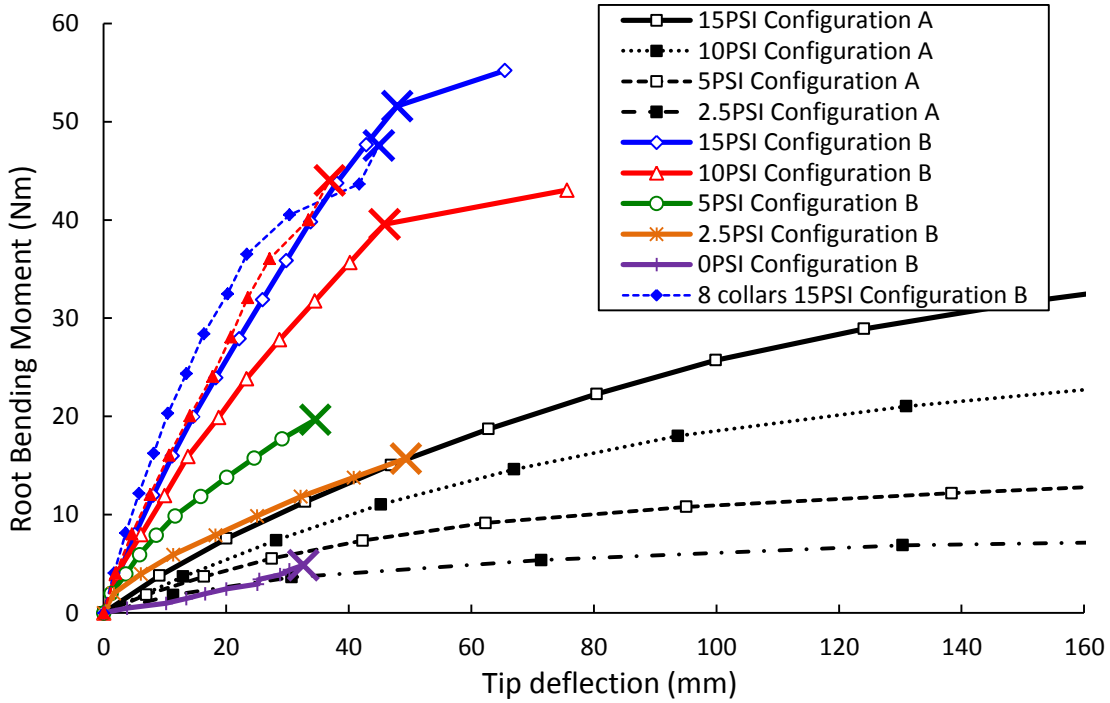

Figure 7.11: Average moment-deflection response comparison between configurations A and B up to 15 PSI with 4 attachment collars.

Increasing the number of pressure intervals shows an almost linear increase in boom rigidity with respect to inflation pressure while there is a distinct peak moment performance change between 5 and 10 PSI. At lower pressures the hybrid boom upon tape buckling collapses immediately with very large deflections. At the higher inflation pressures the boom does not collapse catastrophically after the failure point marked 'X' as seen in Figure 7.11. It is observed the inflatable boom at these pressures support the tape spring as it buckles and the combined structural support results in a significantly stronger boom. This will be investigated in greater detail with the FEA model where a greater number of pressure intervals are easily tested to confirm this trend.

In comparison to an inflatable boom the hybrid boom in configuration B with 4 attachment collars has shown to have a similar moment-deflection response at 2.5 PSI as an inflatable boom at 6 times the inflation pressure at 15 PSI up to failure at 16 Nm. The peak moment of this 2.5 PSI hybrid boom occurs at 65% of the 15 PSI configuration A M_w. The hybrid boom can also operate at 0 PSI as the tape springs and attachment collars create a framework structure around the inflatable boom. At 0 PSI the structure can sustain an average peak moment of 4.2 Nm with the same deflection response as the 2.5 PSI inflatable boom. Hybrid boom failure occurs at 108% of the 2.5 PSI inflatable boom M_w.

7.3 Single and Double Tape Springs

The effect of tape location was explored in more depth to identify the most effective position one and two tape springs can be located. It is known from the previous section the hybrid boom maintains the greatest stiffness and maximum bending moment when opposed tapes are placed vertically aligned to the applied load. However an opposite sense bend provides the greater buckling moment for a tape spring. Therefore one and two tape springs are attached to the boom on the top and bottom surfaces as shown in Figure 7.1 for configurations E, F, G and H to determine the optimum tape placement. The test procedure remained the same using 8 evenly spaced attachment collars on a 0.4 m long inflatable boom at 10 PSI.

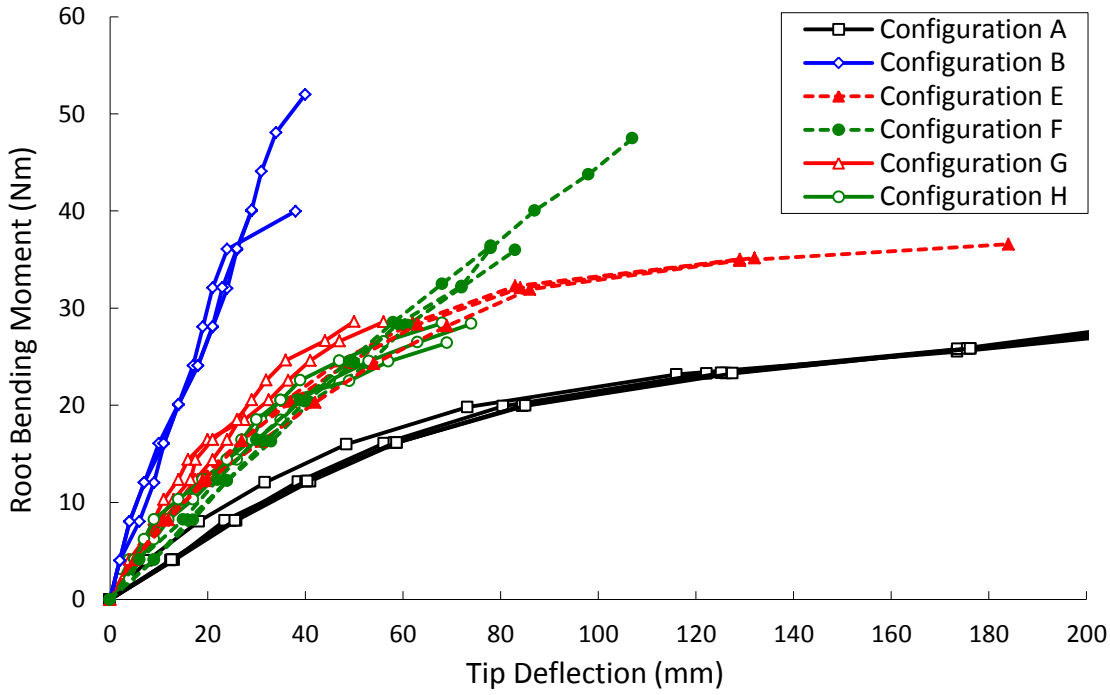

Figure 7.12: Single tape spring orientation comparison at 10 PSI using 8 attachment collars.

Figure 7.12 shows how the hybrid boom performance changes between the single and double tape spring configurations alongside configurations A and B. Figure 6.9 shows that tape springs placed in the opposite sense have a greater buckling moment compared to equal sense bending. However the single tape spring results of configurations G and H show that the tape spring on the top surface of the boom, and subsequently in the weaker equal sense bending but in tension, provide a slightly stiffer boom than when placed in their opposite sense in compression on the lower surface. This is particularly surprising as inflatable fabric booms can only sustain compression forces from the internal pressure. More significantly, adding a second tape shows little different between boom rigidities but a considerable increase of failure bending moment from 21 to 39 Nm between configurations H and F respectively. The yielding seen in configurations E and G corresponds to the torsional bending response of equal sense bend tape spring. For deflections greater than 90 mm these hybrid booms exhibited a corresponding stiffness to the inflatable boom of configuration A suggesting the tape spring has reached the steady state bend.

Table 7.4 quantifies the boom structural performance for the six configurations. The single top tape provides an average boom stiffness of 1649 N/m. This is over 200 N/m greater than a tape placed on the lower surface. Configuration F using two tapes springs in opposite sense bending shows a comparable peak moment to configuration B of 39 Nm. However it is clearly displayed that placing two tapes in configuration B vertically aligned to the applied load and on opposite surfaces, with the combined structure operating in both tension equal sense bend and compressive opposite sense bend, produces the most rigid boom for the added mass with a stiffness 2.9 times greater than configuration F.

Table 7.4: Average boom performance for single tape configurations (* peak values).

Boom configuration	Boom mass (g)	Pressure (PSI)	M_{fail} (Nm)	Stiffness (N/m)
A (No tapes)	135	10	16	781
B (Vertically aligned)	317	10	41	3258
G (Single top tape)	290	10	25	1649
H (Single bottom tape)	290	10	21	1412
E (Double top tapes)	299	10	32	1184
F (Double bottom tapes)	299	10	39	1128

This section has given the hybrid boom structural performance data of single and double tape springs and identifies that a single tape is best placed on the top surface of the boom while two tape springs are best attached inline to the applied load opposing each other

(configuration B). To improve the performance of a hybrid boom in this configuration the inflatable boom and tape spring properties can be varied. The inflatable boom properties have been investigated in the previous chapter 4, while the following section focuses on the tape springs.

7.4 Tape Spring Thickness

The simplest means to affect the tape spring properties is to increase their thickness. This section investigates how the structural performance changes with increased tape thickness for comparison to the similar study of the skin thickness of the inflatable boom. This will determine trends and optimise the hybrid boom in terms of mass and volume. Configuration B has shown to be the most effective hybrid boom construction using two tape springs with the collar attachments and is used to compare the structural performance when varying the tape spring thickness. The thickness was adjusted by layering the tapes into double and triple sets for configurations I and J respectively and shown in Figure 7.1. The mass increase of these booms was 7 and 14% to 260 and 277 g respectively. The limitation of this approach is the tape springs are free to move relative to each other between the collar attachment points and may have to be considered when being applied to computational models. The hybrid boom setup used 4 evenly spaced attachment collars and had 5 test inflation test pressures of 0, 2.5, 5, 10 and 15 PSI.

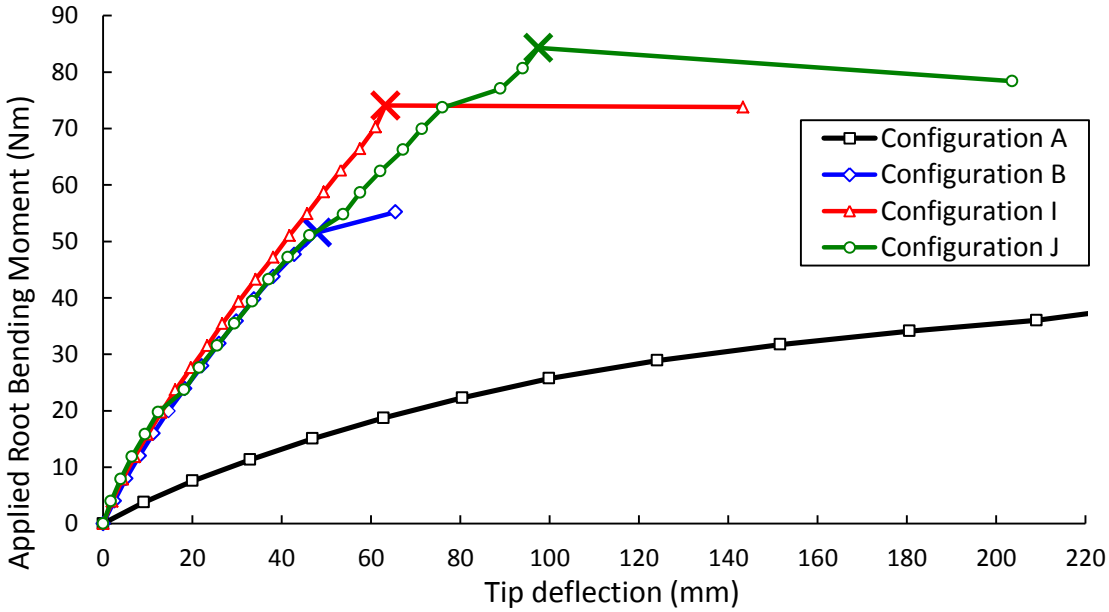

Figure 7.13: Average tip deflection response of a hybrid boom with varying tape spring thickness at 15 PSI using 4 attachment collars.

Figure 7.13 illustrates the typical moment-deflection response seen at all inflations pressures for the three hybrid boom configurations showing continued performance benefit over an inflatable boom at the same pressure. Figures 7.14 and 7.15 give the failure moments and rigidities of these hybrid booms across the inflation pressures up to 15 PSI respectively. The rigidity of configurations I and J remain relatively constant while peak moment increases with tape thickness. Placing another tape pair from configuration B to I increases M_{fail} from 49 to 71 Nm at 15 PSI while also changing the response of the hybrid boom system. The failure deflections seen in Figure 7.13 for configurations I and J are significantly increased as the hybrid boom fails immediately upon tape spring buckling in a sudden catastrophic manner unlike configuration B. The effectively thicker tape springs of configurations I and J caused the inflation pressure not to be sufficient for the inflatable boom to support the tape springs as they buckled. This leads to nonlinear increases in peak moments with respect to tape spring thickness and the failure mode to be dependent on both inflation pressure, and material properties of the hybrid boom. The peak moment was also affected by the significantly higher tip loads causing failure of the attachment collars and clamps. This occurred indeterminately from 60 Nm which limits the reliability of the peak moments for configurations I and J at 10 and 15 PSI but can still be utilised to determine the average boom rigidity before failure.

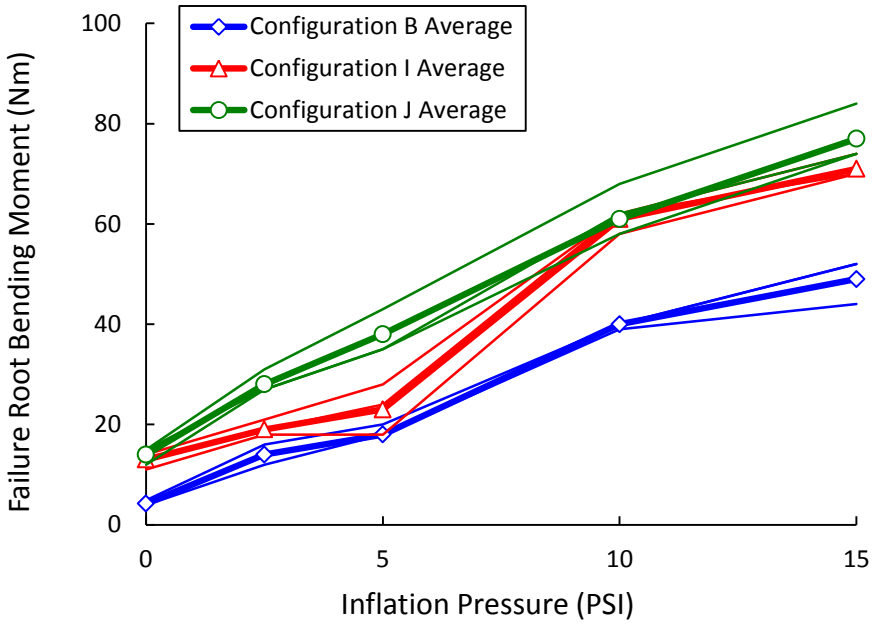

Figure 7.14: Failure moment of the hybrid boom with 4 attachment collars and varying tape thickness.

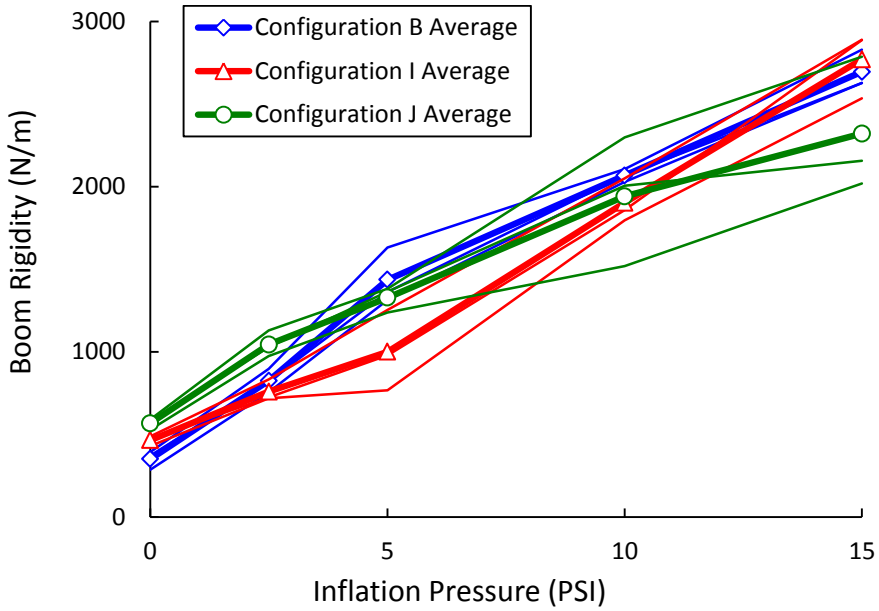

Figure 7.15: Hybrid boom rigidity with 4 attachment collars and varying tape thickness.

7.5 Cross Formation

The cross formation has four tapes evenly spaced around the circumference of the boom as shown in Figure 7.1. This arrangement of tape springs was implemented by Lou et al. (2000)[15] which used larger tape springs with the same 38 mm inflatable boom radius. The research focused on Euler buckling from boom compression down the boom length. However for tip deflection tests and potential asymmetric orientations it is important to know how the hybrid boom structural performance changes with respect to the cantilever tip load direction. The cross formation could potentially allow applications to ignore boom loading direction as a tape spring pair or combination of tape springs will always be in the stronger opposed orientation. This allows a reduction in complexity to integrate the boom into an application with the additional mass of two tape springs and clamps being relatively low at 35 g. The experimental 4 taped cross formation hybrid booms were tested in three orientations; square, 22.5^0 and diagonally to the applied load, and illustrated in Figure 7.1 for configurations K, L and M respectively. The mass of these booms was increased by 14% from configuration B to 278 g. For each cross configuration 5 inflation pressures of 0, 2.5, 5, 10 and 15 PSI were tested with 4 evenly spaced attachment collars. The remaining setup and procedure stays constant to previous tests.

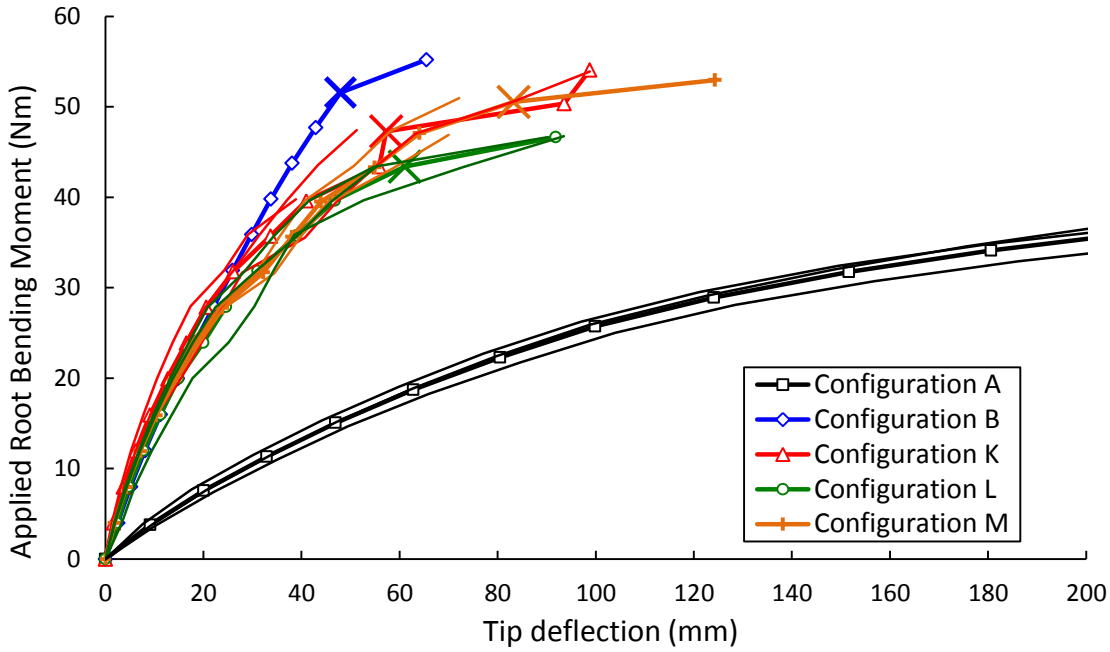

Figure 7.16: Average tip deflection response of a cross formation hybrid boom with 4 attachment collars at varying orientations at 15 PSI.

The four cross configuration shows no performance advantage over the two opposed tapes of configuration B and causes a yielding of the boom as it approaches peak moments in all configurations. This is comparable to configurations C and D where tapes out of line of the applied load buckle similarly to an Euler - Bernoulli beam seen in Figure 7.10. The advantage of the four crossed hybrid boom configurations is the performance is relatively constant between the three orientations considered, where the opposed tapes of configurations B, C and D are altered significantly as shown in Figure 7.9. Table 7.5 quantifies the structural performance change of the four crossed tapes, as the applied load is effectively rotated around the axis for each configuration, showing the performance trends remain constant over the inflation pressures 0 – 15 PSI. An exception is the boom rigidities at pressures below 10 PSI where the four crossed tape configurations show an increase in stiffness in comparison to the opposed tapes of configuration B. This is likely due to the failure mode change also seen in configuration B between 5 and 10 PSI at which point the additional two tape springs appear to provide significant additional support over configuration B. It should also be noted the four crossed tape springs did not yield as seen in Figure 7.16 for inflation pressures below 10 PSI. This resulted in the apparent reduction in boom stiffness from 5 to 10 PSI for configurations K, L and M further confirming this failure mode change for the four crossed tape configurations. This failure mode change leads to the tape spring collar framework providing a greater proportion of the structural rigidity which is better supported with the addition of two further tape springs in all the four cross configurations over configuration B.

Table 7.5: Hybrid boom structural performance of 2 opposed and 4 crossed hybrid booms with 4 attachment collars.

Configuration	Pressure (PSI)	M_{fail} (Nm)	Rigidity (N/m)
B	15	49	2695
K-L-M		47 ±4	2138 ±202
B	10	40	2067
K-L-M		38 ±2	1509 ±86
B	5	18	1436
K-L-M		17 ±3	1913 ±270
B	2.5	14	825
K-L-M		13 ±3	1569 ±199
B	0	4.2	351
K-L-M		6 ±2	614 ±94

7.6 Summary

The experimental hybrid boom investigation has proved their feasibility and shown significant structural performance increases can be achieved against a standard inflatable boom. Preliminary studies on tape spring attachment methods have considered maintaining tape spring curvature and the relative movement between the tape springs and the inflatable boom to maximise their potential highlighting the importance of the attachment method with respect to both structural and stowage performances. The attachment inserts show a possible method with significant structural performance gains while the rigid collar system maximises the tape spring potential at the cost of significant added mass and inflexibility. Although creating a framework supportive structure around the inflatable boom, the attachment collars were selected for the experimental investigation of the hybrid boom due to their desirable benefits as a prototype. The setup significantly reduced manufacture and setup costs enabling rapid repetitive testing totalling 129 individual tests across a wide range of permutations and configurations providing performance trends. A more likely final design would attach the tape springs directly to the inflatable boom from which it would be possible to roll the structure onto a mandrel providing a suitable stowage solution. The selected configuration for a final design can utilise the attachment method comparison data to provide an initial structural performance estimate where gluing the tapes along the whole length has shown a moment and rigidity performance drop of 36 and 38% respectively in comparison to the 4 collar attachment approach in configuration B.

Twelve hybrid boom configurations were tested across five inflation pressures ranging between 1 and 4 tape springs added to an inflatable boom using the collar attachment system. The opposed tape springs vertically aligned to the applied load of configuration B using 8 collars produced the greatest structural performance gain in comparison to an inflatable boom of over 2.6 and 4.9 times for failure bending moment and rigidity respectively. At the maximum operating pressure of 15 PSI this 0.4 m long hybrid boom with a 0.05 m radius can sustain 39 Nm with a rigidity of 4058 N/m. The moment-deflection response also highlighted a change in the failure mode of the structure between 5 and 10 PSI. The inflatable boom at higher pressures was able to provide sufficient support to limit deflections as the tape springs were taken through buckling.

Increasing the tape thickness simulated by tape layering in configurations I and J showed no significant change to the tape spring rigidity whilst increasing the peak bending moments. It was not possible to determine the relationship between tape thickness and M_{fail} due a change in the failure mode, and tape spring defects and thickness inaccuracies caused by the low manufacture tolerances of the tape springs used.

The four crossed tape spring configurations K, L and M showed little difference in the failure moment in comparison to configuration B with small rigidity losses and gains at high and low inflation pressures respectively. This is marked by the change in the failure mode between 5 and 10 PSI. The four crossed tape spring configurations demonstrated small variations in structural performance as the applied tip load is rotated around the boom circumference. This offers applications to treat a hybrid boom similarly to an inflatable boom where structural performance is assumed constant regardless of the loading direction for a mass increase of 14% from configuration B.

The experimental hybrid boom results have shown structural performance gains with respect to an inflatable boom. They can also be used to validate numerical models. The following chapter develops a FEA hybrid boom model using the experimental results to confirm trends and identify in greater precision the moment-deflection response of a cantilever hybrid boom.

Chapter 8

Finite Element Analysis of a Hybrid Boom

This chapter aims to create a FEA model of a hybrid boom by combining the developed inflatable boom and tape spring models of chapters 5 and 6. The hybrid boom FEA model is validated with the experimental data of the previous chapter. The model is used to advance the understanding of the hybrid boom structural performance and confirm trends with greater clarity and depth where permutations are quickly and easily investigated. The developed FEA hybrid boom model is then able to investigate other boom permutations not considered experimentally.

8.1 Background and Construction

This section outlines the FEA conducted in this chapter and provides detail on the hybrid boom FEA model construction. The subsequent sections provide time and mesh convergence studies with an initial hybrid structure in configuration B. This configuration is then used to show an initial model performance comparison against the experimental data leading to an in depth material properties investigation followed by analysis of the remaining experimental configurations. This includes tape spring thickness and 4 tape springs placed in the cross formation. The final FEA section focuses on other hybrid boom permutations not investigated in the previous experimental chapter 7. This includes three distinct areas of interest; collar attachment and attachment frequency, compression effects, and circumferential tape spring placement. An additional attachment study is also briefly investigated with the chapter being summarised in the final section.

The hybrid boom was constructed in ABAQUS 6.9-3, selected as it is a robust solver for gossamer structures[94,95,104,108] and modelled using explicit dynamic time steps providing good convergence through the nonlinear buckling of the boom. The validated inflatable boom and tape spring FEA models previously defined in Table 5.3 and 6.1 respectively were used to

create a 0.4 m long hybrid boom shown in Figure 8.1. The inflatable boom and tape springs used M3D4R membrane and S4R shell elements respectively.

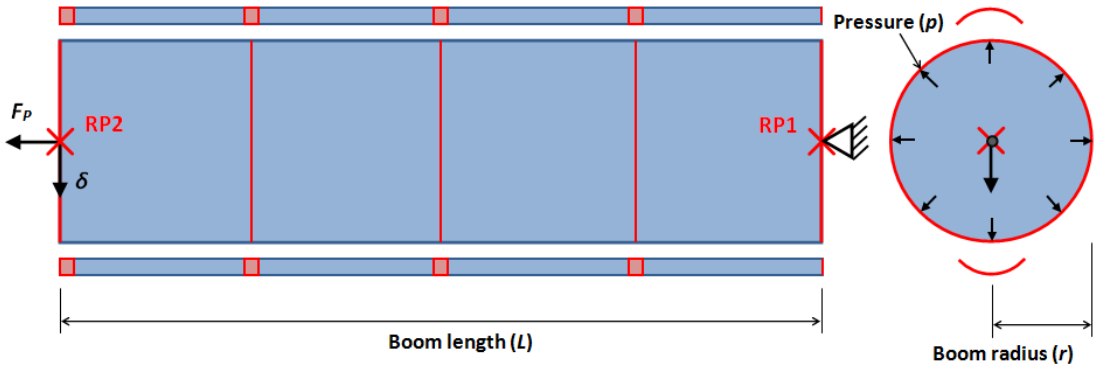

Figure 8.1: FEA hybrid boom model in configuration B.

Figure 8.1 shows the hybrid boom assembly with two opposed tape springs of configuration B. The FEA model considered the collars in the experimental study by offsetting the tape spring from the surface of the boom by 10 mm giving a maximum diameter of 0.12 m. The tape spring and inflatable boom root edges were rigidly tied to RP1 simulating the root attachments for both the inflatable boom and tape springs used in the hybrid boom experimental study. The boom tip was rigidly tied to RP2 from which axial inflation pressure and tip deflections are applied. The tape springs were tied to the boom at the attachment locations on the inflatable boom and include the 5 mm collar thickness. The remaining boundary and loading conditions including root fixing, inflation and applied displacement were identical to the defined inflatable boom given in chapter 5 and summarized in Table 5.3. The tape springs were modelled on the idealised constant radius and no twist. This was because of the constant radius of the attachment collars shown in Figure 7.6 which forced the tape springs into the idealised profile at the attachment points and straight along the tape length when clamped. A brief investigation into the two tape spring profiles previously displayed little variation in the bending moment characteristics shown in Figure 6.8. This led to the simplification of a constant idealised profile along the entire tape length. The initial mesh and time steps were based upon the previous FEA models. The tape springs had 8 elements across their width and the boom had 64 around its circumference known as 8TS64B. Both used structured regular square elements. The inflation and tip deflection time steps were both set to 0.5 s where both mesh convergence and time step were investigated in the following preliminary studies. Table 8.1 gives an overview of the hybrid boom FEA model parameters.

Table 8.1: Key parameters of a 0.4 m hybrid boom for FEA.

Parameter	Value	
	Inflatable boom	Tape spring
Element type	M3D4R	S4R
Radius	$r = 50 + \frac{4.5\times10^{-3}}{p}$ mm	Constant 14.5 mm
Embrace	-	1.73 Rad
Length	0.4 m	
Constraints	ENCASTRE rigid boom and tape root (RP1)	
	Rigid boom tip (RP2)	
	Tied tapes to boom circumference (x4)	
Loads	Internal pressure, p	-
	Tip force (RP2), $F_p = \pi r^2 p$	-
	Tip displacement (RP2)	-
$E_H = E_w$	438 MPa	195.3 GPa
$E_L = E_f$	314 MPa	-
$v_{HL} = v_{wf}$	0.21	0.3
$G_{HL} = G_{wf}$	280p Pa	75 GPa
t	0.195 mm	0.11 mm
ρ	588 kg/m^3	7860 kg/m^3

8.2 Preliminary Studies

The preliminary studies consisted of a time step and mesh convergence analysis to validate the hybrid boom FEA model. These studies were conducted using the hybrid boom configuration B at 10 PSI inflation pressure with the model shown in Figure 8.1 and the parameters in Table 8.1 unless otherwise stated.

8.2.1 Time Step and Mesh Convergence Studies

The tip deflection step was found to be the most influential in determining the inflatable boom solution convergence. The model stability limit was found to be 0.1 s to ensure the boom rigidity is accurately captured. The peak moment converges to 36.8 ±0.3 N from 0.1 s time steps where a longer time step continually reduces oscillations.

A similar assessment on the inflation time step revealed negligible change in the model response of 0.3% in M_{max} and no effect to the boom rigidity between 0.01 and 10 s. Therefore to ensure an accurate capture of the model response the selected time steps for subsequent tests are 0.1 and 1 s for inflation and tip deflection respectively.

The hybrid boom mesh convergence study considered both tape spring and inflatable boom mesh densities. The element sizes were based upon the previous inflatable boom and tape spring mesh convergence studies in chapter's 5 and 6. The tape springs, labelled TS, were meshed using 4, 6, and 8 elements across their width. The inflatable boom, labelled B, used 16, 32 and 64 elements around the circumference. Figure 8.2 shows three of the meshes to illustrate the combinations.

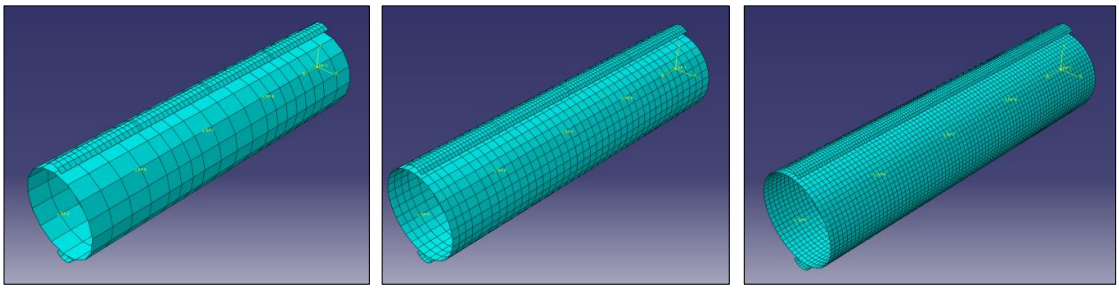

a) 4TS16B = 864 elements b) 6TS32B = 2472 elements c) 8TS64B = 7280 elements

Figure 8.2: Three hybrid boom mesh densities in configuration B

Figure 8.3 displays the tip deflection responses for the various mesh densities showing the rigidities and buckling bending moments are predominantly dependent on the tape spring and inflatable boom mesh densities respectively. The rigidity tends to converge for booms with 6TS with rigidity remaining relatively constant for all finer meshes. The large deflection moment response converges for meshes with elements greater than 16B. The 32B booms are within 2 Nm and 6% of the finest 64B mesh peak moment of 35.0 Nm. The 6TS32B allows for a reduction in computational expense of over 52% in comparison to the finest 8TS64B mesh. The computational expense is an important consideration as the differing orders of magnitude between the two material properties create a very large stiffness matrix that requires a significant increase in the number of iterations to converge on a solution. For comparison the hybrid boom FEA model is 10 and 4 times more computationally expensive than the equivalent inflatable and tape spring FEA models respectively. The 6TS32B mesh is selected for subsequent tests as it accurately captures the hybrid boom tip deflection response with rigidity and peak moments within 6% while minimising the significant computational expense.

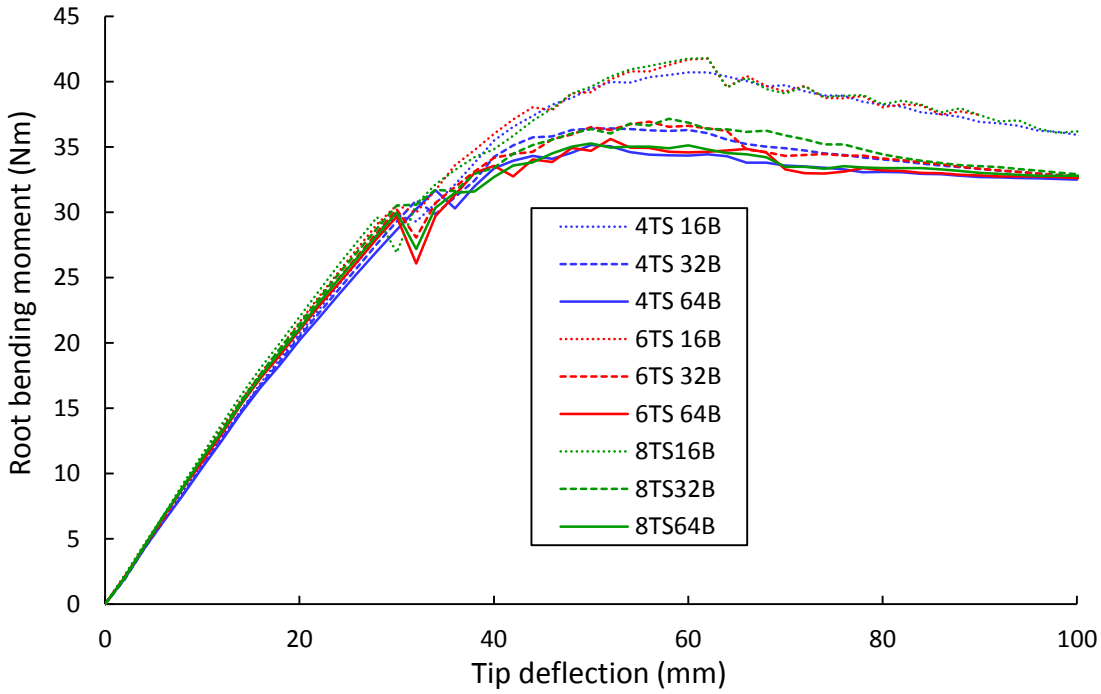

Figure 8.3: Mesh convergence study of a 0.4 m hybrid boom in configuration B at 10 PSI inflation.

From this setup various other configurations are simulated to further verify the model against the experimental data and investigate in detail other permutations.

8.3 Hybrid Boom FEA Results

The hybrid boom FEA results are split into two sections; model verification and model permutations. The model is verified and compared against the experimental results including the single, double, opposed and 4 crossed configurations at the inflation pressures tested. The model is then able to investigate other boom permutations of interest including additional pressure intervals, attachment points, and compression effects.

8.3.1 Configuration B FEA Validation with Experimental Results

The experimental hybrid boom results concluded configuration B to be the optimum setup for a tape spring pair. Figure 8.4 displays the tip deflection response of the FEA model and experimental data in configuration B over the 5 inflation pressures tested showing a close correlation between the data. The peak moments are within the experimental range and 11% of the average for all inflation pressures 0 to 15 PSI.

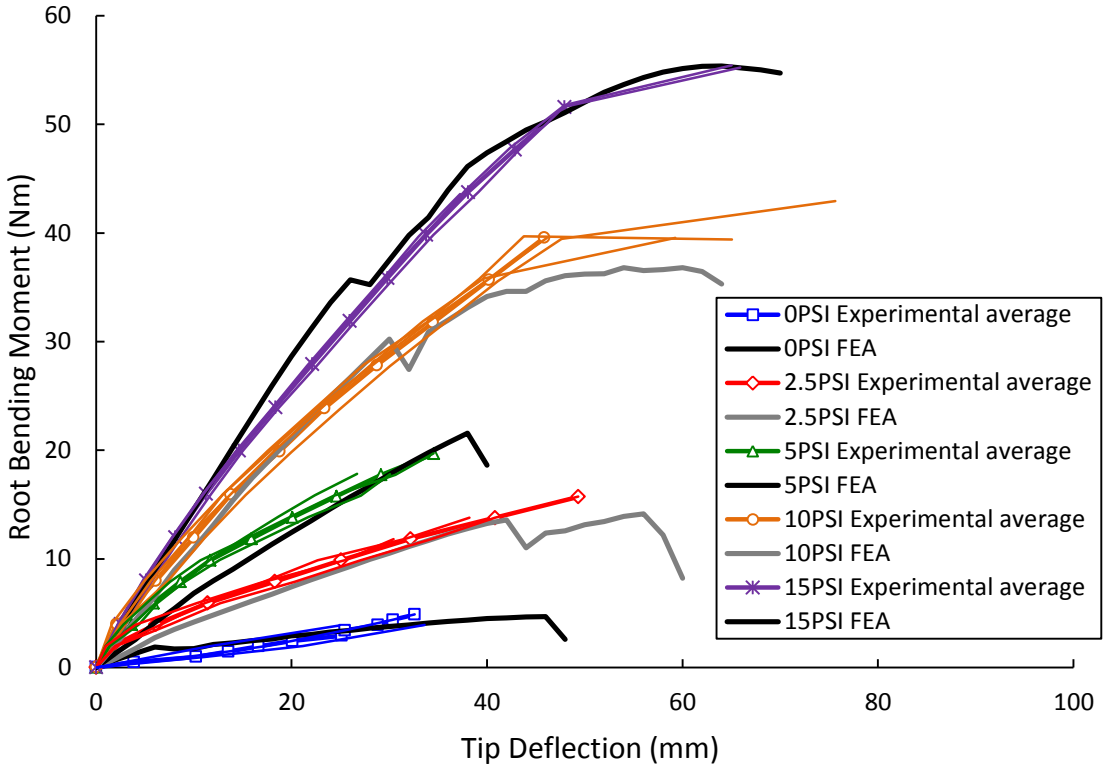

Figure 8.4: Tip deflections for the hybrid boom experimental and FEA model in configuration B.

The booms have similar tip deflection responses between the data sets. There is a key difference between the model and the experimental procedure. The FEA model applies a tip deflection and reports the forces acting at the root, whereas the experiments applied a force and measure the resultant tip deflections. This difference allows the FEA model to highlight bending moment behaviour not seen in the experimental data. For the higher pressures of 10 and 15 PSI there is a change in the boom response after 30 and 36 Nm respectively. At these bending moments the tapes buckle as shown in Figure 8.5 b), however the additional inflation pressure now provides sufficient structural support to reach an increased M_{max} in combination with the bottom tape spring partially buckled in a two point bend.

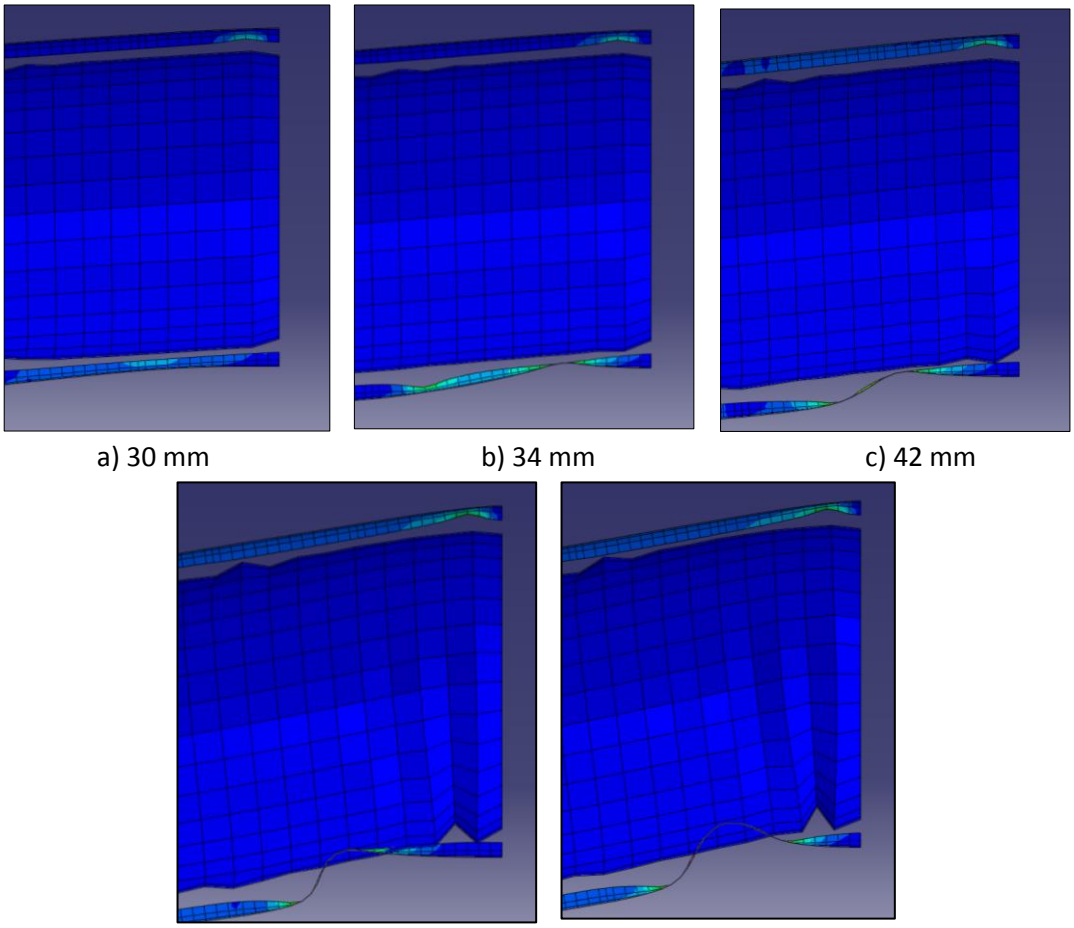

a) 30 mm b) 34 mm c) 42 mm

d) 56 mm e) 66 mm

Figure 8.5: FEA hybrid boom root buckling at 10 PSI showing a) peak moment pre buckling, b) initial 2 bend buckle, c) converged 2 bend buckle, d) peak moment, e) buckled boom.

The boom rigidity from this point is considerably reduced, yielding as the partially buckled tape spring converges into a continuous 2 point bend as tip deflections increase. The inflatable boom also contributes to a greater proportion of the structural performance. This is limited by the pressure acting against bending compression forces causing wrinkling which is seen in Figure 8.5. This can be seen in some of the 10 and 15 PSI experimental data in Figure 8.4 where the applied moment causes a sudden change in boom stiffness but not complete failure. As the experiment uses larger discrete loading intervals this was not always achieved. This also caused the initial partial tape buckling to be missed in the data although the converged two bend buckle is observed in Figure 8.6 further verifying the FEA model. The FEA model did not use a contact control where the parts are able to pass through each other as displayed in Figure 8.5. This fundamental difference to the experiment can explain why the 10 PSI experimental data has a greater M_{max} response where the pressurised boom acts on the bottom tape spring causing a delay in total tape buckling. As M_{fail} is within 3% of the experimental data and does not occur for lower pressures a contact solution was not

implemented to save computational expense. This does not occur for pressures lower than 10 PSI as the inflation pressure does not provide sufficient support to stop the tape spring buckling straight from a) to e) in Figure 8.5. The two failure modes are named; boom supported and boom unsupported tip deflection failure, where initial partial tape buckling does and does not occur respectively.

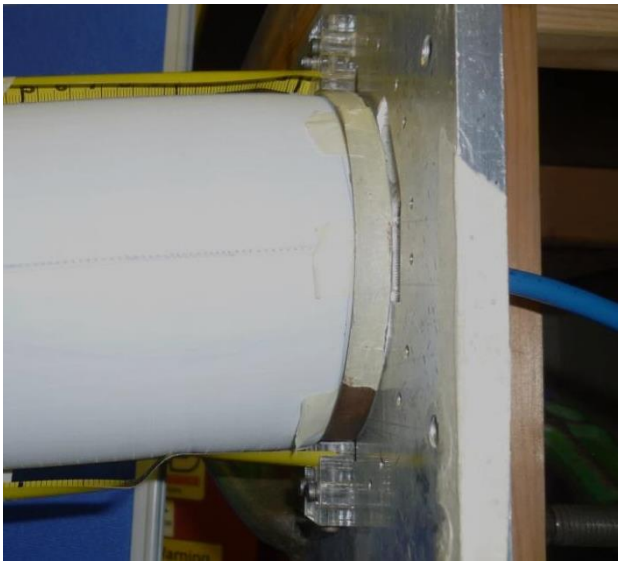

Figure 8.6: 15 PSI configuration B experimental hybrid boom at peak moment.

Another significant difference between the FEA and experimental data is the under prediction of the initial boom rigidity. The experimental data although appearing linear in comparison to an inflatable boom in Figure 7.11 has a yielding stiffness prior to any tape buckling. This is shown in Figure 8.4 where all pressurised booms are initially underestimated by the FEA model. The inflatable boom also presented stiffness yielding due to the nonlinear fabric properties where the shear modulus was the greatest contributor to the variable stiffness and is considered among other inputs in a material properties study.

8.3.2 Material Properties Study

The shear modulus was shown to be a non-constant parameter for the inflatable boom and was therefore considered over a similar range of values to determine if it can account for the stiffness yielding in the experimental hybrid booms. Figure 8.7 displays the model response for several shear moduli at 5 PSI inflation pressure where the disparency between experimental and FEA boom rigidities is greatest.

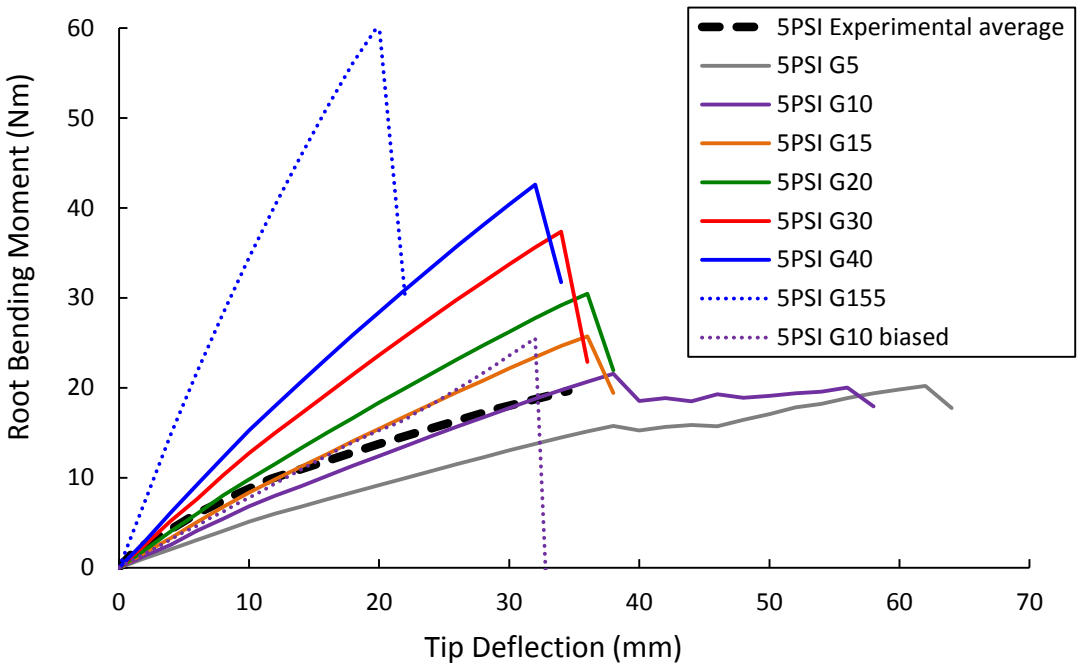

Figure 8.7: FEA 5 PSI configuration B hybrid boom with various shear moduli.

Increasing the shear modulus from the estimated 10 MPa (named G10) shows a significant increase in structural performance. The boom rigidity increases by approximately 7%/MPa from 1427 N/m when *G* = 10 MPa. The increased rigidity matches the experimental data at various tip deflections where the required shear modulus drops with increased deflection. It clearly shows the calculated shear modulus value of 20 MPa in chapter 3 cannot be used as a material constant. Similarly to the inflatable boom, the hybrid boom shear modulus value depends on inflation pressure and applied loading. The FEA model could be improved to match the experimental data using a variable shear modulus decreasing from 40 to 5 MPa with increasing loads. However the shear modulus relationship of $G = 280p$ from the inflatable boom investigations still provides a suitable approximation for structural performance where the majority of the moment-deflection response is within the 5% variability seen in the experimental results.

The peak moment also increases with shear modulus. This suggests maximising the hybrid boom structural performance by using an isotropic or stiff in shear boom material. A FEA model is run with a shear modulus of 155 MPa. This significantly higher value is calculated from the isotropic relationship of the averaged Young's moduli and shows the importance of inflatable boom material when used in a hybrid structure. A similar isotropic material would increase the peak moment and boom rigidity by 2.8 and 5.4 times respectively over the Nylon

fabric used to 60 Nm and 7650 N/m respectively. For comparison, the performance gain for an equivalent inflatable boom is 0 and 33% for peak moment and rigidity respectively.

Another option is to realign the fabric to limit the effect of the low shear stiffness. A final FEA model rotated the material orientation 45^0 around the normal (n), shown in Figure 8.1, to match the biased boom in Figure 3.11 and maximise the boom shear stiffness in bending. The biased fabric hybrid boom shows an increase of 18 and 8% in peak moment and rigidity respectively. However the FEA biased hybrid model displayed a significant increase in radius and decrease in boom length that was similarly found in the material property study of section 3.7. This caused the hybrid boom tapes to buckle due to compression forces prior to tip deflections at inflation pressures greater than 5 PSI. The FEA indicates the biased fabric orientation advantage is limited to low inflation pressures, however further experimental tip deflection tests would be required to confirm the continuum fabric model remains valid and the potential of biased hybrid booms. The dimension data of an inflatable boom with no tape springs is displayed in Table 8.2 where there is a considerable difference between the biased experimental and FEA model suggesting additional factors such as shear locking[114,115] and the inter-fibre frictional effects seen in Figure 3.16 also need to be considered.

Table 8.2: Inflated dimensions of a biased configuration A boom at 5 PSI.

Boom	Radius (mm)		Length (mm)	
	Experimental	FEA	Experimental	FEA
Biased	51.6	58.2	396	364
Non-biased	50.8	50.9	405	404

A final observation shows it is possible to delay tape buckling by reducing the shear modulus. Figure 8.7 shows when G = 5 MPa the reduction in rigidity allows the bottom tape spring to buckle similarly to the higher pressures as shown in Figure 8.4. This effectively delays boom failure to a larger tip deflection at a similar peak moment in comparison to G = 10 MPa.

There is still a discrepancy between the data sets where the experimental hybrid boom buckles at a lower peak bending moment and tip deflection in comparison to the FEA model. It is therefore important to quantify the potential error in the model that is caused by material property measurements. By considering the measured error ranges given in Table 3.3 the Young's and shear moduli, Poisson's ratio and density for both materials and the thickness of the inflatable boom contribute to a combined error of 6 and 8% for rigidity and buckling moment respectively. However the tape spring thickness was shown to have a significant

effect on the buckling moment in chapter 6 and may have a similar effect in a hybrid boom system.

The tape spring thickness of the FEA hybrid boom model was adjusted to 0.11 ± 0.01 mm show with the data given in appendix V. The boom rigidity varies by a maximum of 1.6%. However the peak bending moment can be significantly affected. It is increased for thicker tapes where 10 and 15 PSI inflation pressures correspond to small changes of 36.9 ±0.4 and 55.4 ±0.5 Nm respectively. For lower inflation pressures where the tape spring does not partially buckle prior to M_{max} tape spring thickness has a greater effect. In this situation the tip deflection buckling ranges from 6 to 10 mm between the two tape thicknesses. This has an increasing effect on M_{max} as boom rigidity increases with inflation pressure. At 5 PSI the peak moment is 21.1 ±1.8 Nm. This explains why the experimental repeat data have small variations in boom rigidities with much larger variations in peak moments particularly at lower inflation pressures.

Table 8.3 quantifies the structural performance variations of the FEA hybrid boom model when considering the combined material properties error range showing a maximum FEA inaccuracy of 8 and 15% for rigidity and peak moment respectively. The experimental data is also presented showing averaged experimental results are within the FEA error range except at the average 10 and 15 PSI. At these higher pressures the boom rigidity results vary due to the yielding boom supported failure to peak moment in the FEA measurement which was difficult to define during the experimental tests with discrete loading intervals.

Table 8.3: Hybrid boom FEA model and experimental error range in configuration B.

Data	Inflation pressure	M_{max}		Averaged stiffness	
	(PSI)	(Nm)	(% range)	(N/m)	(% range)
FEA	0	4.7 ±0.7	15%	303 ±13	4%
Experimental		4.2 ±0.4	9%	351 ±57	16%
FEA	2.5	14 ±1	7%	811 ±62	8%
Experimental		14 ±2	14%	825 ±71	9%
FEA	5	21 ±2	10%	1427 ±102	7%
Experimental		19 ±1	5%	1436 ±171	12%
FEA	10	37 ±1	3%	1677 ±133	8%
Experimental		39 ±1	3%	2067 ±40	2%
FEA	15	55 ±1	2%	2223 ±188	8%
Experimental		51 ±6	12%	2695 ±117	4%

8.3.3 FEA Hybrid Boom Model Configurations

To further verify the experimental hybrid boom trends the remaining configurations were considered in the FEA model. The setup remained the same as the configuration B FEA model with the tip deflection data for all 60 permutations given in appendix V. The model fitted well with the experimental results for all configurations and pressures with structural performance comparisons given in table 8.4 for some key hybrid booms at 10 PSI.

Table 8.4: Structural performance comparison between FEA and experiemental results of key configurations at 10 PSI.

Configuration	M_{fail} (Nm)		Averaged Stiffness (N/m)	
	FEA	Experimental	FEA	Experimental
A	20	16	739	781
B	37	40	2533	2067
I	61	62	2615	1902
J	92	65	2629	1941
K	45	39	5882	1543
L	42	38	5922	1487
M	40	39	6012	1511

The opposed tape spring configurations B, C and D show a significant structural performance drop as the tapes are rotated around the boom circumference to configuration D. This was also observed in the experimental data where configuration C is within the experimental peak moment range of 28 and 36 Nm when using 4 and 8 attachment collars respectively. However the FEA rigidity of both configurations C and D are significantly higher than the experimental data of over 1 and 1.5 times respectively. This is caused by the tapes pivoting around the attachment clamps when placed on the side of the boom and is a limitation of the designed experimental test rig reducing the potential of the tape springs in these orientations. A similar difference in performance was found for the crossed tape spring configurations K, L and M and is highlighted in the rigidity performance in table xx. A possible adaptation to the FEA model is to change the tied constraint of the tapes to allow rotational degrees of freedom (DOF) at the tie constraints. This will mimic the pivoting of the tapes when placed on the side of the boom observed in the experimental tests. The tip deflection data for this updated model is given in appendix V and shows a good approximation of the experimental tip deflection profile.

As discussed in the experimental section 7.5, the structural performance of the revised FEA configurations K, L and M are reduced with respect to configuration B. The structural performance of configurations B, I and K are given in Table 8.4. In comparison to configuration B, placing two additional tape springs on the boom side that are allowed to pivot reduces the peak moment and final boom rigidity by 14 and 64% respectively. However ensuring a final design prevents tape rotation at the attachment points will improve the boom stiffness by over 2.3 times with an increase in M_{max} of 24%. This is because the tape springs orientated on the side of the inflatable boom are unable to shear in deflection and are restricted in lateral movement due to the collar and opposite tape spring constraint preventing torsional folding. This causes these tape springs to act similarly to a vertical 'I' section beam with the tape spring curvature providing significant structural rigidity. Altering the attachment design will affect this rigidity gain by preventing relative tape spring rotations. Removing the constraining collars leaves only the inflatable boom hoop stress to prevent side orientated torsional folding of tape springs and would reduce rigidity performance at lower inflation pressures.

Table 8.5: FEA structural performance of configurations B, I and K at 10 PSI.

Configuration	Number of tapes	Mass (g)	M_{fail} (Nm)		Average Stiffness (N/m)	
			Boom unsupported	Boom supported	Boom unsupported	Boom supported
B	2	243	30	37	2533	1677
I	4	260	61	-	2615	-
K (Rotational DOF)	4	296	26	32	2552	609
K (No pivoting)	4	296	46	-	5882	-

In contrast configurations B and I display the opposite trend where rigidity remains relatively constant and M_{max} is proportional to tape thickness. Therefore tape placement is optimised for rigidity by placing tapes in the cross configuration while peak moment is maximised by placing two opposed tapes on the top and bottom boom surfaces if tape spring attachment rotations are prevented. An additional advantage of 4 tape springs in the cross formation is the orientation of the boom with respect to the load. This makes little difference to the structural performance of a maximum 7 and 13% in rigidity and peak moment respectively. It is therefore important to make sure tape rotation at the attachment points is prevented. Maintaining a rigid connection between tape springs and the inflatable boom can provide a significant structural performance advantage for the 4 crossed configurations.

Differences between the model and the experimental results were also observed in between configurations I and J with a rigidity increase for the FEA model. The FEA model uses tape

spring thicknesses of 0.11, 0.22, and 0.33 mm. The varying thicknesses were experimentally created with layers of 0.11 mm tapes as illustrated in Figure 7.1 and were only tied to each other at the attachment clamps. The tapes were able to move relative to each other between these points which could have caused the no apparent change in the experimental boom rigidity while increasing the peak moment of the combined tapes. The FEA model also simplifies the cross section of the layered tape springs that can also contribute to the differences between results. Configuration J also shows a significant difference in peak bending moment between the experimental and FEA data. This is caused by a collar failing in each experimental test resulting in immediate boom buckling at a reduced peak moment.

A further configuration using two 0.055 mm thick tapes arranged similarly to configuration B named configuration 0.5B was also examined and is plotted in Figures 8.8 and 8.9. Configuration B has shown that at higher pressures the peak moment occurs after the tape spring initially buckles as displayed in Figure 8.4 and 8.5 as the inflatable boom provides sufficient support to delay immediate boom failure. Increasing the tape spring thickness increases the required inflation pressure for this affect to occur and therefore it does not occur for configurations I and J at 15 PSI whilst it does occur at pressures lower than 2.5 PSI for configuration 0.5B. Further pressure intervals in configuration B show the transition between the failure modes occurs at 6.4 PSI.

The tape spring thickness is directly proportional to the initial tape buckling moment and often the peak moment for the hybrid boom. The data also shows increasing the inflation pressure has a diminishing effect on the initial tape spring buckling moment. However where boom supported failure occurs the delayed boom buckling is increased significantly and can approximate the peak moment to a linear relationship of

$$\boldsymbol{M_{max} = 1.3\pi r^3 p + 1800 t_{Tape}} \qquad \textbf{(Equation 8.1)}$$

where t_{Tape} is the tape spring thickness.

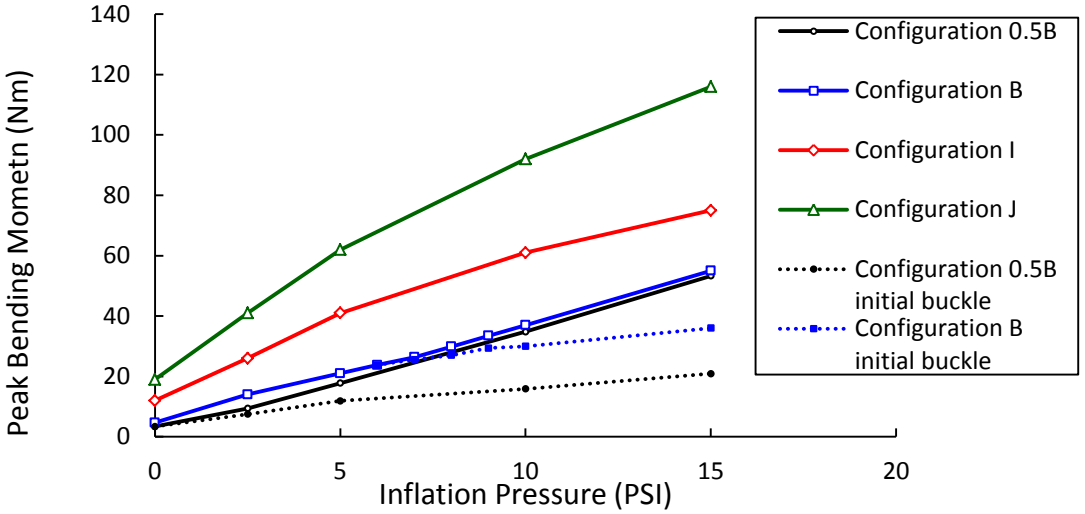

Figure 8.8: FEA peak moments for configuration B with varying tape spring thickness.

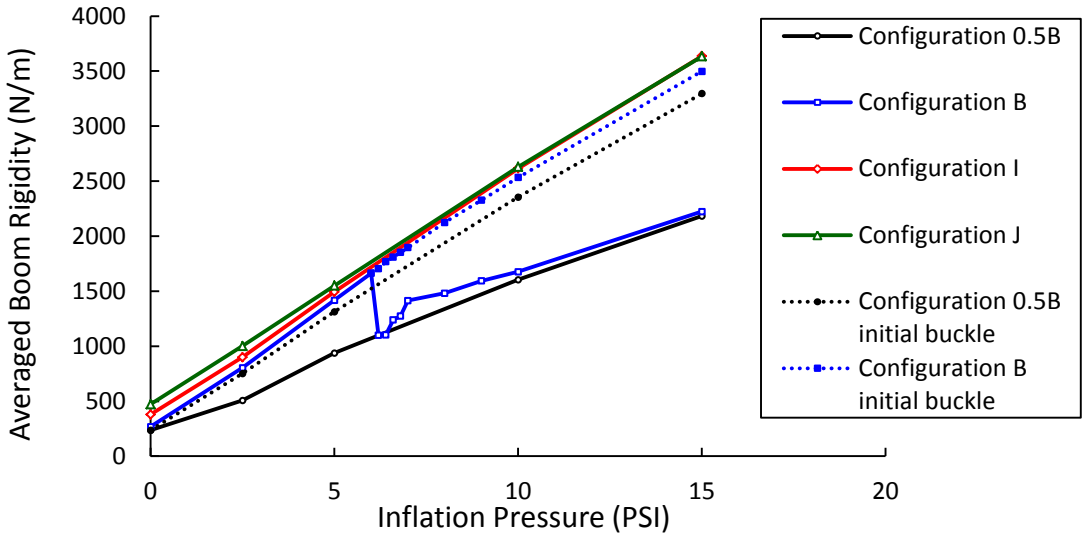

Figure 8.9: FEA averaged boom rigidity for configuration B with varying tape thickness.

A disadvantage of utilising the boom supported failure mode is the potential significant reduction in rigidity. Figure 8.9 gives the averaged boom rigidities with respect to inflation pressure including the values for both failure modes when present. Additional pressure intervals between 6 and 7 PSI highlight the extensive rigidity loss in configuration B as the change in failure mode occurs. The averaged rigidity difference between initial buckling and final failure is a maximum of 664 N/m at 6.4 PSI. This is a stiffness performance loss of 38% where the peak moment is negligibly increased by 0.8%. The structural support of this failure mode after initial buckling increases rapidly for a small pressure increase. At 7 PSI the rigidity and peak moment differences between initial buckling and final failure are 25 and 3% respectively. As inflation pressure continues to increase from 7 PSI both failure modes approximate to linear increases in boom stiffness of

$$\boldsymbol{Rigidity_{BUS}^{config\ B} = 0.031p + 287,} \quad \textbf{(Equation 8.2)}$$

$$\boldsymbol{Rigidity_{BS}^{config\ B} = 0.015p + 670,} \qquad \boldsymbol{[p > 48.3\ kPa],} \quad \textbf{(Equation 8.3)}$$

where the suffixes *BUS* and *BS* are boom unsupported and boom supported failure modes respectively. Considering the data from the three varying tape spring thicknesses Equation 8.2 can be developed for two opposed tape springs to

$$\boldsymbol{Rigidity_{BUS} = 0.031p + 845000t_{Tape} + 194.} \quad \textbf{(Equation 8.4)}$$

Tape spring thickness does not affect the boom rigidity substantially causing a maximum difference of 337 N/m between the 0.055 and 0.33 mm thick tapes at 15 PSI. This is also the case for boom supported peak moments where configurations 0.5B and B can achieve 53 and 55 Nm at 15 PSI respectively. Therefore the hybrid booms with opposed tape springs have a significant structural tradeoff between the peak moment and boom rigidity at inflation pressures where boom supported failure occurs. However, a pair of 0.11 mm thick tape springs make up 11% of the hybrid boom mass when ignoring the attachment mass. The relative lightweight mass of the additional tape spring thickness means the structural performance of a hybrid boom is likely to be designed to the initial buckling of the tape spring (boom unsupported). This will maximise boom rigidity for a specified peak moment.

8.4 Hybrid Boom FEA Permutations

The FEA model allows other hybrid boom permutations to be conducted to analysis the trends in greater detail. This includes compression effects, attachment points and additional pressure intervals.

8.4.1 Collar Attachment

The use of attachment collars for the tape springs presents a rigid object that constrains boom inflation shown in Figure 8.10 and may cause a change in performance to the hybrid boom irrespective of the tape spring configuration. The hybrid boom FEA model is remodelled without tape springs to investigate the potential impact of the attachment collars.

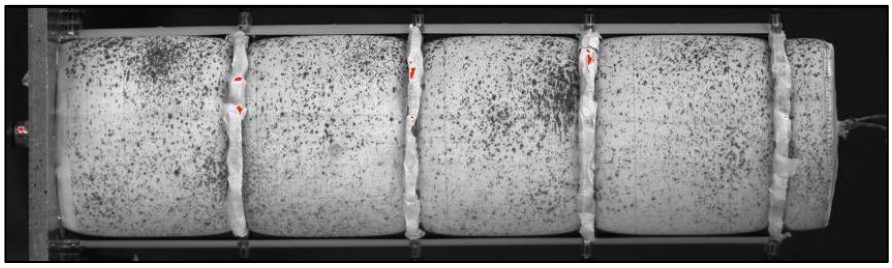

a) Experimental

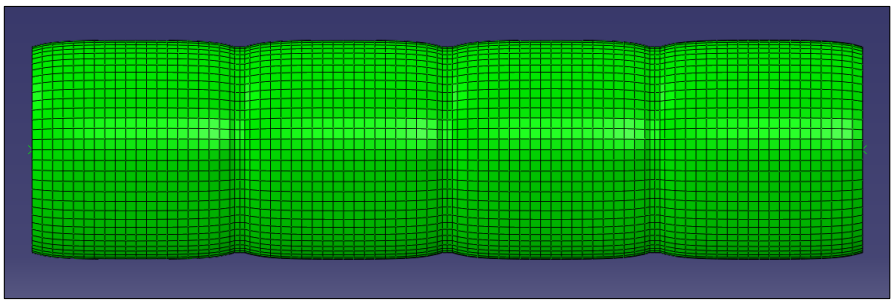

b) FEA model

Figure 8.10: Booms showing radius constraint from the 5 mm thick attachment collars.

The tip deflection profiles for configurations using 1 to 8 collars are given in appendix V. Each configuration is evenly spaced along a 0.4 m long, 0.05 m radius inflatable boom. The boom is inflated at 15 PSI where the radius change due to inflation has the greatest effect and other wise used the same FEA model shown in Figure 8.1 without tape springs. The sustained bending moments are compared at 250 mm tip deflection and show a negligible change of less than 0.8% between 1 and 2 collars. However this increases up to 7 and 10% when 8 collars are included for both bending moment and rigidity performances respectively. Figure 8.11 displays the change in radius of the booms caused by inflation at 15 PSI up to the first constraining collar. Increasing the number of collars reduces the boom volume and average radius where Equation 2.12 expects the bending moment to decrease. However the increase in structural performance is likely due to the additional collars creating an increasing number of volume changes along the boom length which relates to the performance increase determined by Davids and Zhang (2008) for inflatable booms at higher pressures. An additional boom considers 4 constraining collars with a 5 mm thickness to match more closely the experimental setup. The FEA data shows less than a 0.5 and 2.5% difference in bending moment and rigidity performance respectively between the two collar thicknesses and is therefore ignored to simplify the FEA model.

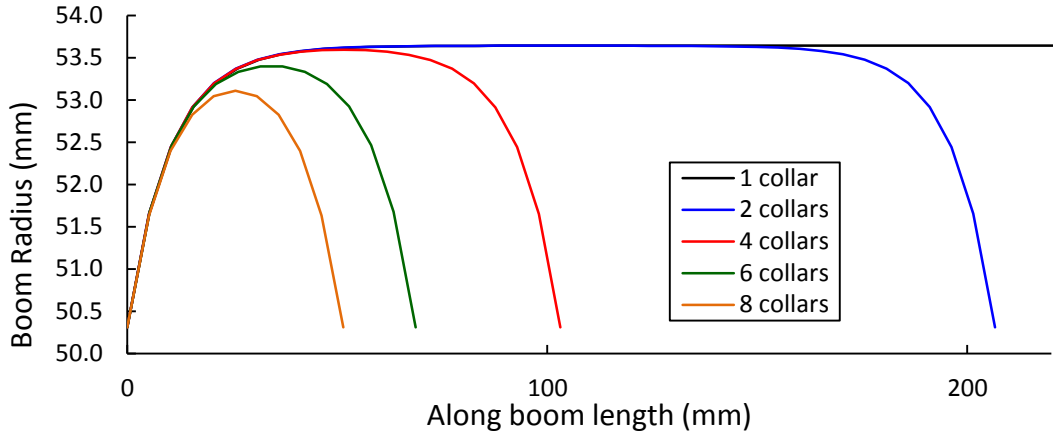

Figure 8.11: Inflatable boom inflation radius at 15 PSI.

The FEA study has determined that the attachment collars have a small but increasing effect on the structural performance of an inflatable boom. However the contribution of the collars needs to be compared against the corresponding hybrid boom performances. These factors should be considered to analyse the performance benefit of the added tape springs as well as the hybrid structure as a whole.

As established in chapter 6 the bending behaviour of tape springs is affected by length and it is recognised that the number of connections between the boom and the tape spring will significantly affect the structural performance of the hybrid boom regardless of the constraining effect of the collars. Altering the attachment intervals will also affect the packing performance of the hybrid boom. There are various ways of folding up these types of structures, including rolling the hybrid boom onto a mandrel, and is highly dependent on the tape spring attachment design. The attachment collars used for this investigative research prevent this approach. However Figure 8.12 displays a diagram of an alternative packing arrangement between the collar attachments as the tape springs are folded into a concertina pattern. Although this is not the most elegant packing solution, it does highlight the important tradeoff between structural and packing performances. Additional stiffness from tape springs added to an inflatable boom will inherently lead to a poorer packing efficiency and will be quantified in detail in the following chapter.

For the packing arrangement shown in Figure 8.12 the maximum number of collar connections is limited by the buckled curvature of the tape springs and the required length to fit in the three tape spring bends. The buckled tape spring has a natural 90^0 equal and 180^0 opposite sense curvature radius of 12 and 15 mm respectively. The natural radius can be reduced and the angles increased to maximise packing performance. This results in an increase in the

steady state moment and can be seen in Figure 6.9 for tape springs shorter than 0.1 m. This is because the limited tape length and constrained tape root and tip require the curvature to be reduced. The limit to this curvature reduction is when the tape spring kinks and permanently deforms. This was observed in the hybrid booms for connecting lengths shorter than 0.1 m as there is not enough tape length to create the three point bend shown in Figure 8.12.

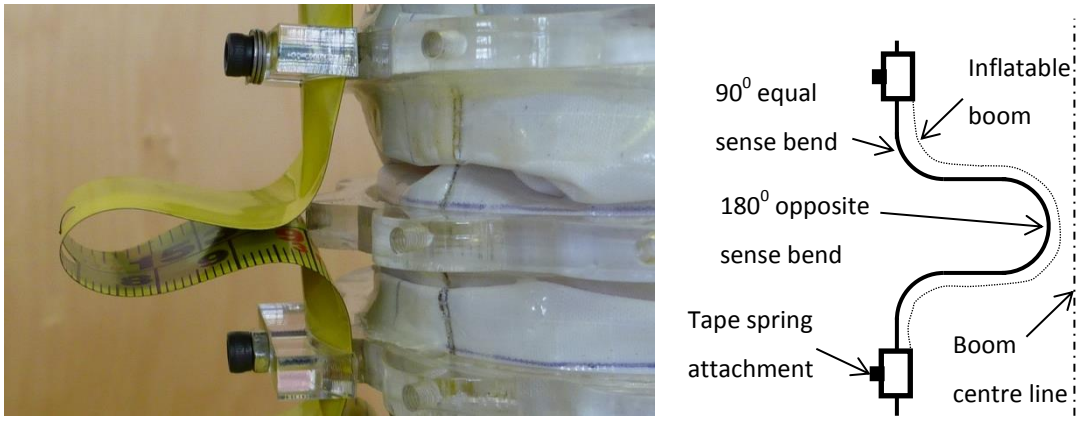

a) Experiment b) Schematic

Figure 8.12: Two potential stowed tape spring configurations.

With this in mind a collar study for configuration B was conducted to establish the structural performance trends. FEA tip deflections were conducted on the hybrid boom with between 1 and 8 attachment collars evenly distributed along the 0.4 m boom. Figure 8.13 shows the boom response at 10 PSI showing the structural performance increase by adding more collars. Configuration A is also plotted for comparison and simply attaching the tape springs at either end of the boom with 1 collar increases the average boom rigidity by 94%. The experimental data for 4 and 8 collars is also presented, displaying good correlation with the FEA model.

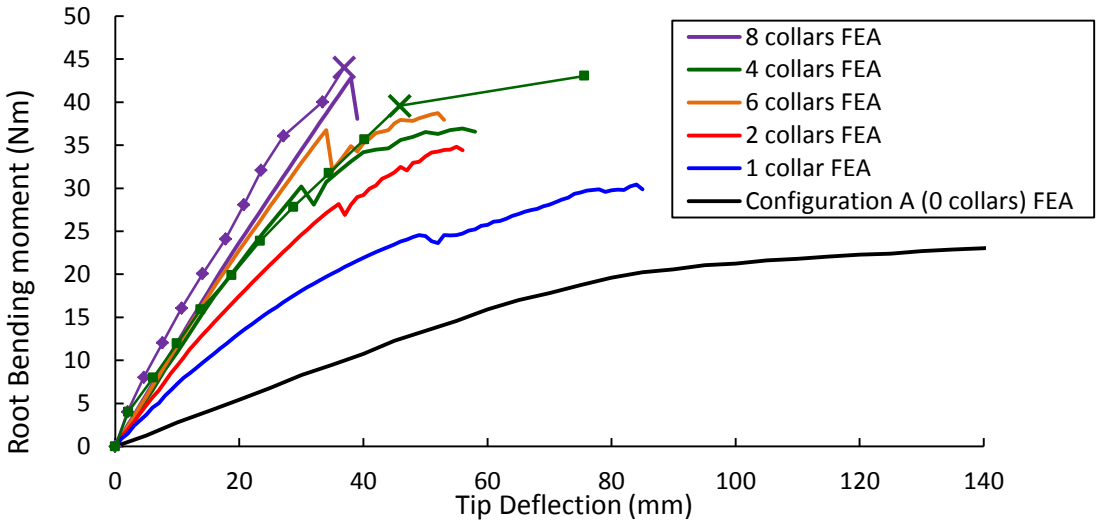

Figure 8.13: Configuration B hybrid boom tip deflections with varying collars at 10 PSI.

The peak moments and average boom rigidity for all the test inflation pressures are given in appendix V and demonstrate a linear trend in structural performance for collar attachment intervals of 100 mm and greater. However for attachment intervals less than 100 mm a significant increase in the peak moment is observed. This occurs because the attachment interval does not allow the tape spring to initially bend in a simple hinge and forces the bottom tape spring to immediately buckle in a two point bend as shown in Figure 8.14. This rigidises the tape spring which can support greater loads prior to this buckling and significantly increases as the interval length is reduced. However short attachment intervals are unlikely to be incorporated into these structures due to the stowage problems previously discussed and are included for completeness.

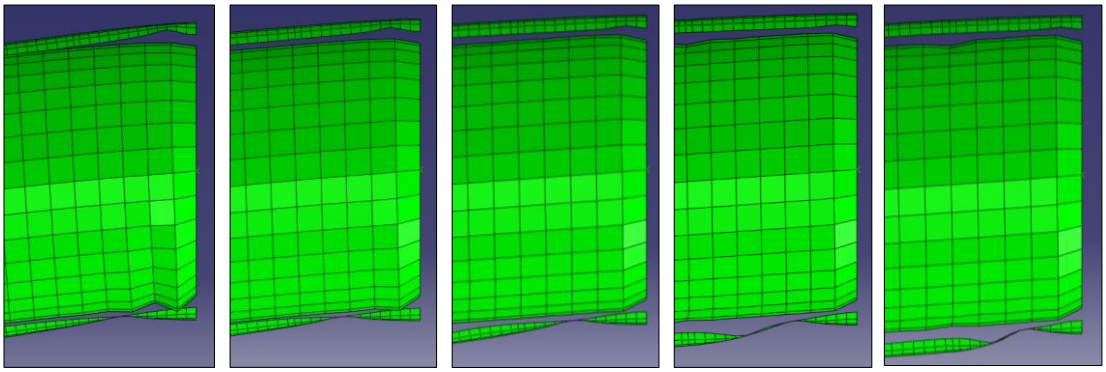

a) 1 collar b) 2 collars c) 4 collars d) 6 collars e) 8 collars

Figure 8.14: Initial tape spring buckling of configuration B at 15 PSI.

The number of attachments has the greatest effect on boom rigidity performance where the stiffness is doubled between 1 and 4 collars for pressures greater than 2.5. The peak moment on the other hand is only increased by between 21 and 38% (10 and 2.5 PSI respectively). The selection of the collar attachment interval will depend on the several tradeoffs including the selected failure mode to specify performance, stowage performance, and attachment mass.

The attachment mass for this boom setup is 18.4 g per collar where the total boom mass and structural performance is given in Table 8.6. The mass of the hybrid boom increases from 188 to 317 g for a single and 8 attachment collars respectively, an increase of 69%. The structural performance increases at a greater rate to the current bulky attachment mass increase, except for M_{max} at pressures greater than 10 PSI where performance gains are reduced. It is therefore advantageous to maximise the number of attachment points with respect to the inevitable tradeoff against packing performance. A final design is expected to minimise mass while

providing sufficient structural attachment capabilities, thereby improving the current structural performance with respect to mass.

Table 8.6: Mass and structural performance of configuration B with varying number of collars.

Number of collars	Mass (g) (percentage increase of *)	M_{max} (Nm) (percentage increase of #,¥)		Average initial stiffness (N/m) (percentage increase of §,†)	
		2.5 PSI	15 PSI	2.5 PSI	15 PSI
1	188[*]	9.8[#]	44.7[¥]	465[§]	1673[†]
2	207 (10%)	11.9 (21%)	55 (23%)	666 (43%)	2619 (57%)
4	243 (29%)	13.5 (38%)	56.1 (26%)	804 (73%)	3498 (109%)
6	280 (49%)	16.5 (68%)	57.8 (29%)	871 (87%)	3817 (128%)
8	317 (69%)	19.6 (100%)	60.7 (36%)	911 (96%)	3996 (139%)

Configuration B using 4 attachment collars has shown an increase in peak moment and rigidity against a comparable inflatable boom of up to 39% and 5.0 times at 15 PSI respectively. Considering the performance change due to the collars the peak moment and rigidity of the hybrid boom is affected by 2 and -1% respectively by the 4 collars. This is a small and negligible effect respectively that will be reduced with lower inflation and increased number of tape springs.

8.4.2 Compression Effect

Another operational consideration is compression effects acting on the boom. This can occur from membrane based designs and has been previously investigated in section 5.3.4 on an inflatable boom. An equivalent study for hybrid booms was also conducted for several configurations. An axial tip force up to 100 N was applied to each configuration. The configurations considered were the varying tape thicknesses of B, I, J and the four tapes in a cross formation named configuration K. The tip deflection responses at 10 PSI are given in Figure 8.24 for 0, 50, and 100 N tip compressions and includes the inflatable boom data for comparison. The remaining pressure intervals showed comparable results and are given in appendix V. Structural performances of the hybrid booms at 10 PSI show a performance reduction that is significantly less in than the inflatable boom. Rotating the cross formation boom into configurations L and M displayed the same trends as configuration K and are also in appendix V.

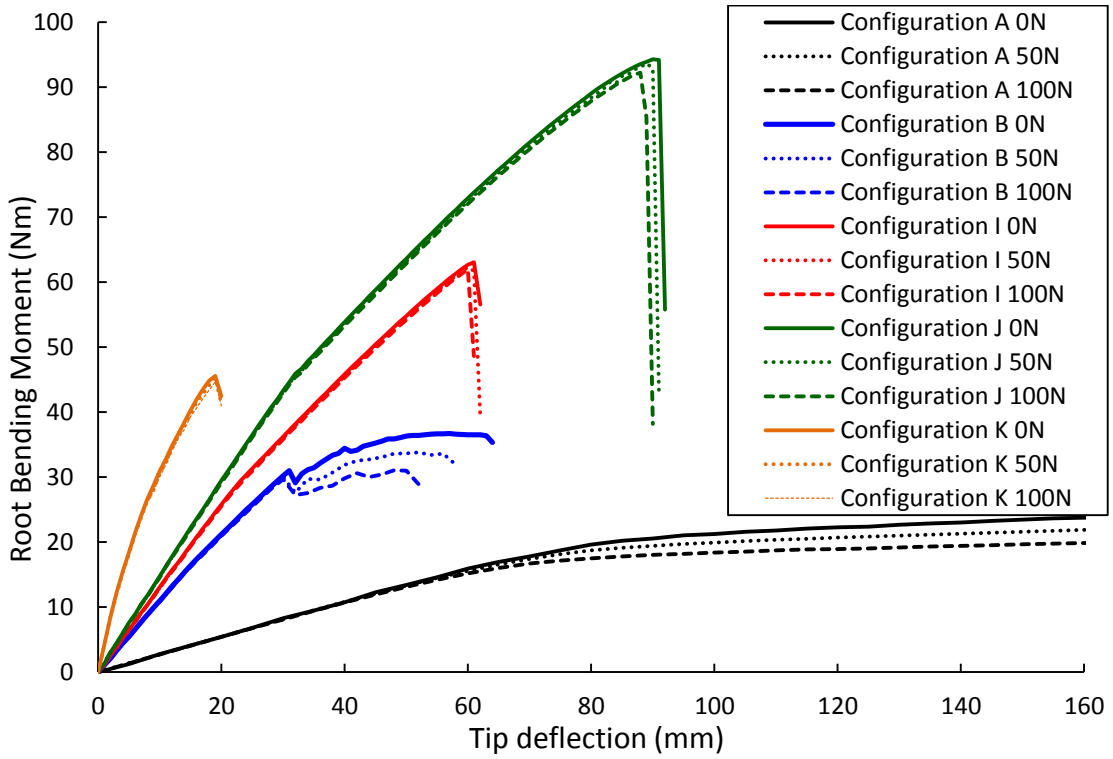

Figure 8.15: 10 PSI tip deflection for compression for configurations A, B, 0.5B, I, J and K.

The maximum M_{max} reduction between hybrid and inflatables booms is halved from 0.6 to 0.3 N per 10 N of compression at 5 PSI in configuration J. However this is for a significantly greater peak bending moment of 62 N resulting in a M_{max} percentage loss of 0.05%/N of compression. This value varies for all pressures and tape thickness's investigated ranging between 0.01 and 0.13%/N showing the peak moment performance of a hybrid boom is no worse and can improve the resistance to compression effects of an inflatable boom by over 10 times. The hybrid booms rigidity is also negligibly affected where configuration B shows a change of 40 ±24 N/m in boom rigidity between 0 and 100 N of applied tip compression.

Compression acting on the hybrid booms has shown to reduce the structural performance. However at the initial buckling of the tape spring in the boom unsupported failure mode the structural performance of the hybrid booms in compression are significantly improved by up to 10 times over an inflatable boom. 20 N is a typical boom tension[7,14] and therefore the gossamer structures created can expect a small performance loss of up to 1.6 Nm and 17 N/m for M_{max} and boom rigidity respectively for hybrid booms in the unsupported failure mode.

8.4.3 Tape springs around the Boom Circumference

To ensure configurations B and K are the optimal location for the tape springs the remaining circumference of the boom is utilised. The attachment collars in Figure 7.6 shows 12 locations for tape springs around the boom circumference. Pairs of opposed tapes were added to each boom and aligned to the loading direction as shown in Figures 8.16 and 8.17.

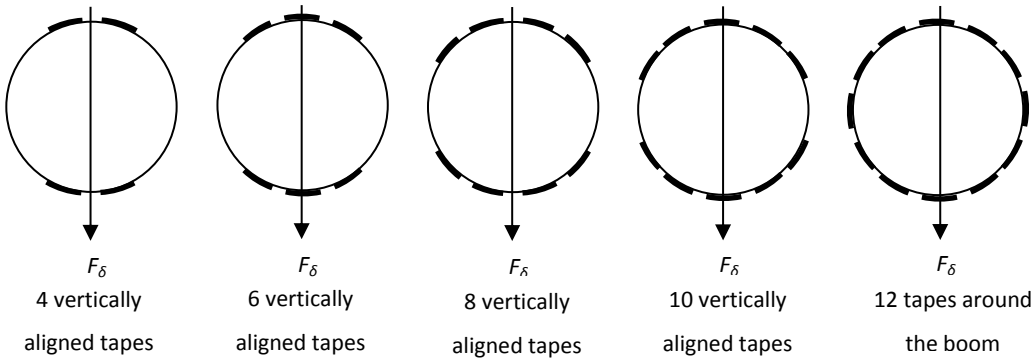

Figure 8.16: Hybrid boom configurations utilising the available circumference of the boom.

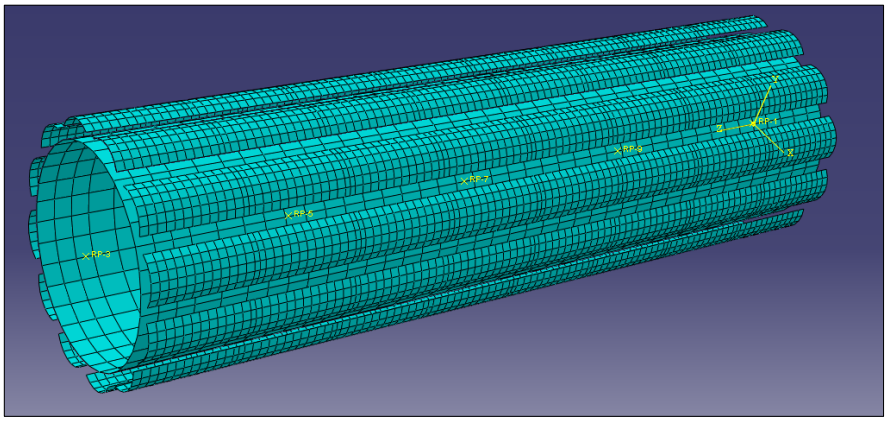

Figure 8.17: FEA hybrid boom model with 12 tape springs placed around the circumference.

The FEA model remained the same as previous investigations using 4 non-pivoting ties between each tape spring and the inflatable boom. Adjusting the model for the 4 tapes in a cross formation has previously shown a performance loss with respect to configuration B when the attachment allows a rotational DOF. Therefore any significant benefit to placing tapes around the circumference will only occur by preventing rotational DOF. Specific peak moment and rigidity performances of these hybrid booms is given in appendix V. They show an increase in structural performance as the number of tape springs increases. This performance gain is amplified at lower pressures where at 0 PSI the peak moment and boom rigidity is increased by 8.7 and 28 times respectively between 2 and 12 tapes. Using 12 tapes has a 72% increase in

boom mass over configuration B. However a direct comparison alongside configurations I, J and K can be employed alongside to assess the effectiveness of tape placement strategies.

Opposed tapes like configuration B and 4 crossed tapes like configuration K have shown a structural performance advantage in peak moment and rigidity respectively creating a tradeoff in optimising the structural performance of the hybrid boom. Placing the tape springs around the circumference may show a compromise and optimise the boom for both peak moment and rigidity. Configurations I, J and K use 4 or 6 tapes and can be multiplied up to compare against the multiple tapes around the circumference. Figure 8.18 illustrates configuration K using 8 and 12 tape springs in the crossed taped location. The opposed tapes are similarly defined in the arrangement of configuration B.

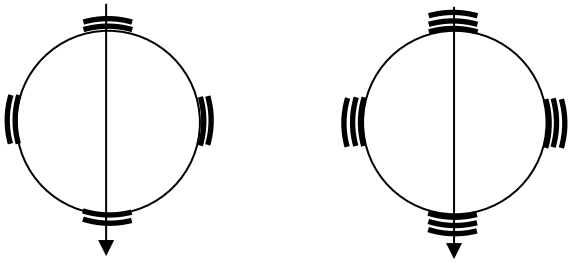

a) 8 tapes b) 12 tapes

Figure 8.18: Cross sectional schematic of Configuration K using multiple layered tape springs in a cross formation.

Figure 8.19 displays the structural performance of the three proposed configurations with increasing numbers of tape springs. The four crossed tapes show a rigidity increase with respect to the opposed tape spring configuration when the number of tape springs, and hence mass, is the same. This is counter intuitive as the second moment of area is maximised by placing the tape springs in the opposed configuration. The side orientated tape springs of the 4 crossed tape springs are constrained by the attachment collars preventing relative lateral movement and causing a significant rigidity increase from these tapes. This results in the side orientated tape springs acting much more substantially and similarly to vertical I section beams with their curvature providing the significant structural rigidity. The hybrid boom is therefore considerably stiffer using the 4 crossed tape spring arrangement with respect to the opposed tape spring configuration. Placing the tapes around the boom circumference does not improve on the peak moment or rigidity with respect to the cross configuration where boom stiffness is less than half and M_{max} is also up to 14 Nm smaller. The opposed tapes simultaneously show the greatest peak moment and poorest stiffness performances where

boom rigidity remains relatively constant at 2.8 ±0.4 kN/m. The data shows the tape location should therefore focus on increasing tape thicknesses in the opposed and crossed tape orientations to tailor peak moment and boom rigidity performances respectively.

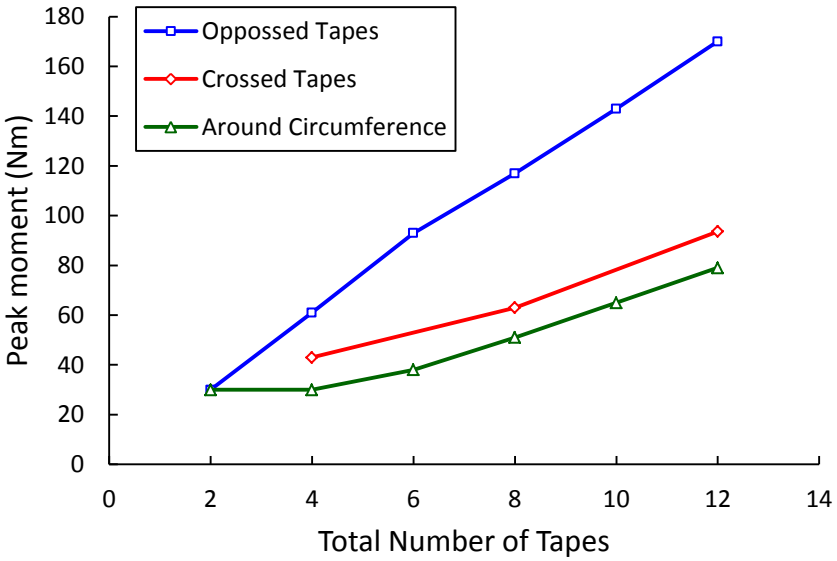

a)

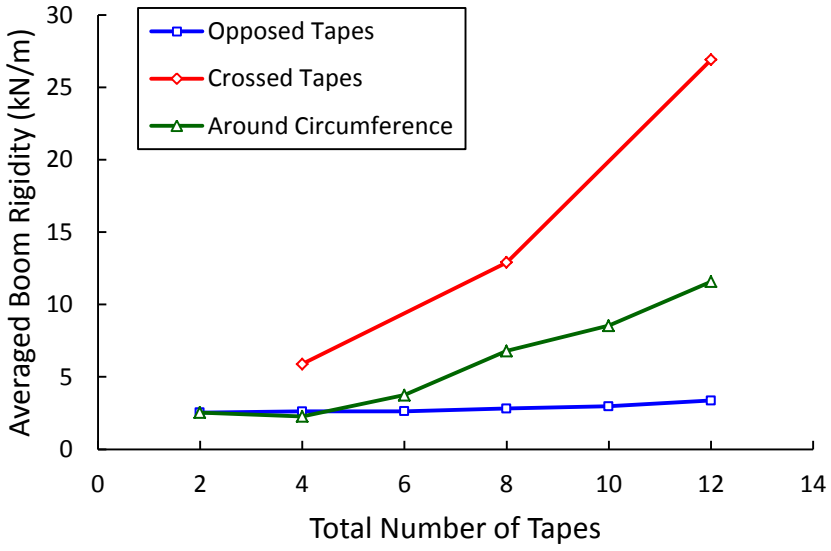

b)

Figure 8.19: Structural performance of hybrid booms with different tape locations at boom unsupported failure, a) peak moment b) averaged rigidity.

8.4.4 Attachments

The collars clamping the tape springs to the inflatable boom is an unlikely attachment system due to their significant mass as previously discussed in chapter 7. Alternative attachment

mechanisms have been also been investigated as shown in Figures 7.3 and 7.5 and include using inserts to fix the tape to the inflatable boom while maintaining the tape spring curvature. A FEA hybrid boom model using this attachment method was created to determine if there is a performance difference between the two approaches and displayed in Figure 8.20. The model uses individual rigid ties between the tape spring and the boom to simulate the Perspex inserts in 8 separate locations for two tapes springs attached in configuration B. The 8 inserts are equivalent to 4 collars where each tape spring is connected to the inflatable boom in the same locations for both attachment methods. The remaining boom setup is unchanged from the collared hybrid boom model.

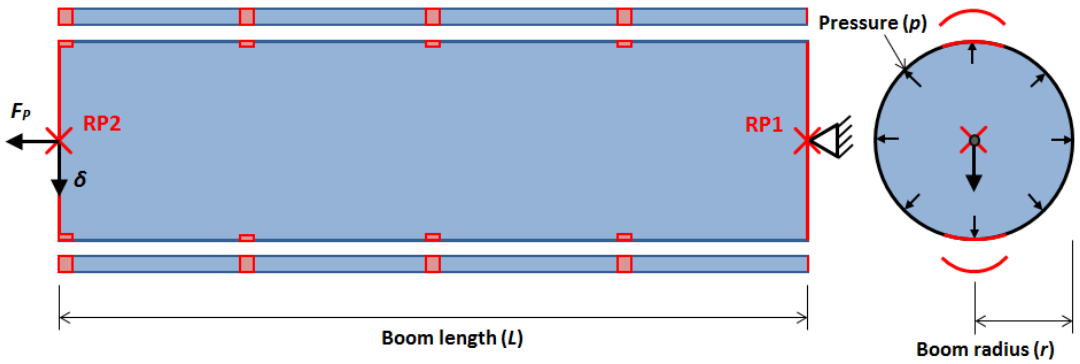

Figure 8.20: FEA hybrid boom model showing 8 rigid attachment points between the tape springs and inflatable boom.

The tip deflection data is presented in appendix V and shows a small difference in structural performance. Both attachment methods show identical trends across the pressure intervals including the two failure modes. Using 8 inserts increases the peak moment by a maximum of 1 N at 5 PSI and a maximum averaged rigidity reduction of 3% at 2.5 PSI in comparison to the 4 collar attachments. This may be due to the lack of boom radius constraint previously caused by the rigid collars that was seen to affect the moment-deflection response in section 8.4.1 of the collar study. The rigid modelled inserts now affect a much smaller surface area of the boom causing much smaller inflation pressure and deformation induced volume changes along the boom length. A preliminary experimental test using these inserts also showed similar initial tip deflections in Figure 7.3 prior to the boom yielding. The experimental yielding was likely caused by the lack of a rigid connection between the upper and lower tape springs previously provided from the collar attachments in addition to the observed adhesive ductile failure between the insert and tape spring joints. Further investigation is required both experimentally and computationally to accurately determine the response of the hybrid boom

utilising this attachment method. The FEA model shows that if sufficient rigid attachment between interfaces is achieved the 8 inserts can provide a mass saving of 51 g over the 243 g four collared boom whilst maintaining structural performance. This would result in a hybrid boom capable of a peak moment and rigidity increase over an equivalent inflatable boom of 2.6 and 4.9 times respectively for a 38% increase in boom mass at 15 PSI. The insert attachment approach will also significantly improve the packing performance of the equivalent hybrid boom using the collar attachments as the tapes becomes unconstrained with respect to one another allowing greater flexibility. Further assessment is required to quantifiably determine these packing performances.

8.5 Summary

An FEA hybrid boom model has been created using the developed inflatable and tape spring models in chapters 5 and 6. Preliminary studies and verification against experimental data have validated the model showing a close and reliable tip deflection response over the 5 experimental inflation pressures for configuration B. The remaining experimental hybrid boom configurations showed the same trends as the experimental data where peak moments increase proportionally to the tape thickness. The FEA model also confirms the experimental trend of 4 tapes in a cross formation. This formation displays a significant benefit as the structural performance varies by a maximum of 13% when the applied load is rotated around the boom circumference. However the FEA highlighted the limitations of the experimental setup when placing tapes on the boom sides showing tape rotation with respect to the attachment points must be prevented. If this is possible, the structural performance is optimised for rigidity with 4 crossed tapes springs in configuration K, and peak moment with opposed tapes vertically aligned to the applied load in configuration B. However this study has not been experimentally verified. In the current experimental setup the hybrid booms are most efficient in configuration B where rigidity is proportional to the number of tape spring attachment points at the inevitable tradeoff to packing performance, or by increasing the inflatable boom skin thickness.

The additional detail afforded from the FEA displayed two failure modes that depend on the interaction between the inflatable boom and tapes springs; boom supported and unsupported failure. Boom unsupported failure occurs immediately upon the bottom tape spring buckling in a two point bend at the boom root causing the whole system to collapse. During boom

supported failure, typically at higher pressures, the inflatable boom provides sufficient support to delay the total collapse and the bottom tape spring partially buckles. In this state the structure can support larger peak moments while yielding until the boom fully collapses when the partially buckled tape spring converges into a two point bend. In boom supported failure the initial buckling of the tape spring continues to follow the structural performance trends of the boom unsupported failures and can be used as a marker for structural performance to ignore the boom supported yielding of the boom and ensure maximum structural rigidity.

A material properties study has shown the error from the measured material properties contributes to a maximum structural performance error of 15% of which the variable tape spring thickness contributes to half the error. The shear modulus has shown to have a very significant effect on the rigidity of the hybrid boom in configuration B where an isotropic material could improve the structural performance by over 2.8 times. Varying the shear modulus to account for the nonlinearity of the fabric material would improve the accuracy of the FEA model at specific tip deflections, however the simplified shear modulus relationship of $G = 280p$ has shown a good approximation to the overall structural performance for all the configurations and permutations considered.

Other boom permutations considered tip compression, the frequency of attachment points, the attachment type, and additional tape spring placement. Tape spring placement around the boom circumference should be avoided. To maximise both rigidity and peak moment configurations K and B should be implemented respectively and tailored to specific requirements assuming no tape spring attachment rotation is achieved. Tip compression has a small effect on hybrid boom performance up to the initial buckling point where a typical tension of 20 N[7,14] will result in a maximum loss of 2.6% in structural performance. The frequency of the attachment points should be maximised for structural performance, however there will be a significant tradeoff in packing performance. Stowing the boom created a minimum attachment interval limit of 0.1 m when using attachment collars. This is to ensure a three point bend in the tape spring between attachment points is possible without permanent deformation of the tape springs. The FEA study into attachment type has displayed a small change in structural performance of up to 3% to the 4 collars when using 8 rigid inserts to attach the tape spring to the inflatable boom. The two attachment approaches show identical hybrid boom structural performance trends when varying inflation pressure in configuration B including changes in failure mode with respect to inflation pressure whilst the inserts save 21% in attachment mass.

From the hybrid boom structural performance trends of the previous chapters configuration K using 4 tape springs in the cross formation square to the applied load is the likely hybrid boom arrangement where tape spring thickness is varied to meet the rigidity and peak moment requirements. To minimise attachment mass and volume, tape spring curvature should match the inflated boom radius causing the inflation pressure to be a design driver of the hybrid structure. In this formation the hybrid boom could be potentially rolled into a stowed position to minimise voids and maximise packing efficiency. With the validated FEA hybrid boom model and experimental data an evaluation of the hybrid boom performance and a comparison against an inflatable boom can be made including mass and packing performances.

Chapter 9

Hybrid Boom Performance Evaluation

The hybrid booms of chapters 7 and 8 have shown a significant structural performance increase over an equivalent inflatable boom; however other performance criteria need to be considered to ensure hybrid booms are a viable solution and this includes mass, stowage capabilities and deployment. This evaluation focuses on configurations A, B and M for a comparison between inflatable and hybrid booms. Configuration B has shown the most significant structural performance increase both experimentally and computationally while the hybrid boom FEA has shown the 4 cross tape configurations have significant potential if tape rotation is restricted with the additional advantage of little structural performance change as the applied load is rotated around the circumference. Configuration M is selected to show the off design and worst case performance of the 4 cross tape configuration. This evaluation uses the structural performances from the FEA models in chapters 5 and 8 where tape rotation with respect to the inflatable boom is prevented by allowing no rotational degree of freedom between the tape spring and inflatable boom tied constraints.

9.1 Structural Evaluation

Figure 8.18 indicates the most suitable location to add tape spring stiffness and therefore 2nd second moment of area of these hybrid booms with respect to failure moment and boom rigidity performance. It can be surmised maximising the second moment of area of the hybrid boom will yield the greatest failure moment performance as might be expected from fundamental beam theory. However this is not necessarily the case with respect to boom rigidity. Figure 9.1 gives the performance of these key configurations against the second moment of area where tapes are placed in the opposed, crossed and circumferential positions as detailed in section 8.4.3. Inflatable boom and hybrid booms at 0 PSI data is also presented for comparison. The structural performance of the inflatable boom is taken from the multi-skinned tests in section 5.3.2.

The structural performance of these hybrid booms is proportional to the second moment of area as shown in Figure 9.1 where configurations B and M give the greatest benefit for peak moments and rigidity respectively. The inflatable boom of configuration A has an I_x = 7.61 x10^4 mm^4. Adding two tapes to create configuration B adds a further 1.71 x10^4 mm^4 or 22%. This has shown to increase boom rigidity and peak moment by 4.7 times and 60% respectively.

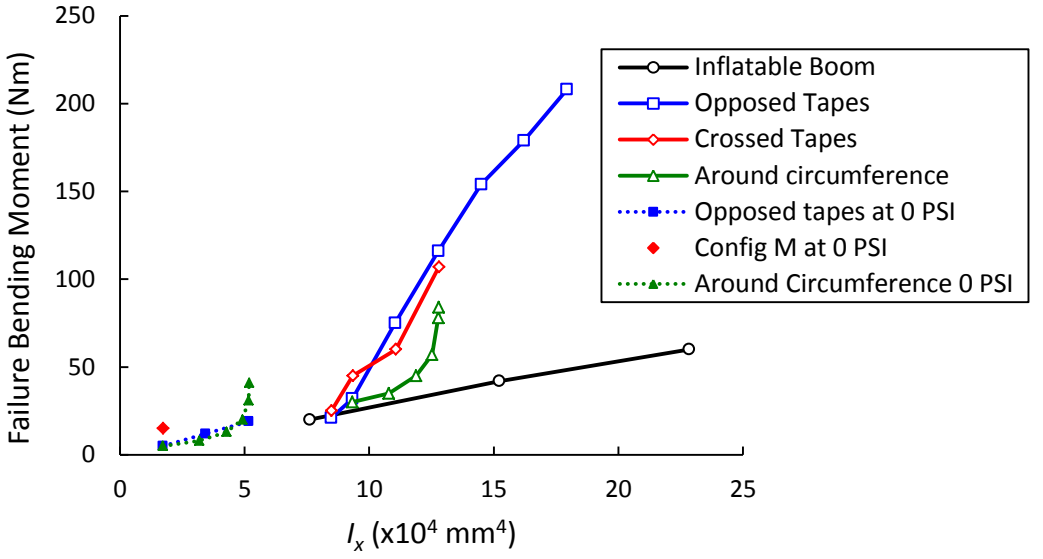

a)

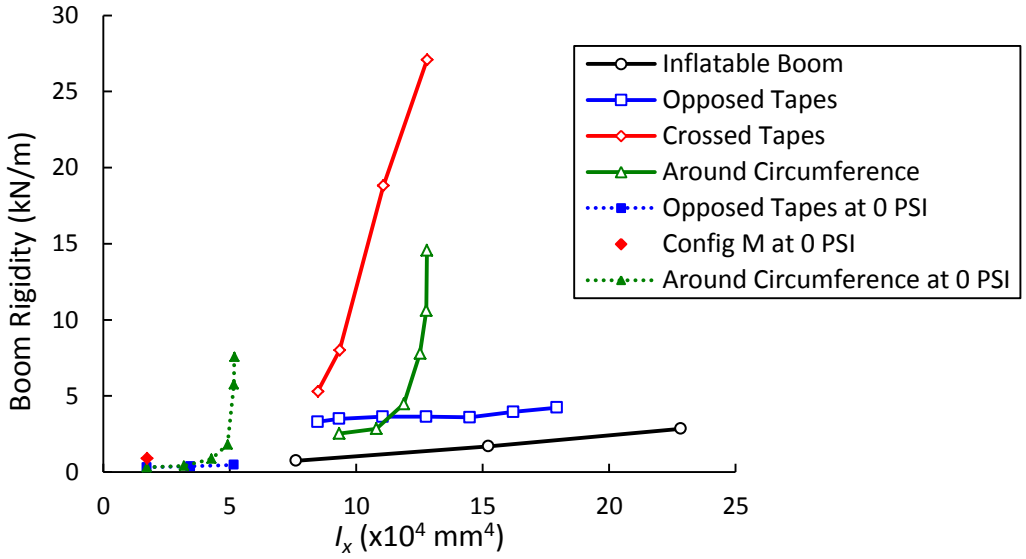

b)

Figure 9.1: Structural performance of hybrid booms using difference tape spring location strategies, a) peak moment b) averaged rigidity

Figure 9.1 a) shows that the failure bending moment is maximised by maximising the second moment of area of the tape springs as expected from simple beam theory where $M_{max} = I_x \sigma_{max}$. Where tapes are placed close to the neutral axis of the cross tape configuration make little difference to the maximum bending moment.

However this is not the case for boom rigidity where maximising tape spring 2nd moment of area by utilising the opposed tape spring location strategy results in hybrid boom rigidity performance rates similar to that of an inflatable boom. Maximising tape spring potential with respect to rigidity is achieved by utilising tapes placed in the cross configuration and is a result of the constraining interaction of the 4 tapes and the attachment to the inflatable boom as explained in section 8.4.3. The gradients of these graphs show a performance rate with respect to 2nd moment of area. The crossed tapes hybrid boom configuration shows a rigidity performance increase against an inflatable boom of over 37 times.

Data is also presented for hybrid booms at 0PSI where the second moment of area is adjusted to ignore the inflatable boom as it does not contribute to the structural performance in this setup. This shows the impact of combining tape spring only and inflatable only booms into a hybrid structure. The effect of combing these two structural components is seen in Figure 9.1 a) where the individual components of the opposed tape spring hybrid boom configuration have a similar performance rate (2.6×10^{-4} Nm/mm^4 and 4.1×10^{-4} Nm/mm^4 respectively) with respect to the second moment of area. Combining tape springs and inflatable booms in this configuration shows a significant increase in this performance of over 5 times showing a significant advantage in combining these two structural technologies to create a hybrid boom.

The structural performance tape springs have on the inflatable boom creating these hybrid structures can be explored in greater depth by comparing particular configurations using simple Euler-Bernoulli cantilever beam theory. Euler-Bernoulli beam tip deflections and bending moments are expressed in Equations 9.1 and 9.2 respectively.

$$\boldsymbol{\delta = \frac{F_\delta L^3}{3EI_x}} \qquad \textbf{(Equation 9.1)}$$

$$\boldsymbol{M = -EI_x \frac{d^2\delta}{dL^2}} \qquad \textbf{(Equation 9.2)}$$

Figure 9.1 gives the structural performance of the various hybrid booms and show well defined trends as the second moment is increased. Boom rigidity is proportional to EI_x where I_x is calculated from the structural components of the inflatable and hybrid booms.
EI_x is typically taken as the level of boom stiffness for a simple isotropic beam and can be calculated by rearranging Equation 9.1 to,

$$\boldsymbol{EI_x = \frac{F_\delta L^3}{3\delta}.} \quad \textbf{(Equation 9.3)}$$

As both inflatable and hybrid booms behave in a nonlinear manner boom stiffness in previous analysis has been reported as the average value up to M_{fail} where $S = \frac{F_\delta}{\delta}$. This leads equation 9.3 to be rearranged to

$$\boldsymbol{EI_x = \frac{SL^3}{3}.} \quad \textbf{(Equation 9.4)}$$

Table 9.1 quantifies the structural performance of key hybrid boom configurations and includes the effective Young's modulus values based on Euler-Bernoulli beam theory. The effective Young's modulus (E^*) is significantly increased when combining these two structural technologies showing an increase of 105% and 66% when adding an inflatable to configurations B and M respectively. Alternatively increasing E^* by 3.9 and 8.8 times from an inflatable boom to hybrid booms B and M respectively. This can be clearly shown in Figure 9.2 with respect to added mass. Figure 9.2 also gives a comparison against inflatable and hybrid boom structural performance rates by increasing either inflatable boom skin or tape spring thickness respectively.

Table 9.1: Structural performances of key inflatable and hybrid boom configurations.

Configuration	I_x (x10^4 mm^4)	Mass (g)	M_{fail} (Nm)	Rigidity (N/m)	E^*I (Nm^2)	E^* (MPa)
A at 15 PSI	7.61	135	20	739	16	207
B at 0 PSI	1.71	108	5	313	7	390
B at 15 PSI	9.32	243	32	3498	75	801
M at 0 PSI	1.73	161	15	1097	19	1097
M at 15 PSI	9.34	296	45	8002	171	1828

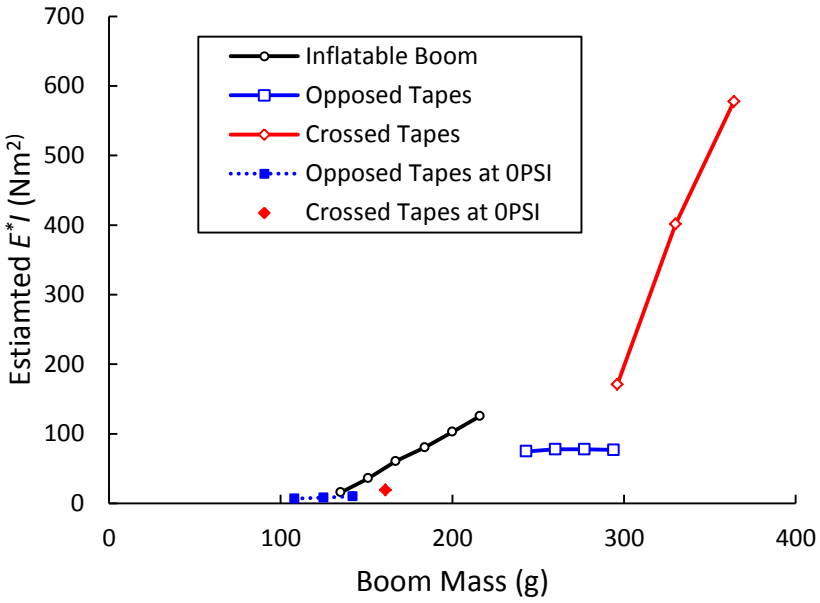

Figure 9.2: Comparative estimated flexural rigidity between key hybrid boom configurations against an inflatable boom with respect to boom mass.

Figure 9.2 shows the estimated flexural rigidity performance rates with respect to boom mass. The data shows the opposed tape spring configuration increases in a step change when including an inflatable boom. This is over 10 times the flexural rigidity from 7 to 75 Nm^2 for configuration B where the inflatable boom of configuration A contributes 16 Nm^2. A similar increase of 9 times the flexural rigidity is seen for configuration M.

Although in the current prototype setup hybrid booms have a significant weight penalty the performance rate with respect to boom mass is significantly increased when utilising the crossed tape hybrid boom configuration. This is from 1.3 to 6.0 Nm^2/g for inflatable and crossed taped hybrid booms respectively showing the significant potential of combining these two structural elements together confirming they can create a superior structure. As this study has used off the shelf components to create prototype hybrid booms the structural performance of these configurations with respect to mass will vary with respect to the attachment system and materials used. This is discussed in greater detail in the following section.

9.2 Mass Evaluation

The mass of configurations A, B and Mare given in Table 9.1 and shows a significant increase from an inflatable boom of 80 and 119% for configurations B and M using 4 attachment collars

respectively. FEA with some preliminary experimental results has shown the rigid insert attachment is a suitable alternative showing negligible performance change and reducing the attachment mass. To avoid the adhesive failure found in Figure 7.3 collar clamps of 2.2 g per attachment will ensure the tape spring remains rigid with respect to the insert and are included in the boom mass. The hybrid boom mass of configurations B and M are reduced to 53 and 105% greater than the inflatable boom respectively when using this attachment system. However the mass breakdown highlights the significant parasitic attachment mass remains for the insert attachment approach and compromises the significant performance gain of hybrid booms.

Table 9.2: Inflatable and hybrid boom mass with two attachment systems and mass breakdown.

Configuration	Number of tape springs	Boom Mass		4 inserts per tape attachment proportional mass breakdown		
		With 4 collars	With 4 inserts per tape	Inflatable boom	Tape springs	Attachment
A	0	135 g	135 g	100%	0%	0%
B	2	243 g	206 g	66%	8%	26%
M	4	296 g	277 g	49%	14%	37%

Adding tape springs to create a hybrid boom allows these inflatable structures to operate at much lower inflation pressures and provide significant structural support. This is highlighted by the framework structure the attachment collars provide allowing the boom to operate at 0 PSI. Figures 9.3 and 9.4 show the structural performance between configurations A, B and M using the FEA data from the models developed. The hybrid booms have failure bending moments of 5 and 13 Nm when using 2 and 4 tape springs respectively. Boom failure, previously defined in chapters 4 and 7, occurs with incipient wrinkling on an inflatable boom and is adjusted for hybrid booms to initial tape spring buckling. The majority of the investigated hybrid booms have incipient wrinkling at the tape spring buckling point. However this cannot be used universally as lower pressures and thicker tapes or vice versa will result in wrinkling occurring prior or subsequent to tape spring buckling respectively. This is intuitive at 0 PSI and demonstrated by the comparison between experimental and FEA data at 15 PSI in Figure 8.4. Further load can be supported for inflatable and some hybrid booms but with a significant loss in stiffness that would render the boom too soft for the majority of applications. The boom rigidity performance is averaged up to these failure limits.

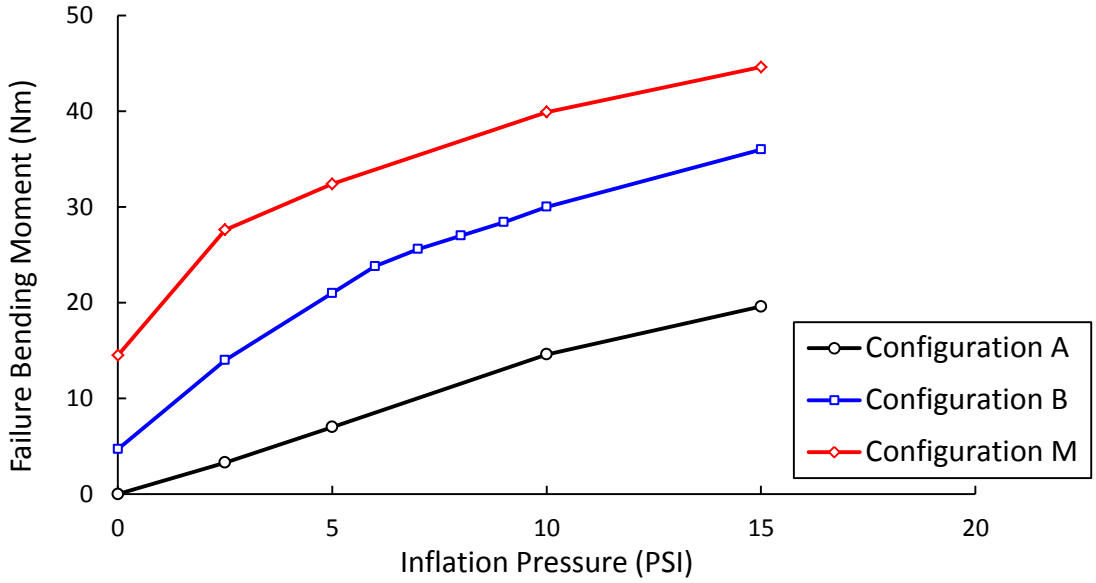

Figure 9.3: Failure bending moment comparison of inflatable and hybrid booms with increasing inflation pressure.

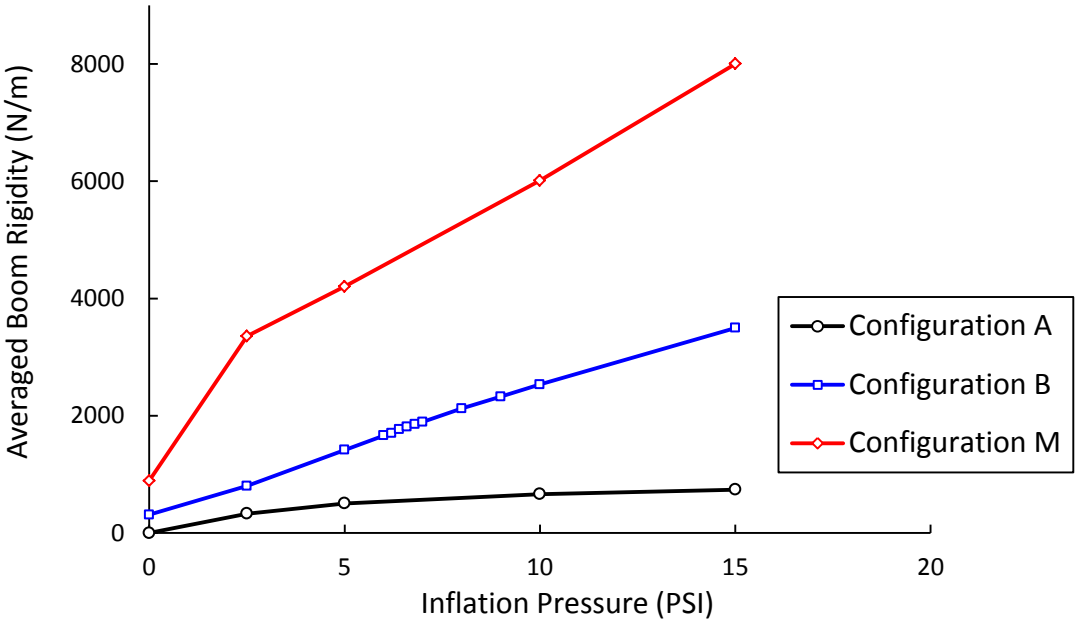

Figure 9.4: Averaged boom rigidity comparison of inflatable and hybrid booms with increasing inflation pressure.

Figures 9.3 and 9.4 show the hybrid booms significantly outperform the inflatable boom. The greatest improvement is at lower pressures where M_{fail} is increased by over 4 and 8 times for configurations B and M respectively at 2.5 PSI inflation pressure. This is continually reduced where at 15 PSI the gains are 1.8 and 2.3 times the inflatable boom failure moment limiting the tape spring effectiveness for their significant added parasitic mass. However, the boom rigidity remains relatively low at 0 PSI. Utilising the inflation pressure displays an almost linear increase in hybrid boom rigidity performance with an exception and considerable increase of 10 times for a modest pressure rise from 0 to 2.5 PSI in configuration M. In comparison the

inflatable boom has a relatively static failure rigidity dependent on the nonlinearity of the fabric shear modulus showing a change of 408 N/m over the experimental pressure range. The hybrid booms offer a significant increase to the boom rigidity that is increased with pressure. At 15 PSI the hybrid booms increase the stiffness of an inflatable boom by over 4.7 and 10.8 times for configurations B and M respectively.

Specific tape thickness variations of the hybrid booms have also shown structural performance control displayed in Figures 8.19. As boom radius is a constant in this study, the inflatable boom is limited to pressure and skin thickness to control rigidity and M_{fail} respectively. This is used to determine the effectiveness of the hybrid booms in comparison to inflatable booms with respect to the change in mass of the structures. Figures 9.3 and 9.4 show the structural performance of the three configurations with respect to varying the boom mass. The mass of the structures are varied in terms of thickness of the main structural component. For the inflatable boom of configuration A the thickness is adjusted by the Nylon fabric. The hybrid booms of configurations B and M vary the thickness of the tape springs alone. The structural components are increased in discrete intervals similarly to layering the fabric skins or tapes in previous studies shown in Figures 5.16 and 8.18. Each Nylon shell has a thickness of 0.195 mm and increases the inflatable boom mass by 16.2 g per skin. The inflatable boom of configuration A considers skin thicknesses up to 1.17 mm creating a boom of 216 g. The tape springs are 0.11 mm and increase the hybrid booms mass by 8.6 g per tape. Both hybrid booms use up to 12 tape springs in their respective locations where configuration M places 3 layered tapes in each location of the cross formation. The additional attachments create significantly heavier structures of up to 292 and 380 g for configurations B and M respectively. The structural performance of these configurations is set to the maximum operating pressure to maximise performance. The maximum operating pressure for configurations B and M is 15 PSI where additional skin thickness allows a proportional increase up to 90 PSI when using 1.17 mm thick Nylon. For comparison the 15 PSI configuration A performance is also plotted. Configuration M also plots the structural performance using the boom supported failure mode. The remaining data uses the failure criteria previously defined in this chapter.

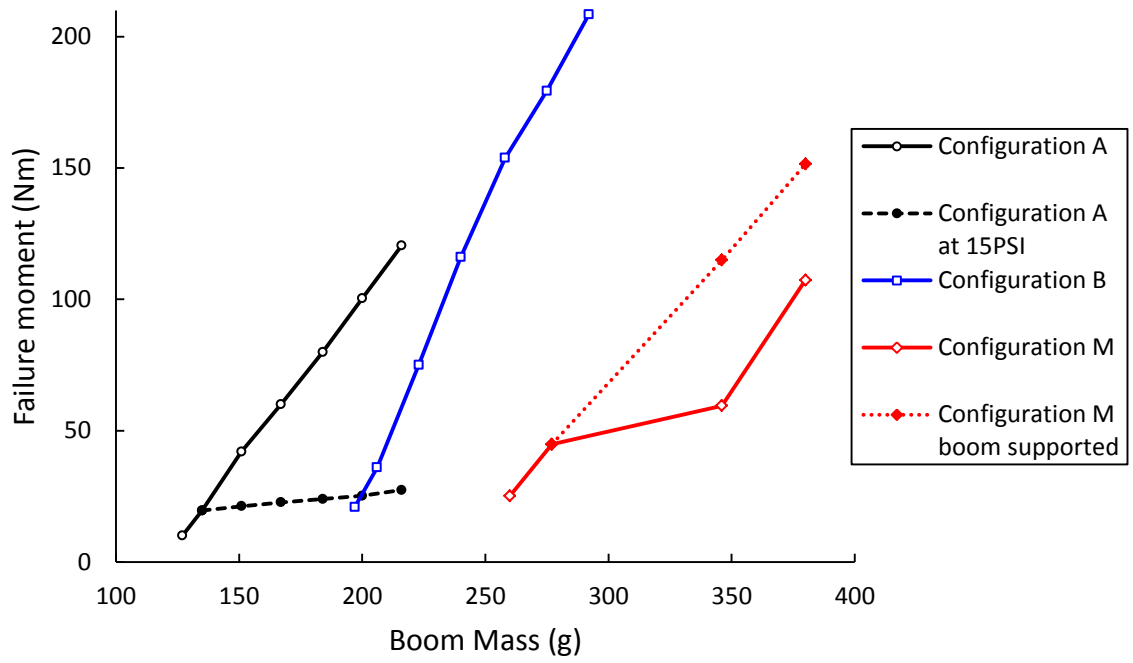

Figure 9.5: Failure moment performance against total boom mass of configurations A, B and M with varying structural mass at maximum operating pressure.

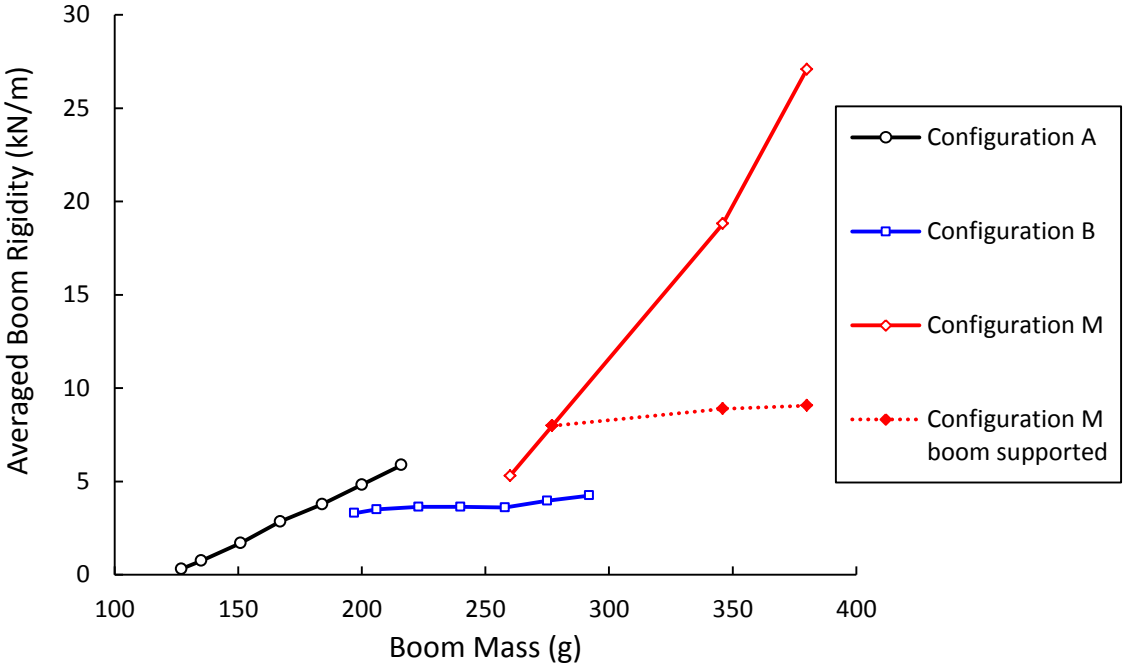

Figure 9.6: Rigidity performance against total boom mass of configurations A, B and M with varying structural mass at maximum operating pressure.

Figures 9.5 and 9.6 show configurations B and M make best use of the increase in structural mass for the failure moment and boom rigidity respectively. Configuration A shows a shallower gradient but the significantly lower initial boom mass means for the majority of structural specifications the inflatable boom provides the optimum solution for the 0.4 m long, 0.05 m

radius booms created. In practice the radius of the boom will be selected depending on the specification. For an inflatable boom the radius is proportional to the cube root of the failure moment shown in Equation 2.12. Therefore a reduction in the boom radius will significantly increase the advantage of using tape springs for hybrid booms. Another option is to scale up the tape springs similar to the experimental permutations using two tape spring sizes considered by Walker et al (2011). Both approaches would expect to refine the performance potential of a hybrid boom but requires further research to confirm trends. For the 0.05 m radius booms created the hybrid booms are viable solutions with respect to mass only for high performance requirements. There is also a trade-off when considering both structural parameters equally. The limited boom rigidity of configuration B suggests configurations A and M should be selected for low and high overall structural performance requirements respectively.

The significant advantage of inflatable structures is the reduction in mass, stowage volume and complexity. However their main disadvantage is the significant cost of maintaining a pressurised system. This includes the stored gas prior to inflation and the insulation and puncture protection required from the space environment. This cost will be the same between inflatable and hybrid booms at the same inflation pressure but is likely to rise for booms taken to higher pressures that must consider higher leakage rates. The hybrid booms would reduce this cost by operating at lower pressures and reduce the dependency on highly critical pressurising systems. The structural performance results of the inflatable boom where the pressure is maintained at 15 PSI show a greatly reduced performance rate for the added mass. In comparison, hybrid booms can achieve significantly greater failure bending moments and boom rigidities once the parasitic attachment mass is less than the mass of the added Nylon skins. Further investigation of the pressurisation cost with respect to inflation pressure is needed to fully define the boom mass of configuration A and requires a boom leakage study.

Other factors will affect the comparative performance between inflatable and hybrid booms including utilising space grade materials and optimising the attachment design. This research has focused on the feasibility and the structural performance gains tape springs can provide to an inflatable structure considering COTS materials. Other materials could be utilised and developed to minimise mass including carbon fibre tapes and a low density attachment material. Figures 9.7 and 9.8 display the structural performance against the mass of the booms ignoring the tape spring attachment mass showing the theoretical maximum achievable structural - mass performance of the hybrid booms.

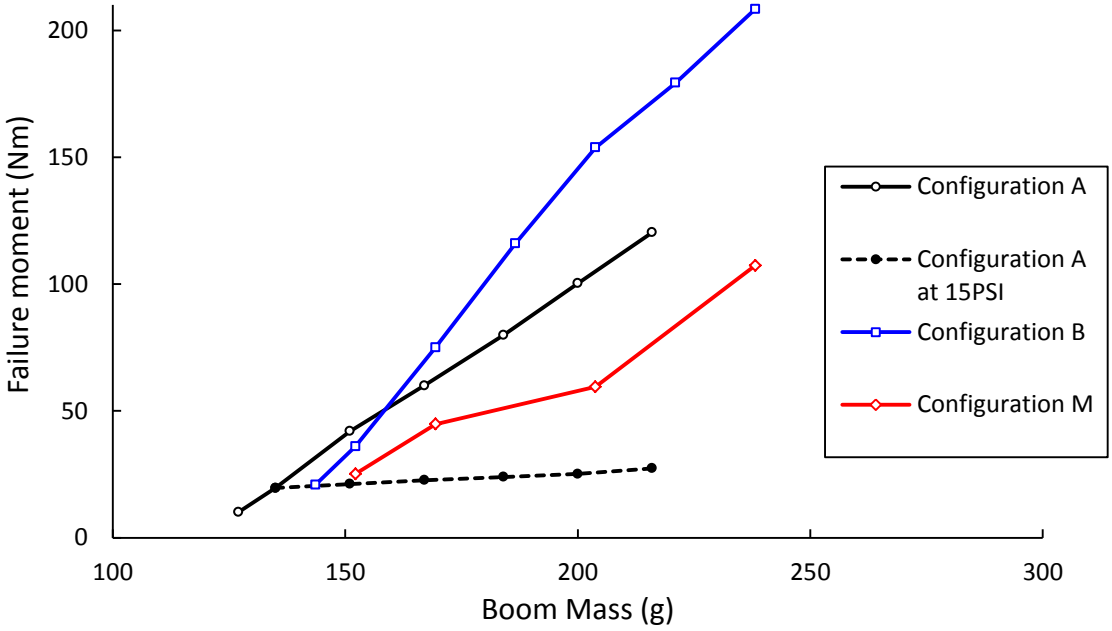

Figure 9.7: Failure moments performance assuming no attachment mass of configurations A, B and M with varying structural mass.

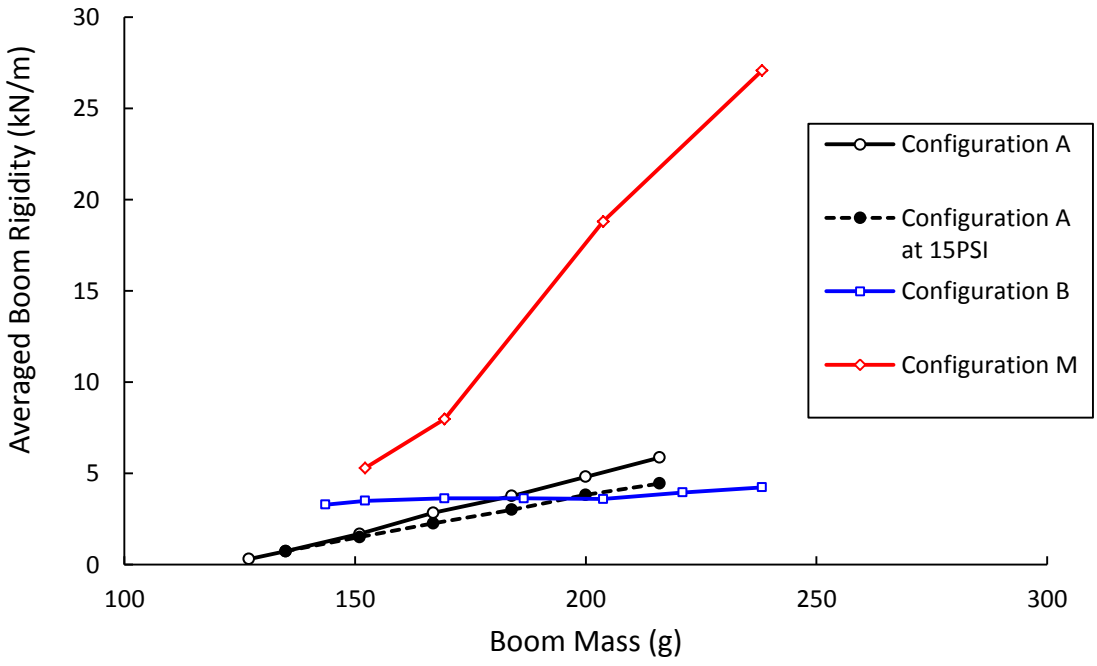

Figure 9.8: Rigidity performance assuming no attachment mass of configurations A, B and M with varying structural mass.

Figures 9.7 and 9.8 show hybrid booms have significant potential if the parasitic attachment mass is minimised where rigidity and the failure moment can be increased up to 3.8 and 5.9 times for a 200 g boom respectively. The data shows tape springs should not be added in configuration B to improve the boom rigidity of an inflatable boom but used to maximise the

failure moment. The four crossed tape formation offers a significant gain in overall structural performance which becomes the optimum solution over an inflatable boom depending on the structural performance requirements and attachment mass. This performance gain seen in Figures 9.7 and 9.8 is increased a further 10% if the load is applied square to the tape springs in configuration K.

It is clear the placement and the thickness of tape springs determines the boom rigidity and failure moment performances that can be adjusted to meet specific mission requirements. This logically leads to further research varying the tape spring thickness with respect to location around the boom circumference and along its length to optimise the structural performance of the boom with respect to mass. Similar studies for inflatable boom optimisation have taken place and include reducing the radius along the boom length[96,99,103]. Research by Brayley et al. (2011) has also investigated reinforcing sections of the boom along its length. This was done with a different fabric material to the beam using four polyester straps bonded to the surface of the structure. An alternative method can be to simply stitch in additional fabric to increase the thickness locally similarly to the non -uniform thickness investigation research in section 4.4.3 which found an initial mass saving of 6% with no loss in structural performance. Varying the boom thickness around the circumference of the boom will maximise rigidity while optimising the placement of additional fabric mass. The key limitation of these inflatable booms is they remain unable to sustain compressive loads unlike the developed hybrid booms utilising tape springs as structural stiffeners presented in this research. As both technologies mature and future optimisation studies improve the performance of both inflatable and hybrid booms, the comparison between the two approaches will change and need to be re-evaluated determining which approach best suits a given specification.

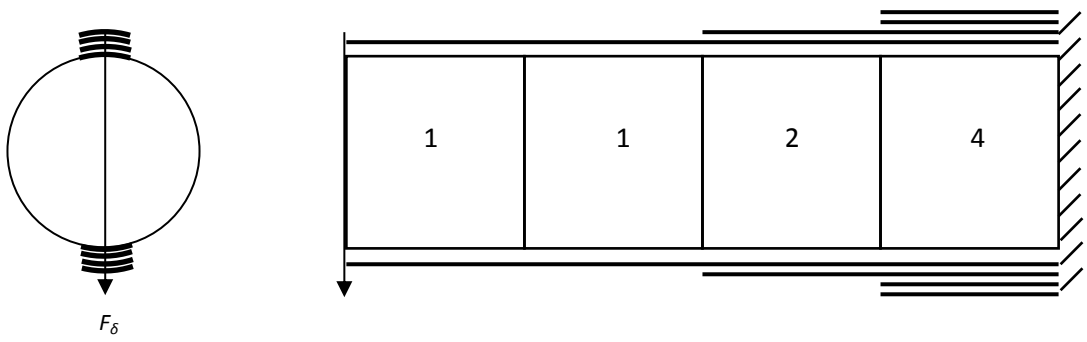

Figure 9.9: Schematic of configuration B with varying tape spring thickness using up to four layered tapes between attachment points showing the 1124 arrangement.

A preliminary illustrative FEA study varying the tape spring thickness along the boom length of configuration B to demonstrate the structural performance variation with tape spring mass placement is given in Figure 9.10. The four attachment points allow distinct integers of tape springs to be layered along the boom length. This is easily replicated in the current experimental setup for validation without the difficulties of manufacturing a tape spring with varying thickness along its length. Figure 9.9 illustrates the discrete tape layering and the associated labelling system showing a configuration B hybrid boom with the 1124 tape spring arrangement where each tape layer is 0.11 mm thick. Each number specifies the number of tape spring layers between attachment points from boom tip to root. The preliminary study confirms an expected result where overall structural performance is maximised by a linear increase in tape spring thickness along the boom length towards the root shown by configuration setup 1234. However this is not conclusive and varies between peak moment and rigidity. Further in depth research specifically on configuration K using the 4 crossed formation and tape spring layering independent of other tape locations is required to fully optimise the tape spring mass placement and maximise the hybrid boom potential.

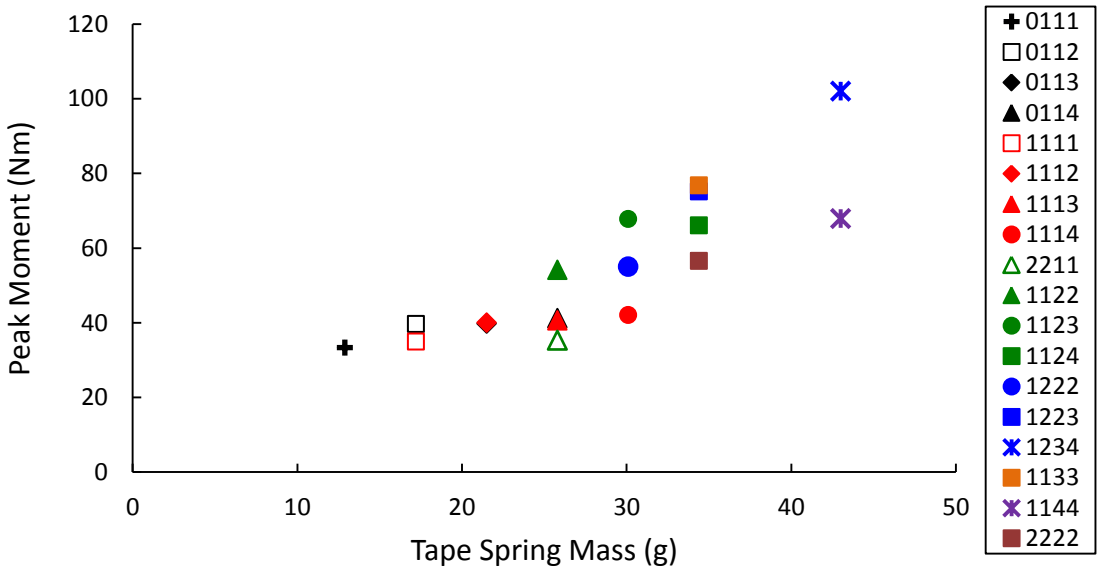

a)

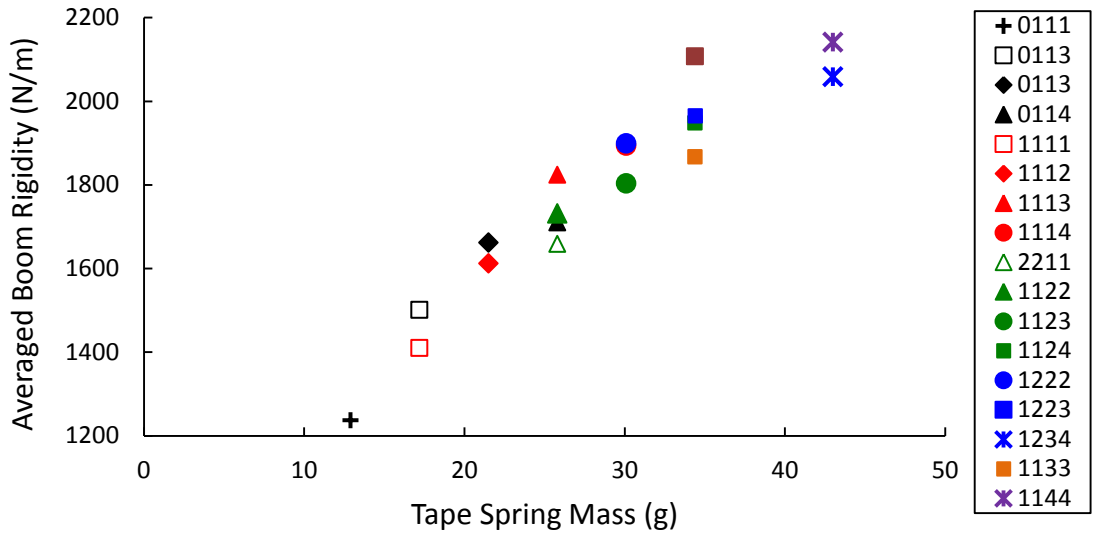

b)

Figure 9.10: Configuration B structural performance for varying tape spring mass and location at 10 PSI

a) Failure moment, b) Boom rigidity.

9.3 Packing Efficiency

Another important performance consideration that is exploited by gossamer structures is the packing performance. It is important to consider and compare between structures to ensure a boom can be manufactured to provide sufficient structural support and still fit into a launch vehicle where mass and stowed volume are the chief driving parameters in design. Implementing a hybrid structure will significantly affect the packing performance in comparison to an equivalent inflatable boom. This is an initial study to demonstrate the packing performance tradeoff as stiffness is added to the structure. Detailed packing analysis of a final hybrid boom design, although required, is outside the scope of this research. Figure 8.12 displays a possible stowage configuration of the hybrid booms using the attachment collars where the tape springs are packed into a zigzag 3 point bend between attachment points. This figure clearly shows these hybrid booms will create significant voids limited by the tape spring curvature without causing permanent deformation. Along with the added volume from the tape springs and attachment mechanism a hybrid boom will significantly affect the packing performance.

The packing performance of a deployable structure can be quantified by two parameters, packing ratio and packing efficiency and are defined in Equations 9.5 and 9.6 respectively where V is the volume of the structure.

$$\boldsymbol{Packing\ Ratio} = \frac{\boldsymbol{V_{stowed}}}{\boldsymbol{V_{inflated}}} \quad \textbf{(Equation 9.5)}$$

$$\boldsymbol{Packing\ Efficiency} = \frac{\boldsymbol{V_{material}}}{\boldsymbol{V_{stowed}}} \text{ [50]} \quad \textbf{(Equation 9.6)}$$

All parts of the booms were considered above the root attachment inner plate for each calculated volume. The volumes were calculated using the projected cross sectional area of the boom tip and height during stowed and inflated configurations from the assumption any voids in these areas are unusable and therefore parasitic. For the stowed configuration, data was taken from experimental measurements of configuration B and extrapolated to determine the packing performance of configuration M. The distance between each attachment point in its stowed state was minimised without causing permanent deformation of the tape springs and remained constant at 40 mm. To minimise frontal area the tape springs were assumed folded within the cross-sectional area of the boom tip.

As previously discussed in the collar attachment study in section 8.4.1, the minimum interval between attachment points is 0.1 m to allow the three point bend to form the zigzagged folding pattern without permanent deformation to the tape springs. This results in up to 4 collars being investigated on the 0.4 m long hybrid booms created.

Table 9.3: Individual component volumes for 0.4 m long 0.05 m radius inflatable and hybrid booms.

Component	Volume (cm^3)
Nylon skin	27
Bladder	73
Tip disc	5.2
Attachment Collar	8.9
Collar Clamp	0.4
Tape Spring	1.1
Attachment Insert	1.3

The efficiency of the stowed boom is a measure of the total material volume against the stowed volume and quantifies the voids that are present in the structure. Table 9.3 gives a volume breakdown of the component parts. Table 9.4 quantifies the packing performance of configurations A, B and M and also includes the ultimate packing ratio (UPR) defined by Equation 9.7 where all voids in the stowed structure are prevented.

$$\boldsymbol{Ultimate\ Packing\ Ratio} = \frac{\boldsymbol{V_{material}}}{\boldsymbol{V_{inflated}}} \quad \textbf{(Equation 9.7)}$$

The UPR of these structures may not be achieved in future developments but provides the performance potential and comparison between inflatable and hybrid booms if the attachment design is developed further in future research. The full breakdown of the booms measurements are given in appendix VI.

The results in Table 9.4 show that an inflatable boom has the lowest packing ratio and is currently packed most efficiently. This is the inherent advantage of inflatables being highly flexible when deflated leading to minimal voids while occupying a small total volume. This packing efficiency could be easily improved by creating a vacuum and removing all voids within the boom. This will also need to be considered as out-gassing during launch will cause problems with the boom if any gas is still present. The internal bladder provides 70% of the total material volume and can also be optimised to reduce the packing ratio further. However, these techniques will not improve hybrid boom stowage performances as the attached collars and tape springs become the limiting factor. Adding collars results in the packing ratio increasing and the efficiency dropping considerably caused by the many voids between the tape spring folds. The stowed length and packing ratio is directly proportional to the number of collars used and not the number of tape springs. This is because adding further tape springs increasingly utilises the voids within the stowed structure at a negligible volume cost of 1.1 cm^3 per tape and 0.4 cm^3 per clamp. Similarly increasing the tape spring thickness is expected to alter the stowed length negligibly as the minimum non-deformable curvature is anticipated to be negligibly affected by tape spring thickness.

Table 9.4: Stowage performance for inflatable and hybrid booms using the tape spring collar attachment (* peak values).

Configuration	Number of collars	Packing Ratio (%)	Packing Efficiency (%)	Ultimate Packing Ratio (%)	Stowed Length (cm)	Total Material Volume (cm^3)
A	0	5*	66.8*	3.3	2*	105*
B	1	10	26.7	2.7*	4	117
B	2	20	14.5	2.9	8	127
B	4	40	8.3	3.3	16	146
M	1	10	27.3	2.7*	4	120
M	2	20	14.9	3.0	8	130
M	4	40	8.6	3.4	16	151

As more collars are incorporated into the hybrid boom the structural performance increases as shown by the collar attachment study in section 8.4.1, while packing performance decreases. Extrapolating the structural performance data with this study data along with the inflatable

boom thickness study in section 5.3.2 creates a structural performance profile with respect to packing ratio. The structural performance is increased by adding attachment collars to the hybrid booms and skin layers for the inflatable boom. These results assume the packing efficiency remains constant for additional Nylon skins and all booms are operating at 15 PSI to ensure the unquantified inflation protection costs that will increase the total material volume of the booms are equal between all configurations.

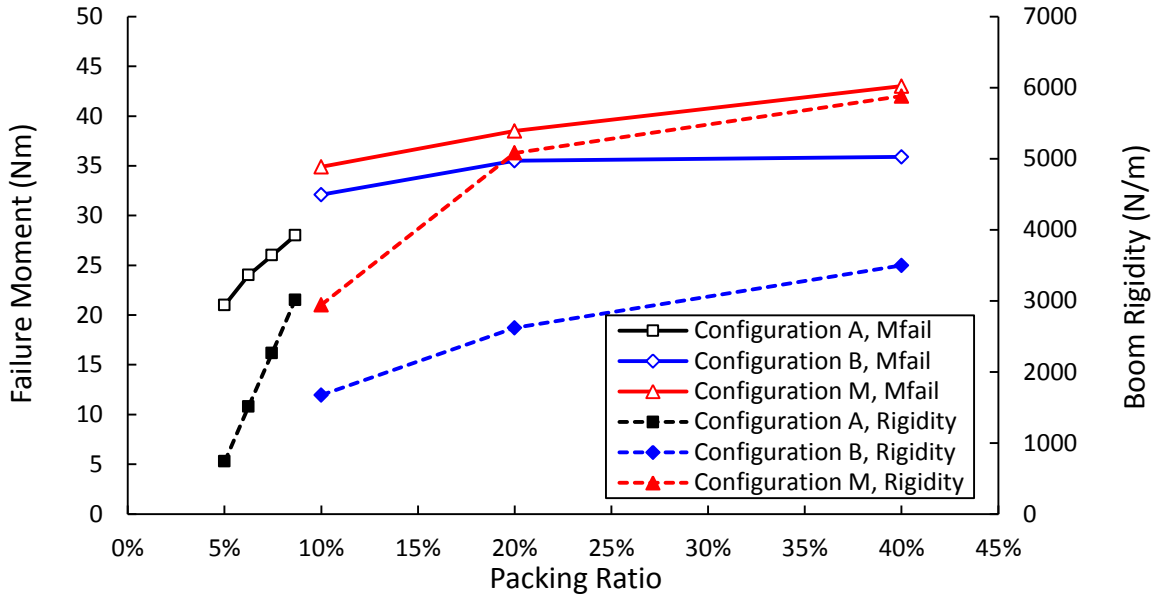

Figure 9.11: Current packing ratios against the structural performance of configurations A, B and M using the collar attachment design at 15 PSI.

Figure 9.11 gives the structural performance of configurations A, B and M with respect to the packing ratio of the current booms. It is clear the collar attachment approach is not viable, particularly when using 2 or more collars on the 0.4 m long boom. However increasing the number or thickness of the tape springs will not significantly affect the packing performance of the hybrid booms as seen between configurations B and M in Figure 9.11. Each tape spring increases the boom volume by 2.8 cm^3 per meter length. The increase in packing ratios between configurations B and M by adding 2 tapes and the required clamps is 0.04%. This assumes tape spring thickness does not substantially affect the minimum non-deformable curvature that constrains the stowed boom length. In comparison the inflatable boom increases by 1.2% per additional skin assuming the packing efficiency is constant. Taking the UPR of these inflatable booms creates a slightly lower increase of 0.8% per additional skin. This shows significant hybrid boom potential as greater structural performance requirements are easily met by increasing the number of tape springs once the limitations of the attachment

system are overcome. It also highlights further attachment development is crucial in creating a viable hybrid structure in terms of structural and packing performances.

It is clear the current attachment collar cannot be used in a final design due to poor mass and volume performances. Using the attachment inserts shown in the preliminary studies of chapter 7 and Figure 7.5 in configuration B with 4 attachment points per tape will save 25 cm^3 over the collar attachments reducing the total material volume to 121 cm^3 and an attachment volume saving of 64%. This would reduce the UPR from 3.3 to 2.7% however the voids caused by the tape spring folds still remains the greatest inhibitor to packing performance. Using inserts will reduce voids as the boom will have greater flexibility as shown in Figure 9.12 where the tape springs are no longer constrained to one another and will improve the current packing ratios and efficiency using the tape folding approach. Further research is required to quantify these values.

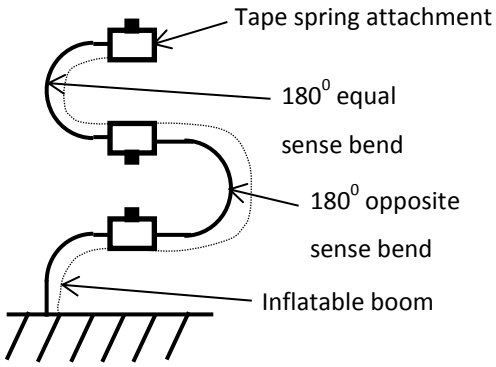

Figure 9.12: Possible stowage configuration of a hybrid boom using attachment inserts.

When using fewer attachment points it is important to determine if the tape springs can fold into the available stowed space currently set at 4 cm per attachment collar. Performing a back of the envelope geometry calculation using the available stowed volume and the natural curvatures of the tape springs showing a tape of up to 0.45 m long can be stowed per quadrant of boom before protruding from the deployed cross sectional area similarly to Figure 8.12 a). Figure 9.13 illustrates a potential tape spring fold arrangement where future studies may look into overlapping tapes that can be used in conjunction with the boom deployment to further maximise available tape length within the 4 cm height constraint. The consequence of this is the stowed length limit and hence a minimum achievable packing ratio of 8.8% assuming tape springs do not protrude from the deployed cross-sectional area.

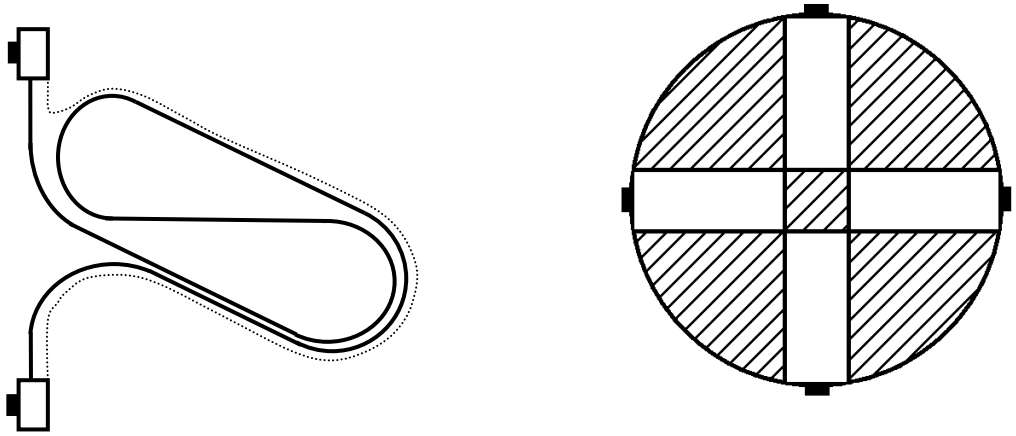

a) b)

Figure 9.13: Potential tape spring folding pattern and 4 available cross sectional areas.

Another potential stowage arrangement is to roll the tape springs similar to the omega boom in Figure 2.3. This could be done by collapsing the tape springs onto each other and rolled onto a mandrel as demonstrated by Lou et al. (2002) in Figure 9.14 where the stowed length will be determined by the spool diameter. This method will be most successful for hybrid booms without rigid attachment components such as collars and inserts that will prevent the structure being easily rolled up and cause significant voids. The largest natural radius of the current tape springs is 15 mm in the opposite sense direction leading to a spool diameter and potential stowed length of 30 mm resulting in a packing ratio initial estimate of 7.5%. This would likely increase to accommodate the rest of the structure and a root attachment as seen in Figure 9.14 a). However this packing solution efficiency will increase proportionally to boom length and can be refined using a smaller spool diameter until permanent deformation of the tape springs occurs.

Assuming the structural performance remains constant for both packing approaches the improved packing ratio may outperform the inflatable boom when adjusting the data in Figure 9.11. Further packing performance investigation is outside the scope of this research however these preliminary calculations need to be rigorously tested to confirm these potential packing ratios while maintaining structural performance. Both spooled and folded tape springs offer a further advantage with the stored strain energy able to drive boom deployment as utilised by Walker et al (2012).

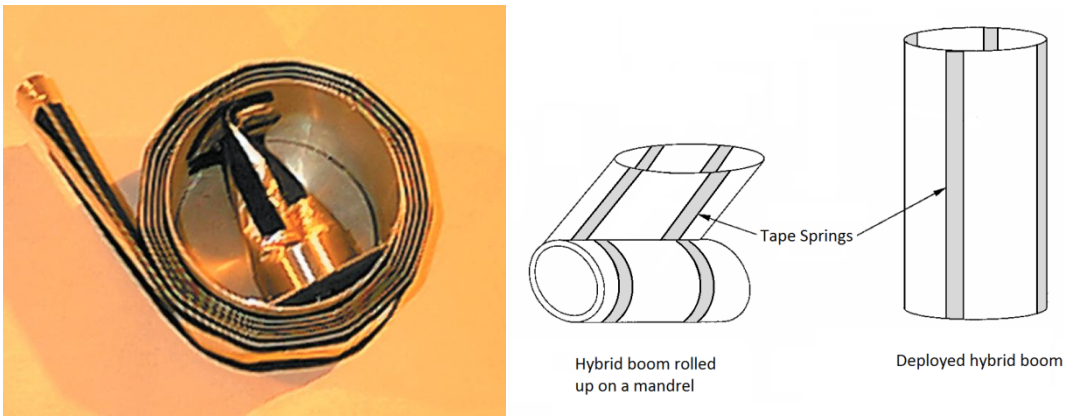

a) Picture b) Diagram

Figure 9.14: A 5 m hybrid boom stowed on a 0.165 m diameter mandrel[137, 16].

9.4 Deployment

Gossamer boom deployment can be problematic as shown by the experimental tests of the uncontrolled Omega boom displayed in Figure 9.15 where chaotic systems may lead to a loss of satellite attitude control[77]. Both inflatable booms and tape springs have shown unpredictable deployment if sufficient control is not applied[2,14,16]. Tape springs can also suffer from significant shocks as each hinge is unloaded and taken back through the buckling peak moments. The shocks are caused by the flattened tapes changing back to the unstrained transverse curvature suddenly. This was observed of a self-deployable three dimensional structure using 148 tape springs illustrated in Figure 2.17 where shocks of 200 g were recorded as full deployment took less than 1 s. These shocks can be significantly reduced or eliminated if tape springs are rolled so no hinges are formed as shown in Figure 9.15 while still maintaining stored strain energy capable of driving deployment[69].

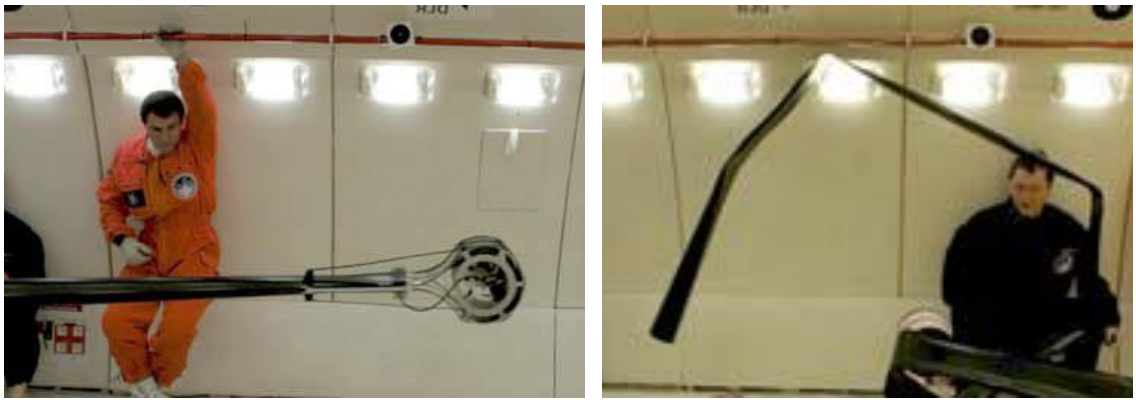

a) b)

Figure 9.15: Omega boom deployment a) with and b) without deployment control[77].

Inflatable booms require deployment control due to their lack of bending stiffness and have been controlled through folding strategies such as the tetragonal accordion deployment control system (TACEDS) device displayed in Figure 9.16 or spooled as shown in Figure 9.17 that will be used for the JWST sunshield. Deployment actuation can be from boom inflation or constant force springs embedded in the spool. Both approaches require additional mass and volume to the complete system with the later adding 2.97 kg as a tip mass to a 0.065 m radius boom.

a) b)

Figure 9.16: Inflatable boom a) folding pattern and b) the TACEDS deployment device[7].

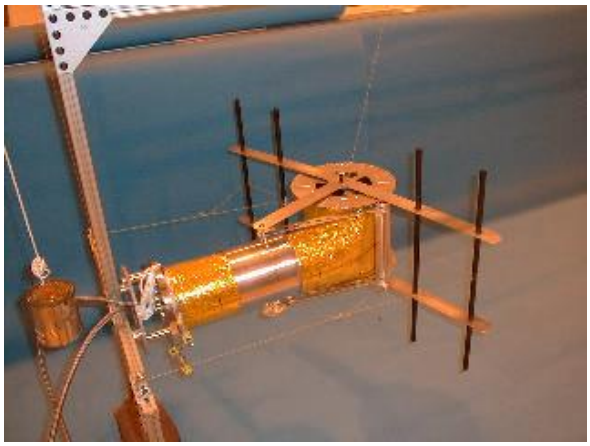

Figure 9.17: JWST sunshield inflatable boom deployment device[14].

This research has not focused on boom deployment and requires further study and development to determine the full hybrid boom system mass and volume as well as deployment dynamics. However, inflatables have a significant cost associated with boom deployment where the added mass of the tape springs can contribute significantly to both the structural performance and boom deployment. Tape springs can store their strain energy in

both hinged and spooled configurations which will impact on mass, stowage and structural performances. There are several benefits of combining these technologies together into a hybrid boom including; tape springs guiding inflation deployment and the inflatable boom mass increasing tape spring lateral stability during deployment and reduced tape spring lock out shocks in addition to mass and volume savings by utilising a multifunctional component.

The current hybrid boom design uses several attachment collars forcing stowage and deployment to use a folding tape spring pattern that can be utilised to drive deployment. In this arrangement and assuming each tape spring is stowed in the 3 point bend as shown in Figure 8.12 b) at the natural bend radii of 12 and 15 mm, each hinge will have a constant steady state bending moments of 29 and 55 Nmm for equal and opposite sense bends respectively. The initial opening force from stowage for configurations B and M with 5 attachment points per tape will be 26 and 53 N respectively where each tape spring has eight 90^0 and four 180^0 equal and opposite sense bends respectively. Hinge tape spring deployment creates shocks and loads to the system caused by unloading through the peak moments prior to locking into place at full deployment. This was seen in the self-deployable tape spring structure investigated by Walker et al. (2011). Stowage was achieved using the same 3 point bend where the static opening force increased by 7 times at 99% of full deployment and shocks measured in excess of 200 g during dynamic testing[11,13]. Damping of tape spring hinges has successfully reduced shocks of the TSR[110] while Velcro has been used for deployment control as shown in Figure 9.14. This low cost, low complexity approach could be used between tape spring hinges to delay specific hinges from opening and force sequential hinge deployment or during controlled deployment of a spool boom or tape spring. This may negate other deployment devices such as the TACEDS removing significant parasitic mass and complexity. Spooling the tape springs has an additional potential packing performance advantage as previously discussed at the cost of structural performance. It is therefore evident further research analysing hybrid boom deployment performance to determine the full costs associated with both inflatable and hybrid systems is required.

9.5 Summary

The hybrid booms have been evaluated against a comparative inflatable boom with respect to structural performance, mass, packing and deployment. The structural performance studied in detail in previous chapters is taken from FEA models that have been verified with experimental

results. The evaluation considered configurations B and M using two opposed and 4 crossed tape springs each with 5 attachment points per tape along the boom length and compared against the inflatable boom of configuration A.

The addition of tape springs into configurations B and M showed a significant structural performance increase over the inflatable boom. This was significantly marked at 2.5 PSI where the failure moment and boom rigidities where increased by 4 and 2 times for configuration B and 8 and 10 times for configuration M respectively. This is at a mass cost of 53 and 105% when using 4 insert attachments with clamps per tape spring for respective configurations. Performance of all structures continues to increase with inflation pressure with the hybrid booms providing a reducing level of performance gain over the inflatable boom.
The structural performance can also be adjusted with tape spring and Nylon skin thicknesses for hybrid and inflatable booms. This was considered against the mass increase to each configuration at maximum operating pressures showing the inflatable boom outperforming the current hybrid booms at modest failure moments and rigidities. However the rate of structural performance to mass gain is lower than hybrid booms for failure moment in configuration B and rigidity in configuration M. Mass gain from this initial attachment system is the greatest inhibitor to the hybrid boom performance. The focus of the research as a whole has been on feasibility and the potential structural performance gains from utilising tape springs with an inflatable boom. As such the attachment design is not optimised for the other performance criteria including total boom mass. Ignoring attachment mass for comparison highlighted the significant structural performance potential of hybrid booms. The hybrid booms also operate at lower inflation pressures reducing costs associated with maintaining higher pressurised systems. Inflatable booms increase their failure moment with a pressure rise for this constant radius study. When considering a constant inflation pressure of 15 PSI to ensure maintaining inflation costs are equal between all configurations the failure moment gains of hybrid booms are increased significantly. Configurations A and B increase M_{fail} by 96 and 1982 Nm/kg respectively. At maximum operating pressures configuration A is increased to 1239 Nm/kg when ignoring maintaining inflation costs. A preliminary study varying tape spring thickness along the boom length demonstrates a potential optimisation procedure to increase the structural-mass performance further. Initial results suggest a linear decrease in thickness from the boom root maximises this.

The stowage performance is evaluated with packing ratio and efficiency. The inflatable boom can attain a 5% ratio at an efficiency of 68%. Configurations B and M are limited by the

attachment collars and the minimum radius of tape spring hinges. With 4 attachment collars the packing ratio and efficiency is 40% and less than 9% respectively for both hybrid configurations. The inflatable boom total material volume is increased by 39 and 44% for configurations B and M with four attachment collars respectively. Reducing collars to attachment points at the root and tip only improves the stowage performances to a ratio of 10% at an efficiency of 27%. However the tape springs as a series of folds still creates significant voids within the stowed structure. This is shown by the hybrid boom UPRs that are within or less than 0.1% of the inflatable boom UPR. Varying the packing performance with respect to attachment collars and skin thickness for hybrid and inflatable booms respectively shows the structural-stowage performance trends between the booms configurations. It shows hybrid booms should minimise the number of attachment points where one tip collar and root clamp on a 0.4 m long boom can provide a comparable structural-stowage performance of an inflatable boom with a skin thickness of 0.78 mm. Increasing tape spring thickness has minimal effect on packing performance assuming natural curvatures of the tape folds remain constant. Therefore hybrid booms should minimise the number of attachment points while increasing the tape spring thickness to the required structural performance to minimise both mass and packing ratios. Comparing configuration B to M shows a packing ratio increase of 0.04% at the addition of two tape springs. The inflatable boom increases the packing ratio by a minimum of 4.1% per millimetre skin thickness while increasing tape spring thickness results in 0.36% per millimetre. The hybrid booms packing ratios remain limited by the current constraining attachment collar where future designs may improve performance further. This includes using spooled tape springs to remove voids created by tape spring folds by rolling the hybrid boom onto a mandrel.

Boom deployment is also linked to the tape spring attachment design where stored strain energy of the tape springs can be utilised to drive deployment and provide structural support negating the need for previous deployment control required for inflatable booms. The current hybrid boom design has an estimated opening force of 26 and 53 N for configurations B and M respectively. This will need to be verified with experimental deployment research including dynamic testing alongside other deployment designs.

This chapter has evaluated the hybrid boom structural performance showing significant potential from this initial research and highlighting the need for further attachment design combined with packing and deployment analysis. The following chapter outlines the areas for future research of hybrid booms alongside key research results from this thesis.

Chapter 10

Conclusions and Future Research

This final chapter summaries the thesis with conclusions highlighting the most significant areas of research. It also outlines suitable areas for future research that are required to advance this novel technology forward.

10.1 Project Summary

This research project aimed to investigate the benefit of using tape springs as structural stiffeners on inflatable booms for space applications. Potential benefits include; low mass, low complexity, high packing efficiency, the potential of self-deployment using stored strain energy from stowed tape springs and low cost 'commercial off the shelf' components that could provide a simple add-on module to significantly increase small satellite surface areas. The research consisted of experimental and computational analysis of inflatable and hybrid booms with a focus on structural performance.

The project background is introduced in the first two chapters outlining the current state of the art space grade gossamer booms along with inflatable and tape spring structures identifying the limited knowledge of combining these components into a hybrid structure. Theoretical development of both inflatable booms and tape springs is presented providing a concise understanding of the hybrid boom component parts.

Using easily sourced COTS components led to the selection of carpenter tape springs and Nylon sailcloth where it was identified a detailed understanding of the orthotropic woven fabric was required for inflatable systems. Material testing of the fabric is described in chapter 3 which included uniaxial and biaxial tensile testing using DIC to collect strain data in both axes to the fabric plane to attain the ripstop Nylon material properties. The effect of a seam was also investigated which reduced the UTS by 32% to 50 MPa when using a double stitch across the fill yarns. This was confirmed with a boom inflation failure test attaining a maximum inflation pressure of 24 PSI before failure, equivalent to 48 MPa boom hoop stress with the

weaker fill yarns in the boom hoop axis. It was concluded that the stronger warp orientated yarns should be placed in the hoop axis with a double stitched seams to maximise the operating pressure of the inflatable boom. Stitch pull-out was also considered showing a discontinuity in the DIC strain field maps that was taken into account in FEA models.

The structural performance properties of inflatable and hybrid booms were determined from tip deflection testing of the structures mounted as a cantilever. The inflatable boom was constructed with a seam along the boom length and capped with a stitched fabric disc to provide structural support. A rubber bladder provided an airtight seal for inflation and a steel disc placed between the Nylon and bladder forced a flat tip minimising tip deflection and boom length measurement errors. The 0.4 m long booms with a 0.05 m radius have a total mass of 135 g which is 205 g/m boom length plus 53 g at the boom tip. Inflatable boom tip deflection testing was conducted for a baseline performance comparison to the developed hybrid booms. Varying the Nylon skin thickness confirmed predicted structural performance trends and allowed a structural-mass performance evaluation between inflatable and hybrid booms. The experimental results also allowed computational model validation of the inflatable boom. This included 5 boom lengths and 8 inflation pressures between 0.2 – 1.0 m and 2.5 – 45 PSI respectively totalling 234 individual tests.

An aim of the research was to construct a computational model of a hybrid boom. The first step was to create and validate models of its component parts to ensure a robust final model. A FEA model of the inflatable boom was constructed using the material properties determined in chapter 3 and verified with the experimental results of chapter 4. Chapter 6 focused on tape spring FEA modelling which was brought together with the inflatable boom FEA model to create a hybrid boom FEA model in chapter 8. This was also verified with the hybrid boom experimental data in chapter 7.

The FEA of the inflatable boom modelled the woven fabric as a continuum and considers the nonlinearity and discontinuities of the booms under inflation seen in the material properties chapter 3. This was taken into account as an effective length and radius change dependent on the inflation pressure. The model was validated with mesh and time step convergence studies and verified with experimental results. The inflatable boom FEA model confirmed the fabric orientation and varying skin thickness conclusions of the experimental results and allowed the effects of boom compression to be investigated easily. The structural performance of inflatable booms was defined to be $M_w = M_{fail}$ and the rigidity averaged up to incipient wrinkling due to

the rapid softening of these structures beyond this point leaving them unsuitable for applications.

Chapter 6 constructed a tape spring FEA model verified with experimental data and the Mansfield equation for peak and steady state bending moments respectively. Tape twist, cross-sectional profile, thickness and length were considered in the analysis to confirm constraining effects when placed into a hybrid structure.

Experimental testing of hybrid booms was conducted to ensure the feasibility of the structure. Preliminary studies identified the collar attachment system most suited for investigations with many permutations whilst maximising the structural performance from the tape springs. The experimental hybrid boom conducted 129 individual tests consisting of 12 tape spring configurations across 5 inflation pressures. It was concluded that the opposed tape pair vertically aligned to the applied load provided the greatest structural performance which is increased further with inflation pressure and tape spring thickness. The off design structural performance of the opposed tape pair showed a significant loss as the tapes are placed at 45^0 and horizontally to the applied load. The addition of two further tape springs to create a cross formation on the hybrid boom cross-section shows no structural performance improvement to the opposed tape pairing. However placing the applied load in the off design alignment of 22.5^0 and 45^0 showed small differences in structural performance between the three orientations. The limitations of this experimental setup are the mass and volume penalty using the collar tape spring attachment system, the tape spring pivoting with respect to the clamped attachment points observed in all tape springs not placed directly on top or beneath the inflatable boom, and the collars failing from 60 Nm applied boom bending moment. These limitations affect hybrid boom packing performance, boom rigidity performance for tapes placed on the side of a hybrid boom, and tape spring thickness studies at inflation pressures greater than 10 PSI respectively.

The FEA hybrid boom model was constructed from the inflatable boom and tape spring models using mesh and time step convergence studies to validate and experimental results to verify the moment-deflection response of the model. The hybrid boom FEA model confirmed the experimental limitations of rigidity and peak moment for tape rotation and collar strength respectively. The model also showed boom rigidity and peak moments are optimised with placement of tape springs in the 4 cross and 2 vertically opposed configurations respectively if these limitations are overcome. The FEA supported the experimental hybrid boom test results

where two failure modes were observed where at higher inflation pressures the inflatable boom can support the tape spring system. This increases the maximum achievable bending moment at the cost of a yielding structure. Other boom permutations included tip compression, attachment point frequency and attachment method.

The final research chapter evaluated the hybrid structures of two opposed and four crossed tape spring configurations against the inflatable boom. The structural performances were considered with respect to boom mass, packing performance and deployment. This research has focused on the feasibility and structural performance benefit of using tape springs to create hybrid booms and as such requires further research on packing and deployment to fully develop this new type of structure. It has been identified the tape spring attachment technique is a significant performance driver in these areas anticipated to be at the tradeoff of structural performance. The structural performance with respect to mass of the current hybrid booms shows significant potential by improving rigidity and peak moments of an inflatable boom whilst reducing the operational importance of maintaining pressurised systems. These 0.4 m long hybrid booms with an inflatable radius of 0.05 m have shown the greatest performance improvement at 2.5 PSI with an increase of over 8 and 10 times for peak moment and boom rigidity when adding 4 tapes in a cross formation to the inflatable boom with an added mass of 105% totalling 277 g.

10.2 Key Research Results

10.2.1 Material Testing of Fibremax 94

The Fibremax 94 ripstop Nylon is highly nonlinear showing inter-fibre frictional effects, decrimping and yarn extension sequentially for warp and fill orientated specimens in uniaxial extension each with an associated elastic Modulus. Bias uniaxial tensile testing also showed a nonlinear relationship exhibiting inter-yarn frictional effects, yarn slippage and shear locking sequentially.

The warp and fill Poisson's ratios therefore vary between each extension mechanism between 0.21 ±0.02 and 0.25 ±0.02 respectively.

Biaxial testing of the fabric in an inflatable boom demonstrated linear behaviour at pressures greater than 8 PSI where equivalent hoop and length stresses are 14 and 7 MPa respectively. By assuming the Poisson's ratio is constant during linear biaxial stress-strain, the averaged uniaxial Poisson's ratios can complete the stiffness matrix. This is done alongside biaxial elastic moduli to determine the Young's modulus of the fabric in both yarn directions for an inflatable boom. The constant 2:1 biaxial warp and fill Young's moduli are 438 and 314 MPa respectively. The elastic modulus ratio between the warp – fill yarns is constant at 1:0.72 in both biaxial and averaged uniaxial tests.

This material properties understanding of woven fabrics has allowed successful computational models of inflatable fabric booms to be implemented that would be representative of other similarly woven cloths that can be brought forward to examine space grade materials.

10.2.2 Inflatable Boom Testing and Analysis

Variable skin layers are proportional to boom rigidity similarly to skin thickness where FEA shows negligible moment-deflection response differences between the two approaches. Peak moments are proportional to inflation pressure where the maximum operating pressure is determined by the total skin thickness and the UTS of the stitched fabric.

The relatively high pressures of 10 and 15 PSI displayed increased peak moments with respect to the Comer- Levy model as a result of the deformation induced volume changes causing a stiffening response as analysed in detail by Davids (2007) and previously reported by Thomas and Weilgosz (2004).

The 19 MPa shear modulus of the fabric is calculated using the Kilby equation[126] however the material properties are not constant with respect to inflation pressure and tip deflections. Adjusting the shear modulus to the relationship $G = 280p$ provides the FEA model an adequate approximation within 5% of the experimental variance across the tested pressure range up to 15 PSI. The uniaxial bias testing is not sufficient to determine the shear modulus in biaxial inflatable fabric boom systems. Inflatable boom shear tests through axial torsion described by Hutchings et al. (2009) and Turner et al. (2008) over the operating pressure range are, although more involved experimentally, most likely to provide an accurate shear modulus relationship with respect to inflation pressure.

10.2.3 Hybrid Boom Testing and Analysis

The shear modulus inflation pressure relationship for an inflatable boom remains appropriate for hybrid booms across the same pressure range operating at significantly higher rigidities and peak moments. Shear modulus remains a significant hybrid boom parameter in configuration B showing large changes in boom stiffness and peak moments for modest changes in shear modulus. Two opposed tapes at 5 PSI have shown a rigidity increase of 7% per 1 MPa increase in shear modulus.

Comparison between FEA and experimental hybrid boom results highlight the limits of the experimental testing where detail is missed between the discrete tip loads. Refined applied loads and detailed boom observation including tape spring condition is required to improve the experimental accuracy of regions of interest including boom failure.

Two failure modes in cantilever hybrid booms under tip loading; boom supported and unsupported failure, have been identified through FEA and is dependent on inflation pressure and tape spring thickness. Boom supported failure significantly increases the peak moments achieved by the structure at a cost of yielding boom rigidity. However it is likely structural failure limits will be applied from the initial tape spring buckling corresponding to boom unsupported failure. All setups show linear increases in structural performance with pressure in this failure mode. This maximises hybrid boom rigidity where the peak moment can be increased with tape spring thickness at a small mass cost.

Tape spring thickness makes a significant effect to the moment-curvature relationship of individual tape springs showing up to 28% variance for a 10% change in thickness. A hybrid boom also exhibits a similar effect where a 10% thickness change can alter the peak moment by up to 15%.

Hybrid boom tape spring permutations have identified two configurations to maximise structural performance. Two opposed tapes vertically aligned to the applied loading and four tapes in a cross formation square to the applied load maximises peak moments and boom rigidity respectively. This assumes tape rotation with respect to the attachment points is prevented. The off design performance of the four tape cross formation is small showing a maximum structural performance loss of 13%.

The FEA tape spring model clamped similarly to the hybrid boom set up has shown length affects the peak moments in both equal and opposite sense bends. This result transfers to hybrid booms where altering the number of attachment points and therefore tape spring free length shows a significant change in structural performance. This is due to the constrained end effects effectively rigidising the tape springs for attachment intervals shorter than 0.1 m.

Attachment collars maximised the structural performance of the connected tape springs by maintaining the initial transverse curvature and fixed relative to the inflatable boom to maximise hybrid boom peak moment capacity and rigidity respectively. However they create a framework structure around the inflatable boom that becomes the primary load bearing component capable of sustaining loads under no inflation pressure. The collars are ideal for hybrid boom prototypes providing rapid testing of numerous configurations and permutations. However they are significantly restricting with respect to stowage performance in addition to a significant mass penalty. Other attachment systems have been investigated including attachment inserts used to maintain tape spring transverse curvature and gluing directly onto the inflatable boom. The latter is a likely final design approach where a lack of rigid attachment components is expected to create suitable packing efficiencies by rolling the hybrid boom onto a mandrel and removing the voids in stowage.

10.2.4 Hybrid Boom Evaluation

Hybrid booms reduce the importance of inflation pressure of an inflatable structure whilst maintaining structural performance. The tape springs offer the greatest structural performance improvement when working in conjunction with an inflatable at low inflation pressures therefore lowering the costs associated with maintaining a pressurised system. At 2.5 PSI the four tape springs in a cross formation increased the peak moment and boom rigidity by over 8 and 10 times respectively for an added mass of 105% totalling 277 g.

The attachment system, although not optimised with regards to added mass, significantly affects the hybrid boom structural-mass and structural-stowage performance in comparison to the inflatable boom. The attachment collars significantly restrict the tape spring stowage arrangement with a packing ratio proportional to the number of attachment points. The current folding configuration for hybrid boom stowage is limited by the minimum tape spring

curvature in each fold creating significant voids within the stowed structure and hence a poor packing efficiency.

The inflatable boom has a packing ratio of 5%. The current collar attached hybrid booms have a minimum packing ratio of 10% when using one attachment point, however increasing the tape spring thickness for structural performance has a minimal effect on the packing ratio of 0.18%/mm per 0.4 m long tape. In comparison the inflatable boom increases by 4.1%/mm increase in skin thickness.

Ignoring attachment mass that requires further development and optimisation, the structural performance rate of the hybrid booms with respect to added mass significantly improves upon a purely inflatable boom. Two opposed tapes vertically aligned to the applied load and four tape springs in a cross formation maximise with respect to mass the failure moment and boom rigidity respectively. At 15 PSI the two opposed tape springs have a M_{fail} = 1982 Nm/kg in comparison to an inflatable boom of M_{fail} = 1239 Nm/kg where fabric thickness (and thus mass) sustains greater operating pressures. Maintaining a constant inflation pressure and boom radius severely limits the achievable structural performance of an inflatable boom regardless of mass added by increasing the skin thickness. This reduces the failure moment boom mass rate to 96 Nm/kg for a constant 15 PSI inflation pressure.

10.3 Specific Achievements

10.3.1 Chapter 3: Material Properties Study

- A non-invasive accurate longitudinal and transverse strain measurements using 3D DIC on fabric strips and inflatable booms was achieved to determine Poisson's ratios, Young's and shear moduli of both yarn orientations of the woven fabric.

- DIC using speckled and non-speckled specimens displayed no mechanical effect from the applied spray paint to a lightly impregnated Nylon fabric. It also demonstrated the weave as the unique tracking pattern is suitable for DIC where loose weave or non-impregnated cloths may alter their mechanical properties with an applied spray paint.

- Fibremax 94 ripstop Nylon fabric under 2:1 biaxial stress in an inflatable boom exhibits nonlinear and linear behaviour up to and beyond 8 PSI inflation respectively.

10.3.2 Chapter 4: Experimental Structural Analysis of an Inflatable Boom

- Successful manufacture and testing of small inflatable booms with a radius of 0.05 m up to 1 m long using COTS materials with a mass in grams of (205 x boom length) + 53.

- DIC afforded detailed tip deflections of cantilever booms identifying the quasi-static response of an inflatable boom with an equilibrium time greater than 5 minutes.

- Fabric orientation and various stitching types have increased the maximum inflation pressure and structural performance. Placing the warp yarns in the hoop direction maximises the inflation pressure limit at negligible cost to structural performance. A double stitch can achieve a 14% greater maximum operational inflation pressure over single stitched seams at a cost of 0.16 g/m.

10.3.3 Chapter 5: Finite Element Analysis of an Inflatable Boom

- Constructed an inflatable boom FEA model validated with mesh and time step convergence studies and verified against experimental results to within the moment-deflection response variance in repeat tests.

- Tip compression results in an effective pressure drop with proportional reductions in peak and wrinkling moments with the relationship $M_{max} = M^0_{max} - F_c r$. This provides a good approximation for low inflation pressures up to 10 PSI where deformation induced volume changes become significant at higher pressures causing an overestimation of the structural performance reduction.

10.3.4 Chapter 6: Tape Spring Analysis

- Created a cantilever tape spring FEA model considering tape profile, natural longitudinal twist, thickness and length verified with Mansfield's steady state equation[106] and experimental peak moment data.

10.3.5 Chapter 7: Experimental Structural Analysis of a Hybrid Boom

- Determined the feasibility of creating a hybrid structure identifying several attachment approaches focusing on maintaining tape spring transverse curvature and fixing relative position to the inflatable boom to maximise the structural performance potential of the tape springs.

- Collars have been placed at intervals along the inflatable boom length which creates a framework structure to attach the tape springs around the boom circumference in various configurations allowing rapid testing for various hybrid boom permutations.

- Twelve tape springs configurations were tested across 5 inflation pressures with identified structural performance trends and optimum configurations.

- Configuration B using two opposed tape springs attached with 4 collars at 2.5 PSI inflation pressure describes a slightly rigidised moment-deflection response of the 15 PSI inflatable boom up to 65% M_w with a failure moment of 16 Nm.

10.3.6 Chapter 8: Finite Element Analysis of a Hybrid Boom

- Assembled a FEA model of a hybrid boom from the verified inflatable boom and tape spring component models validated with mesh, time step and material property studies creating a suitable model showing a good approximation to the hybrid boom experimental results.

- Identified two hybrid boom failure modes dependent on pressure and material properties where boom supported failure significantly increases peak moment during

boom yielding. Initial tape spring buckling present in both failure modes provides a failure limit where structural performance increases consistently with inflation pressure and material properties.

- Tip compression of a hybrid boom shows a significant gain over inflatable booms if limited to boom unsupported failure with negligible change in rigidity in the hybrid boom permutations considered and a maximum failure moment reduction of 0.13%/N of compression.

In addition to the research presented in this thesis this research has generated a conference publication, Cook et al. (2011) “Experimental research on the use of tape springs on inflatable structures,” and was well received. The journal article titled “Experimental research on tape spring supported space inflatable structures” has been accepted for publication in Acta Astronautica. A further article, “Material Properties of a Fabric Inflatable Boom Determined from Inflation” has also been submitted to the Composite Structures journal and is pending review.

10.4 Future Research

This research has created a hybrid boom alongside computational structural models that can simulate their tip moment-deflection response. However this thesis has highlighted two key research areas that require further investigation to fully determine the performance benefit of hybrid booms: further detailed analysis of hybrid boom stowage performance and the tradeoff against other performance criteria, and the development and test of hybrid boom deployment systems. The performance of hybrid booms in both these areas is highly dependent on the attachment system that has previously shown structural performance dependency in chapter 7. The collar attachment approach has provided a valuable tool for testing hybrid booms in a multitude of permutations but is severely restricting with respect to added mass and stowage limiting the performance benefit over an inflatable boom. The three interlinked performance criteria must be developed concurrently to achieve the full hybrid boom potential as the technology is refined.

This research has focused on the structural performance of hybrid booms and as such has identified optimisation parameters for future inquiry:

- Development of the tape spring attachment with respect to mass and tape spring rotation prevention.

- Nonlinear tape spring placement in both boom length and circumference to maximise both peak moment and boom rigidity.

- Nonlinear inflatable boom fabric thickness as a comparative approach.

- Adjust hybrid boom component dimensions including tape spring curvature, and inflatable boom radius.

- Varying material properties including space grade materials such as Kevlar fabric and carbon fibre tape springs to expand the numerical model. Chapter 8 suggests an isotropic material such as Mylar may have a significant impact on the structural performance of some hybrid booms.

This research has progressed the state of the art of hybrid structures by providing a detailed understanding of their structural performance trends across a wide range of permutations. An original thoroughly validated FEA model for these hybrid booms has been created allowing a structural assessment during design. This technology is highly flexible where tape spring placement can be tailored with confidence in peak moment and rigidity performance optimisation. Combining these components allows a particularly low cost method of achieving an effective structure.

Appendix I

Theoretical Tape Spring Moment-Curvature Functions

$$\eta = 2\nu\bar{\kappa}_x - \bar{\kappa}_{y,0} - \nu\bar{\kappa}_{x,0}$$

$$\lambda = \bar{\kappa}_{xy}^2 - \bar{\kappa}_{xy,0}^2 + (\bar{\kappa}_x - \bar{\kappa}_{x,0})(\nu\bar{\kappa}_x - \bar{\kappa}_y)$$

$$\Psi_1(\bar{\kappa}_x) = \frac{1}{\bar{\kappa}_x^2}\left[1 - \frac{1}{\bar{\kappa}_x^{\frac{1}{2}}}\left(\frac{\cosh(2\bar{\kappa}_x^{\frac{1}{2}}) - \cos(2\bar{\kappa}_x^{\frac{1}{2}})}{\sinh(2\bar{\kappa}_x^{\frac{1}{2}}) + \sin(2\bar{\kappa}_x^{\frac{1}{2}})}\right)\right]$$

$$\Psi_2(\bar{\kappa}_x) = \frac{1}{\bar{\kappa}_x^4}\left[1 + \frac{\sinh(2\bar{\kappa}_x^{\frac{1}{2}})\sin(2\bar{\kappa}_x^{\frac{1}{2}})}{(\sinh(2\bar{\kappa}_x^{\frac{1}{2}}) + \sin(2\bar{\kappa}_x^{\frac{1}{2}}))^2} - \frac{5}{4\bar{\kappa}_x^{\frac{1}{2}}}\left(\frac{\cosh(2\bar{\kappa}_x^{\frac{1}{2}}) - \cos(2\bar{\kappa}_x^{\frac{1}{2}})}{\sinh(2\bar{\kappa}_x^{\frac{1}{2}}) + \sin(2\bar{\kappa}_x^{\frac{1}{2}})}\right)\right]$$

Tape Spring Non-Dimensioning Procedure

$$\bar{M} = \left(\frac{3a\{3(1-\nu^2)\}^{\frac{1}{2}}}{Et^4}\right)M$$

$$\{\bar{\kappa}_{x,0}, \bar{\kappa}_{xy,0}, \bar{\kappa}_{y,0}, \bar{\kappa}_x, \bar{\kappa}_{xy}\} = \frac{a^2\{3(1-\nu^2)\}^{\frac{1}{2}}}{4t^4}\{\kappa_{x,0}, \kappa_{xy,0}, \kappa_{y,0}, \kappa_x, \kappa_{xy}\}$$

Appendix II

Experimental Inflatable Boom

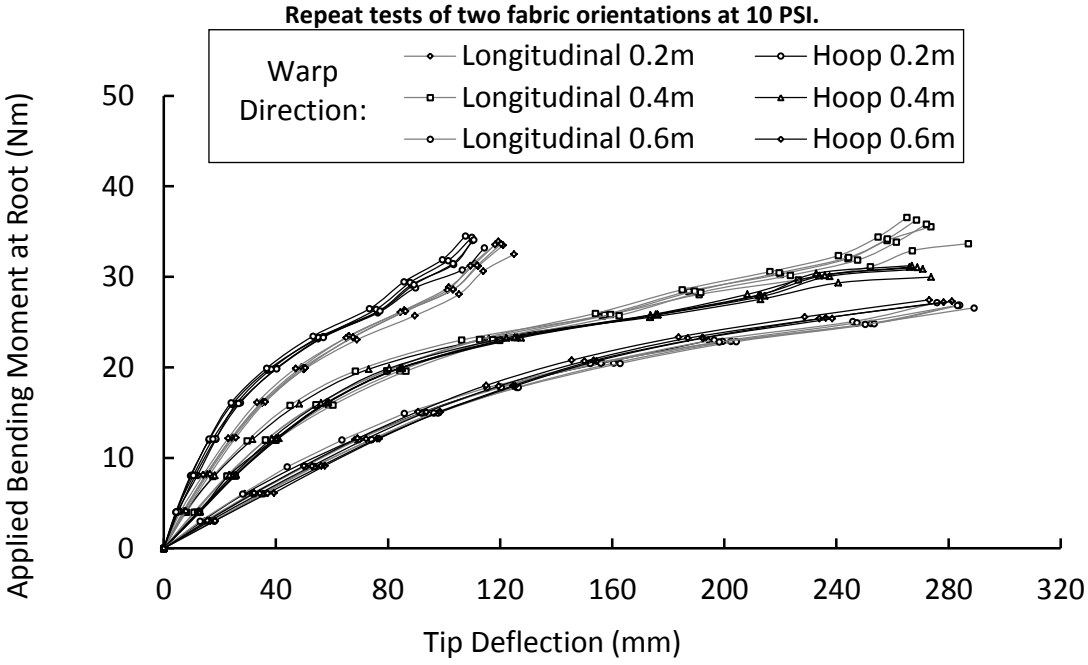

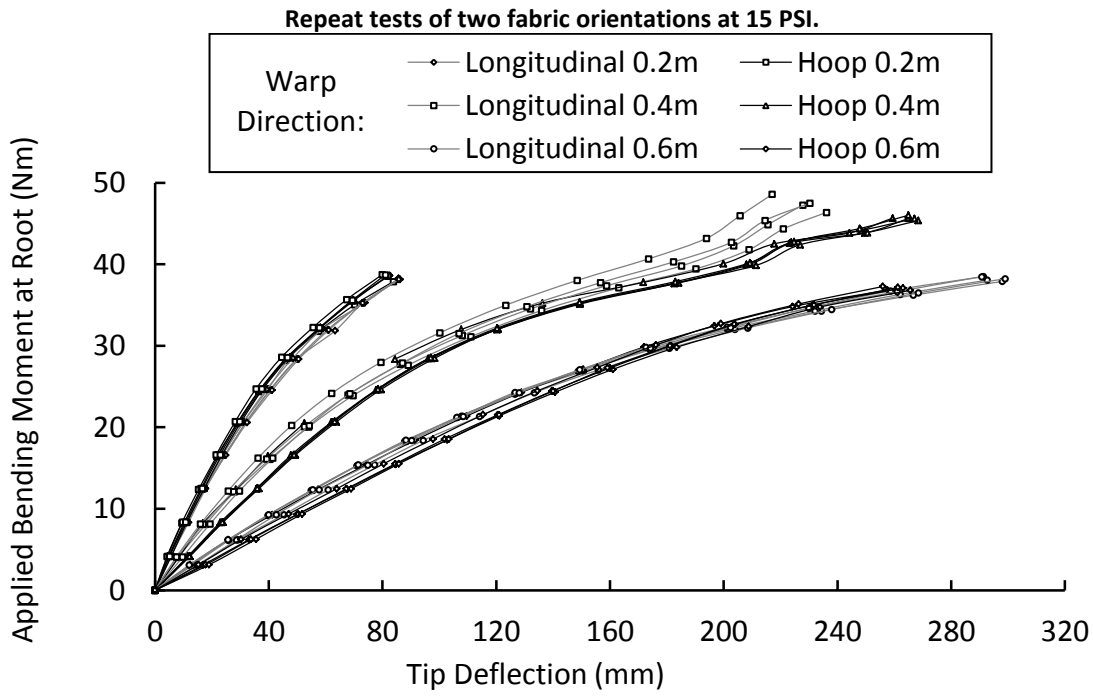

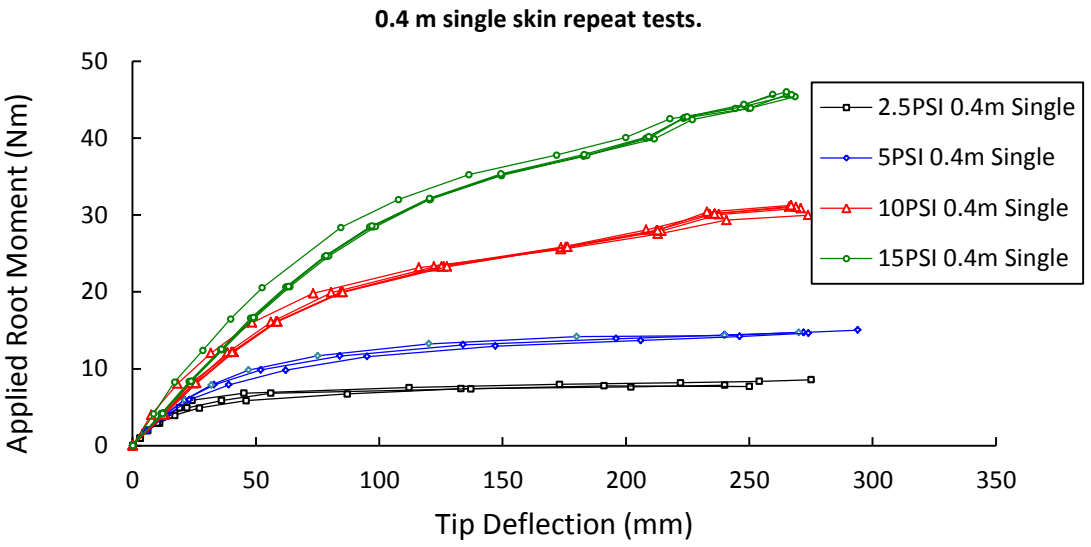
0.4 m single skin repeat tests.
Applied Root Moment (Nm)
Tip Deflection (mm)
2.5PSI 0.4m Single
5PSI 0.4m Single
10PSI 0.4m Single
15PSI 0.4m Single
0
10
20
30
40
50
0
50
100
150
200
250
300
350

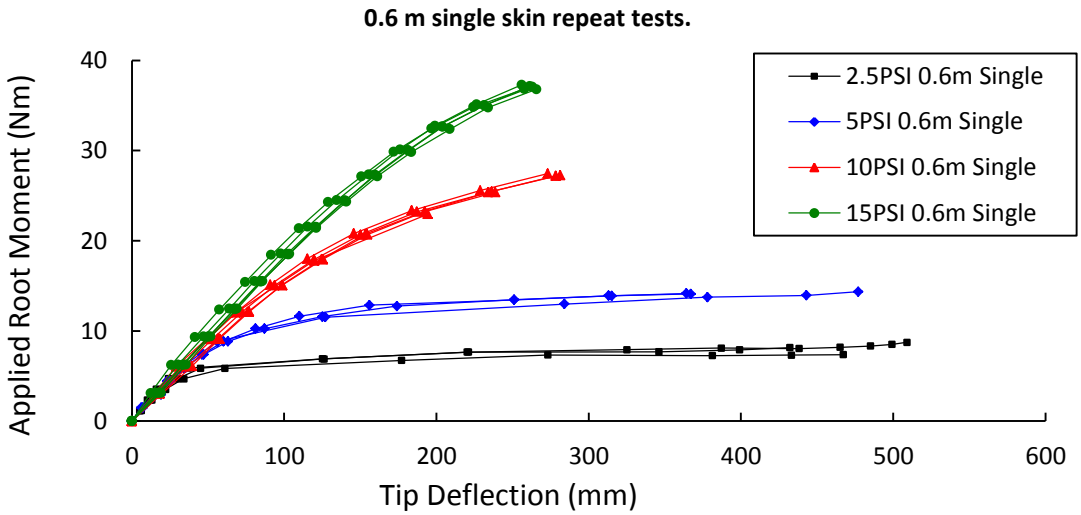
0.6 m single skin repeat tests.
Applied Root Moment (Nm)
Tip Deflection (mm)
2.5PSI 0.6m Single
5PSI 0.6m Single
10PSI 0.6m Single
15PSI 0.6m Single
0
10
20
30
40
0
100
200
300
400
500
600

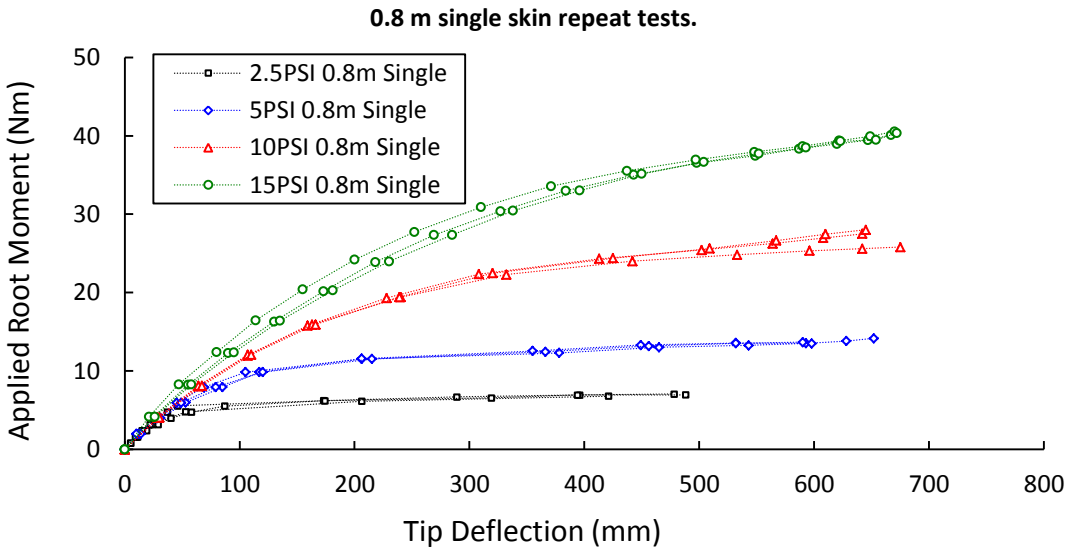
0.8 m single skin repeat tests.
Applied Root Moment (Nm)
Tip Deflection (mm)
2.5PSI 0.8m Single
5PSI 0.8m Single
10PSI 0.8m Single
15PSI 0.8m Single
0
10
20
30
40
50
0
100
200
300
400
500
600
700
800

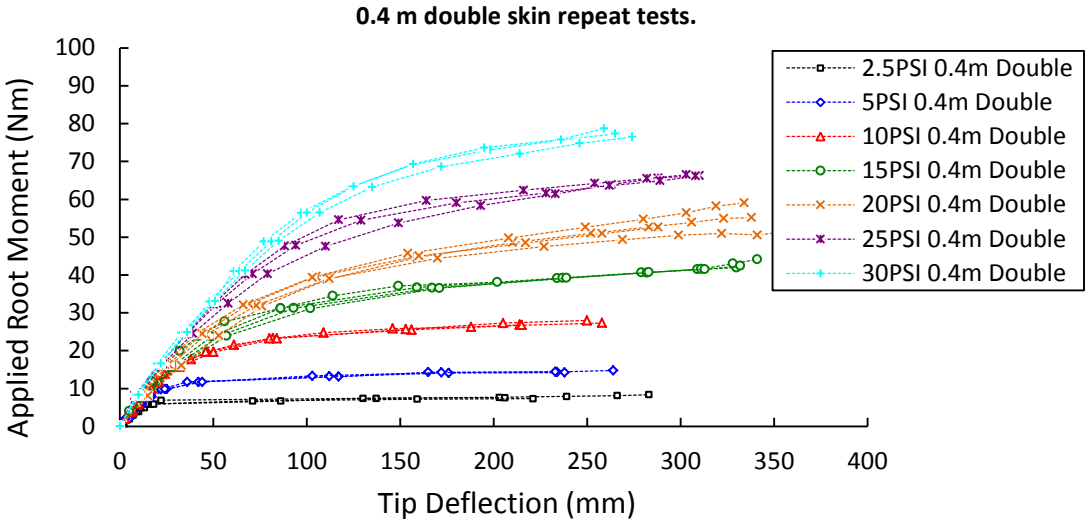
0.4 m double skin repeat tests.
Applied Root Moment (Nm)
Tip Deflection (mm)
2.5PSI 0.4m Double
5PSI 0.4m Double
10PSI 0.4m Double
15PSI 0.4m Double
20PSI 0.4m Double
25PSI 0.4m Double
30PSI 0.4m Double

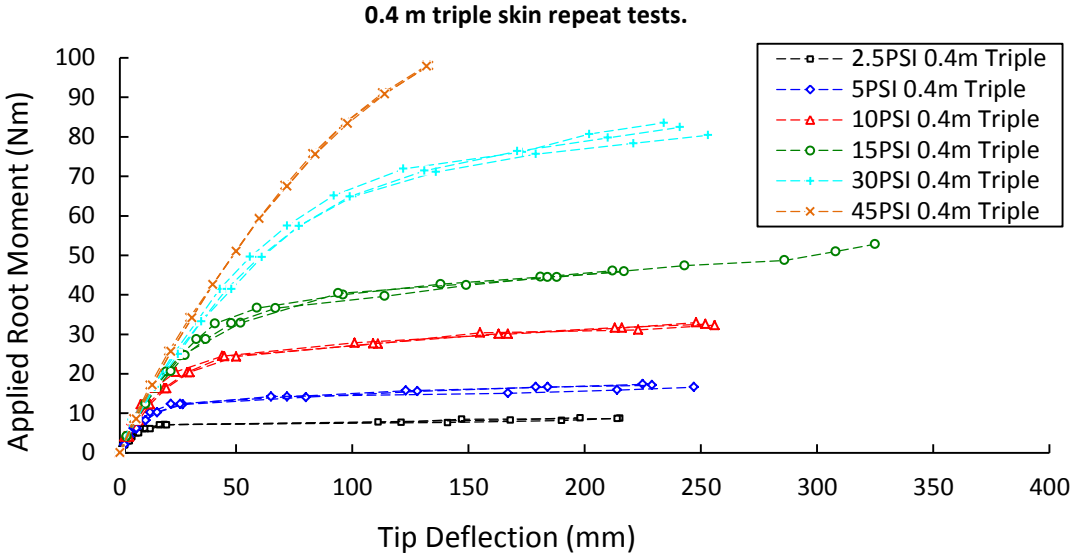
0.4 m triple skin repeat tests.
Applied Root Moment (Nm)
Tip Deflection (mm)
2.5PSI 0.4m Triple
5PSI 0.4m Triple
10PSI 0.4m Triple
15PSI 0.4m Triple
30PSI 0.4m Triple
45PSI 0.4m Triple

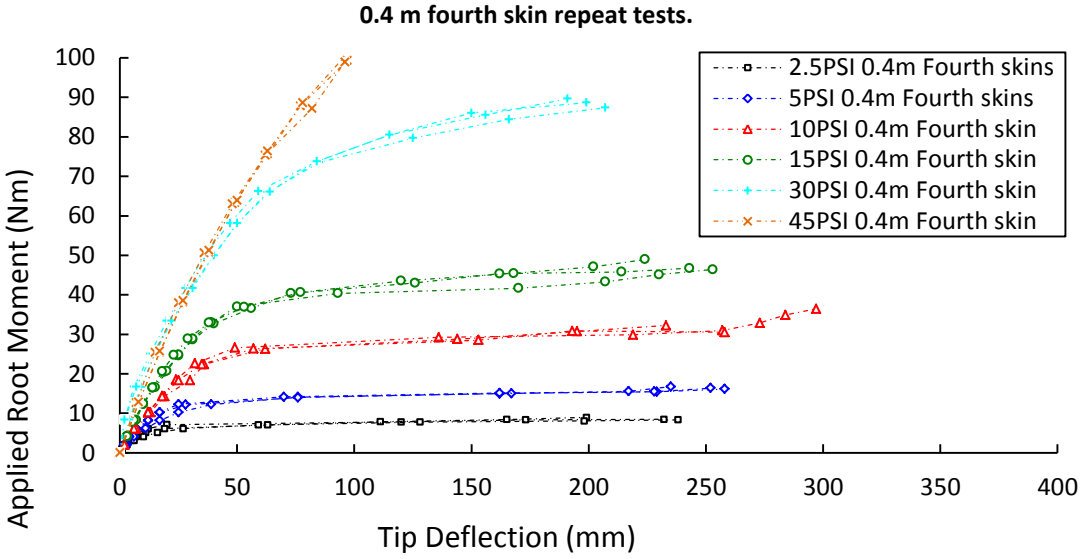
0.4 m fourth skin repeat tests.
Applied Root Moment (Nm)
Tip Deflection (mm)
2.5PSI 0.4m Fourth skins
5PSI 0.4m Fourth skins
10PSI 0.4m Fourth skin
15PSI 0.4m Fourth skin
30PSI 0.4m Fourth skin
45PSI 0.4m Fourth skin

1.0 m single skin repeat tests.

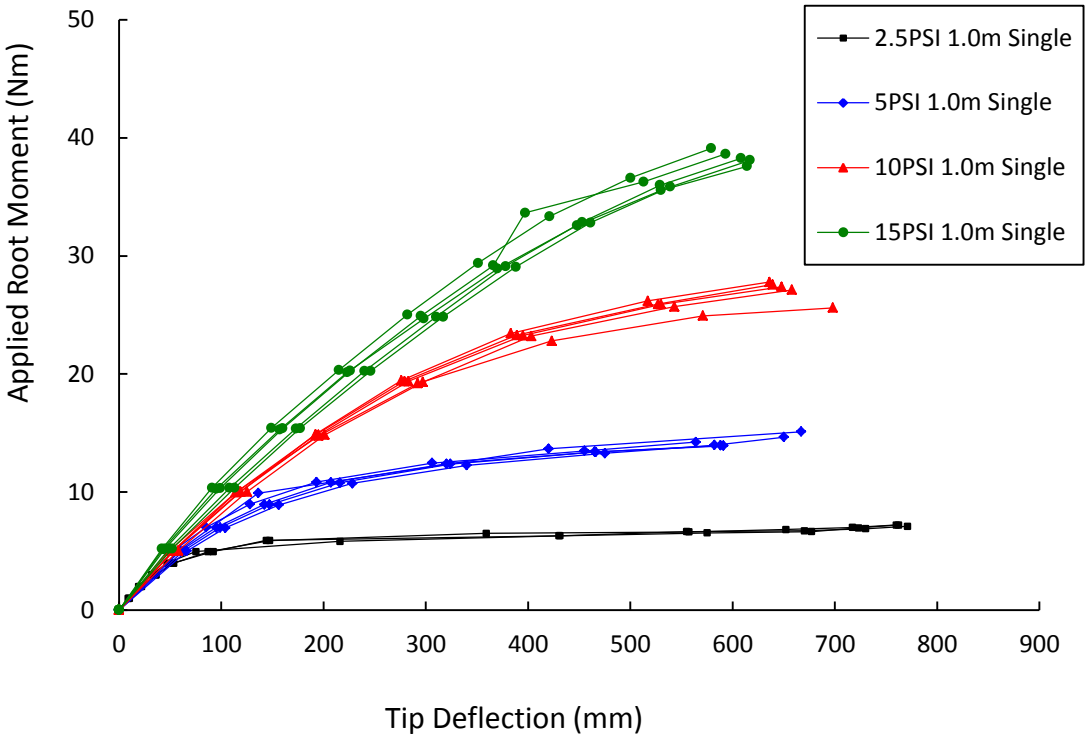

1.0 m double skin repeat tests.

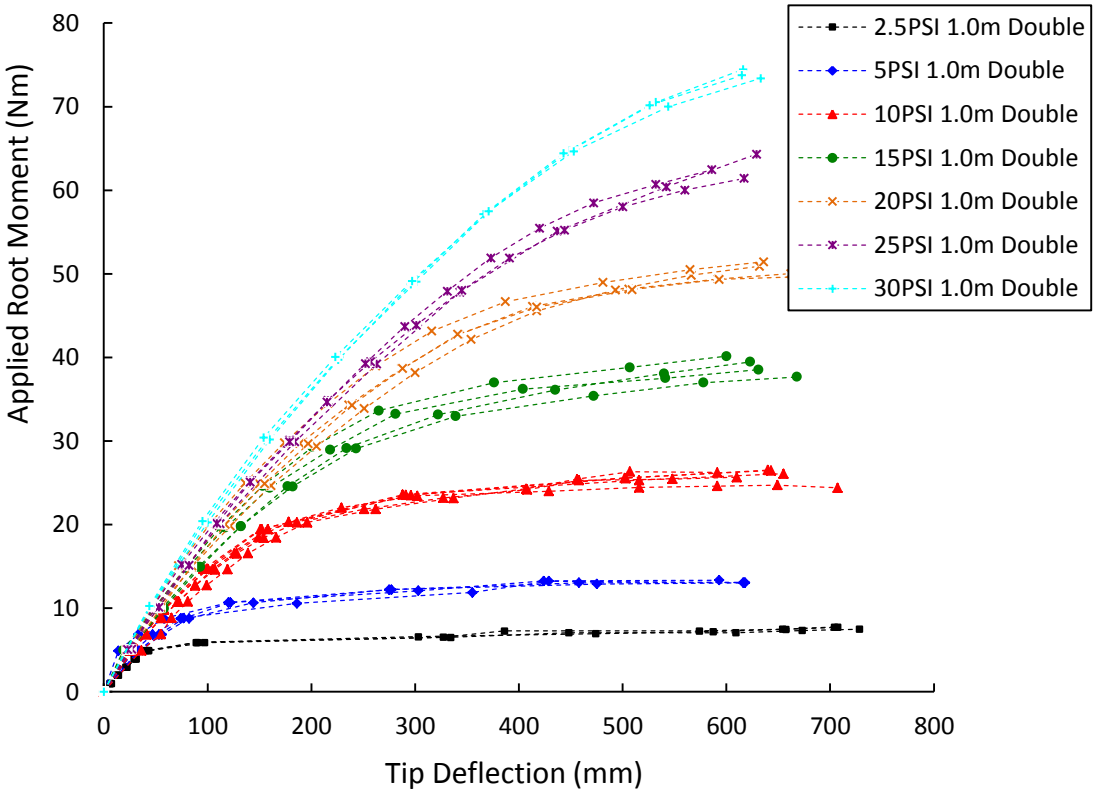

Non uniform skin thickness repeat tests at 10 PSI.

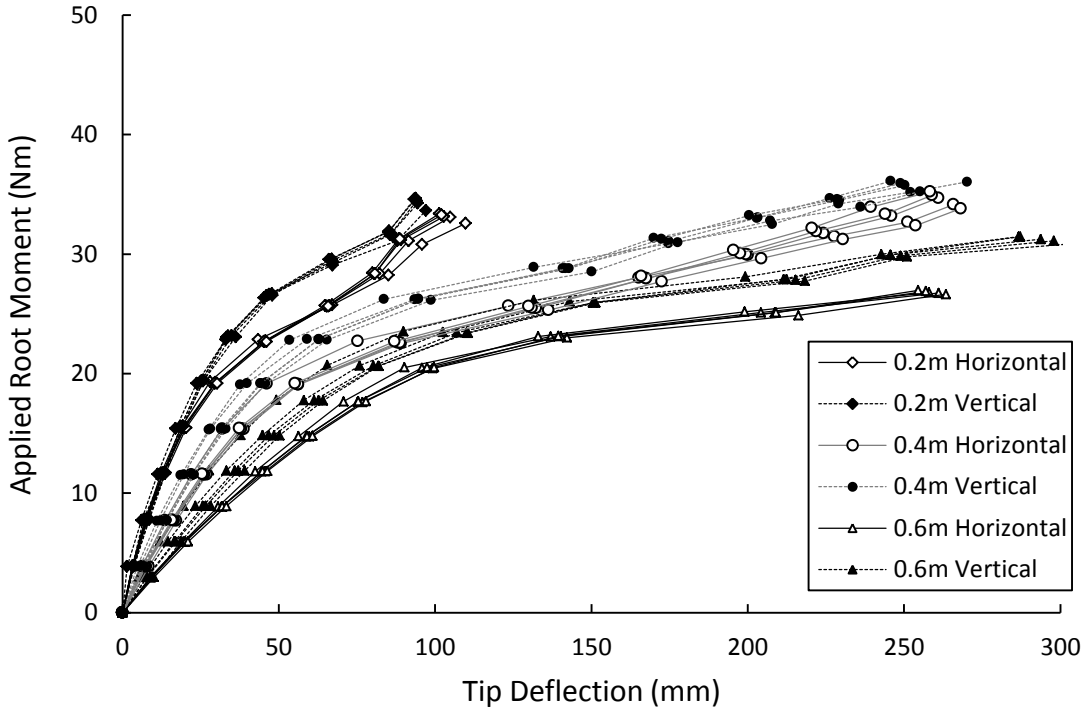

Non unifrom skin thickness repeat tests at 15 PSI.

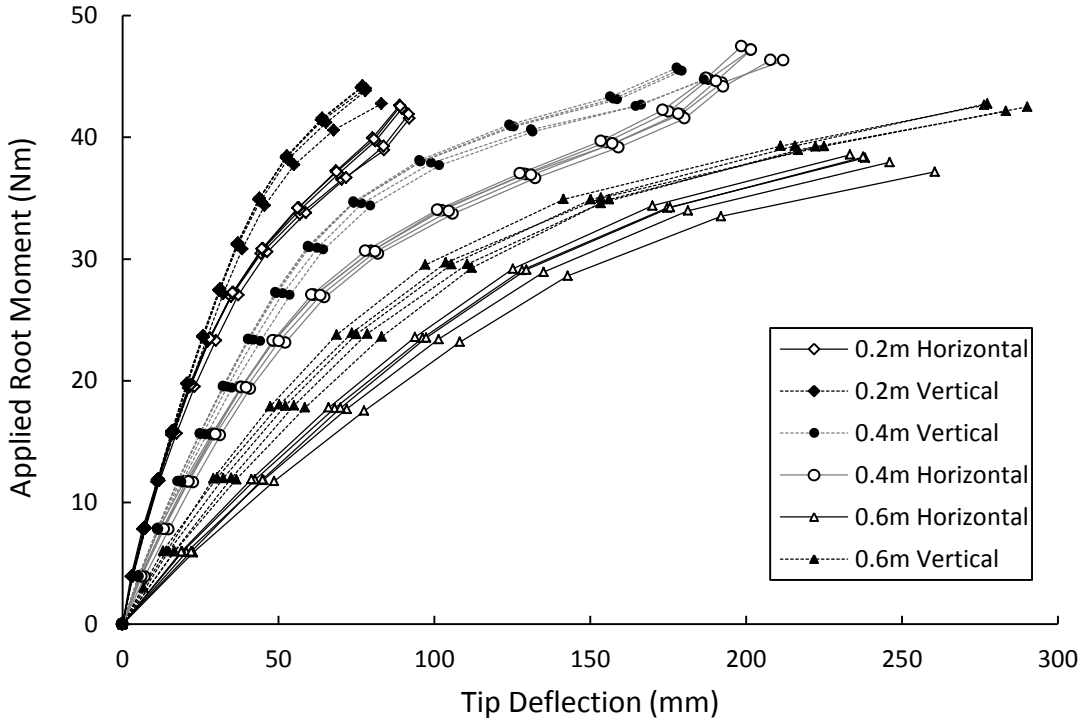

Appendix III

FEA Inflatable Boom

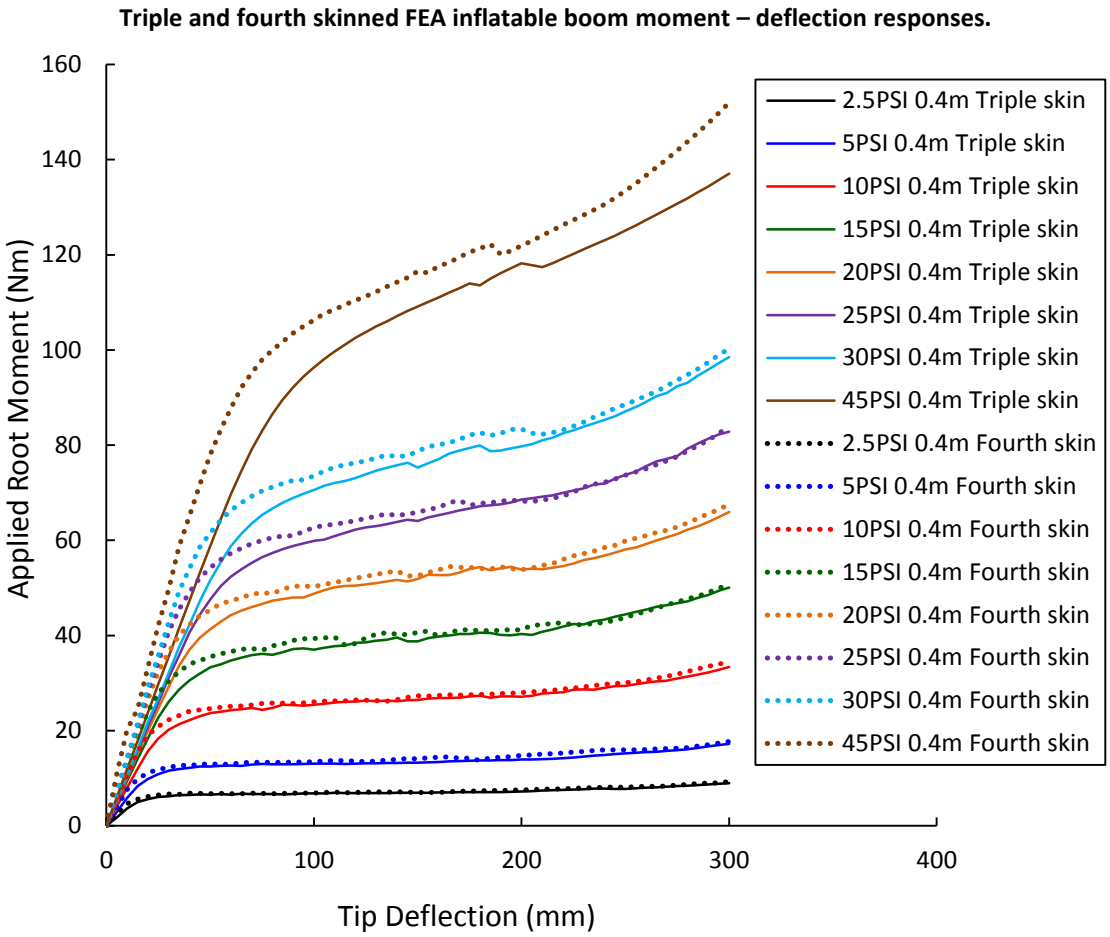

Appendix IV

Experimental Hybrid Boom

Preliminary attachment setup repeat tests.

Glued directly on boom at 4 locations					
Test 1		Test 2		Test 3	
Deflection (mm)	Moment (Nm)	Deflection (mm)	Moment (Nm)	Deflection (mm)	Moment (Nm)
0	0	0	0	0	0
2	2.0	3	2.0	3	2.0
4	4.0	6	4.0	7	4.0
9	6.0	10	6.0	12	6.0
15	8.0	15	8.0	18	8.0
21	10.0	19	10.0	23	10.0
28	12.0	24	12.0	29	12.0
36	14.0	30	14.0	37	14.0
46	16.0	41	16.0	44	16.0
54	17.9	50	18.0	52	18.0
64	19.9	61	19.9	60	19.9
75	21.7	73	21.8	70	21.8
86	23.6	89	23.6	79	23.7
100	25.4	114	25.1	103	25.3
116	27.0	135	26.6	150	26.2

Attached via 4 inserts locations					
Test 1		Test 2		Test 3	
Deflection (mm)	Moment (Nm)	Deflection (mm)	Moment (Nm)	Deflection (mm)	Moment (Nm)
0	0	0	0	0	0
2	2.0	2	2.0	1	2.0
3	4.0	4	4.0	2	4.0
5	6.0	6	6.0	3	6.0
7	8.0	8	8.0	5	8.0
10	10.1	11	10.1	7	10.1
13	12.1	14	12.1	9	12.1
19	14.1	20	14.1	12	14.1
99	15.6	25	16.1	15	16.1
		34	18.0	19	18.1
		43	20.0	24	20.1
		53	21.9	30	22.1
		135	22.8	39	24.0
				52	25.9
				127	26.8

Glued along whole boom length					
Test 1		Test 2		Test 3	
Deflection (mm)	Moment (Nm)	Deflection (mm)	Moment (Nm)	Deflection (mm)	Moment (Nm)
0	0	0	0	0	0
4	4.0	3	4.1	4	4.1
11	8.0	9	8.1	10	8.1
18	12.0	15	12.2	17	12.2
27	16.0	22	16.2	33	20.2
35	19.9	30	20.2	44	24.2
43	23.9	41	24.2	63	28.1
54	27.7	57	28.1	94	31.6
72	31.5	90	31.7	140	34.4
116	34.5	133	34.5	160	37.4
156	36.9	157	37.5		
170	40.0				
175	43.3				

4 attachment collars					
Test 1		Test 2		Test 3	
Deflection (mm)	Moment (Nm)	Deflection (mm)	Moment (Nm)	Deflection (mm)	Moment (Nm)
0	0	0	0	0	0
6	8.0	3	4.0	2	4.0
13	15.9	7	7.9	5	8.0
23	23.9	11	11.9	9	12.0
34	31.7	15	15.9	13	16.0
46	39.6	20	19.8	18	19.9
73	47.0	25	23.8	22	23.9
		30	27.7	27	27.9
		36	31.7	34	31.8
		41	35.6	39	35.8
		48	39.5	44	39.7
		76	42.9	65	39.4

Two opposed tape springs repeat tests at 15 PSI.

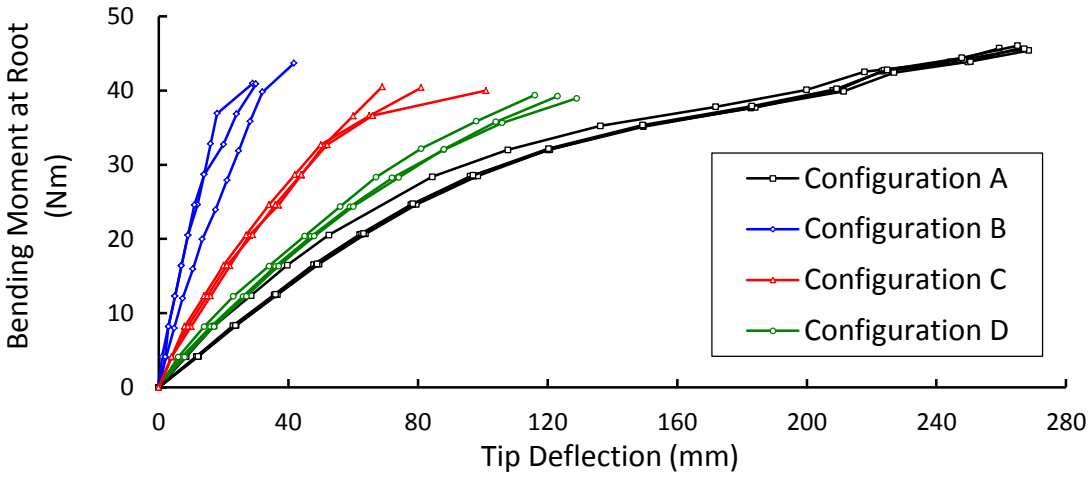

Two opposed tape springs repeat tests at 0 PSI.

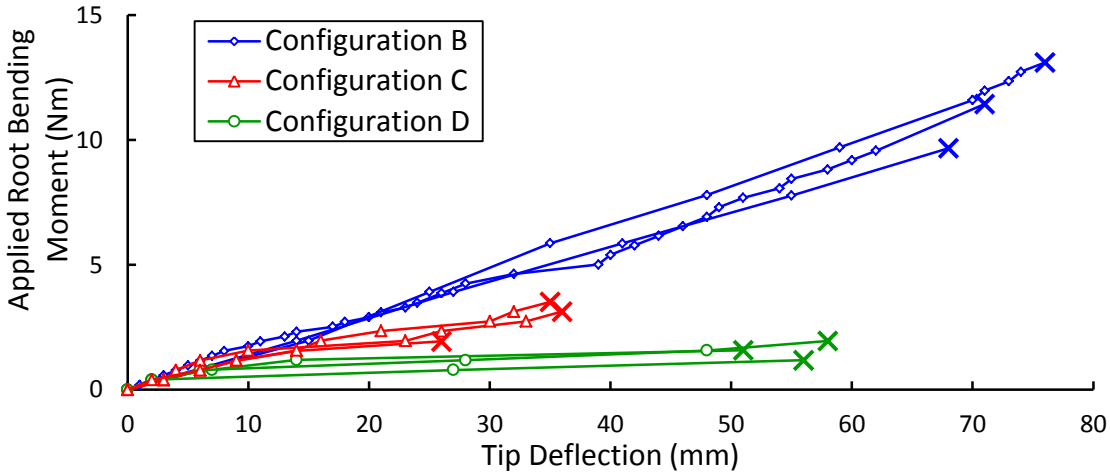

Varying tape spring thicknesses repeat tests, a).

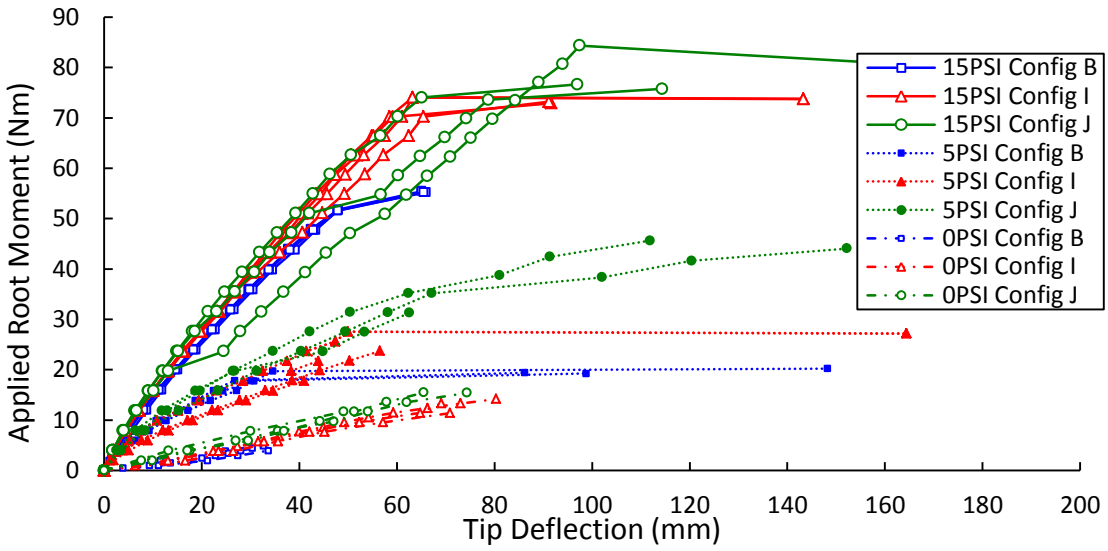

Varying tape spring thicknesses repeat tests, b).

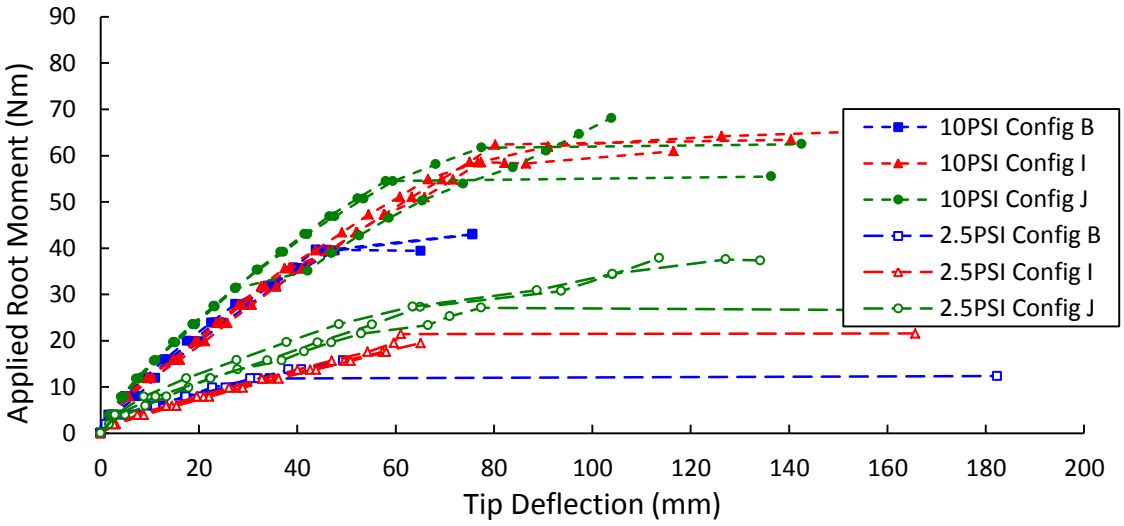

Four tape springs in the cross formation repeat tests, a).

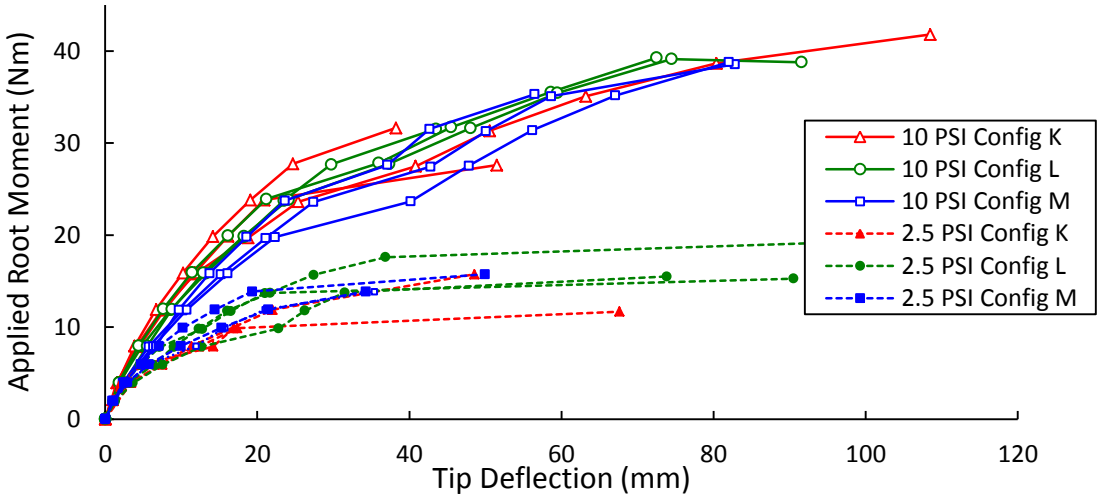

Four tape springs in the cross formation repeat tests, b).

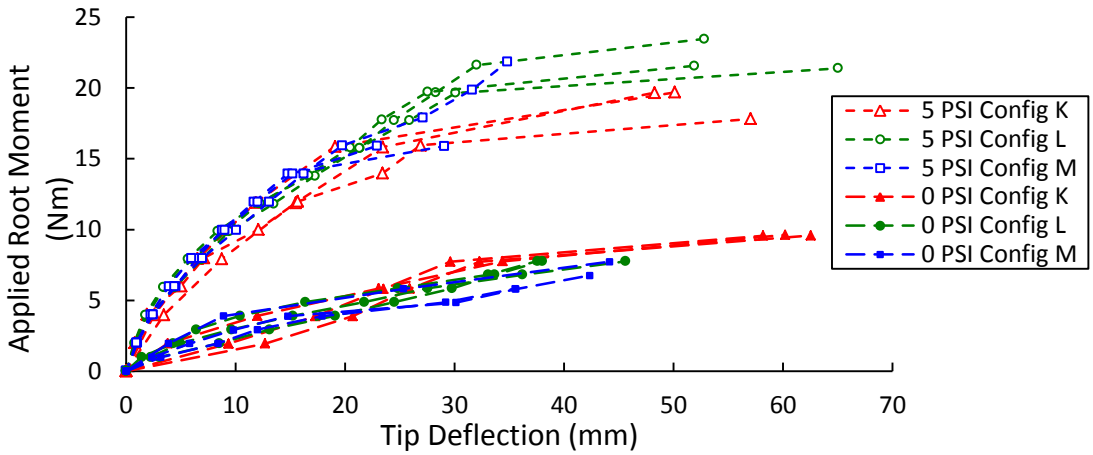

Appendix V

FEA Hybrid Boom

Tape spring thickness sensitivity study for the hybrid boom FEA model in configuration B.

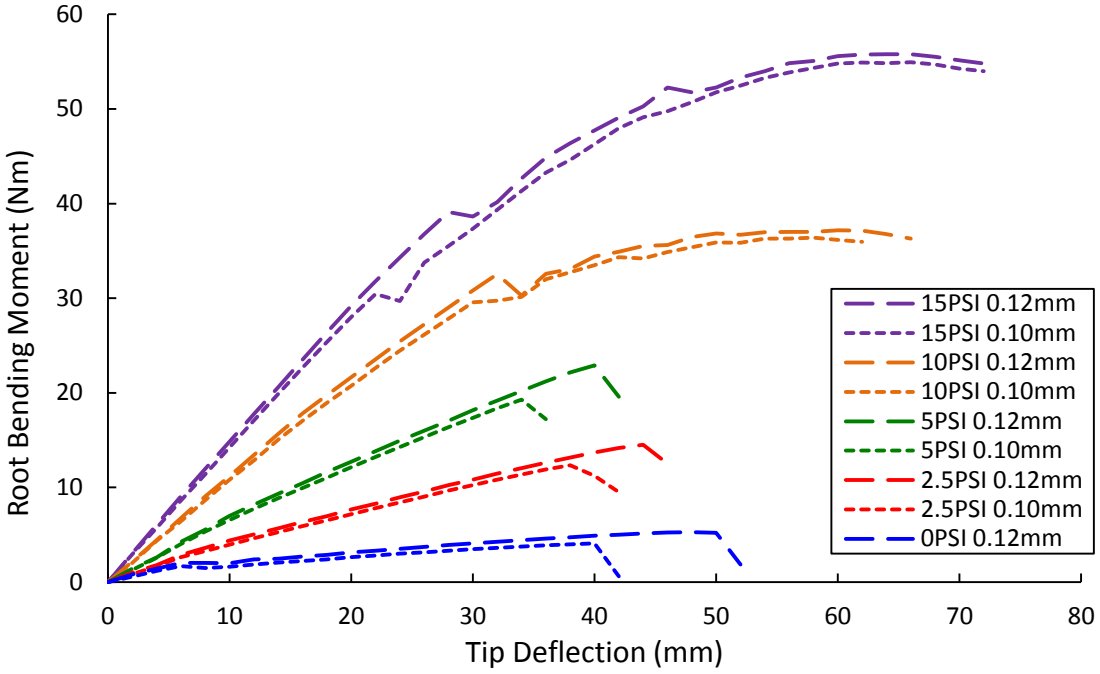

Opposed Tape Spring Configurations at 10 PSI.

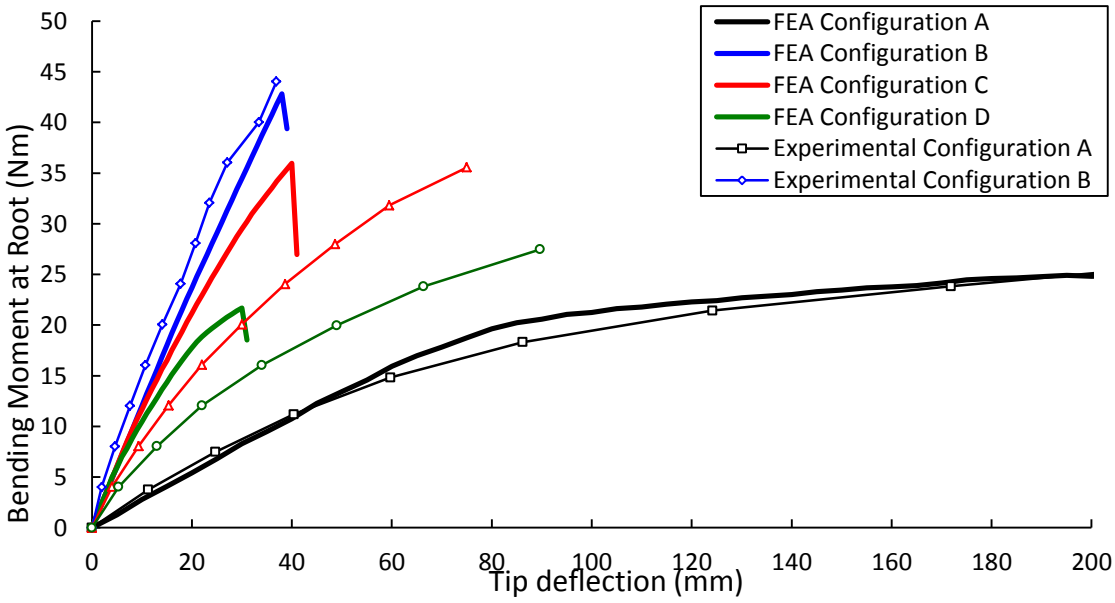

Single sided tape springs configurations at 10 PSI.

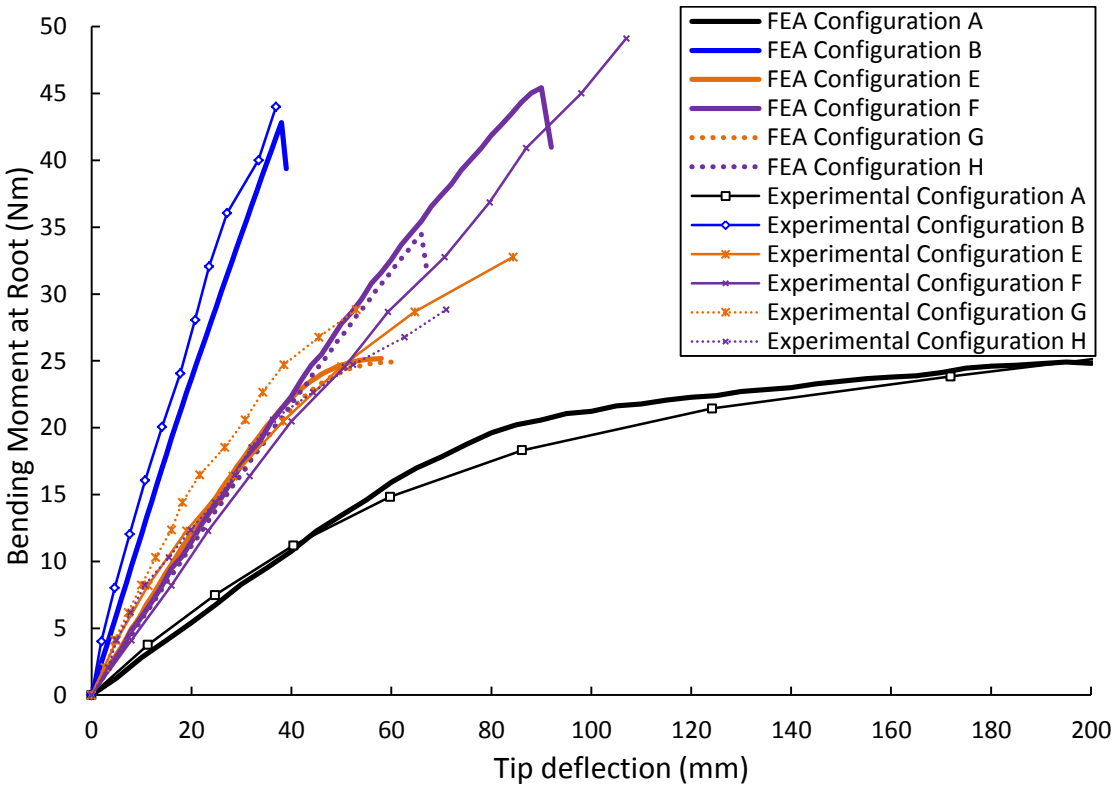

Experimental and FEA of configurations B, I and J at 10 PSI.

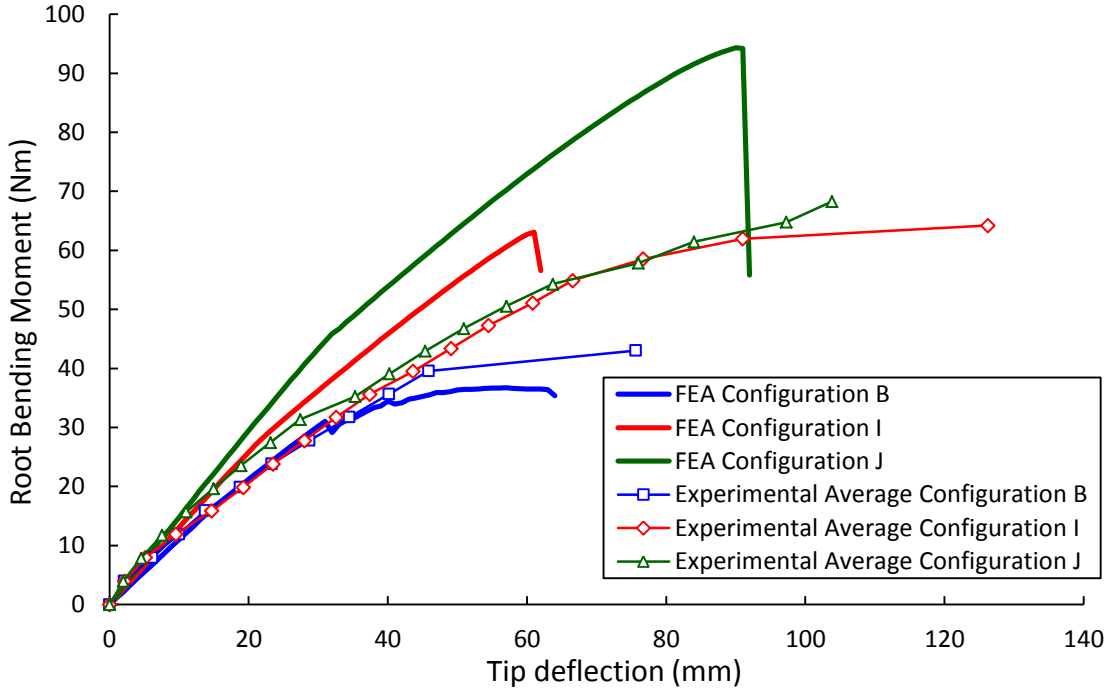

Tip deflection for hybrid booms with 4 tapes in a cross formation at 10 PSI.

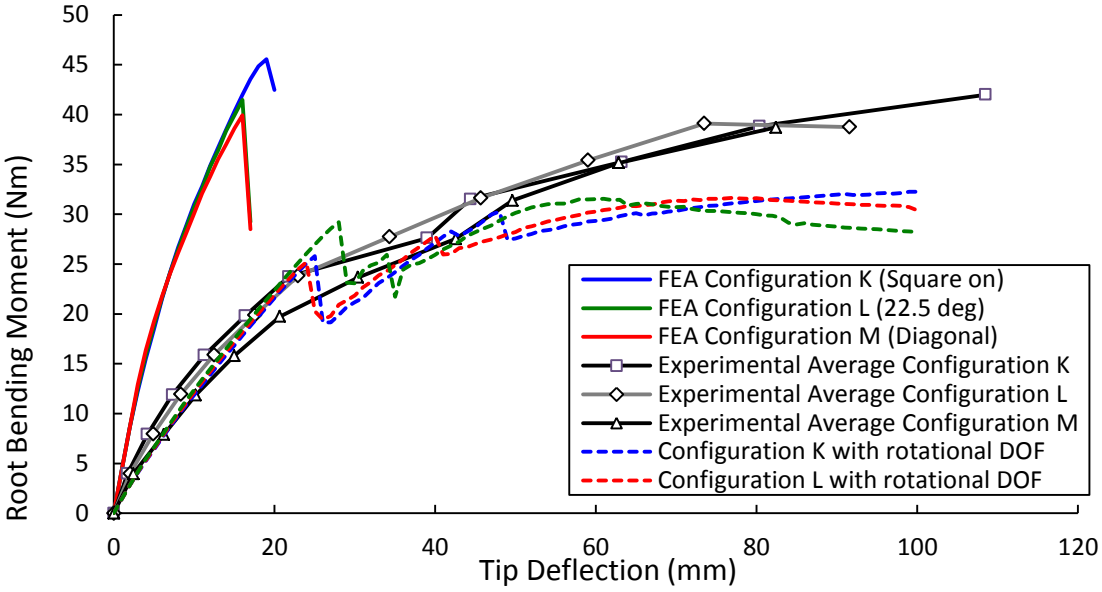

Varying opposed tape spring orientation at 15PSI.

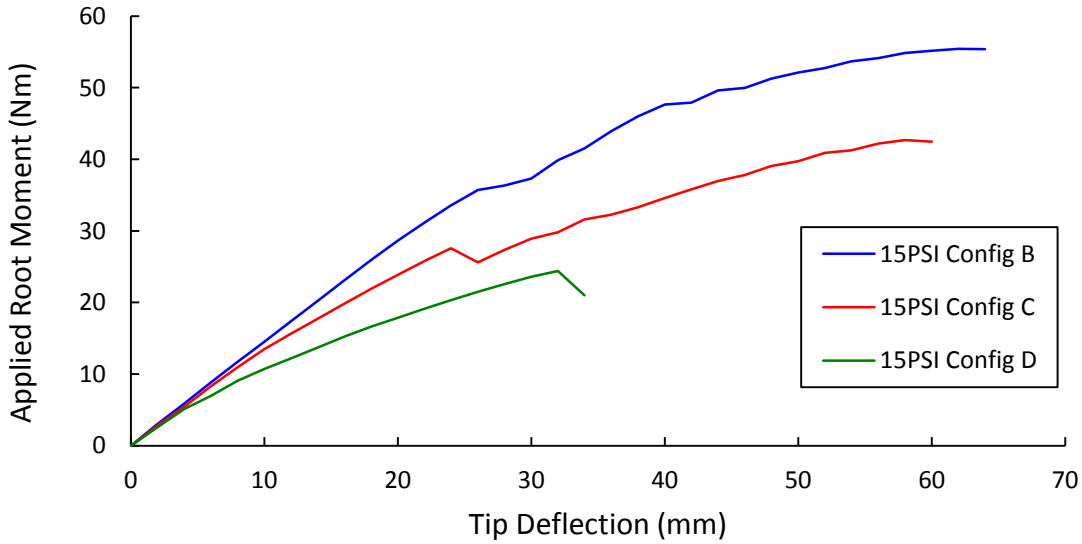

Varying opposed tape spring thickness and inflation pressure.

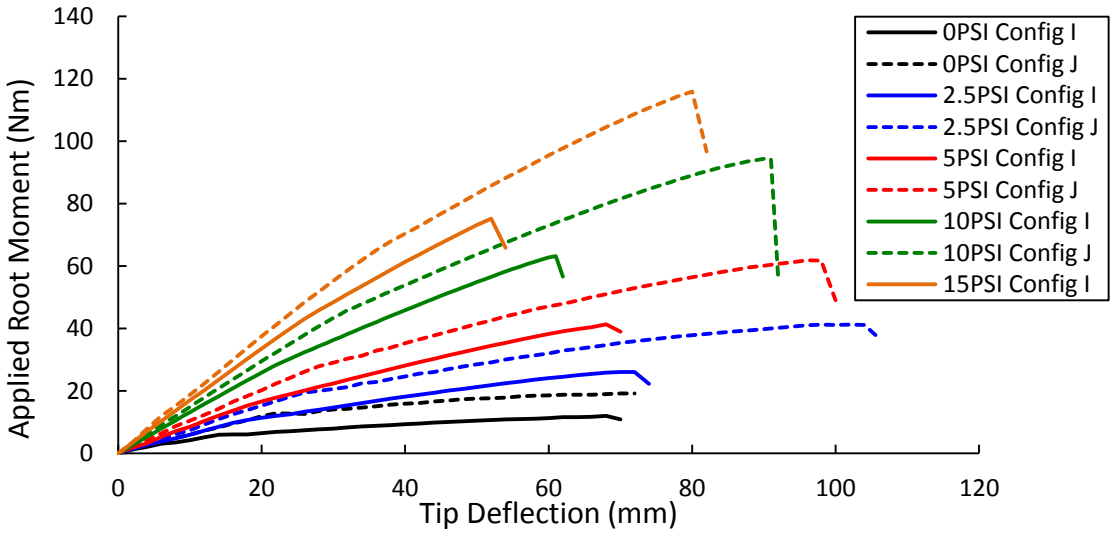

Varying 4 crossed tapes orientation and inflation pressure.

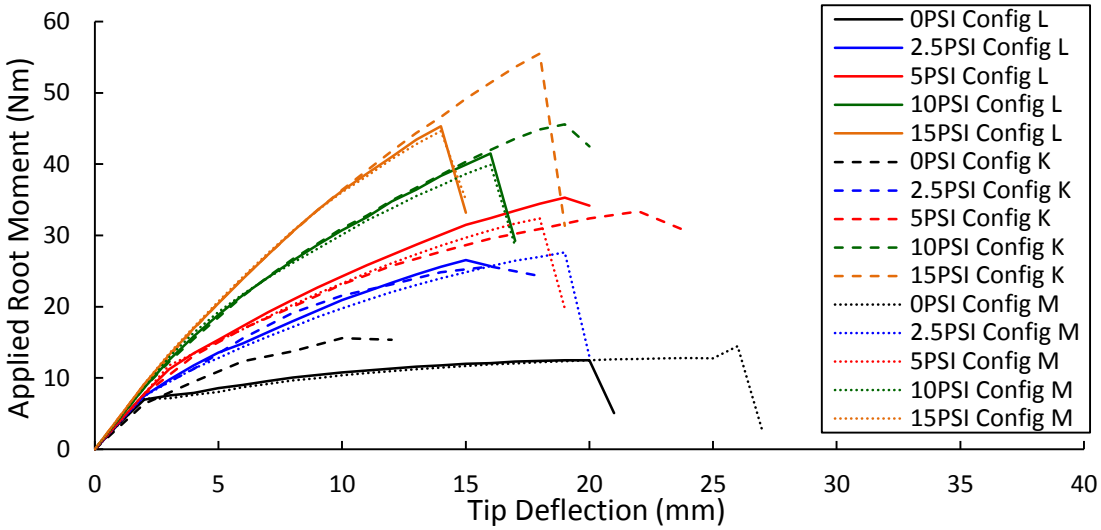

Peak moments of configuration B hybrid boom with varying collar intervals.

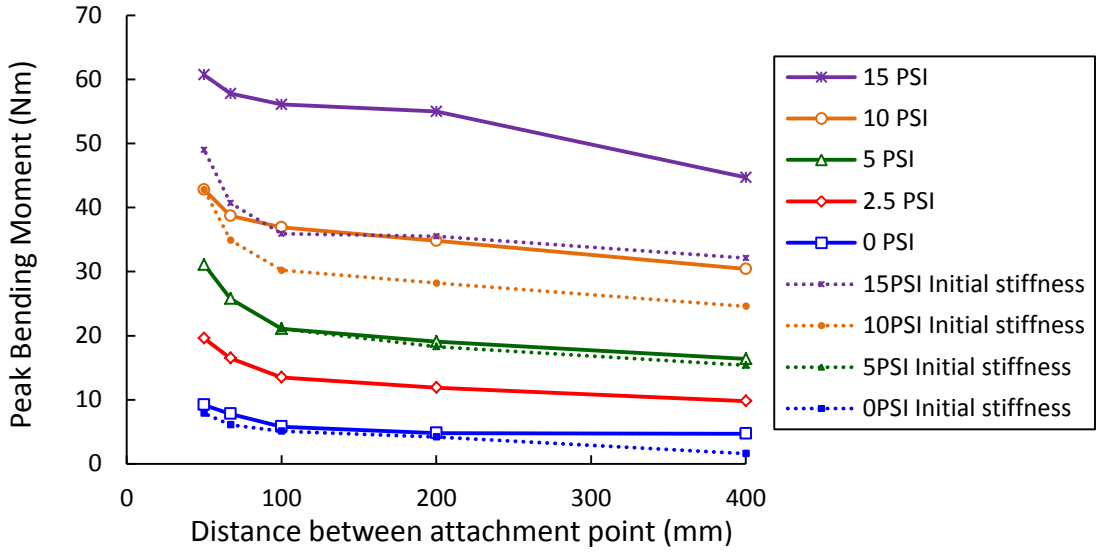

Averaged boom rigidity of configuration B hybrid boom with varying collar intervals.

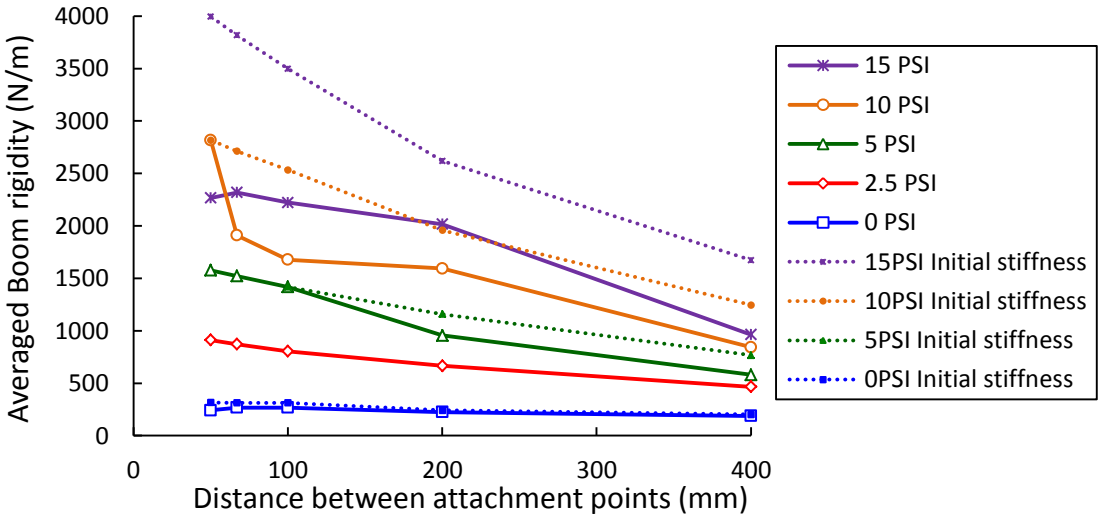

15PSI hybrid boom tip compression FEA data.

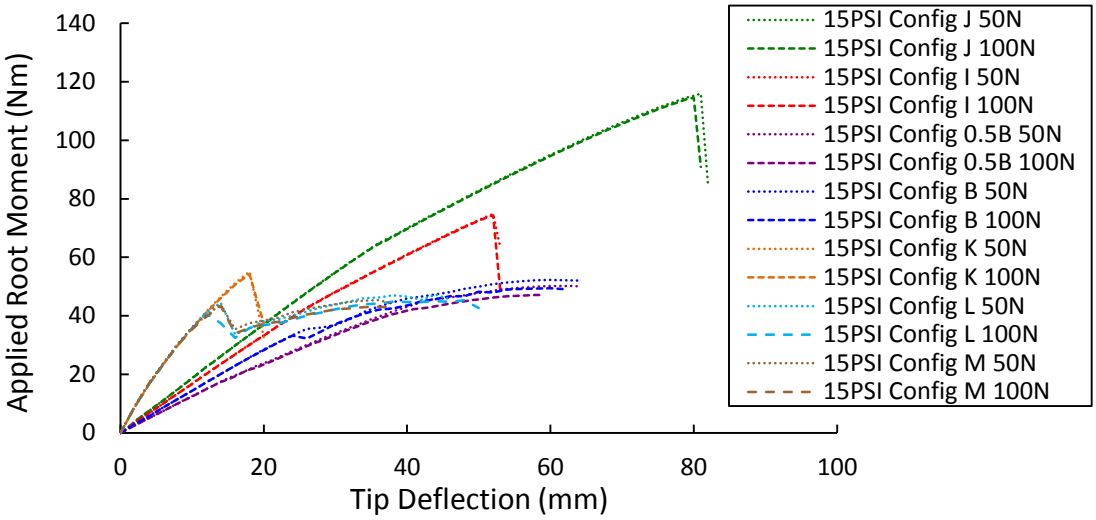

10PSI hybrid boom 4 cross formation tip compression FEA data.

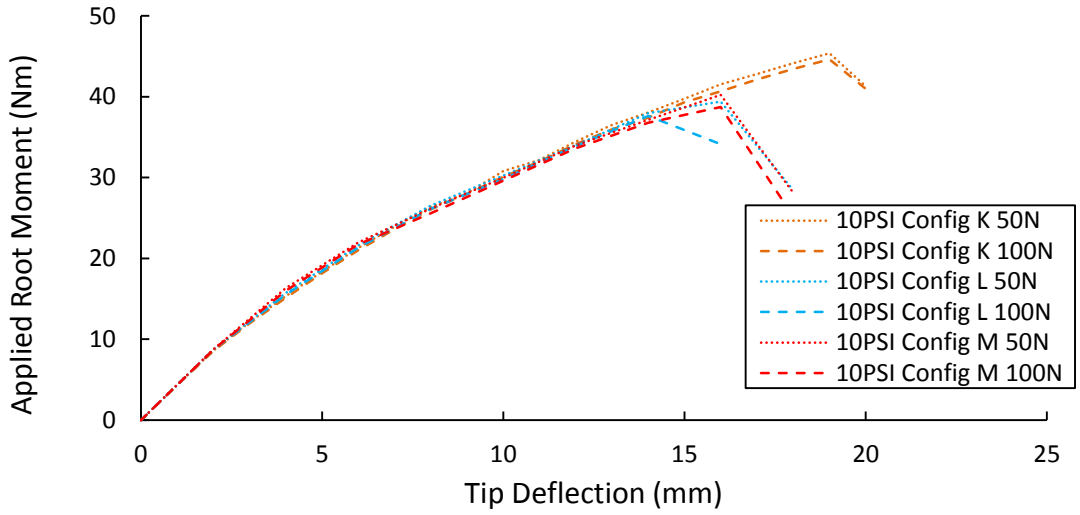

5PSI hybrid boom tip compression FEA data.

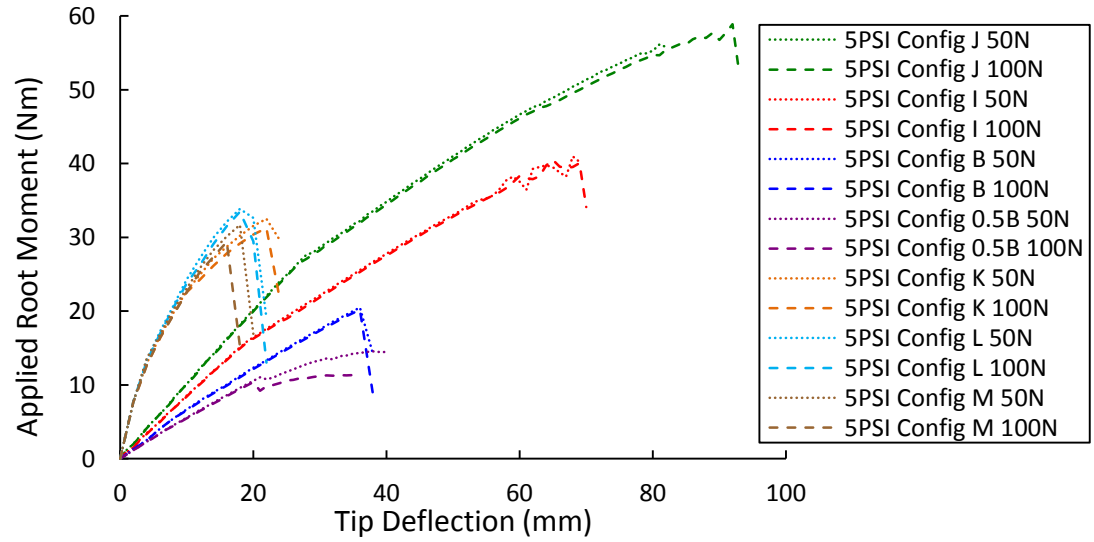

2.5PSI hybrid boom tip compression FEA data.

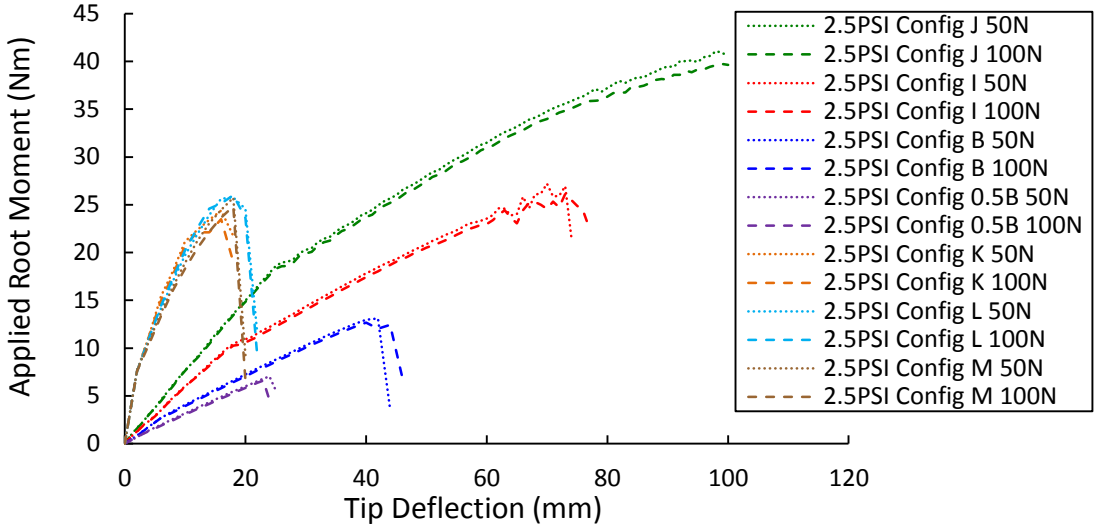

0PSI hybrid boom tip deflection FEA data.

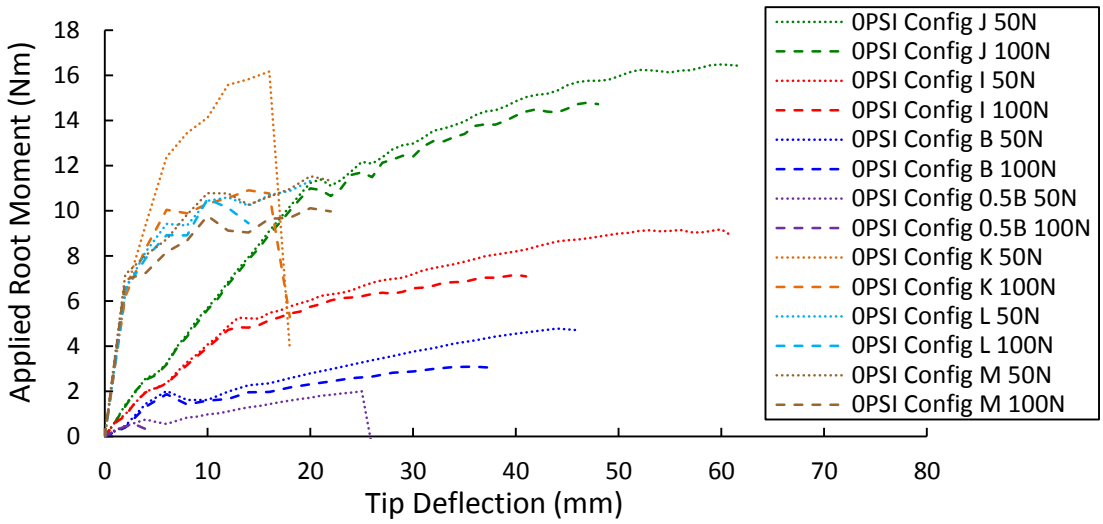

Peak moments of the FEA hybrid boom model with increasing number of tape springs around the circumference.

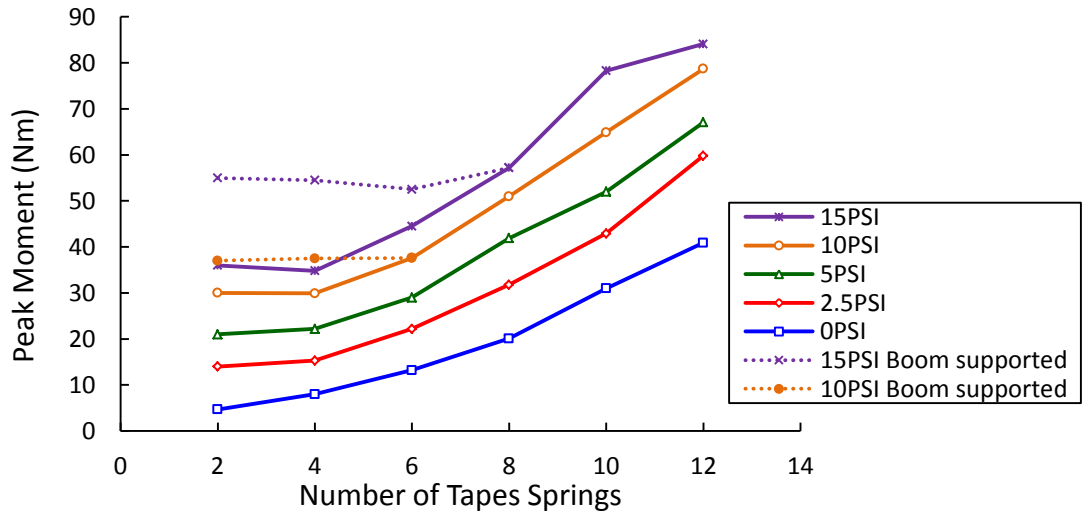

Averaged rigidity of the FEA hybrid boom model with increasing number of tape springs around the circumference.

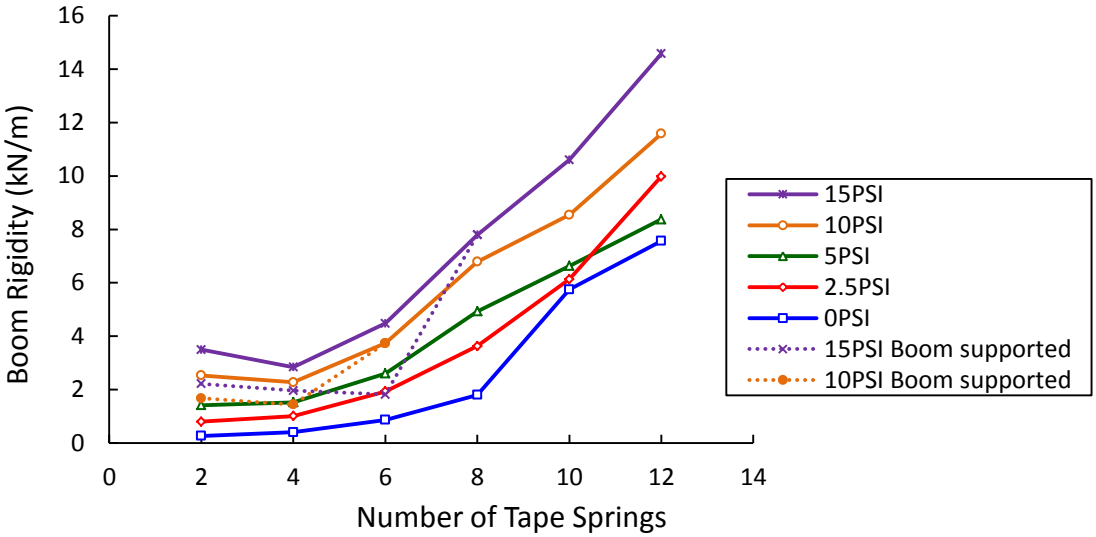

Tip deflections of 4 collars and 8 insert attachment methods.

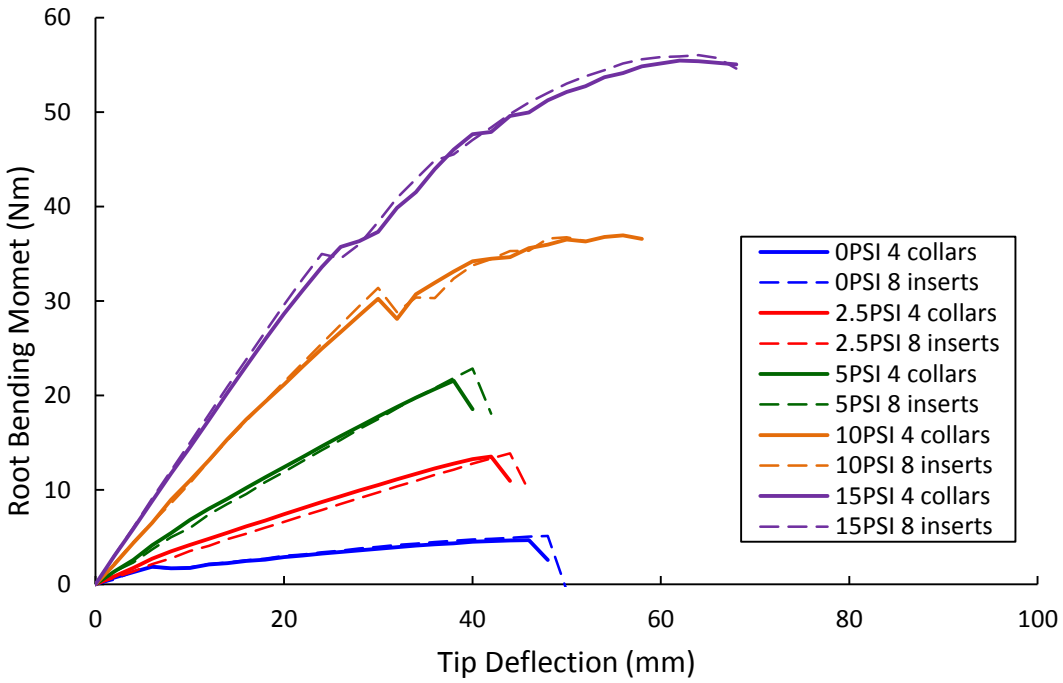

Appendix VI

Boom Stowage Data

Configuration		Stowed Length (cm)	Stowed Surface Area (cm^2)	Stowed Volume (cm^3)	Inflated Length (cm)	Inflated Surface Area (cm^2)	Inflated Volume (cm^3)
Collars	Tapes						
0	0	2	78.5	157	40	95.0	3800
1	2	4	115.3	461	40	115.3	4612
2	2	8	115.3	922	40	115.3	4612
4	2	16	115.3	1845	40	115.3	4612
1	4	4	117.5	470	40	117.5	4700
2	4	8	117.5	940	40	117.5	4700
4	4	16	117.5	1880	40	117.5	4700

References

1 Futron corporation, “Space transportation costs: trends in price per pound to orbit 1990-2000,” Bethesda, Maryland, USA, Sept 6, 2002, URL: http://www.futron.com/pdf/resource_center/white_papers/FutronLaunchCostWP.pdf [cited 11 Oct 2011].

2 Seffen, K.A., and Pellegrino, S., “Deployment dynamics of tape springs,” *Proceedings of Mathematical, Physical and Engineering Sciences,* Published by The Royal Society, London, Vol. 455, pp. 1003-1048, Mar 8, 1999.

3 Walker, S.J.I., McDonald, A.D., Niki, T., and Aglietti, G.S., "Initial performance assessment of hybrid inflatable structures,” *Acta Astronautica,* Vol. 68, No. 7-8, pp. 1185-1192, Apr-May, 2011.

4 de la Fuente, H., Raboin, J., Spexarth, G., and Valle, G., “TransHab: NASA’s large-scale inflatable spacecraft,” *Proceedings of the 41st AIAA/ ASME/ASCE/AHS/ASC Structures, Structural Dynamics, and Materials Conference,* AIAA, Atlanta GA, USA, pp. 1-9, Apr 3-6, 2000.

5 Messerschmid, E.W., and Renk, F., “Space stations,” Encyclopedia of Aerospace Engineering, John Wiley & Sons, Ltd, Hoboken, 1st ed., Dec 15, 2010, Chap 2, URL: http://onlinelibrary.wiley.com/doi/10.1002/9780470686652.eae424/full [cited 11 Oct 2011].

6 Foust, J., “Bigelow still thinks big,” *The Space Review*, Nov 1st, 2010, URL: http://www.thespacereview.com/article/1719/1 [cited 11 Oct 2011].

7 Peypoudat, V., Defoort, B., Lacour, D., Brassier, P., Couls, O.L., Langlois, S., Lienard, S., Bernasconi, M., and Gotz, M., “Development of a 3.2m-long inflatable and rigidizable solar array breadboard,” *46th AIAA/ASME/ASCE/AHS/ASC Structures, Structural Dynamics & Materials Conference,* Austin, TX, Apr 18-21, 2005.

8 Givois, D., Sicre, J., and Mazoyer, T. “A low cost hinge for appendices deployment: design, test, and applications,” *Proceedings of the 9th European Space Mechanisms and Tribology Symposium, ESA/ESTEC*, ESA-SP-480, Liege, Belgium, pp. 145-151, Sep 19-21, 2001.

9 Walker, S.J.I., and Aglietti, G.S., “An application of tape springs in small satellite area deployment devices,” *Proceedings of the 5th International Conference on Dynamics and Control of Systems and Structures in Space,* Cranfield University Press, UK, pp. 131-137, 2002.

10 Fernandez, J.M., Lappas, V.J., Daton-Lovett, A.J.D., "Completely stripped solar sail concept using bi-stable reeled composite booms," Acta Astronautica, Vol. 69, No. 1-2, pp. 78-85, Jul-Aug, 2011.

11 Walker, S.J.I., Aglietti, G.S., Cook, A.J., and McDonald, A.D., "Modelling Built Up, Tape Spring Based, Space Deployable Structures," *Proceedings of the 62nd International Astronautical Congress,* IAC-11.C2.2.1, Cape Town, South Africa, Oct 3-7, 2011.

12 Costantine, J., Tawk, Y., Christodoulou, C.G., Banik, J., and Lane, S., "CubeSat deployable antenna using bistable composite tape-springs," *IEEE Antennas and Wireless Propagation Letters,* Vol. 11, pp. 285- 288, 2012.

13 Walker, S.J.I., Kiley, A., Aglietti, G.S., Cook, A.J., and McDonald, A.D., "Modelling Three Dimensional, Tape Spring Based, Space Deployable Structures," *Proceedings of the 12th European Conference on Spacecraft Structures, Materials and Environmental Testing,* Noordwijk, Netherlands, Mar 20-23, 2012.

14 Sandy, C.R., "Next generation space telescope inflatable sunshield development," *Proceedings of Aerospace Conference,* IEEE, Vol. 6, Big Sky, MT, pp. 505-519, Mar 18-25, 2000.

15 Lou, M., Fang, H., and Hsia, L., "A combined analytical and experimental study on space inflatable booms," *IEEE Aerospace Conference Proceedings*, IEEE, Vol. 2, Big Sky, MT, pp. 503-512, Mar, 2000.

16 Lou, M., Fang, H., and Hsia, L., "Self-rigidizable inflatable boom," *Journal of Spacecraft and Rockets*, Vol. 29, No. 5, pp. 682-690, Sep-Oct, 2002.

17 Freeland, R.E., Bilyeu, G.D., Veal, G.R., and Mikulas, M.M., "Inflatable deployable space structures technology summary," *49th International Astronautical Congress, IAF-98-I.5.01, Melbourne, Australia,* Sept-Oct 28-2, 1998.

18 Bernasconi, M.C., Pagana, E., and Reibaldi, G.G., "Large Inflatable, Space-Rigidised Antenna Reflectors: Land Mobile Services Development," *Paper IAF-87-315, 38th International Astronautical Congress*, Brighton, UK, Oct 10-17, 1987.

19 Perrin, M.D., Soummer, R., Choquet, E., N'Diaye, M., Levecq, O., Lajoie, C., Ygouf, M., et al. "James Webb space telescope optical simulation testbed I: Overview and first results," *In SPIE Astronomical Telescopes+ Instrumentation*, International Society for Optics and Photonics, pp. 914309-914309, Aug, 2014.

20 Lou, M., "Development and application of space inflatable structures," Proceedings of the 22nd International symposium on space technology and science, ISTS, Morioka, Japan, pp. 537-545, May-Jun 28-4, 2000.

21 Lichodziejewski, D., Derbès, B., and Veal, G., "Testing of a 10 m-quadrant solar sail," *Proceedings of the 5th Earth-Sun System Technology Conference,* B1P4, Jun 28-30, 2005.

22 Lappas, V., Wie, B., McInnes, C.R., Tarabini, L., Gomes, L., and Wallace, K., "Solar kites for Earth magneto-tail monitoring," *ESA, First Workshop on Innovative System Concepts*, Noordwijk, Netherlands, Feb 21, 2006.

23 Macdonald, M., Hughes, W,G., McInnes, C., Lyngvi, A., Falkner, P., and Atzei, A., " GeoSail: An elegant solar sail demonstration mission," *Journal of Spacecraft and Rockets,* Vol. 44, No. 4, pp. 784-796, 2007.

24 Alhom, D.C., "Feathersail – The next generation of Nano-class sail vehicle," *Proceedings of the International Symposium for Solar Sails,* New York City, NY, Jul 20-22, 2010.

25 Galea, P., "Project ICARUS: Solar sail technology for the ICARUS interstellar mission," *Proceedings of the 2nd International Symposium on Solar Sailing,* New York City, NY, pp. 69-74, Jul 20-22, 2010.

26 Brown, M.A., "A deployable mast for solar sails in the range of 100 to 1,000 meters," *Advances in Space Research,* Vol. 48, No. 11, pp. 1747-1753, Dec 1, 2011.

27 Lappas, V., Adeli, N., Visagie, L., Fernandez, J., Theodorou, T., Steyn, W., and Parren, M., "CubeSail: A low cost CubeSat based solar sail demonstration mission," *Advances in Space Research,* Vol. 48, No. 11, pp. 1890-1901, Dec 1, 2011.

28 Tsuda, Y., Mori, O., Funase, R., Sawada, H., Yamamoto, T., Saiki, T., Endo, Yonekura, K., Hoshino, H., and Kawaguchi, J., "Achievement of IKAROS – Japanese deep space solar sail demonstration mission," *Acta Astronautica,* Available online May 7, 2012.

29 Pacini, L., Kaufman, D., Adams, M., Lou, M., and Carey, J., "Next generation space telescope (NGST) pathfinder experiment, inflatable sunshield in space (ISIS)," *Proceedings of a conference held at Hyannis,* ASP Conference Series, edited by E. P. Smith, and K. S. Long, Vol. 207, Next Generation Telescope Science and Technology, Hyannis, MA, pp. 365-375, Sept. 13-16, 1992.

30 Pacini, L. Kauffman, D., Adams, M, Culver, H., and Lou, M., "Design and Flight Testing of an Inflatable Sunshield for the NGST," Proceedings of the 41st AIAA/ASME/ASCE/AHS/ASC Structures, Structural Dynamics, and Materials conference, Atlanta, GA, April, 2000.

31 Bernasconi, M.C. and Koese, S., "The Space-Rigidized Thermal Shield for the ESA Far-Infrared Space Telescope (FIRST)," *3rd European Symposium on Space Thermal Control and Life Support Systems*, Noordwijk, NL, ESA Sp-288, 165173.

32 Cadogan, D., and Lin, J., "Inflatable Solar Array Technology," AIAA Paper 99-1075, 1999.

33 Malone, P.K., and Williams, G.T., "A Lightweight Inflatable Solar Array," *Proceedings of the 9th Annual AIAA/USU Conference on Small Satellites*, AIAA, Washington, DC, 1995.

34 Cadogan, D.P., and Grahne, M.S., "Deployment Control Mechanisms for Inflatable Space Structures," *Proceeding of the 33rd aerospace mechanisms conference*, Vol. 5, pp. 1-12, May, 1999.

35 Cui, D., Yan, S., Guo, X., Chu, F., "An overview of dynamics modeling of inflatable solar array," *Energy Procedia*, pp. 1967-1972, Vol. 14, 2012.

36 Jenkins, C.H.M., and Zarchan, P. (ed.), "Gossamer spacecraft: membrane and inflatable structures technology for space applications," *Progress in Astronautics and Aeronautics*, Vol. 191, AIAA, Reston, VA, 2001.

37 Cadogan, D., Lin, J., Huang, J., and Ferial, A., "An Inflatable Microstrip Reflectarray Concept for Ka-Band Applications," AIAA Paper 2000-1831, 2000.

38 Freeland, R.E., Bilyeu, G.D., Veal, G.R., Steiner, M.D., and Carson, D.E., "Large inflatable deployable antenna flight experiment results," *Acta Astronautica*, Vol. 41, No. 10, pp. 267-277, Aug-Nov, 1997.

39 Lou, M.C., Feria, V.A., and Huang, J., "Development of An Inflatable Space Synthetic Aperture Radar," *Presented at the 39th AIAAIASMEIASCEI AHSIASC Structures*, *Structural Dynamics, and Material Conference,* AIAA Paper 98-2103,Long Beach, California, Apr, 1998.

40 Cadogan, D., Lin, J., and Grahne, M., "The Development of Inflatable Space Radar Reflectarrays," AIAA Paper 99-1517, 1999.

41 Huang, J., "The development of inflatable array anetennas," IEEE Antennas and Propagation Magazine, Vol. 43, No. 4, pp. 44-50, Aug, 2001.

42 Chen, C.W., Moussessian, A., "MEO SAR system concepts and technologies for Earth remote sensing," *Proceedings of the Space 2004 conference and exhibit,* San Diego, CA, AIAA 2004-5904, Sept 28-30, 2004.

43 Freeland, R.E., Helms, R.G., Mikulas, M.M., Stuckey, W., Steckel, G., Watson, J., and Willis, P., "Inflatable space structures technology development for large radar antennas," Proceedings of the 24th International Symposium on Space Technology and Science, Vancouver, Canada, Oct 4-8, 2004.

44 Leipold, M., Runge, H., Sickinger, C., "Large SAR membrane antennas with lightweight deployable booms," Proceedings of the 28th ESA Antenna Workshop on Space Antenna Systems and Technologies, May-Jun 31-3, 2005.

45 Grossman, G., and Williams, G., "Inflatable Concentrators for Solar Propulsion and Dynamic Space Power," *Journal of Solar Energy Engineering*, Vol. 112, pp. 229-236, 1990.

46 Forward, R.L. & Hoyt, R.P., and Uphoff, C., "Application of the Terminator TetherTM electrodynamic drag technology to the deorbit of constellation spacecraft," *34th AIAA/ASME/SAE/ASEE Joint propulsion Conference & Exhibit*, AIAA Paper 98-3491, Cleveland, OH, Jul 13-15, 1998.

47 Bruno, C., Anselmo, L., Bussolino, L., Cioeta, M., Iess, L., Licata, R., Marchetti, M., Schirone, L., Somensi, L., and Ulivieri, C., "EDOARD: an electrodynamic tether device for efficient spacecraft de-orbiting," *Proceedings of the 3rd European Conference on Space Debris,* Darmstadt, Germany, ESA-SP-473, pp.707-712, Mar 19-21, 2001.

48 Nishida, S., Kawamoto, S., Okawa, Y., Terui, F., and Kitamura, S., "Space debris removal system using a small satellite," *Acta Astronautica*, Vol. 65, No. 1-2, pp. 95-102, Jul-Aug, 2009.

49 Hoyt, R.P., Barnes, I.M., Voronka, N.R., Slostad, J.T., "The Terminator TapeTM: A cost-effective de-orbit module for end-of-life disposal of LEO satellites," *Proceedings of the AIAA Space 2009 Conference and Exposition*, Pasadena, CA, pp. 6733-6741, Sept 14-17, 2009.

50 Maessen, D., "Development of a generic inflatable de-orbit device for CubeSats," *Proceedings of the 58th International Astronautical Congress,* IAC-07-A6.3.06, May, Hyderabad, India, Sept, 2007.

51 Roberts, P.C.E., Harkness, P.G., "Drag sail for end-of-life disposal from low Earth orbit," *Journal of Spacecraft and Rockets*, Vol. 44, No. 6, pp. 1195-1203, Nov-Dec, 2007.

52 Lücking, C., McInnes, C.R., Colombo, C., "A passive high altitude deorbiting strategy," *Proceedings of the 25th Annual IAA/USU Conference on Small satellites*, Logan, UT, Aug 8-11, 2011.

53 Nock, K.T., McRonald, A.D., Aaron, K.M., Global Aerospace Corporation*, Balloon device for lowering space object orbits*, U.S. Pat. 6,830,222.

54 Clark, I.G., Hutchings, A.L., Tanner, C.L., and Braun, R.D., "Supersonic inflatable aerodynamic decelerators for use on future robotic missions to Mars," *IEEE Aerospace Conference*, Big Sky, MT, pp. 1-17, Mar 1-8, 2008.

55 Cadogan, D., Sandy, C., and Grahne, M., "Development and Evaluation of the Mars Pathfinder Inflatable Airbag Landing System," International Astronautical Federation, 1998.

56 Jones, J.A., and Wu, J.J., "Inflatable technology for robotics," *Robotics 2000*, ASCE, pp. 328-332, 2000.

57 Sokolowski, W.M., and Tan, S.C., "Advanced self-deployable structures for space applications," *Journal of Spacecraft and Rockets*, Vol. 44, No. 4, pp. 750-754, Jul-Aug, 2007.

58 Smith, S.W., Jacob, J.D., Jones, R.J., Scarborough, S.E., and Cadogan, D.P., "A high-altitude test of inflatable wings for low-density flight applications," *Proceedings of the 7th AIAA Gossamer Spacecraft Forum*, May, 2006.

59 Cadogan, D., Graham, W., and Smith, T., "Inflatable and rigidizable wings for unmanned aerial vehicles," *2nd AIAA "Unmanned Unlimited" Systems, Technologies and Operations,* AIAA 2003-6630, San Diego, CA, Sept 15-18, 2003.

60 McDonald, A.D., and Walker, S.J.I., "Use of multiple SMA wires for morphing of inflatable wings," *Proceedings of the ASME 2010 Conference on Smart Materials, Adaptive Structures and Intelligent Systems*, ASME, pp. 7-16, Jan, 2010.

61 Darooka, D.K., and Jensen, D.W., "Advanced space structure concepts and their development", *Proceedings of the 42nd AIAA/ASME/ASCE/AHS/ASC Structures, Structural Dynamics, and Materials Conference and Exhibit,* AIAA-2001-1257, Seattle, WA, Apr 16-19, 2001.

62 Russell, I.W., and Hanssen, N.S., "The application of a gelatin resin system to aerospace expandable sandwich structures," GCA Corp., Contract AF33 (615)-2058, AFAPL-TR-65-84, Oct, 1965.

63 Lou, M., and Feria, V.A., "Development of Space Inflatable/Rigidizable Structure Technology," *Proceedings of the IUTAM-IASS Symposium on Deployable Structures: Theory and Applications*, Springer Netherlands, Vol. 80, pp. 251-260, Jan, 2000.

64 Cadogan, D.P., and Scarborough, S.E., "Rigidizable materials for use in gossamer space inflatable structures," *Proceedings of the 42nd AIAA/ASME/ASCE/AHS/ASC Structures, Structural Dynamics, and Materials Conference and Exhibit,* AIAA-2001-1417, Seattle, WA, Apr 16-19, 2001.

65 Cadogan, D.P., Scarborough, S.E., Lin, J.K., and Sapna, G.H., "Shape memory composite development for use in gossamer space inflatable structures," *43rd AIAA/ASME/ASCE/AHS/ASC Structures, Structural Dynamics, and Materials Conference, AIAA Gossamer Spacecraft Forum,* Denver, CO, p. 1372, Apr 22-25, 2002.

66 Allred, R.E., McElroy P.M., Scarborough, S., and Cadogan D.P., "UV Rigidizable Carbon-reinforced isogrid inflatable booms," *43rd AIAA/ASME/ASCE/AHS/ASC Structures, Structural Dynamics, and Materials Conference,* Denver, CO, p. 1202, Apr 22-25, 2002.

67 Higuchi, K., Ogi, Y., Watanabe, K., and Watanabe, A., "Verification of practical use of an inflatable structure in space," *Proceedings of the 26thInternational symposium on space technology and science, ISTS,* 2008-c-08, Hamamatsu, Japan, 2008.

68 Brandon, E.J., Vozoff, M., Kolawa, E.A., Studor, G.F., Lyons, F., Keller, M.W., Beiermann, B., White, S.R., Sottos, N.R., Curry, M.A., Banks, D.L., Brocato, R., Zhou, L., Jung, S., Jackson, T.N., and Champaigne, K., "Structural health management technologies for inflatable/deployable structures: Intergrating sensing and self-healing," *Acta Astronautica,* Vol. 68, No. 7-8, pp. 883-903, Apr, 2011.

69 Johnson, L., Whorton, M., Heaton, A., Pinson, R., Laue, G., and Adams, C., "NanoSail-D: A solar sail demonstration mission," *Acta Astronautica,* Vol. 68, No. 5-6, pp. 571-575, Mar-Apr, 2011.

70 Biddy, C., Alford, C., Bertino, M., Diaz, A., Nehrenz, M., and Svitek, T., " Challenges and design of Lightsail-1 boom deployment module," *Proceedings of the 2nd International Symposium on Solar Sailing,* New York City, NY, Jul 20-22, 2010, pp. 87-90.

71 Thomas, G.M., "Prototype development and dynamic characterization of deployable cubesat booms," *Air Force Institute of Technology,* Thesis, Wright-Paterson Air Force Base, Ohio, Mar, 2010.

72 Rimrott, F.P.J., "Storable tubular extendible members," *Engineering Digest*, Sept, 1966.

73 Leipold, M., Garner, C.E., Freeland, R., Herrmann, A., Noca, M., Pagel, G., Seboldt, W., Sprague, G., and Unckenbold, W., "ODISSEE – A proposal for demonstration of a solar sail in Earth orbit," *Acta Astronautica*, Vol. 45. No. 4-9, pp.577-566, 1999.

74 Sickinger, C., Herbeck, L., and Breitbach, E., "Structural engineering on deployable CFRP booms for a solar propelled sailcraft," *Acta Astronautica,* Vol. 58, No. 4, pp. 185-196, Feb, 2006.

75 Sickinger, C., and Fischer, C., "Probabilistic formulation of design parameters for the design of deployable CFRP booms for a solar sail," *Internal Report IB 131-2002/22, German Aerospace Center, Institute of Structural Mechanics* (in German), 2002.

76 Sickinger, C., and Herbeck, L., "Deployment strategies, analyses and tests for the CFRP booms of a solar sail," *Proceedings of European Conference on Spacecraft Structures, Materials and Mechanical Testing,* CNES, Toulouse, France, 2002.

77 Block, J., Straubel, M., and Wiedemann, M., "Ultralight deployable booms for solar sails and other large gossamer structures in space," *Acta Astronautica,* Vol. 68, No. 7-8, pp. 984-992, Apr-May, 2011.

78 McEachen, M.E., Trautt, T.A., and Murphy, D.M., "The ST8 SAILMAST validation experiment," *Proceedings of the 46th AIAA/ASME/ASCE/AHS/ASC Structures, Structural Dynamics, and Materials Conference and Exhibit,* AIAA-2005-1884, Austin, TX, Apr 18-21, 2005.

79 Tibert, G., "Deployable tensegrity structures for space applications," *Doctoral Thesis,* Royal Institute of Technology Department of Mechanics, Stockholm, Sweden, 2002.

80 Murphy, D.M., Murphey, T.W., and Gierow, P.A., "Scalable solar sail subsystem design considerations," *Proceedings of the 43rd AIAA/ASME/ASCE/AHS/ASC Structures, Structural Dynamics, and Materials Conference and Exhibit,* AIAA-2002-1703, Denver, CO, Apr 22-25, 2002.

81 Santerre, B. et al., "The Innovative Deorbiting Aerobrake System "IDEAS" for small satellites: the use of gossamer technology for a cleaner space," *Proceedings of the 4S Symposium Small Satellites Systems and Services,* Rhodes, Greece, May 26-30, 2008.

82 Megson, T.H.G., "Structural and stress analysis", *2nd ed., ELSEVIER Butterworth-Heinemann*, Oxford, UK, Chap. 7, 2005.

83 Ikema, K., Gubarevich, A. V., and Odawara, O., "Deformation Analysis of a Joint Structure Designed for Space suit with the Aid of an Origami Technology," *Proceeding of the 28th International Symposium on Space Technology and Science,* ISTS-2009-p-07, Okinawa, Japan, Jun 5-12, 2011.

84 Leonard, R.W., and Brooks, G.W., and McComb, H.G., "Structural considerations of inflatable re-entry vehicles," NASA TND-457, Los Angeles, USA, Sep, 1960.

85 Comer, R.L., and Levy, S., "Deflections of an inflatable circular cylinder cantilever beam," *AIAA Journal*, Vol. 1, pp. 1652–1655, Jul, 1963.

86 Webber, J.P.H., "Deflections of inflated cylindrical cantilever beams subjected to bending and torsion," *Aeronautical Journal*, Vol. 86, No. 858, pp. 306-312, Oct, 1982.

87 Main, J.A., Peterson, S.W., and Strauss, A.M., "Load-deflection behavior of space-based in fabric beams," *Journal of Aerospace Engineering*, Vol. 7, No. 2, pp. 225-238, 1994.

88 Main, J.A., Peterson, S.W., and Strauss, A.M., "Beam-type bending of space-based inflated membrane structures," *Journal of Aerospace Engineering*, Vol. 8, No. 2, pp. 120-125, Apr, 1995.

89 Thomas, J.C., and Wielgosz, C., "Deflections of highly inflated fabric tubes," *Journal of Thin-Walled Structures*, Vol. 42, pp. 1049-1066, 2004.

90 Davids, W.G., "Finite-element analysis of tubular fabric beams including pressure effects and local fabric wrinkling," *Finite Element in Analysis and Design*, Vol. 44, No. 1-2, pp. 24-33, Dec, 2007.

91 Davids, W.G., and Zhang, H., "Beam finite element for nonlinear analysis of pressurized fabric beam-columns," *Engineering Structures*, Vol. 30, pp. 1969-1980, 2008.

92 Davids, W.G., "In-plane load-deflection behaviour and buckling of pressurized fabric arches," *Journal of Structural Engineering*, Vol. 135, pp. 1320-1329, Nov, 2009.

93 Brayley, K.E., Davids, W.G., and Clapp, J.D., "Bending response of externally reinforced inflated braided fabric arches and beams," *Construction and Building Material*, Vol. 30, pp. 50-58, 2012.

94 Apedo, K.L., Ronel, S., Jacquelin, E., Massenzio, M., Bennani, A., "Theoretical analysis of inflatable beams made from orthotropic fabric," *Thin-Walled Structures*, Vol. 47, pp. 1507-1522, 2009.

95 Apedo, K.L., Ronel, S., Jacquelin, E., Bennani, A., and Massenzio, M., "Nonlinear finite element analysis of inflatable beams made from orthotropic woven fabric," *International Journal of Solids and Structures*, Vol. 47, pp. 2017-2033, Apr, 2010.

96 Du, Z., Tan, H., and Wang, C.G., "Wrinkling characteristic of membrane inflated truncated cone," *Proceedings of the 18th International Conference on Composite Materials*, Edinburgh, U.K, Jul 27-31, 2009.

97 Wang, C., Tan, H., Du, X., and He, X., "A new model for winkling and collapse analysis of membrane inflated beam," *Acta Mechanica Sinica*, Vol. 26, No. 4, pp. 617-623, May, 2010.

98 Lampani, L., and Gaudenzi, P., "Numerical simulation of the behaviour of inflatable structures for space," *Acta Astronautica*, Vol. 67, No. 3, pp. 362-368, 2010.

99 Wang, C.G., Du, Z.Y., Tan, H.F., "Initial wrinkling and its evolution of membrane inflated cone in bending," *Thin-Walled Structures*, Vol. 59, pp. 97-102, 2012.

100 Nguyen, T., Ronel, S., Massenzio, M., Apedo, K.L., and Jacquelin, E., "Analytical buckling analysis of an inflatable beam made of orthotropic technical textiles," *Journal of Thin-Walled Structures*, Vol. 51, pp. 186-200, 2012.

101 Ligaro, S.S., Barsotti, R., "Shear deformation in inflated cylindrical beams: An old model revisited," *Thin-Walled Structures*, Vol. 60, pp. 137-144, 2012.

102 Tamadapu, G., and DasGupta, A., "Finite inflation analysis of a hyperelastic toroidal membrane of initially circular cross-section," *International Journal of Non-Linear Mechanics*, Vol. 49, pp. 31-39, 2013.

103 Veldman, S.L., "Wrinkling prediction of cylindrical and conical inflated cantilever beams under torsion and bending," *Thin - Walled Structures,* Vol. 44, No. 2, pp. 211-215, Feb, 2006.

104 Veldman, S.L., Bergsma, O.K., and Beukers, A., " Bending of anisotropic inflated cylindrical beams," *Thin-Walled Structures,* Vol. 43, No. 3, pp. 461-475, 2005.

105 Walker, S.J.I., and Aglietti, G.S., "A study of tape spring fold curvature for space deployable structures," *Journal of Aerospace Engineerin*g, Vol. 221, No. 3, pp. 313-325, Mar 1, 2007.

106 Mansfield, E.H., "Large-deflection torsion and flexure of initially curved strip," *Proceedings of the Royal Society*, Vol. 334, London, U.K, pp. 279-298, 1973.

107 Chater, E., Hutchinson, J.W., and Neale, K.W., "Buckle propagation on a beam on a nonlinear elastic foundation," *Collapse*, (ed. Thompson, J. M. T. and Hunt, G. W.), Cambridge University Press, pp. 31-41, 1983.

108 Walker, S.J.I., "A study of three dimensional tape spring folds for space applications," *Ph.D. thesis*, University of Southampton, U.K, Nov, 2004.

109 Vyvyan, W.W., "Self-actuating, self-locking hinge," U.S. Patent 3,386,128, Jun 4, 1968.

110 Watt, A.M., and Pellegrino, S., "Tape - spring rolling hinges," *Proceedings of the 36th Aerospace Mechanisms Symposium*, Cleveland, OH, pp. 1-14, May 15-17, 2002.

111 Walker, S.J.I. and Aglietti, G.S., "Modelling the hinge moment of skew-mounted tape spring folds," *Journal of Aerospace Engineering*, Vol. 20, No. 2, pp. 102-115, 2007.

112 Glaser, R., and Caccese, V., "Experimental methods to determine in-plane material properties of polyurethane-coated nylon fabric," *Journal of the Textile Institute*, Vol. 104, No. 7, pp. 682-698, 2013.

113 "Fibremax Stabilized Nylon," *Challenge Sailcloth Sales Brochure*, 2009.

114 Cavallaro, P.V., Sadegh, A.M., and Quigley, C.J., "Contributions of strain energy and PV-work on the bending behavior of uncoated plain-woven fabric air beams," *Journal of Engineered Fibres and Fabrics*, Vol. 2, No. 1, pp. 16-30, 2007.

115 Lin, J., "Prediction of elastic properties of plain weave fabric using geometrical modelling," *Woven Fabric Engineering (Book)*, Polona Dobnik Dubrovski (Ed.), pp. 135-154, ISBN:978-953-307-194-7, InTech, Published Aug, 2010.

116 Xia, W., and Nadler, B., "Three-scale modelling and numerical simulation of fabric material," *International Journal of Engineering Science*, Vol. 49, pp.229-239, 2011.

117 Buet-Gautier, K., and Boisse, P., "Experimental analysis and modelling of biaxial mechanical behaviour of woven composite reinforcements," *Experimental Mechanics*, Vol. 41, No. 3, pp. 260-269, Sep, 2001.

118 Sun, H., Pan, N., and Postle, R., "On the Poisson's ratios of a woven fabric," *Composite Structures*, Vol. 68, No. 4, pp. 505-510, May, 2005.

119 Leaf, G.A., and Sheta, A.M.F., "The initial shear modulus of plain-woven fabrics," *Journal of The Textile Institute*, Vol. 75, No. 3, pp. 157-163, 1984.

120 Williams, R.W., "Measuring and modelling the anisotropic, nonlinear and hysteretic and behaviour of woven fabrics," *Thesis*, University of Iowa, http://ir.uiowa.edu/etd/907, 2010.

121 Quaglini, V., Corazza, C., and Poggi, C., "Experimental characterization of orthotropic technical textiles under uniaxial and biaxial loading," *Composites, Part A: applied science and manufacturing*, Vol. 39, pp. 1331-1342, 2008.

122 Potluri, P., Perez Ciurezu, D.A., and Ramgulam, R.B., "Measurement of meso-scale shear deformations for modelling textile composites," *Composites: Part A applied science and manufacturing,* Vol. 37, pp. 303-314, 2006.

123 Diehl, T., Dixon, R.D., Lamontia, M.A., and Hanks, J.A., "The development and use of a robust modelling approach for predicting structural performance of woven fabrics using ABAQUS," *Proceeding of the ABAQUS USERS' conference*, Munich, Germany, Jun 4-6, 2003.

124 Hutchings, A.L., Braun, R., Masuyama, K., Welch, J.V., "Experimental determination of material properties for inflatable aeroshell structures," *Proceedings of the 20th AIAA Aerodynamic Decelerator Systems Technology Conference and Seminar,* AIAA-2009-2949, Seattle, WA, May 4-7, 2009.

125 Zhu, D., Mobasher, B., Vaidya, A., and Rajan, S.D., "Mechanical behaviours of Kevlar 49 fabric subjected to uniaxial, biaxial tension and in-plane larger shear deformation," *Composites Science and Technology*, Vol. 74, pp. 121-130, 2013.

126 Kilby, W.F., "Planar stress-strain relationships in woven and fabrics," *Journal of Textile Institute*, Vol. 54, pp. 9-27, 1963.

127 Pan, B., Qian, K., Xie, H., and Asundi, A., "Two-dimensional digital image correlation for in-plane displacement and strain measurement: a review," *Measurement science and technology*, Vol. 20, pp. 1-17, 2009.

128 "DaVis 8.1 Software product-manual," Manual *1003017_StrainMaster_D81.pdf*, LaVision GmbH, Gottingen, Germany, Dec, 2012.

129 Welch, J.V., Wang, S., Blandino, J.R., and McEvoy, K., "Super pressure balloon non-linear structural analysis and correlation using photogrammetric measurements," *AIAA 5th ATIO and 16th Lighter than air sys tech. and balloon systems conferences*, AIAA-2005-7447, Virginia, US, Sep 26-28, 2005.

130 Jinyun, Z., Yi, L., Lam, J., and Xuyong, C., "The Poisson ratio and modulus of elastic knitted fabrics," *Textile research journal*, Vol. 80, No. 18, pp. 1965-1969, 2010.

131 Solderman, K.L., and Giroud, J.P., "Relationships between uniaxial and biaxial stresses and strains in geosynthetics," *Geosynthetics International*, Vol. 2, No. 2, pp. 495-504, 1995.

132 Jauffrès, D., Sherwood, J.A., Morris, C.D., and Chen, J., "Discrete mesoscopic modelling for the simulation of woven-fabric reinforcement forming," *International Journal of Material Forming*, Vol. 3, No. 2, pp. 1205-1216, Sep, 2010.

133 Dridi, S., Dougui, A., and Boisse, P., "Finite element analysis of bias extension test using an orthotropic hyperelastic continuum model for woven fabric," *Journal of the Textile Institute*, Vol. 102, No. 9, pp. 781-789, 2011.

134 Aboshio, A., Green, S., and Ye, J., "Structural performance of a woven-fabric reinforced composite as applied in construction of inflatable offshore fender barrier structures," *International Journal of Structural Stability and Dynamics*, 2014.

135 Turner, A.M., Kabche, J.P., Peterson, M.L., and Davids, W.G., "Tension/torsion testing of inflatable fabric tubes," *Experimental Techniques*, Vol. 32, No. 2, pp. 47-52, Mar-Apr, 2008.

136 Hibbitt, Karlsson and Sorensen, "Getting started with ABAQUS/explicit," *ABAQUS user's manual* (ABAQUS), Version 6.9, 2009.

137 Fang, H., Lou, M., and Hah, J., "Deployment study of a self-rigidizable inflatable boom," *Journal of Spacecraft and Rockets*, Vol. 43, No. 1, pp. 25-30, Jan-Feb, 2006.

138 Cook, A.J., Walker, S.J.I., and Dobbs, H., "Experimental Research on the use of Tape Springs on Inflatable Structures," *28th International Symposium on Space Technology and Science*, 2011-c-37, 5-12th Jun, Okinawa, Japan, 2011.

139 Cook, A.J., Walker, S.J.I., "Experimental research on tape spring supported space inflatable structures," *Acta Astronautica,* Accepted 21 Oct, Available online 31 Oct, 2015, Pending publication.

140 Cook, A.J., Walker, S.J.I., "Material Properties of a Fabric Inflatable Boom Determined from Infaltion," *Composite Structures Journal,* Pending publication.

141 Pukniel, A., Coverstone, V., Burton, R., Carroll, D., "Attitude control of the Cubesail Solar Sailing spacecraft in low Earth orbit," *Proceedings of the 2nd International Symposium on Solar Sailing*, New York City, NY, Jul 20-22, 2010, pp. 87-90.

142 Ash, R., Andrew, L., Tynis, J., Laub, J., "CubeSat deorbit devices," *Old Dominion University*, Dec 10, 2010.

143 Stark, J., Swinerd, G., Fortescue, "Spacecraft systems engineering," Stark, J., Swinerd, G.*,(ed), Wiley*, 2003.

144 Jacchia, L.G., "Variations in the Earth's upper atmosphere as revealed by satellite drag," *Reviews of modern physics,* Vol. 35, Issue 4, 1963, pp. 973-991.